ALMA MATER STUDIORUM
UNIVERSITÀ DI BOLOGNA

DEPARTMENT OF PHYSICS AND ASTRONOMY ”A. RIGHI”

SECOND CYCLE DEGREE

PHYSICS

Supercooled first-order phase transitions and gravitational waves in sub-GeV dark sectors

Supervisor
Prof. Silvia Pascoli

Co-supervisor
Dr. Salvador Rosauro-Alcaraz

Defended by
Matteo Zandi

Graduation Session 09/2025

Academic Year 2024/2025

Abstract

In the summer of 2023, various pulsar timing array (PTA) collaborations reported the first evidence for a stochastic gravitational wave background (SGWB) in the nHz frequency range. Among the possible explanations for this signal, a cosmological first-order phase transition (FOPT) is one of the most intriguing, as its realisation would open a new window into the early Universe to probe new physics. In this thesis, we present a novel semi-analytic, model-independent framework to study supercooled FOPTs in classically scale-invariant models. The goal is to establish the relation between the Lagrangian parameter space and the SGWB signal as clearly as possible. The main idea is to exploit collective couplings and the high-temperature expansion to write the effective potential as a polynomial, for which analytic results for the bounce action are known. We then derive a simplified equation for the computation of the percolation temperature, together with analytic expressions for the thermal parameters that enter into the expected SGWB spectrum. To validate and illustrate our proposal, we apply our framework to phenomenological sub-GeV dark abelian $U(1)_D$ models, which are able to explain the PTA signal. We find that our approach not only reproduces full numerical analyses with high accuracy and significantly reduced computational time, but also provides valuable physical insights.

Contents

List of Figures

List of Acronyms

BBN Big Bang Nucleosynthesis

BSM Beyond the Standard Model

CMB Cosmic Microwave Background

DS Dark Sector

EW Electroweak

FLRW Friedmann-Lemaitre-Robertson-Walker

FOPT First-Order Phase Transition

GR General Relativity

GW Gravitational Waves

NANOGrav North American Nanohertz Observatory for Gravitational Waves

PT Phase Transition

PTA Pulsar Timing Array

QCD Quantum Chromodynamics

QFT Quantum Field Theory

RGE Renormalisation Group Equation

RSB Radiative Symmetry Breaking

SGWB Stochastic Gravitational Wave Background

SM Standard Model

SSB Spontaneous Symmetry Breaking

VEV Vacuum Expectation Value

1 Introduction

So little we know about the Universe, yet so much we have already learned. The quest to understand Nature through the laws of physics has been driven by curiosity and creativity, guiding scientists to unveil the underlying principles that govern reality: from the smallest building blocks described by Quantum Field Theory (QFT), to the largest cosmic structures explained by General Relativity (GR). Among the many unanswered questions, the early Universe represents a fascinating frontier, not only to trace its earliest moments, but also to investigate the nature of fundamental interactions. Thus, the early Universe emerges as a natural laboratory at the intersection of cosmology and high-energy particle physics.

Cosmological observations, such as the Cosmic Microwave Background (CMB) radiation [1] and the primordial abundances of light elements produced during Big Bang Nucleosynthesis (BBN) [2], indicate that the early Universe was a thermal plasma, whose temperature increases as one approaches the Big Bang. This epoch is of particular interest for high-energy particle physics, because it reached energy scales far beyond those accessible in terrestrial experiments. However, our current direct observational access is limited by the CMB: no electromagnetic signal from epochs earlier than photon decoupling can reach us. This constraint does not apply to Gravitational Wavess (GWs), as they decouple from the thermal plasma near the Planck scale and propagate unaltered through cosmic history, preserving information from times earlier than the CMB. Other species, such as neutrinos, also decouple before recombination and could provide complementary insights into the early Universe.

For this reason, the groundbreaking discovery of GW from binary black hole mergers by the Laser Interferometer Gravitational-Wave Observatory (LIGO) collaboration in 2015 [3], a century after their prediction in 1916 by Einstein [4, 5], inaugurated a new era of astronomical and cosmological observations. More recently, in 2023, several Pulsar Timing Array (PTA) collaborations, namely North American Nanohertz Observatory for Gravitational Waves (NANOGrav) [6], Chinese Pulsar Timing Array (CPTA) [7], European Pulsar Timing Array (EPTA) [8] and Parkes Pulsar Timing Array (PPTA) [9], have reported the first compelling evidence at the 3-4σ level of a Stochastic Gravitational Wave Background (SGWB) in the nHz frequency range. This breakthrough may open an unprecedented observational window into the early Universe.

Due to the weakness of the gravitational interaction, only the most violent events can explain the PTA signal, which may originate from astrophysical or cosmological sources. The leading astrophysical candidates are Supermassive Black Hole Binaries (SMBHBs) [10–14], but they require departures from standard astrophysics [15] and no individual SMBHB has been detected [16]. These uncertainties motivate the hypothesis that at least part of the observed PTA signal may have a cosmological origin [17–22], including cosmic inflation, scalar-induced GWs, First-Order Phase Transitions (FOPTs), metastable cosmic strings and domain walls. In particular, a cosmological FOPT [23–27] fits the PTA signal better than SMBHBs do, given the large amplitude and spectral shape [28]. All this evidence provides strong motivation to investigate cosmological FOPTs, both refining theoretical methods and developing phenomenological models.

Phase Transitions (PTs) are common phenomena in Nature and may also occur in a cosmological scenario, where the vacuum of the theory, driven by the temperature dependence of the scalar effective potential, changes during the evolution of the Universe and gives the scalar field a Vacuum Expectation Value (VEV), through the mechanism of Spontaneous Symmetry Breaking (SSB). In a FOPT,

a metastable symmetric false vacuum is separated by a barrier from a lower-energy true vacuum. The transition proceeds via quantum tunneling through the barrier [29, 30] or thermal fluctuations [31–33] over the barrier, leading to the nucleation of bubbles of true vacuum within the false vacuum sea, similar to bubbles in boiling water. If the bubbles are large enough, the pressure from the potential energy difference will overcome the surface tension and the bubbles will expand [29]. Collisions between bubbles, together with sound waves and turbulence in the surrounding thermal plasma, break spherical symmetry and generate GWs, which subsequently propagate freely until today [34–37]. On the other hand, if the PT is second-order or a crossover, the absence of the barrier makes the transition between the vacuum states smooth and continuous, so that no abrupt events can generate observable GWs.

The SM of particle physics predicts the occurrence of two PTs: the Electroweak (EW) PT and the Quantum Chromodynamics (QCD) PT, both of which are expected to be crossover [38–44]. However, it is known that the SM fails to describe a number of observed phenomena in the Universe, such as neutrino oscillations, baryon asymmetry, and dark matter, which motivates the development and search for Beyond the Standard Model (BSM) physics. Interestingly, the characteristics of the PTA signal point toward a VEV on the order of hundreds of MeV, hinting at new particles below the GeV scale. This is suitable for Dark Sectors (DSs), extensions of the SM involving new particles and interactions, which couple to it through renormalisable interaction portals, such as the kinetic mixing between a dark photon and a SM gauge boson, or the interaction between a dark scalar and the Higgs boson. Experimental searches for these scenarios are ongoing [45, 46].

In this thesis, we investigate supercooled FOPTs in classically scale-invariant or nearly-conformal models. In this class of models, the barrier between the false and true vacuum is absent at zero temperature and is generated by thermal corrections, leading to significant supercooling. This occurs when the onset of the PT is significantly delayed, so that the vacuum energy density becomes comparable to or even exceeds the radiation energy density, inducing a period of inflation followed by reheating [47–50]. This process releases a large amount of latent heat, making these models candidates to explain a strong observable SGWB [51–61].

In particular, we propose a new semi-analytic, model-independent framework to study supercooled FOPTs in classically scale-invariant models. The aim of this thesis is to establish the relation between the Lagrangian parameter space and the SGWB signal as clearly as possible, clarifying how macroscopic thermal parameters governing the FOPT emerge from fundamental microscopic couplings. The main advantage of this approach is to obtain rapid information about the SGWB spectrum once a model is specified, without performing a heavy numerical analysis, and to provide valuable insights into the underlying physics. This framework builds upon and supersedes previous results in Refs. [58–61].

Chapter 2 presents the relevant background, such as cosmology and the history of the early Universe, the theory of GWs and SGWB with their detection via PTAs, the SM and the mechanism of SSB, and dark sector scenarios. In Chapter 3, we review the theory of cosmological FOPTs. We develop the general expressions for the effective potential and the false vacuum decay rate, including one-loop and finite-temperature contributions. We then compute the false vacuum fraction to define the percolation temperature T_p, at which the thermal parameters characterising the FOPT are evaluated: the transition strength α, the inverse transition duration β, and the bubble wall velocity v_w. Chapter 3 concludes with the presentation of the expected SGWB spectrum, based on Laser Interferometer Space Antenna (LISA) Cosmology Working Group's latest results [62].

Building upon the knowledge of the previous chapters, we present the novel semi-analytic, model-independent framework in Chapter 4. The starting point consists of writing the most general form of the effective potential in a polynomial form, so that a closed-form analytic bounce action can be used to compute the nucleation rate. We then derive a root-finding equation to calculate the percolation temperature T_p, which replaces the expensive integrals in its definition, along with explicit analytic expressions for the thermal parameters. We apply this framework to phenomenological sub-GeV dark abelian $U(1)_D$ extensions of the SM, which include a dark photon, a dark scalar, and a dark fermion. We compare our approach against full numerical computations and validate it using posterior distributions from the NANOGrav 15-year dataset, while also drawing physical insights.

2 Cosmology, gravitational waves and particle physics

The theory of cosmological PTs is an interdisciplinary field situated at the intersection of various areas of physics, including GR and QFT. In this chapter, we present relevant concepts that are necessary for their understanding: cosmology is introduced in Sec. 2.1, GWs are studied in Sec. 2.2, and particle physics is covered in Secs. 2.3 and 2.4, focusing on the SM and its possible DS extensions.

2.1 Cosmology

The theoretical description of modern cosmology, which is the field of physics that accounts for the origin, evolution, and structure of the Universe, started with the formulation of the theory of GR by Einstein in 1915 [63, 64], when he realised that spacetime is not a static background upon which objects move, but a dynamical entity whose geometry both affects and is affected by any form of energy. In the following decades, theoretical models to describe the Universe began to appear: in the 1920s by Friedmann [65, 66] and Lemaître [67–69], followed in the 1930s by Robertson [70–72] and Walker [73]. These models are known today as Friedmann-Lemaitre-Robertson-Walker (FLRW) models.

In parallel with these theoretical developments, astronomical observations helped shape our understanding of the Universe. One of the most important discoveries was the expansion of the Universe and the measurement of the relation between galaxy recession velocity and redshift in 1929 by Hubble [74]. As a consequence, at early times, the Universe must have been in a hot dense state, hence the name Hot Big Bang, proposed by Hoyle in 1948 in contrast to his steady-state theory, formulated together with Bondi and Gold [75, 76]. Evidence supporting the Hot Big Bang scenario accumulated in the following years: the successful calculation of the primordial abundance of light elements in 1948 by Alpher, Bethe, Gamow and Herman [77–79], and the discovery of the CMB radiation in 1965, predicted by Dicke, Peebles and Wilkinson [80] and accidentally observed in the same year by Penzias and Wilson [81]. These discoveries marked the beginning of modern precision cosmology, with the subsequent refinement of instruments to probe the Universe, such as electromagnetic telescopes and GW detectors (interferometers, PTAs).

Further observations indicated the presence of non-luminous components in the Universe: dark matter and dark energy. The first evidence of dark matter dates back to 1933, when Zwicky [82, 83] found a discrepancy between the mass inferred from visible electromagnetic radiation and the one derived from the average velocity dispersion of galaxies in the Coma cluster. Additional evidence came in the late 1970s, when Rubin, Ford and Thonnard [84, 85] found a disagreement between the mass distribution of spiral galaxies extracted using observed light distribution and the one estimated from the circular velocity of stars and gas. This observation can be explained by a spherical halo of dark matter extending beyond the visible galaxy. Since then, more evidence has emerged: visible mass distribution is insufficient to explain gravitational lensing in galaxy clusters [86–89], including the case of colliding clusters [90–92]; the star formation rate is consistent with observations when performing large-scale N-body simulations of the Universe; and the amplitudes and peak positions of the CMB power spectrum, together with Baryon Acoustic Oscillations (BAO), provide the most precise measurements of dark matter abundance [1]. On the other hand, the first evidence of dark

energy came in 1998 from observations of Type Ia supernovae [93, 94], confirmed also by BAO measurements. At the time of writing, the nature of dark matter and dark energy remains unknown.

These results have led to the formulation of the Standard Model of Cosmology, known as the ΛCDM model, where Λ represents dark energy and CDM stands for cold dark matter. In this section, after introducing the FLRW metric, the ΛCDM model and the thermodynamic properties of the primordial plasma, we describe the most relevant events in the thermal history of the Universe, following Refs. [95–97].

2.1.1 The ΛCDM model

Within the framework of GR, the geometry of spacetime is described by the metric $g_{\mu\nu}$, which allows measuring distances in curved spacetime by means of the invariant element

$$ds^2 = g_{\mu\nu} dx^\mu dx^\nu \ . \tag{2.1.1}$$

The dynamics of the spacetime geometry is determined by the distribution of matter and energy within it, as described by the Einstein field equations

$$G_{\mu\nu} = R_{\mu\nu} - \frac{1}{2} R g_{\mu\nu} = 8\pi G T_{\mu\nu} \ , \tag{2.1.2}$$

where $G_{\mu\nu}$ is the Einstein tensor, constructed non-linearly upon the metric $g_{\mu\nu}$ and its derivatives through the Ricci tensor $R_{\mu\nu}$, the Ricci scalar R, and the Christoffel symbols $\Gamma^\alpha_{\mu\nu}$, defined as

$$R_{\mu\nu} = \partial_\alpha \Gamma^\alpha_{\mu\nu} - \partial_\nu \Gamma^\alpha_{\mu\alpha} + \Gamma^\alpha_{\alpha\lambda}\Gamma^\lambda_{\mu\nu} - \Gamma^\alpha_{\nu\lambda}\Gamma^\lambda_{\mu\alpha} \ , \tag{2.1.3}$$

$$R = g^{\mu\nu} R_{\mu\nu} \ , \tag{2.1.4}$$

$$\Gamma^\alpha_{\mu\nu} = \frac{1}{2} g^{\alpha\beta} \left(\partial_\mu g_{\nu\beta} + \partial_\nu g_{\mu\beta} - \partial_\beta g_{\mu\nu} \right) \ . \tag{2.1.5}$$

Finally, $T_{\mu\nu}$ is the energy-momentum tensor, which describes the density and flux of energy and momentum in spacetime. The Einstein field equations in Eq. (2.1.2), together with the metric in Eq. (2.1.1), can be simplified by exploiting the symmetries of the system.

In the case of the Universe, numerous observations, such as the large-scale distribution of galaxies and the uniformity of the CMB radiation, which exhibits anisotropies of order 10^{-5} once the dipole due to our relative motion is removed, suggest that the Universe is spatially homogeneous and isotropic on scales larger than $\mathcal{O}(100\ \text{Mpc})$. This assumption is known as the cosmological principle. Homogeneity implies that the properties of the Universe are the same at all points in space, thus the metric depends only on time. Isotropy means that the Universe looks the same in all directions, so that the metric is diagonal and has equal spatial components[1]. The most general metric that fulfils these criteria is the FLRW metric

$$ds^2 = -dt^2 + a(t)^2 \left(\frac{dr^2}{1 - kr^2} + r^2 (d\theta^2 + \sin^2\theta d\phi^2) \right) \ , \tag{2.1.6}$$

[1]Mathematically speaking, isotropy is the invariance under rotations, which results in three Killing vectors, and homogeneity is invariance under translations, which adds three more Killing vectors.

where (r, θ, ϕ) are comoving spherical coordinates, $a(t)$ is the cosmic scale factor, and k is the curvature parameter, which, after a suitable rescaling, can take the values $k = 0, +1, -1$ for flat, closed, and open Universes, respectively.

To be consistent with the symmetries of the metric, the energy-momentum tensor must also share these properties. The simplest realisation is a perfect fluid with energy density ρ and pressure p

$$T_{\mu\nu} = (\rho + p)u_\mu u_\nu + p g_{\mu\nu} \,, \tag{2.1.7}$$

where u_μ is the four-velocity of the fluid. The $\mu = 0$ component of energy-momentum conservation, $\nabla_\mu T^{\mu\nu} = 0$, leads to the continuity equation

$$\dot{\rho} + 3\frac{\dot{a}}{a}(\rho + p) = 0 \,. \tag{2.1.8}$$

Inserting the energy-momentum tensor for a perfect fluid in Eq. (2.1.7) inside Einstein's equation in Eq. (2.1.2) with the FLRW metric in Eq. (2.1.6), we obtain two independent differential equations for the cosmic scale factor $a(t)$, known as Friedmann equations

$$\left(\frac{\dot{a}}{a}\right)^2 = \frac{8\pi G}{3}\rho - \frac{k}{a^2} \,, \tag{2.1.9}$$

$$\frac{\ddot{a}}{a} = -\frac{4\pi G}{3}\left(\rho + 3p\right) \,. \tag{2.1.10}$$

The two Friedmann equations in Eqs. (2.1.9) and (2.1.10), and the continuity equation in Eq. (2.1.8) are not independent, as the continuity equation can be derived by differentiating the first Friedmann equation in Eq. (2.1.9) with respect to time and subtracting the second Friedmann equation in Eq. (2.1.10).

In order to solve these equations, we need to specify an equation of state, which relates the pressure p to the energy density ρ. For a barotropic equation of state, characterised by a constant time-independent parameter w

$$p = w\rho \,, \tag{2.1.11}$$

the continuity equation in Eq. (2.1.8) becomes

$$\dot{\rho} + 3\frac{\dot{a}}{a}(1 + w)\rho = 0 \quad \Rightarrow \quad \rho \propto a^{-3(w+1)} \,. \tag{2.1.12}$$

Moreover, assuming a flat Universe with $k = 0$ and inserting the solution of the continuity equation in Eq. (2.1.12) into the first Friedmann equation in Eq. (2.1.9), we find that, for $w \neq -1$, the cosmic scale factor $a(t)$ of each component evolves as

$$\dot{a} \propto a^{-\frac{1+3w}{2}} \quad \Rightarrow \quad a(t) \propto t^{\frac{2}{3(1+w)}} \,. \tag{2.1.13}$$

For $w = -1$, the energy density is constant $\rho =$ const and the cosmic scale factor $a(t)$ evolves as

$$a(t) \propto e^{\sqrt{\frac{8\pi G\rho}{3}}t} \,. \tag{2.1.14}$$

According to the value of w in Eq. (2.1.11), we can distinguish different components of the Universe:

- $w = 0$ describes a set of collisionless non-relativistic particles called matter or dust. From Eq. (2.1.12), the energy density of matter scales as $\rho \propto a^{-3}$, while from Eq. (2.1.13), the cosmic scale factor evolves as $a(t) \propto t^{\frac{2}{3}}$. Examples of matter are baryons and dark matter.

- $w = \frac{1}{3}$ describes a set of relativistic particles called radiation, consistent with the vanishing trace of the energy-momentum tensor. From Eq. (2.1.12), the energy density of radiation scales as $\rho \propto a^{-4}$, while from Eq. (2.1.13), the cosmic scale factor evolves as $a(t) \propto t^{\frac{1}{2}}$. Examples of radiation are photons and neutrinos.

- $w = -1$ describes vacuum energy or the cosmological constant. In this case, the energy density is constant and the cosmic scale factor evolves exponentially as shown in Eq. (2.1.14).

From the different scaling of the energy density for these components, we can understand the dominant component at different epochs of the Universe. Both matter and radiation dilute as the Universe expands, but radiation dilutes faster. Hence, at very early times, the Universe was radiation dominated, but eventually matter became the dominant component until it diluted sufficiently for vacuum energy to prevail, as it does today. The evolution of the energy densities of the three different components is plotted in Fig. 1.

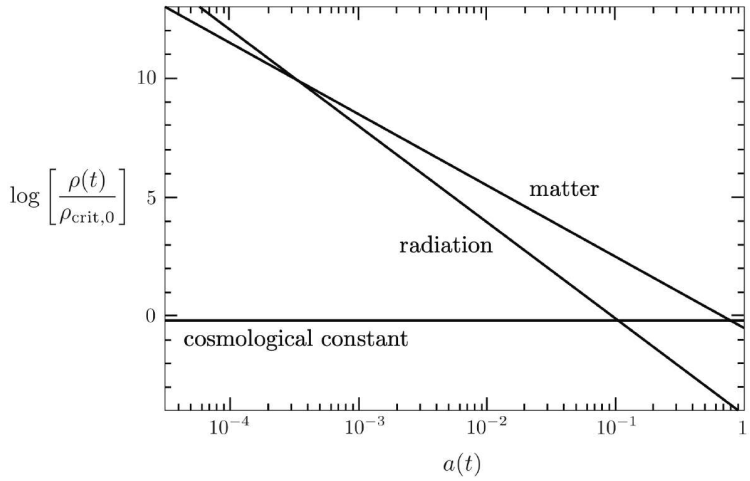

Figure 1: The energy densities ρ of the components of the Universe over the current critical one $\rho_{\mathrm{crit},0}$ as a function of the cosmic scale factor $a(t)$. Figure taken from Ref. [97].

We introduce the Hubble parameter, which measures the expansion rate of the Universe

$$H = \frac{\dot{a}}{a}\,, \tag{2.1.15}$$

and, for each component i of the Universe, we define the dimensionless density parameter

$$\Omega_i = \frac{\rho_i}{\rho_c}\,, \tag{2.1.16}$$

where $\rho_c = \frac{3H^2}{8\pi G}$ is the critical density. The critical density is the energy density corresponding to a flat Universe, i.e. the case $k = 0$ in the first Friedmann equation in Eq. (2.1.9). In terms of the Hubble

parameter H in Eq. (2.1.15) and the density parameter Ω in Eq. (2.1.16), the first Friedmann equation in Eq. (2.1.9) becomes

$$\Omega - 1 = \frac{k}{a^2 H^2} \,, \tag{2.1.17}$$

where $\Omega = \sum_i \Omega_i$ is the total density parameter. Since $a^2 H^2 > 0$ in Eq. (2.1.17) is always positive, the sign of the curvature parameter k is determined entirely by whether the density parameter Ω is greater than, equal to or less than 1: if $\Omega > 1$, then $k > 0$ and the Universe is closed; if $\Omega = 1$, then $k = 0$ and the Universe is flat; if $\Omega < 1$, then $k < 0$ and the Universe is open.

Including the different components of the Universe, we can write the first Friedmann equation in Eq. (2.1.9) as

$$H^2 = \frac{8\pi G}{3} \sum_i \rho_i - \frac{k}{a^2} = H_0^2 \left(\Omega_{r,0} a^{-4} + \Omega_{m,0} a^{-3} + \Omega_{k,0} a^{-2} + \Omega_{\Lambda,0} \right) \,, \tag{2.1.18}$$

where the subscript 0 denotes the present-day value of the corresponding quantity, and we have adopted the convention that the present cosmic scale factor is normalised to unity, $a_0 \equiv a(t_0) = 1$. Observations of the CMB by the Planck telescope [1], in combination with Type Ia supernovae and BAO, have allowed precise measurements of the energy content of the Universe [98], finding that it is spatially flat

$$\Omega_{k,0} = 0.0007 \pm 0.0019 \,, \tag{2.1.19}$$

and the density parameters are

$$\Omega_{\Lambda,0} \simeq 0.686 \,, \quad \Omega_{\text{DM},0} \simeq 0.266 \,, \quad \Omega_{\text{b},0} \simeq 0.0494 \,, \quad \Omega_{\gamma,0} \simeq 5.38 \times 10^{-5} \,, \quad 0.0012 < \Omega_{\nu,0} < 0.003 \,. \tag{2.1.20}$$

Here $\Omega_{\Lambda,0}$ corresponds to dark energy, $\Omega_{\text{DM},0}$ to dark matter, $\Omega_{\text{b},0}$ to baryonic matter, $\Omega_{\gamma,0}$ to photons, and $\Omega_{\nu,0}$ to neutrinos, with the upper bound set by oscillation experiments and the lower bound by CMB and BAO data.

There is an unresolved tension in the Hubble parameter today H_0: indirect determinations from CMB and BAO [1] yield $H_0 = (67.4 \pm 0.53)$ km s^{-1} Mpc^{-1}, while local measurements from stellar redshift [99] indicate a higher value of $H_0 \simeq (73.2 \pm 1.3)$ km s^{-1} Mpc^{-1}. It is customary to express the Hubble parameter today as

$$H_0 = 100h \text{ km s}^{-1}\text{Mpc}^{-1} \,, \tag{2.1.21}$$

where $h = 0.674$ using the Planck measurements [1].

2.1.2 Thermodynamics in the early Universe

Since the Universe is expanding, going backwards in time corresponds to a smaller cosmic scale factor $a(t)$, as shown in Eq. (2.1.13), while the temperature T increases. In the Hot Big Bang model, the early Universe is described as a hot thermal plasma of particles in thermal equilibrium, maintained by rapid interactions. It is studied using the tools of statistical mechanics, following how particle distributions change over time rather than the dynamics of individual particles. We introduce thermodynamic quantities to describe the thermal plasma: the number density n, the energy density ρ

and the pressure p

$$n = g \int \frac{d^3p}{(2\pi)^3} f(|\mathbf{p}|) \,, \tag{2.1.22}$$

$$\rho = g \int \frac{d^3p}{(2\pi)^3} E(|\mathbf{p}|) f(|\mathbf{p}|) \,, \tag{2.1.23}$$

$$p = \frac{g}{3} \int \frac{d^3p}{(2\pi)^3} \frac{|\mathbf{p}|^2}{E(|\mathbf{p}|)} f(|\mathbf{p}|) \,, \tag{2.1.24}$$

where g is the number of degrees of freedom and $f(|\mathbf{p}|)$ is the distribution function, depending only on the magnitude of the momentum $|\mathbf{p}|$ and not on $\mathbf{x}$ because of homogeneity or the full vector $\mathbf{p}$ because of isotropy. The energy of a particle with momentum $\mathbf{p}$ and mass m is $E(|\mathbf{p}|) = \sqrt{|\mathbf{p}|^2 + m^2}$, where we have neglected interaction energies among particles. The distribution function $f(|\mathbf{p}|)$ controls how particles are distributed according to their momentum $\mathbf{p}$ and is determined by the Fermi-Dirac or Bose-Einstein statistics

$$f(|\mathbf{p}|) = \frac{1}{e^{\frac{E(|\mathbf{p}|)-\mu}{T}} \pm 1} \,, \tag{2.1.25}$$

where $+$ $(-)$ is for fermions (bosons) and μ is the chemical potential. At low temperatures, both quantum distributions in Eq. (2.1.25) reduce to the classical Maxwell-Boltzmann distribution

$$f(|\mathbf{p}|) = e^{-\frac{E(|\mathbf{p}|)-\mu}{T}} \,. \tag{2.1.26}$$

For relativistic species, whose mass and chemical potential are much smaller than the temperature $\mu,\ m \ll T$, the thermodynamic quantities in Eqs. (2.1.22) (2.1.23) and (2.1.24) can be approximated as

$$n = g \frac{\zeta(3)}{\pi^2} T^3 \times \begin{cases} 1 & \text{for bosons} \\ \frac{3}{4} & \text{for fermions} \end{cases} \,, \tag{2.1.27}$$

$$\rho = g \frac{\pi^2}{30} T^4 \times \begin{cases} 1 & \text{for bosons} \\ \frac{7}{8} & \text{for fermions} \end{cases} \,, \tag{2.1.28}$$

$$p = \frac{\rho}{3} \,, \tag{2.1.29}$$

where $\zeta(3) \simeq 1.202$. For non-relativistic species with temperature smaller than their mass $T \ll m$ and energy given by $E = m + \frac{p^2}{2m}$, the thermodynamic quantities in Eqs. (2.1.22) (2.1.23) and (2.1.24) can be approximated as

$$n = g \left(\frac{mT}{2\pi}\right)^{3/2} e^{-\frac{m}{T}} \,, \tag{2.1.30}$$

$$\rho = mn + \frac{3}{2} nT \simeq mn \,, \tag{2.1.31}$$

$$p = nT \ll \rho \,, \tag{2.1.32}$$

Comparing the relativistic limits in Eqs. (2.1.27) and (2.1.28) with the non-relativistic counterparts in Eqs. (2.1.30) and (2.1.31), we see that non-relativistic species have number and energy densities that are exponentially suppressed relative to the relativistic case. Consequently, we can neglect the

contribution of non-relativistic species to the energy density, which can be written as

$$\rho = \sum_i \rho_i = g_*(T)\frac{\pi^2}{30}T^4 \,, \tag{2.1.33}$$

where we have defined the effective number of relativistic degrees of freedom

$$g_*(T) = \sum_i^{\text{bosons}} g_i \left(\frac{T_i}{T}\right)^4 + \frac{7}{8}\sum_i^{\text{fermions}} g_i \left(\frac{T_i}{T}\right)^4 \,, \tag{2.1.34}$$

and taken into account the possibility to have different temperatures for different species. The evolution of the SM effective number of relativistic degrees of freedom $g_*(T)$ is illustrated in Fig. 2, in which each arrow with a particle corresponds to the time when they decouple from the thermal plasma or a PT.

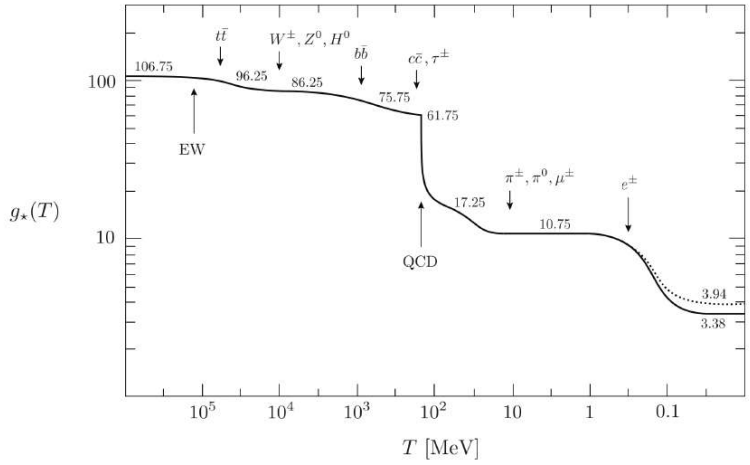

Figure 2: The effective number of relativistic degrees of freedom $g_*(T)$ (solid) and the effective number of relativistic degrees of freedom for entropy $g_{*s}(T)$ (dotted) for the SM particle content as a function of the temperature. Decoupling of particles and phase transitions are represented with an arrow. Figure taken from Ref. [97].

For a flat Universe $k = 0$, the first Friedmann equation in Eq. (2.1.9) combined with the energy density ρ in Eq. (2.1.33) relates the Hubble parameter H in Eq. (2.1.15) to the temperature T

$$H = \sqrt{\frac{8\pi G}{3}}\rho = \sqrt{\frac{\pi^2 g_*(T)}{90\bar{m}_{\text{Pl}}^2}}T^2 \simeq 1.66 g_*^{1/2}(T)\frac{T^2}{\bar{m}_{\text{Pl}}} \,, \tag{2.1.35}$$

where we have introduced the reduced Planck mass $\bar{m}_{\text{Pl}} = \sqrt{\frac{1}{8\pi G}} \simeq 2.43 \times 10^{18}$ GeV, related to the Planck mass m_{Pl} by $m_{\text{Pl}} = \sqrt{8\pi}\bar{m}_{\text{Pl}}$.

The entire Universe is a closed system, its total entropy is therefore conserved and can be used

to track its evolution. The entropy density s is related to the energy density ρ and pressure p by[2]

$$s = \frac{\rho + p}{T} \,. \tag{2.1.36}$$

As with the energy density ρ in (2.1.33), the entropy density s is dominated by relativistic species, which can be written as

$$s = \frac{2\pi^2}{45} g_{*s}(T) T^3 \,, \tag{2.1.37}$$

where we have defined the effective number of relativistic degrees of freedom for entropy

$$g_{*s}(T) = \sum_i^{\text{bosons}} g_i \left(\frac{T_i}{T}\right)^3 + \frac{7}{8} \sum_i^{\text{fermions}} g_i \left(\frac{T_i}{T}\right)^3 \,. \tag{2.1.38}$$

The evolution of the SM relativistic degrees of freedom for entropy $g_{*s}(T)$ is illustrated in Fig. 2. It only deviates from $g_*(T)$ after $e^\pm$ decoupling. Exploiting conservation of the total entropy

$$S = \frac{2\pi^2}{45} g_{*s}(T) T^3 a^3 \,, \tag{2.1.39}$$

we obtain a relation between the temperature T and the cosmic scale factor a

$$T \propto g_{*s}^{-1/3}(T) a^{-1} \,. \tag{2.1.40}$$

The factor $g_{*s}^{-1/3}(T)$ accounts for the entropy transferred to the plasma when a particle species becomes non-relativistic.

For a species to remain in equilibrium, its interactions must occur frequently. In particular, if its interaction rate Γ exceeds the expansion rate of the Universe H, then the species stays in equilibrium and shares the common temperature of the plasma. We can distinguish different types of equilibrium:

- Kinetic equilibrium is maintained when elastic self-interactions (e.g. $aa \to aa$) or elastic scatterings with other species (e.g. $ab \to ab$) redistribute kinetic energy without changing particle numbers. Its loss is referred to as decoupling.

- Chemical equilibrium holds when number-changing interactions (e.g. $a\bar{a} \to b\bar{b}$ or $ab \to cd$) occur at equal rates in both directions, keeping the chemical potentials of the interacting species in balance. Its loss is called freeze-out.

- Thermal equilibrium is achieved when all species share a common temperature, with no net energy exchange. This requires that both kinetic and chemical equilibrium are satisfied.

In an expanding Universe, particles are not always in thermal equilibrium. A useful rule of thumb[3]

[2] This can be shown by using the first law of thermodynamics $dU = TdS - pdV$ with the definitions of the density quantities, $dU = d(\rho V)$ and $dS = d(sV)$, so that $dV(\rho + p - Ts) + Vd\rho - TVds = 0$. Since dV is extensive while $d\rho$ and ds are intensive, they vanish independently, leading to $s = \frac{\rho+p}{T}$.

[3] A more rigorous treatment involves the use of the Boltzmann equation $\mathcal{L}[f] = C[f]$, where $\mathcal{L}[f]$ is the Liouville operator, which relates the distribution function f of particles to geodesics, and $C[f]$ is the collision operator, which relates f to the interactions among particles.

to estimate whether a particle species is in equilibrium is to compare the expansion rate H of the Universe with the interaction rate Γ

$$\Gamma \simeq H \,, \tag{2.1.41}$$

where $\Gamma = n\langle\sigma v\rangle$ is the definition of the interaction rate, where $\langle\sigma v\rangle$ is the thermal average of the product of the cross section σ and the relative velocity v of the incoming particles. When $\Gamma \gg H$, the interaction timescale is much shorter than the expansion timescale ($t_{\text{int}} \ll t_{\text{exp}}$), and interactions efficiently maintain equilibrium despite the expansion of the Universe. However, as the Universe expands and cools, the interaction rate decreases more rapidly than the expansion rate. Eventually, there will be a time when the interaction rate is comparable to the expansion rate $\Gamma \sim H$ or $t_{\text{int}} \sim t_{\text{exp}}$: from this moment on, interactions are no longer frequent enough to maintain thermal equilibrium, and the species falls out of equilibrium, with the decoupling temperature roughly given by the particle mass.

2.1.3 Thermal history of the Universe

Equipped with the tools developed in the previous sections, we can now describe the thermal history of the Universe, which is summarised in Table 1.

Event	Temperature T
Planck scale	1.42×10^{19} GeV
Inflation	?
Baryogenesis	?
EW phase transition	100 GeV
QCD phase transition	150 MeV
Neutrino decoupling	1 MeV
e^+e^- annihilation	500 keV
BBN	100 keV
Matter-radiation equality	0.75 eV
Recombination	0.26-0.33 eV
Photon decoupling	0.23-0.28 eV
Reionization	2.6-7.0 meV
Dark energy-matter equality	0.33 meV
Today	0.24 meV

Table 1: Thermal history of the Universe: timeline of key cosmological events with their approximate temperatures.

Due to the limitations of GR and QFT, there is no fundamental theory to describe energies above the Planck scale 1.42×10^{19} GeV. This also prevents us from clarifying the nature of the initial singularity, which appears if we extrapolate the cosmic scale factor $a(t)$ backwards in time.

The first events after the Big Bang are hypothetical scenarios proposed to solve open problems in physics: the horizon problem, which arises to explain why the CMB appears so homogeneous across causally disconnected Hubble patches, and the flatness problem, which emerges to account for the reason why the Universe appears to be so flat on large scales, a feature that would otherwise require extreme fine-tuning. The leading explanation is an inflationary period in which the cosmic scale factor $a(t)$ increases exponentially fast, driven by an inflaton scalar field. After inflation ends, the inflaton

decays, creating the thermal bath of SM particles. Another open problem is the observed baryon-antibaryon asymmetry of the Universe, which cannot be attributed to asymmetric initial conditions, because they would be washed out by inflation. In 1967, Sakharov [100] proposed three conditions that need to be satisfied in order to have a dynamical baryogenesis: B violation, otherwise baryon number would be conserved; C and CP violation, otherwise every baryon-producing process would be exactly balanced by its conjugate; departure from equilibrium, otherwise $\dot{B} = 0$.

Subsequently, two SSB PTs occurred: EWPT at $T \sim 100$ GeV and QCD PT at $T \sim 150$ MeV. In the EWPT, the Higgs field acquires a VEV and gives mass to gauge bosons and fermions. In the QCD PT, quarks and gluons, which are asymptotically free, become confined into hadrons (baryons and mesons), and quarks form a non-zero chiral condensate. As the temperature dropped below their rest masses, all massive species either froze out of equilibrium or became exponentially Boltzmann suppressed.

Around the MeV scale, the thermal plasma consists of photons, neutrons, protons, electrons, positrons, and neutrinos. Neutrinos are the first species to decouple. They remain in equilibrium through weak interactions such as $\bar{\nu}_e \nu_e \leftrightarrow e^- e^+$ or $e^- \bar{\nu}_e \leftrightarrow e^- \bar{\nu}_e$, whose estimated interaction rate is $\Gamma \sim G_F^2 T^5$, where $G_F = 1.17 \times 10^{-5}$ GeV^{-2} is the Fermi constant. Using the Hubble parameter H in radiation dominated era in Eq. (2.1.35), which can be estimated as $H \simeq \frac{T^2}{m_{\text{Pl}}}$, we can use the rule of thumb in Eq. (2.1.41) $\Gamma \sim H$ to obtain the decoupling temperature

$$G_F^2 T^5 \simeq \frac{T^2}{m_{\text{Pl}}} \quad \Rightarrow \quad T_\nu \simeq \left(\frac{m_{\text{Pl}}}{G_F^2}\right)^{\frac{1}{3}} \simeq 1 \text{ MeV} . \tag{2.1.42}$$

Below this temperature, neutrino species decouple from the thermal plasma. Their energy density then scales as $\rho \propto a^{-4}$, and initially they inherit the same temperature as the photons. Shortly after neutrino decoupling, when $T \lesssim m_e$, electrons and positrons annihilate into photons. Their entropy is transferred to photons but not to neutrinos, since they are no longer in thermal equilibrium. Using entropy conservation in Eq. (2.1.40) and counting relativistic degrees of freedom in Eq. (2.1.34), before $e^\pm$ annihilation $g_* = 2 + 4 \times \frac{7}{8} = \frac{11}{2}$ and after $e^\pm$ annihilation $g_* = 2$, the temperature of neutrinos is related to the temperature of photons by

$$T_\nu = \left(\frac{4}{11}\right)^{1/3} T_\gamma . \tag{2.1.43}$$

Inserting the value of $T_\gamma \simeq 2.7$ K inferred from the CMB, we find that $T_\nu \simeq 1.95$ K. No further relativistic species alter the photon temperature, so this ratio remains constant until neutrinos become non-relativistic. Using the relation in Eq. (2.1.43), we can write the energy density of neutrinos as

$$\rho_\nu(T) = \frac{7\pi^2}{40} T_\nu^4 = N_{\text{eff}} \frac{7\pi^2}{120} \left(\frac{4}{11}\right)^{4/3} T_\gamma^4 , \tag{2.1.44}$$

where N_{eff} is the effective number of neutrino species. In the ideal SM case, $N_{\text{eff}} = 3$, but taking into account that neutrino decoupling is not instantaneous, it can be partially reheated by $e^- e^+$ annihilation, the distribution is not a perfect Fermi-Dirac one, and corrections arise from oscillations, finite-temperature effects and the fact that electrons and positrons are not fully ultra-relativistic, the effective number of neutrino species becomes $N_{\text{eff}} = 3.0440 \pm 0.0002$ [101].

After that, BBN takes place: the formation of light nuclei such as hydrogen, deuterium, helium, and lithium from the primordial plasma of protons and neutrons. Neutrons and protons are kept in equilibrium by weak interactions, e.g. $n\nu_e \leftrightarrow p^+e^-$ and $ne^- \leftrightarrow p^+\bar{\nu}_e$. Assuming negligible chemical potentials for electrons and neutrinos, we have $\mu_n = \mu_p$, so the neutron-to-proton ratio follows the non-relativistic expression in Eq. (2.1.30)

$$\frac{n_n}{n_p} = \left(\frac{m_n}{m_p}\right)^{3/2} e^{-\frac{m_n - m_p}{T}} \simeq e^{-\frac{Q}{T}} , \tag{2.1.45}$$

where the mass difference is $Q = m_n - m_p \simeq 1.3$ MeV. Thus, as T drops below the MeV scale, neutrons become exponentially suppressed relative to protons. However, neutron freeze-out must be taken into account, which computed using the rule of thumb in Eq. (2.1.41) $\Gamma \simeq H$ gives $T_{\text{fo}} \simeq 1.2$ MeV[4], and substituting this temperature in the neutron-to-proton ratio in Eq. (2.1.45) yields

$$\frac{n_n}{n_p} \simeq \frac{1}{6} . \tag{2.1.46}$$

Because direct pp or nn fusion is inefficient, the former due to the Coulomb barrier, the latter because nn is unstable, BBN begins once deuterium D is formed through the reaction $p^+n \leftrightarrow D\gamma$, which is delayed until the temperature drops below 0.1 MeV due to the Boltzmann-tail of high energy photons that cause deuterium to photodisintegrate. During this delay, free neutrons decay with lifetime $\tau_n \simeq 880$ s, so the neutron-to-proton ratio in Eq. (2.1.46) does not remain truly constant, but actually slowly decreases to

$$\frac{n_n}{n_p} = e^{-\frac{Q}{T}} e^{-\frac{t}{\tau_n}} \simeq \frac{1}{7} . \tag{2.1.47}$$

The equilibrium abundance of deuterium can be estimated as

$$\frac{n_D}{n_n n_p} = \frac{3}{4}\left(\frac{2\pi m_D}{m_n m_p T}\right)^{3/2} e^{-\frac{B}{T}} , \tag{2.1.48}$$

where $B = m_p + m_n - m_D \simeq 2.2$ MeV is the deuterium binding energy. Introducing the baryon-to-photon ratio η as

$$n_b \simeq \eta n_\gamma = \eta \frac{2\zeta(3)}{\pi^2} T^3 , \tag{2.1.49}$$

and approximating $m_D \simeq 2m_p \simeq 2m_n$, the ratio of deuterium over protons in Eq. (2.1.48) becomes

$$\frac{n_D}{n_p} \simeq \eta \left(\frac{T}{m_p}\right)^{3/2} e^{\frac{B}{T}} . \tag{2.1.50}$$

Because η is small, the production of deuterium is delayed until the temperature drops below the binding energy. Once deuterium survives, helium forms efficiently through a chain of 2-particle reactions: $n + p \to D + \gamma$, $D + p \to {}^3\text{He} + \gamma$ and $D + {}^3\text{He} \to {}^4\text{He} + p$. This is called deuterium bottleneck,

[4] Solving the Boltzmann equation, the freeze-out temperature of neutrons is $T_{\text{fo}} = 0.8$ MeV.

since helium formation requires deuterium as an intermediate. The helium mass fraction is given by

$$Y = \frac{4n_{\text{He}}}{n_n + n_p} = \frac{2n_n}{n_n + n_p} = 2\frac{n_n/n_p}{1 + n_n/n_p} \,, \tag{2.1.51}$$

where we have used the fact that two neutrons go into one nucleus of ^{4}He. Inserting the value of the neutron-to-proton ratio of Eq. (2.1.47) into Eq. (2.1.51), we obtain $Y \simeq 0.25$, which is in agreement with observations: low metallicities galaxies where star formation has just started give 75% of hydrogen, 25% of helium and very little lithium.

The predicted helium abundance is sensitive to the details of BBN. In particular, the number of relativistic degrees of freedom g_*, the number of neutrino species N_{eff}, and the baryon-to-photon ratio η at the time of BBN are crucial. This implies that BBN provides constraints on BSM physics. An increase in g_*, which enters in the Hubble parameter $H \propto g_*^{1/2}$, raises the freeze-out temperature T_{fo}, which in turn increases the neutron-to-proton ratio at freeze-out in Eq. (2.1.45), and ultimately leads to a larger helium fraction Y in Eq. (2.1.51). Moreover, the addition of a new relativistic component decoupled from the thermal plasma, such as GWs, contributes to the energy density of the Universe as

$$\rho_\nu + \rho_{\text{extra}} = N_{\text{eff}}\frac{7}{8}\left(\frac{4}{11}\right)^{4/3}\rho_\gamma \quad \Rightarrow \quad \rho_{\text{extra}} = \Delta N_{\text{eff}}\frac{7}{8}\left(\frac{4}{11}\right)^{4/3}\rho_\gamma \,, \tag{2.1.52}$$

where ΔN_{eff} accounts for the additional relativistic degrees of freedom. Current observational constraints, combining BBN and CMB data [102], give

$$N_{\text{eff}} = 2.941 \pm 0.143 \,, \tag{2.1.53}$$

which is consistent with the SM prediction, but it also leaves room for BSM contributions.

Because radiation and matter dilute differently, the matter-radiation equality temperature T_{eq} is defined as the temperature at which their energy densities coincide

$$\rho_\gamma(T_{\text{eq}}) = \rho_m(T_{\text{eq}}) \,, \tag{2.1.54}$$

which is given by $T_{\text{eq}} \simeq 0.8$ eV.

At temperatures below 1 eV, the Universe becomes transparent to electromagnetic radiation, since photons no longer interact efficiently with free electrons. Before this epoch, photons were tightly coupled to the plasma via Compton scattering, but once the temperature decreases sufficiently, free electrons and nuclei combine to form neutral atoms. This process, called recombination, reduces the free electron density. Protons and photons are kept in thermal equilibrium through the reaction $e^- p^+ \leftrightarrow H\gamma$. Charge neutrality implies that $n_e = n_p$, baryon number conservation that $n_H + n_p = n_B$ and chemical equilibrium that $\mu_p + \mu_e = \mu_H$. Hence, using the non-relativistic number densities n in Eq. (2.1.30), we obtain

$$n_H = n_p n_e \frac{g_H}{g_p g_e}\left(\frac{m_e T}{2\pi}\right)^{-\frac{3}{2}} e^{-\frac{B}{T}} \,, \tag{2.1.55}$$

where $B \simeq 13.6$eV is the hydrogen binding energy and we have used the approximation $m_H \simeq m_p$. We define the fractional ionization $X_e = \frac{n_e}{n_b}$ and use the baryon-to-photon ratio η in Eq. (2.1.49),

ignoring all nuclei other than protons $n_b \simeq n_p + n_H = n_e + n_H$, to find the Saha equation

$$\frac{1 - X_e^{eq}}{(X_e^{eq})^2} = \frac{2\zeta(3)}{\pi^2}\eta \left(\frac{2\pi T}{m_e}\right)^{\frac{3}{2}} e^{\frac{B}{T}} . \tag{2.1.56}$$

The recombination temperature T_{rec} is defined by $X_e^{eq} = 0.1$, which means that 90% of the electrons are bound to protons, and it is given by $T_{\text{rec}} \simeq 0.3$ eV. Meanwhile, photons are coupled to free electrons through Thomson scattering $e^-\gamma \leftrightarrow e^-\gamma$, with an interaction rate $\Gamma = n_e\sigma_T$, where σ_T is the Thomson cross-section. Photon decoupling occurs when $\Gamma \sim H$ in Eq. (2.1.41). Since this epoch lies in matter domination, the decoupling temperature is $T_{\text{dec}} \simeq 0.27$ eV. The background of relic photons is the CMB observed today: an almost perfect black body spectrum with average temperature of $T = 2.73$ K and anisotropies of the order 10^{-5}. Expanding these anisotropies in spherical harmonics yields the angular power spectrum, from which precise information about the age, expansion rate, and energy content of the Universe can be extracted.

After the surface of last scattering, the Universe remained dark until baryonic matter fell into potential wells of dark matter and formed the first stars, which burned hydrogen and helium to form elements up to iron. The emission of ionising photons reionised the surrounding gas, making the Universe partially opaque but still transparent to the CMB, in a process called reionization. Hierarchical structure formation followed: stars, small galaxies, large galaxies, galaxy clusters, superclusters and large voids. Eventually, the Universe became vacuum-dominated by dark energy, as it is today.

All the information discussed so far comes directly or indirectly from electromagnetic radiation, with the surface of last scattering marking the earliest epoch directly observed. However, GWs can provide information about much earlier times. To see this, we use the rule of thumb in Eq. (2.1.41) $\Gamma \sim H$ and compare the interaction rate due to gravitational interaction $\Gamma \simeq G_N^2 T^5 \simeq \frac{T^5}{m_{\text{Pl}}^4}$ with the Hubble parameter H in radiation-dominated era in Eq. (2.1.35)

$$\frac{T^5}{m_{\text{Pl}}^4} \simeq \frac{T^2}{m_{\text{Pl}}} \quad \Rightarrow \quad T_{\text{GW}} \simeq m_{\text{Pl}} , \tag{2.1.57}$$

which shows that GWs decoupled at temperatures close to the Planck scale.

2.2 Gravitational waves

The existence of wave solutions in the theory of GR was first predicted by Einstein himself in 1916 [4, 5]. The physical reality of GWs was debated for decades. Einstein himself was doubtful and, together with Rosen, mistakenly argued in 1936 [103] that such solutions contained singularities, later understood to be a coordinate artifact. It was only in 1957 that Pirani [104] clarified this issue by showing that GWs would indeed move test masses. The first indirect confirmation of the existence of GWs is due to Hulse and Taylor in 1974 [105, 106] through the observed orbital period decay of PSR B1913+16, consistent with the cumulative shift of its periastron time predicted by GW emission. In the 1970s, Forward and Weiss [107, 108] proposed a laser-interferometric detector concept, inspired by the Michelson-Morley experiment [109], while Sazhin and Detweiler suggested millisecond pulsars as natural low-frequency detectors [110, 111]. A century later, the first direct detection of a GW produced by a binary black hole merger was achieved in 2015 by the LIGO collaboration [3] and the first evidence for a SGWB was found in the summer of 2023 by several PTA collaborations [6–9].

GWs arise naturally in the linearised theory of GR, as outlined in the first part of this section. Then, we review the energy density carried by GWs, before turning to the properties of a SGWB and its detection with PTAs, following Refs. [95, 112–114].

2.2.1 Linearised theory and plane wave solutions

The linearised theory of GR consists of expanding small perturbations $h_{\mu\nu}$ around a flat-spacetime background metric $\eta_{\mu\nu}$, i.e.

$$g_{\mu\nu} = \eta_{\mu\nu} + h_{\mu\nu} + \mathcal{O}(h^2) \,, \quad |h_{\mu\nu}| \ll 1 \,, \tag{2.2.1}$$

which means that the gravitational field is so weak that the magnitude of non-zero components of $h_{\mu\nu}$ is small. Physically, it implies that there exists a reference frame where we can decompose the metric $g_{\mu\nu}$ into Eq. (2.2.1), on a sufficiently large region of space. Linearisation consists of keeping only terms linear in $h_{\mu\nu}$ and neglecting higher-order ones. Indices are raised and lowered with the Minkowski metric $\eta_{\mu\nu}$, and the Christoffel symbols $\Gamma^{\alpha}_{\mu\nu}$ in Eq. (2.1.5), the Ricci tensor $R_{\mu\nu}$ in Eq. (2.1.3) and the Ricci scalar R in Eq. (2.1.4) become

$$\Gamma^{\alpha}_{\mu\nu} = \frac{1}{2}\eta^{\alpha\beta}\left(\partial_\mu h_{\nu\beta} + \partial_\nu h_{\mu\beta} - \partial_\beta h_{\mu\nu}\right) + \mathcal{O}(h^2) \,, \tag{2.2.2}$$

$$R_{\mu\nu} = \frac{1}{2}\left(\partial_\alpha\partial_\mu h^{\alpha}{}_{\nu} + \partial_\alpha\partial_\nu h^{\alpha}{}_{\mu} - \partial_\mu\partial_\nu h - \Box h_{\mu\nu}\right) + \mathcal{O}(h^2) \,, \tag{2.2.3}$$

$$R = \partial_\alpha\partial_\beta h^{\alpha\beta} - \Box h + \mathcal{O}(h^2) \,, \tag{2.2.4}$$

where $h = \eta^{\alpha\beta}h_{\alpha\beta}$ is the trace and $\Box = \eta^{\alpha\beta}\partial_\alpha\partial_\beta$ is the flat-spacetime D'Alembertian operator. The Einstein tensor $G_{\mu\nu}$ in Eq. (2.1.2) is given by

$$G_{\mu\nu} = \frac{1}{2}\left(\partial_\alpha\partial_\mu h^{\alpha}{}_{\nu} + \partial_\alpha\partial_\nu h^{\alpha}{}_{\mu} - \partial_\mu\partial_\nu h - \Box h_{\mu\nu} - \eta_{\mu\nu}\partial_\alpha\partial_\beta h^{\alpha\beta} + \eta_{\mu\nu}\Box h\right) + \mathcal{O}(h^2) \,. \tag{2.2.5}$$

It is convenient to introduce the trace-reversed metric perturbation

$$\bar{h}_{\mu\nu} = h_{\mu\nu} - \frac{1}{2}\eta_{\mu\nu}h \,, \tag{2.2.6}$$

called trace-reversed because $\bar{h} = \eta^{\mu\nu}\bar{h}_{\mu\nu} = h - 2h = -h$, so that the Einstein tensor $G_{\mu\nu}$ in Eq. (2.2.5) simplifies to

$$G_{\mu\nu} = \frac{1}{2}\left(\partial_\alpha\partial_\mu \bar{h}^{\alpha}{}_{\nu} + \partial_\alpha\partial_\nu \bar{h}^{\alpha}{}_{\mu} - \Box\bar{h}_{\mu\nu} - \eta_{\mu\nu}\partial_\alpha\partial_\beta\bar{h}^{\alpha\beta}\right) + \mathcal{O}(h^2) \,, \tag{2.2.7}$$

and Einstein's equations in Eq. (2.1.2) now read

$$\Box\bar{h}_{\mu\nu} + \eta_{\mu\nu}\partial_\alpha\partial_\beta\bar{h}^{\alpha\beta} - \partial_\alpha\partial_\mu\bar{h}^{\alpha}{}_{\nu} - \partial_\alpha\partial_\nu\bar{h}^{\alpha}{}_{\mu} = -16\pi G T_{\mu\nu} \,. \tag{2.2.8}$$

Since we work in the weak-field limit, the right-hand side of Einstein's equations in Eq. (2.1.2) is given by the first-order in $h_{\mu\nu}$ of the energy-momentum tensor $T_{\mu\nu}$. The conservation of the energy-momentum tensor is then given by $\partial_\mu T^{\mu\nu} = 0$.

The Einstein-Hilbert action is invariant under the gauge group of all possible coordinate transformations[5] given by $x^\mu \to x'^\mu(x)$, where x'^μ is an arbitrary diffeomorphism[6]. In fact, there may be other coordinate systems in which the metric $g_{\mu\nu}$ can be written as in Eq. (2.2.1), but with different perturbation metric $h_{\mu\nu}$. Under this transformation, the metric transforms as

$$g_{\mu\nu}(x) \to g'_{\mu\nu}(x') = \frac{\partial x^\alpha}{\partial x'^\mu}\frac{\partial x^\beta}{\partial x'^\nu} g_{\alpha\beta}(x) \,. \tag{2.2.9}$$

Since gauge transformations correspond to coordinate redefinitions, choosing coordinates is equivalent to fixing the gauge: get rid of spurious degrees of freedom and leave only physical ones. An infinitesimal coordinate transformation can be written as

$$x'^\mu = x^\mu + \xi^\mu(x) \,, \tag{2.2.10}$$

where $\xi^\mu(x)$ is an arbitrary infinitesimal vector field and the derivatives $\partial_\mu \xi^\nu$ are at most of order $h_{\mu\nu}$, in order to ensure that Eq. (2.2.1) is still valid. The gauge transformation of the perturbation metric $h_{\mu\nu}$ is given by

$$h'_{\mu\nu} = h_{\mu\nu} - (\partial_\mu \xi_\nu + \partial_\nu \xi_\mu) \,, \quad \bar{h}'_{\mu\nu} = \bar{h}_{\mu\nu} - (\partial_\mu \xi_\nu + \partial_\nu \xi_\mu) + \eta_{\mu\nu}\partial^\alpha \xi_\alpha \,. \tag{2.2.11}$$

A convenient gauge choice is the Lorenz condition[7]

$$\partial^\mu \bar{h}_{\mu\nu} = \partial^\mu h_{\mu\nu} - \frac{1}{2}\eta_{\mu\nu}\partial^\mu h = 0 \,, \tag{2.2.12}$$

which, using Eq. (2.2.11) ξ^μ, translates into the condition

$$\partial^\mu \bar{h}_{\mu\nu} = \Box \xi_\nu \,. \tag{2.2.13}$$

Since Eq. (2.2.13) is a wave equation for ξ, and the d'Alembert operator is invertible in flat spacetime, it is always possible to find a solution and impose the Lorenz gauge condition. In this gauge, the linearised Einstein tensor $G_{\mu\nu}$ in Eq. (2.2.7) remarkably simplifies to

$$G_{\mu\nu} = -\frac{1}{2}\Box \bar{h}_{\mu\nu} \,, \tag{2.2.14}$$

and Einstein's equations in Eq. (2.1.2) to

$$\Box \bar{h}_{\mu\nu} = -16\pi G T_{\mu\nu} \,. \tag{2.2.15}$$

Note that the symmetric perturbation metric $h_{\mu\nu}$ has 10 components, but imposing 4 gauge degrees of freedom in Eq. (2.2.12), leaving 6 independent ones.

In vacuum, where the energy-momentum tensor $T^{\mu\nu}$ vanishes, Einstein's equations in the Lorenz

[5] This is the principle of general covariance, which states that the laws of physics must take the same form in all coordinate systems.

[6] A diffeomorphism is map which is invertible, differentiable and with differentiable inverse.

[7] This is analogous to the Lorenz gauge $\partial_\mu A^\mu = 0$ in electromagnetism.

gauge in Eq. (2.2.15) reduce to

$$\Box\bar{h}_{\mu\nu} = 0 \,. \tag{2.2.16}$$

However, the gauge is not completely fixed, since the Lorenz condition in Eq. (2.2.12) is not spoiled by a further gauge transformation in Eq. (2.2.10), as long as $\Box\xi^\mu = 0$. In particular, we can choose ξ^0 such that $\bar{h} = 0$ is traceless, so that $\bar{h}_{\mu\nu} = h_{\mu\nu}$, and ξ^i such that $\bar{h}_{0i} = 0$ is purely spatial. As a consequence, 0-component of the Lorenz gauge in Eq. (2.2.12) reads

$$0 = \partial^0 h_{00} + \partial^i h_{0i} = \partial^0 h_{00} \,, \tag{2.2.17}$$

which means that h_{00} becomes automatically constant in time, which can be set to zero $h_{00} = 0$ since we are interested in time-dependent propagating solutions, and for the j-components

$$0 = \partial^0 h_{0j} + \partial^i h_{ij} = \partial^i h_{ij} \,, \tag{2.2.18}$$

which implies that the spatial metric perturbation is transverse. We can summarise the full set of conditions defining the Traceless-Transverse (TT) gauge, in the following way

$$h^{0\mu} = 0 \,, \quad h^i{}_i = 0 \,, \quad \partial^i h_{ij} = 0 \,, \tag{2.2.19}$$

and the non-trivial Einstein's equations in Eq. (2.2.16) become

$$\Box h_{ij}^{\mathsf{TT}} = 0 \,. \tag{2.2.20}$$

where we have considered only the spatial components, since in the TT gauge these are the only dynamical fields. $h_{\mu\nu}$ is left with 2 physical degrees of freedom, because we have imposed 4 redundant gauge conditions. Thus, the TT gauge is a convenient choice because it completely fixes the gauge freedom and contains only physical degrees of freedom, and explicitly shows that wave solutions arise from the linearised Einstein's equations in Eq. (2.2.20).

A particular class of solutions of the wave equation in Eq. (2.2.20) is represented by plane waves

$$h_{ij}^{\mathsf{TT}}(x) = \mathsf{Re}\left(C_{ij} e^{ik_\mu x^\mu}\right) \,, \tag{2.2.21}$$

where $k_\mu = (\omega, \mathbf{k})$ is the null wave vector, i.e. $k_\mu k^\mu = -\omega^2 + |\mathbf{k}|^2 = 0$, showing that GWs propagate at the speed of light, and C_{ij} is the constant symmetric transverse traceless polarisation tensor, i.e.

$$C^{ij} k_j = 0 \,, \quad C^i{}_i = 0 \,. \tag{2.2.22}$$

The direction of the propagation of the GW is defined by the unit vector of the wave vector $\hat{\mathbf{n}} = \mathbf{k}/|\mathbf{k}|$. Without loss of generality, we choose $\hat{\mathbf{n}}$ along the $\hat{\mathbf{z}}$-direction, so that

$$k^\mu = (\omega, 0, 0, \omega) \,, \tag{2.2.23}$$

and, imposing the conditions in Eq. (2.2.22), the polarisation tensor C_{ij} is left with only two compo-

nents $(h_+,\ h_\times)$. The metric perturbation $h^{\mathsf{TT}}_{\mu\nu}$ in Eq. (2.2.21) can then be written as

$$h^{\mathsf{TT}}_{\mu\nu}(t,z) = \begin{bmatrix} 0 & 0 & 0 & 0 \\ 0 & h_+ & h_\times & 0 \\ 0 & h_\times & -h_+ & 0 \\ 0 & 0 & 0 & 0 \end{bmatrix} \cos(\omega(t-z)) \,, \tag{2.2.24}$$

or in terms of the infinitesimal line element ds^2 in Eq. (2.1.1)

$$\begin{aligned} ds^2 = &- dt^2 + dz^2 + (1 + h_+ \cos(\omega(t-z)))\, dx^2 + (1 - h_+ \cos(\omega(t-z)))\, dy^2 \\ &+ 2h_\times \cos(\omega(t-z)) dx dy \,. \end{aligned} \tag{2.2.25}$$

Therefore, for a plane wave propagating in the z-direction, the GW is completely characterised by its two polarisation amplitudes $(h_+,\ h_\times)$ and the frequency f.

The most general solution of the wave equation in Eq. (2.2.20) is a superposition of plane waves, which in Fourier space can be written as

$$h^{\mathsf{TT}}_{ij}(x) = \int \frac{d^3k}{(2\pi)^3} \left(\mathcal{A}_{ij}(\mathbf{k}) e^{ikx} + \text{c.c.} \right) \,. \tag{2.2.26}$$

Using spherical coordinates for the wave vector $\mathbf{k}$, with $\omega = |\mathbf{k}|$, so that $k_\mu = \omega(1, \hat{\mathbf{k}})$, or equivalently in terms of the frequency $f = \frac{\omega}{2\pi}$ as $k_\mu = 2\pi f(1, \hat{\mathbf{k}})$, the integration measure becomes $d^3k = (2\pi)^3 f^2 df d^2\hat{\mathbf{n}}$ and the superposition of plane waves in Eq. (2.2.26) reads

$$h^{\mathsf{TT}}_{ij}(x) = \int_0^\infty df\ f^2 \int d^2\hat{\mathbf{n}} \left(\mathcal{A}_{ij}(f, \hat{\mathbf{n}}) e^{-2\pi i f(t - \hat{\mathbf{n}}\cdot\mathbf{x})} + \text{c.c.} \right) \,. \tag{2.2.27}$$

The TT gauge conditions in Eq. (2.2.19) impose restrictions such as $\mathcal{A}^i{}_i(\mathbf{k}) = 0$ and $k^i \mathcal{A}_{ij}(\mathbf{k}) = 0$. In case of a superposition of waves with different propagation directions, $h_{ij}(x)$ is no longer reducible to a 2×2 matrix, since contributions also arise in the third spatial direction. We introduce the polarization tensors $C^A_{ij}(\hat{\mathbf{n}})$ for $A = +, \times$ defined as

$$C^+_{ij}(\hat{\mathbf{n}}) = \hat{\mathbf{u}}_i \hat{\mathbf{u}}_j - \hat{\mathbf{v}}_i \hat{\mathbf{v}}_j \,, \quad C^\times_{ij}(\hat{\mathbf{n}}) = \hat{\mathbf{u}}_i \hat{\mathbf{v}}_j + \hat{\mathbf{v}}_i \hat{\mathbf{u}}_j \,, \tag{2.2.28}$$

where $\hat{\mathbf{u}}$ and $\hat{\mathbf{v}}$ are orthonormal vectors to $\hat{\mathbf{n}}$ and to each other. They are normalised such that

$$C^A_{ij}(\hat{\mathbf{n}}) C^{ij}_B(\hat{\mathbf{n}}) = 2\delta^A{}_B \,. \tag{2.2.29}$$

Therefore, in a generic frame, we can write

$$f^2 \mathcal{A}_{ij}(f, \hat{\mathbf{n}}) = \sum_{A=+,\times} \tilde{h}_A(f, \hat{\mathbf{n}}) C^A_{ij}(\hat{\mathbf{n}}) \,, \tag{2.2.30}$$

and Eq. (2.2.26) becomes [112]

$$h^{\mathsf{TT}}_{ij}(t, \mathbf{x}) = \sum_{A=+,\times} \int_{-\infty}^{\infty} df \int d^2\hat{\mathbf{n}}\, \tilde{h}_A(f, \hat{\mathbf{n}}) C^A_{ij}(\hat{\mathbf{n}}) e^{-2\pi i f(t - \hat{\mathbf{n}}\cdot\mathbf{x})} \,. \tag{2.2.31}$$

In TT gauge, we see directly how test masses respond to GWs. Consider two test masses located at $(t, x_1, 0, 0)$ and $(t, x_2, 0, 0)$, separated by a constant coordinate distance $L = x_2 - x_1$. Physical effects are measured through proper, not coordinate, distances. In fact, the proper distance S between the two masses oscillates in time

$$\begin{aligned} S &= \int_{x_1}^{x_2} \sqrt{g_{xx}} dx = \int_{x_1}^{x_2} \sqrt{1 + h_+ \cos(\omega(t-z))} dx \\ &= (x_2 - x_1)\left(1 + h_+ \cos(\omega t)\right)^{1/2} \simeq L\left(1 + \frac{1}{2} h_+ \cos(\omega t)\right) , \end{aligned}$$

where we have used the metric $g_{\mu\nu}$ in Eq. (2.2.25) and Taylor expanded for $h_+ \ll 1$. The relative change in proper distance is then

$$\delta S_x = \frac{L}{2} h_+ \cos(\omega t) . \tag{2.2.32}$$

In the TT gauge, the only non-vanishing component of the Riemann tensor is

$$R_{i00j} = \frac{1}{2} \ddot{h}^{\mathrm{TT}}_{ij} , \tag{2.2.33}$$

so that, for slowly-moving test masses $u^\mu = (1, 0, 0, 0)$, the geodesic deviation equation [8] reads as

$$\ddot{S}^i = R^i{}_{00j} S^j = \frac{1}{2} \ddot{h}^{\mathrm{TT}}_{ij} S^j . \tag{2.2.34}$$

To visualise the effect, consider a ring of test masses in the $(x,\ y)$ plane, and see how it behaves for a GW propagating in the $\hat{\mathbf{z}}$-direction. Since the GW is transverse, if the test particle is at rest at $z = 0$, it will remain at $z = 0$, so we can focus on the $(x,\ y)$ plane. For the $+$ polarisation, the plane wave in Eq. (2.2.24) reads as

$$h^{\mathrm{TT}}_{ij}(t) = \begin{bmatrix} 1 & 0 & 0 \\ 0 & -1 & 0 \\ 0 & 0 & 0 \end{bmatrix} h_+ \sin(\omega t) , \tag{2.2.35}$$

where we have also chosen the origin of time such that $h^{\mathrm{TT}}_{ij}(t = 0) = 0$. Defining $\xi_i(t) = (x_0 + \delta x(t),\ y_0 + \delta y(t),\ 0)$ and using Eq. (2.2.34), we find

$$\ddot{\xi}^i = \begin{bmatrix} \delta\ddot{x}(t) \\ \delta\ddot{y}(t) \\ 0 \end{bmatrix} = \frac{1}{2} \ddot{h}_{ij} \xi^j = -\frac{h_+ \omega^2}{2} \sin(\omega t) \begin{bmatrix} 1 & 0 & 0 \\ 0 & -1 & 0 \\ 0 & 0 & 0 \end{bmatrix} \begin{bmatrix} x_0 + \delta x(t) \\ y_0 + \delta y(t) \\ 0 \end{bmatrix} . \tag{2.2.36}$$

Neglecting the small corrections δx and δy, which are of order $\mathcal{O}(h_+)$, we integrate Eq. (2.2.36) to obtain

$$\delta x(t) = \frac{h_+ x_0}{2} \cos(\omega t) , \quad \delta y(t) = -\frac{h_+ y_0}{2} \cos(\omega t) . \tag{2.2.37}$$

Similarly, for the $\times$ polarisation, we have

$$\delta x(t) = \frac{h_\times y_0}{2} \cos(\omega t) , \quad \delta y(t) = \frac{h_\times x_0}{2} \cos(\omega t) . \tag{2.2.38}$$

[8] The geodesic deviation equation describes how the separation vector ξ^μ between two infinitesimally close geodesics evolves due to spacetime curvature $\frac{D^2 \xi^\mu}{D\tau^2} = -R^\mu_{\nu\rho\sigma}\, \xi^\rho\, u^\nu\, u^\sigma$.

Therefore, the proper distance between particles that are initially at rest in the $(x,\ y)$ plane will oscillate. The effect of the two polarizations of a GW on a ring is illustrated in Fig. 3.

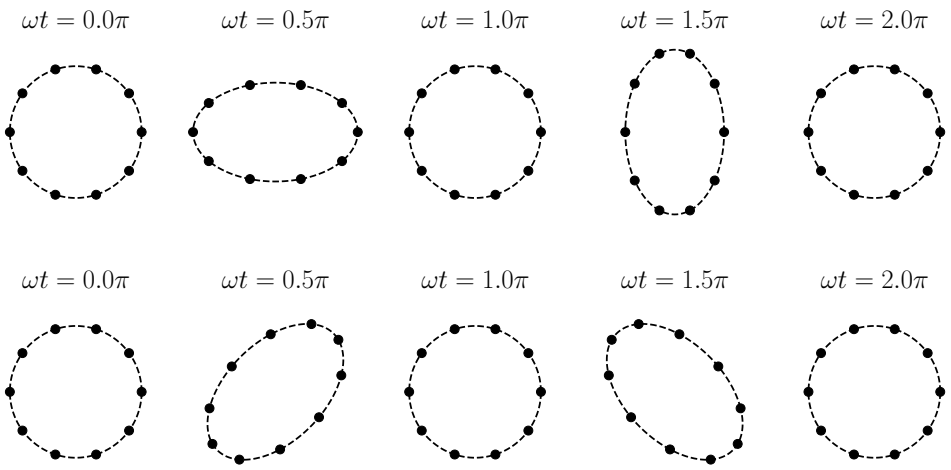

Figure 3: Effect of a passing GW on a ring of test masses: $+$ polarization (top) and $\times$ polarization (bottom).

If the test masses are instead mirrors with a light beam bouncing between them, the oscillating proper distance modifies the round-trip time of the light. This is the working principle of GW interferometers. In PTAs, the mirrors are replaced by pulsars and the Solar System barycenter.

2.2.2 Energy-momentum tensor and gravitational wave sources

Since GWs set in motion initially at rest test masses, conservation of energy requires that the kinetic energy must come from the energy carried by the GWs. To compute the energy-momentum tensor $t_{\mu\nu}$, we split the metric into a generic curved background $\overline{g}_{\mu\nu}(x)$ and a small perturbation $\delta g_{\mu\nu}(x)$, such that $|\delta g_{\mu\nu}(x)| \ll |\overline{g}_{\mu\nu}(x)|$

$$g_{\mu\nu}(x) = \overline{g}_{\mu\nu}(x) + \delta g_{\mu\nu}(x)\ . \tag{2.2.39}$$

In the general case, it is not possible to precisely distinguish a background from perturbations on top of it. This procedure works only if there is a clear distinction between the high-frequency part of the metric, corresponding to the wave part $\delta g_{\mu\nu}(x)$ from the low-frequency part, corresponding to the background $\overline{g}_{\mu\nu}(x)$. Then, we can apply a renormalisation procedure to integrate out short-wavelength modes by spatially averaging in a volume defined by some intermediate length scale [112]. There are two situations where this splitting is possible:

- in cosmology, for GWs with wavelengths much smaller than the Hubble radius, since causality implies only sub-Horizon modes to be produced with wavelength $\lambda = 1/f \leq a_0/(a_* H_*)$, which the expansion of the Universe $a_0 H_0 \ll a_* H_*$ leads to $\lambda \ll H_0^{-1}$;

- on Earth, where even though deviations in the gravitational field $\delta g_{00} \sim 10^{-9}$ of the Earth exceed the characteristic strain amplitudes $\delta g_{ij} \sim 10^{-21}$, we can exploit the quasi-static nature of Earth's gravitational field compared to GWs.

We decompose the Ricci tensor $R_{\mu\nu}$ in Eq. (2.1.3) in powers of δg in the metric decomposition of Eq. (2.2.39) such as $R_{\mu\nu} = R^{(1)}_{\mu\nu} + R^{(2)}_{\mu\nu} + \mathcal{O}(\delta g^3)$ and find that the energy-momentum tensor $t_{\mu\nu}$ arises from the quadratic part of the Ricci tensor $R^{(2)}_{\mu\nu}$

$$t_{\mu\nu} = \frac{1}{16\pi G}\langle \partial_\mu \delta g_{\alpha\beta} \partial^\mu \delta g^{\alpha\beta} \rangle \,, \tag{2.2.40}$$

where the average $\langle \ldots \rangle$ is over intermediate length scale $\lambda \ll l \ll L_{\text{bg}}$ or intermediate time scale $\frac{1}{f} \ll \tau \ll \frac{1}{f_{\text{bg}}}$. In the Lorenz gauge $\partial^\mu \delta g_{\mu\nu} = 0$, the energy-momentum tensor $t_{\mu\nu}$ depends only on $h^{\text{TT}}_{ij} = \delta g_{ij}$. In particular, the t_{00} component is the energy density ρ associated to GWs

$$\rho_{\text{GW}} = t_{00} = \frac{1}{32\pi G}\langle \dot{h}^{\text{TT}}_{ij} \dot{h}^{\text{TT}}_{ij} \rangle = \frac{1}{16\pi G}\langle \dot{h}^2_+ + \dot{h}^2_\times \rangle \,. \tag{2.2.41}$$

Another consequence is that GWs propagate along null geodesics of the background metric, which leads to optical phenomena like gravitational lensing, absorption, or scattering, even though gravitational interaction is so weak that they have negligible effects.

Sources of GWs can be obtained by means of the Green's function method, in which the solution of linearised Lorenz gauged Einstein's equations in Eq. (2.2.15) can be written as

$$\overline{h}_{\mu\nu}(x) = -16\pi G \int d^4x' \, G(x - x') T_{\mu\nu}(x') \,, \tag{2.2.42}$$

where $G(x - x')$ is the Green's function of the D'Alembertian operator, which satisfies the equation $\Box_x G(x - x') = \delta^4(x - x')$. Since the disturbance of the gravitational field at the point $(t, \mathbf{x})$ can be influenced only by sources at the point $(t_{ret}, \mathbf{x} - \mathbf{x}')$ on the past light cone, causality requires that the Green's function in Eq. (2.2.42) is the retarded one

$$G(x - x') = -\frac{1}{4\pi|\mathbf{x} - \mathbf{x}'|}\delta(t_{ret} - t') \,, \tag{2.2.43}$$

where $t_{ret} = t - |\mathbf{x} - \mathbf{x}'|$ is the retarded time. Hence, the solution in Eq. (2.2.42) becomes

$$\overline{h}_{ij}(t, \mathbf{x}) = 4G \int d^3x' \frac{T_{ij}(t_{ret}, \, \mathbf{x}')}{|\mathbf{x} - \mathbf{x}'|} \,, \tag{2.2.44}$$

where we have considered only the spatial components of the metric perturbation, since they are the only dynamical ones. At large distance from a non-relativistic slowly moving source, by geometrical analysis, we can use the approximation $|\mathbf{x} - \mathbf{x}'| = r - \hat{\mathbf{n}} \cdot \mathbf{x}' + \mathcal{O}\left(\frac{1}{r}\right)$, to write the energy-momentum tensor as $T_{ij}(t_{ret}, \mathbf{x}') \simeq T_{ij}(t - r, \mathbf{x}')$ and Eq. (2.2.44) as

$$\overline{h}_{ij}(t, \mathbf{x}) = \frac{4G}{r} \int d^3x' T_{ij}(t - r, \mathbf{x}') \,. \tag{2.2.45}$$

Using the energy-momentum conservation $\partial_\mu T^{\mu\nu} = 0$ and projecting onto the TT part, we obtain the quadrupole formula

$$h^{\text{TT}}_{ij} = \frac{2G}{r}\ddot{Q}_{ij}(t - r) \,, \tag{2.2.46}$$

where $Q_{ij}(t) = \int d^3x' \rho(t, \mathbf{x}') x^i x^j$ is the quadrupole moment of the source and $Q_{ij}^{\mathrm{TT}} = Q_{ij} - \frac{1}{3}\delta_{ij} Q_{kk}$ is its TT part. Unlike in electromagnetism, where dipole radiation dominates, the leading contribution in gravity is quadrupolar. This is because monopole terms are fixed by mass conservation, and dipole terms by momentum conservation, both of which forbid radiation. Thus, only time-varying quadrupole (and higher multipoles) can radiate.

2.2.3 Stochastic gravitational wave backgrounds

There are several types of GW signals, classified by temporal behavior and physical origin. Nearly monochromatic, continuous signals are emitted by rotating, non-axisymmetric neutron stars. Compact binary coalescences from black holes or neutron stars feature the characteristic inspiral-merger-ringdown sequence. Short-duration bursts arise from highly asymmetric core-collapse supernovae or from cusps on cosmic strings. Finally, a SGWB from many unresolved sources can arise either from early-Universe phenomena (quantum fluctuations during inflation, FOPTs and topological defects such as cosmic strings and domain walls) or the incoherent superposition of astrophysical mergers (supermassive black hole binaries), each too weak to be detected individually, but numerous enough that every frequency bin is densely populated.

In the case of a SGWB, unlike for individual sources, the perturbation metric in Eq. (2.2.31) is no longer a deterministic function but a random variable with a statistical distribution, whose variance is related to the energy density ρ [9]

As a consequence of causality, an early Universe source cannot generate correlations on scales larger than the Hubble radius at the time of emission, implying that $l_* \leq H_*^{-1}$ or $\Delta t_* \leq H_*^{-1}$. Therefore, the signal observed today is given by a superposition of many sources that are uncorrelated. We can compare the correlation length scale l_* of a GW signal, produced in the early Universe and redshifted to today $l_0 = l_* \frac{a_0}{a_*}$, to the Hubble horizon today H_0^{-1} [114]

$$\frac{l_0}{H_0^{-1}} \simeq 1.3 \times 10^{-11} \left(\frac{100}{g_*(T_*)}\right)^{1/6} \left(\frac{\mathrm{GeV}}{T_*}\right) . \tag{2.2.47}$$

For example, taking temperatures near the epoch of the EWPT, Eq. (2.2.47) shows that the correlation length scale is extremely small compared to the Hubble horizon today. Furthermore, a causal process at the same epoch consists of a superposition of independent signals emitted by at least 10^{24} uncorrelated regions [114]. This justifies the assumption that an early Universe source of a GW signal would produce a SGWB, which in general is taken to be Gaussian, stationary, isotropic, and unpolarised. Gaussianity, which is justified by the central limit theorem[10], indicates that the statistical information is encoded by its mean, which is set to zero, and its variance, which is the two-point correlator $\langle h_A(t) h_{A'}(t') \rangle$. Since the typical timescale on which the SGWB changes substantially is of the order of the age of the Universe, which is much larger than the timescale of the experiments,

[9] Ensemble averages are formally defined as averages over many realisations of the Universe. Since we do not have copies of it, we can exploit the ergodic hypothesis: the ensemble average is replaced by an average over large portions of spacetime. To satisfy the ergodic hypothesis, we need to have the same initial condition at every point in space, the production mechanism operated within a causal horizon, and the Hubble sphere at that time was smaller than today's. All these requirements are satisfied in the early Universe.

[10] The central limit theorem states that the sum of many independent events produces a Gaussian stochastic process, regardless of the probability distribution of the individual events.

stationarity is reasonable and $\langle \tilde{h}^*_A(f)\tilde{h}_{A'}(f')\rangle \propto \delta(f-f')$. Isotropy is a consequence of the fact that it is generated by processes that happen at the same time in different Hubble patches, analogously with the CMB, and points to $\langle \tilde{h}^*_A(f,\hat{\mathbf{n}})\tilde{h}_{A'}(f',\hat{\mathbf{n}}')\rangle \propto \delta(\phi-\phi')\delta(\cos\theta-\cos\theta')$, where (θ,ϕ) are the polar angles defining $\hat{\mathbf{n}}$. Finally, unpolarised means $\langle \tilde{h}^*_A(f,\hat{\mathbf{n}})\tilde{h}_{A'}(f',\hat{\mathbf{n}}')\rangle \propto \delta_{AA'}$. Combining these properties, we can write the two-point correlator as

$$\langle \tilde{h}^*_A(f,\hat{\mathbf{n}})\tilde{h}_{A'}(f',\hat{\mathbf{n}}')\rangle = \frac{1}{8\pi}\delta(f-f')\delta^2(\hat{\mathbf{n}},\hat{\mathbf{n}}')\delta_{AA'}S_h(f)\,, \tag{2.2.48}$$

where we have introduced the two-sided spectral density $S_h(f)$, independent of polarisation and direction, which uniquely characterises the two-point correlator in Eq. (2.2.48) and allows us to perform a direct comparison with the noise in a detector. The normalization factor of 8π is chosen so that $S_h(f)$ is normalised by the solid angle and by an extra factor of 2 such that it is consistent with the definition of one-sided noise spectral densities. Back in coordinate space, Eq. (2.2.48) reads as

$$\langle h_{ij}(t)h^{ij}(t)\rangle = 4\int_0^\infty df\; S_h(f)\,. \tag{2.2.49}$$

Besides the spectral density $S_h(f)$, the quantity that characterises the SGWB is the energy density ρ_{GW}, written in terms of a dimensionless parameter Ω, normalised over the critical density of the Universe $\rho_{\mathsf{crit}} = \frac{3H_0^2}{8\pi G}$, as

$$\Omega_{\mathsf{GW}} = \frac{\rho_{\mathsf{GW}}}{\rho_{\mathsf{crit}}}\,. \tag{2.2.50}$$

We define the SGWB spectrum as a function of frequency as

$$\Omega_{\mathsf{GW}}(f) = \frac{1}{\rho_{\mathsf{crit}}}\frac{d\rho_{\mathsf{GW}}}{d\ln f}\,. \tag{2.2.51}$$

Inserting the plane wave expansion of Eq. (2.2.31) into the energy-momentum tensor in Eq. (2.2.41) and averaging with the two-point correlator in Eq. (2.2.48), we find that the SGWB spectrum Ω_{GW} in Eq. (2.2.51) is then given by

$$\Omega_{\mathsf{GW}}(f) = \frac{4\pi^2}{3H_0^2}f^3 S_h(f)\,. \tag{2.2.52}$$

2.2.4 Pulsar timing arrays

The existence of neutron stars was first hypothesised by Landau, Baade, and Zwicky in the 1930s [115, 116], and in the 1960s Pacini and Gold proposed that rapidly rotating neutron stars would emit periodic electromagnetic pulses [117, 118], due to conservation of angular momentum: as their progenitor stars contract after nuclear fusion ceases, they spin faster. The first identification of radio sources with a very regular period of 1.337 s with the pulsar PSR J1921+2153 was made by Bell and Hewish in 1967. In the following years, more pulsars were identified, with particular mention for the Hulse-Taylor binary pulsar J1915+1606 which led to the first indirect discovery of GWs [105, 106].

Neutron stars have a strong dipolar magnetic field, whose axis is misaligned with their rotation axis. Thus, a precessing magnetic dipole generates an electric field that accelerates charged particles within the magnetosphere, made of a co-rotating ionized high-energy plasma, which expels beams of electromagnetic radiation in the radio band, emitted along the open magnetic field lines. Therefore,

an observer along the circle swept by the beam of radiation receives a pulse with periodicity equal to the rotational period of the neutron star, analogous to a lighthouse. The signal is extremely stable because of the huge moment of inertia. Furthermore, there is a population of millisecond pulsars, which rotate faster and have more stable rotational periods, typically formed in binary systems where a pulsar accretes mass from its companion and gains angular momentum. Due to the high stability of the orbital period, these pulses can be predicted with extreme precision, accounting for higher time derivatives of the period P, such as the spin-down $\dot{P}$, the effects of the interstellar medium, Earth's proper motion, and the orbital motion of binary pulsars.

The phenomenon that GWs affect the arrival times of these pulsar signals, is known from the 1970s [110, 111] and in 1983, Hellings and Downs [119] provided a way to distinguish GWs from noise, by correlating timing residuals from several pulsars and predicting a characteristic pattern, known as the Hellings-Downs curve. This led to the concept of PTAs [120], in which they looked for a Hellings-Downs correlation curve of a SGWB, that needs to be disentangled from clock errors or mismodeling of the Solar System's barycenter effects. Since the lowest detectable frequency is given by the inverse time span of the arrival data $f \geq \frac{1}{T}$: for a time span of $T = 10$ yr, the sensitivity reaches the nHz band.

In the following, we study how GWs affect the periodicity of the pulsar signal. We place the coordinate origin at the barycenter of the Solar System and identify the pulsar direction with $\mathbf{x} = \hat{\mathbf{n}_a}$, where a label the pulsar. Using the null line element in TT gauge for a pulse in Eq. (2.2.25), the observation time t_{obs} of a pulse emitted at time t_{em} at the distance d_a is given by [113]

$$t_{\text{obs}} = t_{\text{em}} + d_a + \frac{n_a^i n_a^j}{2} \int_{t_{\text{em}}}^{t_{\text{em}}+d_a} dt'\, h_{ij}^{\text{TT}}(t', \mathbf{x}_0(t'))\,, \tag{2.2.53}$$

where we have Taylor expanded for small $\sqrt{1 + h_{ij}^{\text{TT}}}$ and defined $\mathbf{x}_0(t') = (t_{\text{em}} + d_a - t')\hat{\mathbf{n}}_a$. After a rotational period of the pulsar $t'_{\text{em}} = t_{\text{em}} + T_a$, the observation time becomes

$$t'_{\text{obs}} = t_{\text{em}} + T_a + d_a + \frac{n_a^i n_a^j}{2} \int_{t_{\text{em}}}^{t_{\text{em}}+d_a} dt'\, h_{ij}^{\text{TT}}(t' + T_a, (t_{\text{em}} + d_a - t')\hat{\mathbf{n}}_a)\,. \tag{2.2.54}$$

Thus, we can relate the two observation times in Eqs. (2.2.53) and (2.2.54) as

$$t'_{\text{obs}} - t_{\text{obs}} = T_a + \Delta T_a\,, \tag{2.2.55}$$

where ΔT_a is the delay induced by the GW, given by comparing Eq. (2.2.55) with Eqs. (2.2.53) and (2.2.54)

$$\begin{aligned} \Delta T_a &= \frac{n_a^i n_a^j}{2} \int_{t_{\text{em}}}^{t_{\text{em}}+d_a} dt' (h_{ij}^{\text{TT}}(t' + T_a, \mathbf{x}_0(t')) - h_{ij}^{\text{TT}}(t', \mathbf{x}_0(t'))) \\ &\simeq T_a \frac{n_a^i n_a^j}{2} \int_{t_{\text{em}}}^{t_{\text{em}}+d_a} dt' \frac{\partial}{\partial t'} h_{ij}^{\text{TT}}(t', \mathbf{x}_0(t'))\,, \end{aligned} \tag{2.2.56}$$

where we have Taylor expanded T_a since it is typically of order milliseconds, compared to observational times of order years. For a monochromatic GW along the direction $\hat{\mathbf{n}}$, written as $h_{ij}^{\text{TT}}(t, \mathbf{x}) =$

$\mathcal{A}_{ij}(\hat{\mathbf{n}})\cos(\omega_{\rm GW}t - \hat{\mathbf{n}}\cdot\mathbf{x})$, the fractional frequency shift $z_a = \frac{\Delta T_a}{T_a}$ becomes [113]

$$z_a(t) = \frac{n_a^i n_a^j}{2(1+\hat{\mathbf{n}}\cdot\hat{\mathbf{n_a}})}(h_{ij}^{\rm TT}(t,\mathbf{x}=0) - h_{ij}^{\rm TT}(t-\tau_a,\mathbf{x}_a))\,, \tag{2.2.57}$$

where $\tau_a = t_{\rm obs} - t_{\rm em}$ and $\mathbf{x}_a = d_a\hat{\mathbf{n}_a}$. The timing residual of the a-th pulsar is defined by

$$R_a(t) = \int_0^t dt' z_a(t')\,. \tag{2.2.58}$$

Using the plane wave expansion in Eq. (2.2.31), we write the shift z_a in Eq. (2.2.57) as

$$z_a(t) = \sum_{A=+,\times}\int_{-\infty}^{\infty} df \int d^2\hat{\mathbf{n}}\,\tilde{h}_A(f,\hat{\mathbf{n}})F_a^A(\hat{\mathbf{n}})e^{-2\pi i f t}\left(1 - e^{2\pi i f\tau_a(1+\hat{\mathbf{n}}\cdot\hat{\mathbf{n_a}})}\right)\,, \tag{2.2.59}$$

where

$$F_a^A(\hat{\mathbf{n}}) = \frac{n_a^i n_a^j C_{ij}^A(\hat{\mathbf{n}})}{2(1+\hat{\mathbf{n}}\cdot\hat{\mathbf{n_a}})}\,. \tag{2.2.60}$$

For a SGWB, we compute the two-point correlator of the shifts

$$\langle z_a(t)z_b(t)\rangle = \frac{1}{2}\int_0^\infty df\; S_h(f)\int\frac{d^2\hat{\mathbf{n}}}{4\pi}\mathcal{K}_{ab}(t,\hat{\mathbf{n}})\sum_{A=+,\times}F_a^A(\hat{\mathbf{n}})F_b^A(\hat{\mathbf{n}})\,, \tag{2.2.61}$$

where

$$\mathcal{K}_{ab}(f,\hat{\mathbf{n}}) = (1-e^{-2\pi i f\tau_a(1+\hat{\mathbf{n}}\cdot\hat{\mathbf{n_a}})})(1-e^{-2\pi i f\tau_b(1+\hat{\mathbf{n}}\cdot\hat{\mathbf{n_b}})})\,. \tag{2.2.62}$$

We can replace $\mathcal{K}_{ab}(f,\hat{\mathbf{n}}) \to 1+\delta_{ab}$, since the exponentials rapidly oscillate and give negligible contributions to the integral. In fact, for the closest pulsar $\tau_a > 0.1$ kpc and the minimum frequency $f > 1$ nHz, we have $f\tau_a > 10$, unless the GW is parallel to the direction of the pulsar. Furthermore, by switching to spherical coordinates, the integral in Eq. (2.2.61) is evaluated to be [113]

$$C(\theta_{ab}) = \int\frac{d^2\hat{\mathbf{n}}}{4\pi}F_a^A(\hat{\mathbf{n}})F_b^A(\hat{\mathbf{n}}) = x_{ab}\ln x_{ab} - \frac{x_{ab}}{6} + \frac{1}{3}\,, \tag{2.2.63}$$

where $x_{ab} = \frac{1-\cos\theta_{ab}}{2}$ and θ_{ab} is the relative angle between the two pulsars. Therefore, using $S_h(f) = S_h(-f)$, we can write the two-point correlator in Eq. (2.2.61) as

$$\langle z_a(t)z_b(t)\rangle = C(\theta_{ab})\int_0^\infty df\; S_h(f)\,. \tag{2.2.64}$$

The expression in Eq. (2.2.63) is known as the Hellings-Downs curve, and it characterises the correlation between the timing residuals of two pulsars due to a common SGWB. In Fig. 4, we report the Bayesian reconstruction of angular correlations between pulsars in the NANOGrav 15-year analysis from Ref. [6].

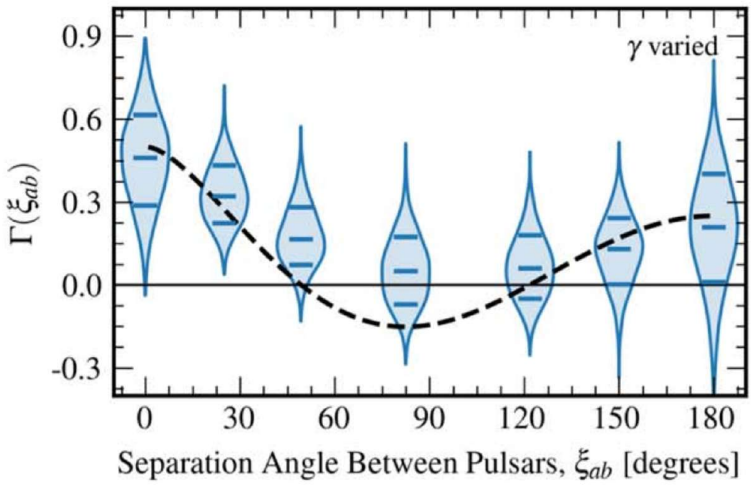

Figure 4: Bayesian reconstruction of angular correlations between pulsars in the NANOGrav 15-year analysis. Light blue violins are the marginal posterior densities with the Hellings-Downs curve as black dashed line. Figure taken from Ref. [6].

2.3 The Standard Model of particle physics

The SM of Particle Physics describes three of the four known fundamental interactions in nature: electromagnetic, weak and, strong. It is able to make astonishing predictions with unprecedented levels of accuracy.

The SM is the result of the last century of progress in particle physics, with synergies between theoretical developments and experimental discoveries. The framework of QFT was first introduced by Dirac in 1926 [121, 122], where he unified Quantum Mechanics with Special Relativity and developed the idea of fermions, after the introduction of the photon by Einstein in 1905 [123] and the relativistic wave equation for bosons by Klein and Gordon in 1926 [124, 125]. The principle of gauge invariance was formulated by Weyl in 1929 [126] and weak interactions were first described by Fermi in 1934 [127]. Then, Quantum Electrodynamics (QED) was developed by Feynman, Schwinger and Tomonaga in the late 1940s [128–130] and non-abelian gauge theories by Yang and Mills in 1954 [131]. The main ideas at the basis of the EW sector of the SM were developed in the 1960s. Electromagnetism and weak interactions were unified by Glashow in 1961 [132]. The SSB mechanism were introduced by Weinberg and Salam in 1967 [133, 134] to provide masses for the vector bosons without violating gauge invariance, which was inspired by the Higgs mechanism [135–138] and the Nambu-Goldstone theorem [139–141]. The renormalizability of the theory, using dimensional regularisation, was proven by 't Hooft and Veltman in 1971 [142–144]. On the other hand, the strong interactions were developed in the 1970s, when QCD, which is a non-abelian gauge theory with color triplet quarks and color octet gluons, was proposed by Gell-Mann, Fritzsch and Leutwyler in 1973 [145, 146], and asymptotic freedom was discovered by Gross, Wilczek and Politzer in 1973 [147, 148].

In this section, after describing the gauge group and the particle content of the SM, we focus on the SSB mechanism, following Refs. [149, 150].

2.3.1 Gauge group and particle content

At the heart of the SM, or in general of any physical theory, there is the concept of symmetry. Naively, a symmetry is a transformation that leaves a physical system invariant [151]. In mathematical language, symmetries are described by groups[11].

In the SM, both the particle content and the interactions are completely determined by the symmetries: the Poincaré group and the gauge group. In fact, particles are irreducible representations[12] of the Poincaré group, which represents the symmetries of spacetime: translations and Lorentz transformations. Particles can be classified according to their spin: scalar particles (spin 0), fermions (spin $1/2$), and vector bosons (spin 1). The spin s of a particle is related to its statistics, which determine how states occupy the phase space: bosons (integer spin) obey Bose-Einstein statistics, while fermions (half-integer spin) obey Fermi-Dirac statistics, already introduced in Eq. (2.1.25). The latter are subject to the Pauli exclusion principle. On the other hand, interactions are described by gauge or local symmetries, in which transformation parameters depend on spacetime coordinates. For each generator of the algebra, we introduce a gauge vector boson field of spin 1, which is the mediator of the interaction. Gauge bosons transform in the adjoint representation, while matter fields transform in the fundamental representation[13].

The SM gauge group is not simple, but it is the product of three simple groups. Before EWSSB, it is given by

$$\mathcal{G}_{\text{SM}} = SU(3)_c \times SU(2)_L \times U(1)_Y \,, \tag{2.3.1}$$

where $SU(3)_c$ is associated to the strong interaction, $SU(2)_L$ to the weak interaction and $U(1)_Y$ to hypercharge. Each group has its own coupling, which determines the interaction strength. There are 8 gauge bosons from $SU(3)_c$, G^a_μ, with $a = 1, \ldots, 8$, which are the gluons, 3 gauge bosons from $SU(2)_L$, W^i_μ, with $i = 1, 2, 3$, which are the weak bosons, and 1 gauge boson from $U(1)_Y$, B_μ, which is the hypercharge boson[14]

$$G = (\mathbf{8}, \mathbf{1})_0 \,, \quad W = (\mathbf{1}, \mathbf{3})_0 \,, \quad B = (\mathbf{1}, \mathbf{1})_0 \,. \tag{2.3.2}$$

After the EWSSB, the SM gauge group in Eq. (2.3.1) becomes

$$\mathcal{G}_{\text{SM}} = SU(3)_c \times U(1)_{\text{EM}} \,, \tag{2.3.3}$$

where $U(1)_{\text{EM}}$ is the electromagnetic gauge group. Its gauge boson, the massless photon A_μ, is generated by a linear combination of the $SU(2)_L$ and $U(1)_Y$ gauge bosons, while the other orthogonal

[11] A group $\mathcal{G}$ is a set of elements equipped with a binary operation $\cdot$ that satisfies three properties: closure, i.e. $\forall g_1, g_2 \in \mathcal{G}$, $g_1 \cdot g_2 \in \mathcal{G}$; associativity, i.e. $\forall g_1, g_2, g_3 \in \mathcal{G}$, $(g_1 \cdot g_2) \cdot g_3 = g_1 \cdot (g_2 \cdot g_3)$; the existence of an identity element $e \in \mathcal{G}$ such that $\forall g \in \mathcal{G}$, $e \cdot g = g \cdot e = g$; and each element $g \in \mathcal{G}$ has an inverse $g^{-1} \in \mathcal{G}$ such that $g \cdot g^{-1} = g^{-1} \cdot g = e$. A Lie group is a group that is also a differentiable manifold, which means that group elements are labelled by continuous parameters.

[12] A representation of $\mathcal{G}$ is a map $\rho : \mathcal{G} \to GL(V)$, where $GL(V)$ is the group of invertible linear transformations on a vector space V, such that $\rho(g_1 g_2) = \rho(g_1)\rho(g_2)$ for all $g_1, g_2 \in \mathcal{G}$. A representation is irreducible if there are no non-trivial invariant subspaces under the action of the group. The dimension of the representation is the dimension of the vector space V on which the group acts.

[13] The fundamental representation is the representation of the group that is the smallest non-trivial representation, i.e. it has dimension greater than 1. The adjoint representation is the representation of the group on its own algebra, i.e. it has dimension equal to the number of generators of the group. Mathematically, it is defined by $T^a_{bc} = -i f^a_{bc}$, where f^a_{bc} are the structure constants.

[14] We use the notation $(c, w)_Y$, where c, w and y are associated to $SU(3)_c$, $SU(2)_L$ and $U(1)_Y$, respectively.

combinations correspond to three massive bosons.

The SM is a chiral theory, which means that left- and right-handed fields do not have the same charges under the SM gauge group. Left-handed fermions are doublets of $SU(2)_L$, while right-handed fermions are singlets. Furthermore, we can divide the matter content into quarks and leptons, which are triplets and singlets of $SU(3)_c$, respectively. We can organise the SM matter content for quarks as

$$Q_L^i = \begin{pmatrix} u_L^i \\ d_L^i \end{pmatrix} = (\mathbf{3},\mathbf{2})_{\frac{1}{6}} \,, \quad u_R^i = (\mathbf{3},\mathbf{1})_{\frac{2}{3}} \,, \quad d_R^i = (\mathbf{3},\mathbf{1})_{-\frac{1}{3}} \,, \tag{2.3.4}$$

while for leptons we have

$$L_L^i = \begin{pmatrix} \nu_L^i \\ e_L^i \end{pmatrix} = (\mathbf{1},\mathbf{2})_{-\frac{1}{2}} \,, \quad e_R^i = (\mathbf{1},\mathbf{1})_{-1} \,. \tag{2.3.5}$$

Here, the index $i = 1, 2, 3$ labels the three generations, since the SM containes 3 families of fermions, which have exactly the same gauge interactions, but different masses.

The last ingredient of the SM is the Higgs boson, which is the only known fundamental scalar particle. It is a singlet under the $SU(3)_c$ group, doublet under the $SU(2)_L$ group, and has hypercharge $Y = \frac{1}{2}$

$$H = \begin{pmatrix} H^+ \\ H^0 \end{pmatrix} = (\mathbf{1},\mathbf{2})_{\frac{1}{2}} \,, \tag{2.3.6}$$

where H^+ is the charged component and H^0 is the neutral component of the Higgs doublet. It generates fermion and weak gauge boson masses through the mechanism of SSB. It was the last SM particle to be discovered, in 2012 by the collaborations ATLAS [152] and CMS [153] at the Large Hadron Collider (LHC).

2.3.2 Lagrangian

Within the framework of QFT, the dynamics of a system is described by a Lagrangian density $\mathcal{L}$, which is a function of the fields and their derivatives. It must satisfy the symmetries of the theory. Thus, in the case of the SM, it must be Lorentz and gauge invariant, which can be accomplished by requiring that all Lorentz indices are contracted and the sum of the charges under each gauge group vanishes. It must also be renormalisable, meaning that divergences can be absorbed into a finite number of parameters. Effectively, it translates into having terms with dimension less than or equal to 4 in natural units.

The Lagrangian of the SM is given by

$$\begin{aligned} \mathcal{L}_{\text{SM}} = &-\frac{1}{4} G^a_{\mu\nu} G^{\mu\nu a} - \frac{1}{4} W^i_{\mu\nu} W^{\mu\nu i} - \frac{1}{4} B_{\mu\nu} B^{\mu\nu} \\ &- i\bar{Q}^i_L \not{D} Q^i_L - i\bar{u}^i_R \not{D} u^i_R - i\bar{d}^i_R \not{D} d^i_R - i\bar{L}^i_L \not{D} L^i_L - i\bar{e}^i_R \not{D} e^i_R \\ &+ (D_\mu H)^\dagger (D^\mu H) - V(|H|) \\ &- \left(y^i_u \bar{Q}^i_L u^i_R H + y^i_d \bar{Q}^i_L d^i_R H^\dagger + y^i_e \bar{L}^i_L e^i_R H^\dagger + \text{h.c.} \right) + \theta \text{ terms} \,, \end{aligned} \tag{2.3.7}$$

where D_μ is the covariant derivative, which is defined as

$$D_\mu = \partial_\mu - i g_s T^a G^a_\mu - i g_2 T^i W^i_\mu - i g_1 Y B_\mu \,, \tag{2.3.8}$$

and g_s, g_2, and g_1 are the strong, weak, and hypercharge coupling constants, respectively.

The first row of Eq. (2.3.7) contains the kinetic term of the gauge bosons and self-interaction terms of non-abelian gauge groups. The field strength tensors are defined as

$$G^a_{\mu\nu} = \partial_\mu G^a_\nu - \partial_\nu G^a_\mu + g_s f^{abc} G^b_\mu G^c_\nu \,, \tag{2.3.9}$$

$$W^i_{\mu\nu} = \partial_\mu W^i_\nu - \partial_\nu W^i_\mu + g_2 \epsilon^{ijk} W^j_\mu W^k_\nu \,, \tag{2.3.10}$$

$$B_{\mu\nu} = \partial_\mu B_\nu - \partial_\nu B_\mu \,, \tag{2.3.11}$$

where f^{abc} and ϵ^{ijk} are the structure constants[15] of $SU(3)_c$ and $SU(2)_L$, respectively.

The second row of Eq. (2.3.7) describes the kinetic term of the fermions and their interactions with the gauge bosons. The covariant derivative ensures that the kinetic term of the fermions is gauge invariant, since it transforms in the same way as the fermions under gauge transformations.

2.3.3 Spontaneous symmetry breaking

Due to gauge invariance, it is not possible to write an explicit mass term for the gauge bosons or fermions in the Lagrangian, observe experimentally to be massive. Nevertheless, it is possible to generate particle masses through the Higgs mechanism, which follows from the Goldstone theorem and gauge invariance.

The Goldstone theorem states that if a global, continuous symmetry G is spontaneously broken to H, then the number of massless Goldstone bosons is given by

$$\dim(G/H) = \dim G - \dim H \,, \tag{2.3.12}$$

where G/H is the coset space[16]. In particular, the generators $\tilde{T}^A$ of the unbroken symmetry group H will annihilate the vacuum state $\langle\phi\rangle$, i.e.

$$\tilde{T}^A \langle\phi\rangle = 0 \,. \tag{2.3.13}$$

Each of the broken generators gives a zero mass eigenstate and a massless Goldstone boson.

The Higgs mechanism consists in introducing a scalar field H

$$H = \begin{pmatrix} H^+ \\ H^0 \end{pmatrix} \,, \tag{2.3.14}$$

which has a non-vanishing VEV that spontaneously breaks the EW gauge group $SU(2)_L \times U(1)_Y$ down to $U(1)_{\mathsf{EM}}$. The VEV is given by the non-zero value of the minimum of the scalar field potential

$$V(H) = -\mu^2 H^\dagger H + \lambda (H^\dagger H)^2 \,, \tag{2.3.15}$$

where $\mu^2 > 0$ and $\lambda > 0$, which is

$$|H|^2 = \frac{\mu^2}{2\lambda} = \frac{v^2}{2} \,, \tag{2.3.16}$$

[15] The structure constants are defined as $[T^a, T^b] = i f^{abc} T^c$ for the $SU(3)_c$ group and $[T^i, T^j] = i\epsilon^{ijk} T^k$ for the $SU(2)_L$ group, where T^a and T^i are the generators of the groups.

[16] The coset space G/H is the space of equivalence classes of G under the action of H.

defining $v = \sqrt{\frac{\mu^2}{\lambda}}$. The mechanism of SSB consists in choosing one of the minima of the potential in Eq. (2.3.15) as the ground state of the theory, parameterised as

$$\langle H \rangle = \frac{1}{\sqrt{2}} \begin{pmatrix} 0 \\ v \end{pmatrix} . \tag{2.3.17}$$

Using the Goldstone theorem and Eq. (2.3.13), we prove that not all the generators of the group $SU(2)_L \times U(1)_Y$ are broken, but there is a linear combination of the hypercharge generator Y and the third generator T^3 of $SU(2)_L$ that annihilate the VEV of the Higgs field in Eq. (2.3.17)

$$Q\langle H \rangle = \left(Y + T^3\right) \langle H \rangle = \begin{pmatrix} 1 & 0 \\ 0 & 0 \end{pmatrix} \begin{pmatrix} 0 \\ \frac{v}{\sqrt{2}} \end{pmatrix} = 0 \, , \tag{2.3.18}$$

where $Q = Y + T^3$ is the Gell-Mann-Nishijima relation to define the electric charge. This shows that the electric charge is an unbroken generator (2.3.13) and that the photon remains massless.

Since the ground state of the theory is given by the VEV of the Higgs field in Eq. (2.3.17), we can expand the radial fluctuations around it

$$H = \frac{1}{\sqrt{2}} \begin{pmatrix} 0 \\ v + h \end{pmatrix} , \tag{2.3.19}$$

where h is the physical Higgs boson. In unitary gauge, the other three degrees of freedom of the Higgs field in Eq. (2.3.14), which correspond to massless Goldstone bosons, are absorbed by the gauge bosons $W^{\pm}$ and Z^0, which become massive. To see this, we expand the kinetic term of the Higgs field in the Lagrangian in Eq. (2.3.7), we substitute the Higgs field in Eq. (2.3.19) and keep only quadratic terms in the gauge bosons, to obtain

$$(D_\mu H)^\dagger (D^\mu H) \supset \frac{v^2}{8} \left[g_2^2 \left((W_\mu^1)^2 + (W_\mu^2)^2 \right) + \left(g_2 W_\mu^3 - g_1 B_\mu \right)^2 \right] . \tag{2.3.20}$$

Then, we diagonalise the mass matrix, by means of a rotation into mass eigenstates Z and A_μ

$$Z_\mu = \frac{g_2 W_\mu^3 - g_1 B_\mu}{\sqrt{g_1^2 + g_2^2}} = W_\mu^3 \cos\theta_W - B_\mu \sin\theta_W \, , \tag{2.3.21}$$

$$A_\mu = \frac{g_1 W_\mu^3 + g_2 B_\mu}{\sqrt{g_1^2 + g_2^2}} = W_\mu^3 \sin\theta_W + B_\mu \cos\theta_W \, , \tag{2.3.22}$$

where the weak angle θ_W is defined as

$$\tan\theta_W = \frac{g_1}{g_2} \, , \quad \sin\theta_W = \frac{g_1}{\sqrt{g_1^2 + g_2^2}} \, , \quad \cos\theta_W = \frac{g_2}{\sqrt{g_1^2 + g_2^2}} \, . \tag{2.3.23}$$

Since W_μ^1 and W_μ^2 do not carry electric charge, they are combined to form the charged W bosons

$$W_\mu^{\pm} = \frac{W_\mu^1 \mp i W_\mu^2}{\sqrt{2}} \, . \tag{2.3.24}$$

Therefore, we substitute the expressions for the gauge bosons of Eqs. (2.3.21), (2.3.22) and (2.3.24)

into the kinetic term of the Higgs field in Eq. (2.3.20), finding

$$(D_\mu H)^\dagger (D^\mu H) \supset \frac{g_2^2 v^2}{4} W_\mu^+ W^{-\mu} + \frac{(g_1^2+g_2^2)v^2}{4} Z_\mu^2 = m_W^2 W_\mu^+ W_-^\mu + \frac{1}{2} m_Z^2 Z_\mu Z^\mu \,, \tag{2.3.25}$$

and we identify the masses of the gauge bosons

$$m_W = \frac{g_2 v}{2} \,, \quad m_Z = \frac{\sqrt{g_1^2+g_2^2}\,v}{2} = \frac{m_W}{\cos\theta_W} \,, \quad m_A = 0 \,. \tag{2.3.26}$$

The Higgs mechanism also gives mass to fermions, which can be found by substituting the Higgs field of Eq. (2.3.19) into the Yukawa terms in the fourth row of Eq. (2.3.7)

$$\mathcal{L}_{\text{Yukawa}} \supset -\frac{y_u^i v}{\sqrt{2}} \bar{u}_R^i u_L^i - \frac{y_d^i v}{\sqrt{2}} \bar{d}_R^i d_L^i - \frac{y_e^i v}{\sqrt{2}} \bar{e}_R^i e_L^i + \text{h.c.} \,, \tag{2.3.27}$$

so that

$$m_u^i = \frac{y_u^i v}{\sqrt{2}} \,, \quad m_d^i = \frac{y_d^i v}{\sqrt{2}} \,, \quad m_e^i = \frac{y_e^i v}{\sqrt{2}} \,, \tag{2.3.28}$$

where m_u^i, m_d^i and m_e^i are the masses of the up-type quarks, down-type quarks and charged leptons, respectively. In the SM, neutrinos are massless, even though there is experimental evidence for neutrino oscillations, which implies that they must have a small mass.

Finally, the Higgs field mass can be obtained by substituting the Higgs field of Eq. (2.3.19) into the potential in Eq. (2.3.15) and keeping only quadratic terms

$$V(|H|) \supset \lambda v^2 h^2 = \frac{1}{2} m_h^2 h^2 \,. \tag{2.3.29}$$

2.4 Dark sectors

The SM has been proven to be a successful theory. However, in addition to the experimental phenomena the SM cannot account for, including neutrino oscillations and masses, baryon asymmetry, and dark matter, there are also a number of theoretical issues for which it does not provide an answer.

While much attention has been given to the possibility that heavy new physics could solve some of these open problems, another interesting explanation could come from hidden or light DSs. These refer to the introduction of new fields, and related particles, which are not charged under the SM gauge group but charged under new dark forces, hence the name dark. They have not been detected so far because of their feeble interactions with SM particles. These models can range from the simplest addition of a dark $U(1)$ gauge vector field to more general models that include DSs with several new states. The connection between the two sectors is possible through the inclusion in the Lagrangian of portals, usually written in the form [154]

$$\mathcal{L}_{DS} = \sum_i c_i \mathcal{O}_i^{SM} \mathcal{O}_i^{DS} \,, \tag{2.4.1}$$

where c_i are couplings, while $\mathcal{O}_i^{SM}$ and $\mathcal{O}_i^{DS}$ are operators containing SM and DS fields, respectively. The latter takes different forms according to the spin nature of the new particles. The most common

lowest dimension portals are summarised in Table 2.

Particle	Spin	Portal
Dark scalar S	0 (scalar)	$(\mu S + \lambda S^2)H^\dagger H$
Axion or axion-like particles a	0 (pseudo-scalar)	$a\tilde{F}_{\mu\nu}F^{\mu\nu}/f_a$, $(\bar{\psi}\gamma^\mu\gamma_5\psi)\partial_\mu a/f_a$
Heavy neutral lepton N	$1/2$ (fermion)	$y_N LHN$
Dark photon A'_μ	1 (vector)	$-\epsilon F'_{\mu\nu}B^{\mu\nu}$

Table 2: Dark sector particles, their spin, and their portal with the Standard Model.

These new particles can be considered only as mediators between the two sectors, or dark matter candidates as well. One of the advantages of introducing such DS portals is that they reduce to a parameter space with only a few free parameters, which are experimentally testable.

In this section, we focus on the vector and scalar portals, following Refs. [155, 156].

2.4.1 Dark photon

The dark photon[17] portal is responsible for the kinetic mixing between a dark and a visible abelian gauge vector boson [157]. The visible one can be identified as the SM photon or the hypercharge boson, depending on whether EWSSB has occurred, while the dark photon arises from an additional $U(1)_D$ gauge symmetry. The meaning of this operator is that the two gauge vector bosons can go into each other as they propagate. The kinetic mixing between two abelian gauge groups is possible since the field strength tensor is invariant under a transformation of that group, a feature that is not possible for non-abelian gauge groups.

We begin by considering the massless case, since an explicit mass term for a gauge boson is forbidden by gauge invariance. The Lagrangian is given by

$$\mathcal{L} = -\frac{1}{4}F_a^{\mu\nu}F_{a\mu\nu} - \frac{1}{4}F_b^{\mu\nu}F_{b\mu\nu} - \frac{\epsilon}{2}F_a^{\mu\nu}F_{b\mu\nu} + eJ_\mu A_b^\mu + e'J'_\mu A_a^\mu \,, \tag{2.4.2}$$

where $F_i^{\mu\nu} = \partial^\mu A_i^\nu - \partial^\nu A_i^\mu$ with $i = a, b$ are the field strength tensors, ϵ is a dimensionless parameter that quantifies the strength of the mixing, J_μ and J'_μ are the electromagnetic and dark currents that couple to the gauge fields with coupling constants e and e', respectively. The Lagrangian in Eq. (2.4.2) is written in the gauge basis (A_a^μ, A_b^μ) that appears to have a non-diagonal kinetic matrix, but it is convenient to work in the physical basis, in which the kinetic matrix is diagonal and canonically normalised with a factor of $-\frac{1}{4}$ in front of the field strength tensors $F_{\mu\nu}$. In the physical basis, fields propagate independently, with mixing effects shifted entirely to the interaction terms. The relation between the gauge basis $(A_a^\mu,\ A_b^\mu)$ and the physical basis $(A_\mu,\ A'_\mu)$ is given by

$$\begin{bmatrix} A_a^\mu \\ A_b^\mu \end{bmatrix} = \begin{bmatrix} \frac{1}{\sqrt{1-\epsilon^2}} & 0 \\ -\frac{\epsilon}{\sqrt{1-\epsilon^2}} & 1 \end{bmatrix} \begin{bmatrix} \cos\theta & -\sin\theta \\ \sin\theta & \cos\theta \end{bmatrix} \begin{bmatrix} A'^\mu \\ A^\mu \end{bmatrix} \,, \tag{2.4.3}$$

where θ is an arbitrary angle. Hence, the kinetic part of the Lagrangian in Eq. (2.4.2) in the physical

[17] In the literature, it is also referred to as hidden, para-, secluded photon or U-boson.

basis, obtained by the transformation in Eq. (2.4.3), is given by

$$\mathcal{L}_{kin} = -\frac{1}{4}F_{\mu\nu}F^{\mu\nu} - \frac{1}{4}F'_{\mu\nu}F'^{\mu\nu} \,, \tag{2.4.4}$$

and the interaction part of the Lagrangian (2.4.2), in the physical basis, becomes

$$\begin{aligned}\mathcal{L}_{int} = &\left(\frac{e'\cos\theta}{\sqrt{1-\epsilon^2}}J'_\mu + e\left(\sin\theta - \frac{\epsilon\cos\theta}{\sqrt{1-\epsilon^2}}\right)J_\mu\right)A'^\mu \\ &+ \left(-\frac{e'\sin\theta}{\sqrt{1-\epsilon^2}}J'_\mu + e\left(\cos\theta + \frac{\epsilon\sin\theta}{\sqrt{1-\epsilon^2}}\right)J_\mu\right)A^\mu \,.\end{aligned} \tag{2.4.5}$$

Note that the arbitrary angle θ is explicit in the Lagrangian, so we need to fix θ. Choosing $\sin\theta = 0$ leaves the SM photon couple only to SM current while the dark photon to both

$$\mathcal{L}_{int} = \left(\frac{e'}{\sqrt{1-\epsilon^2}}J'_\mu - \frac{e\epsilon}{\sqrt{1-\epsilon^2}}J_\mu\right)A'^\mu + eJ_\mu A^\mu \,. \tag{2.4.6}$$

On the other hand, setting $\sin\theta = \epsilon$ gives the opposite situation

$$\mathcal{L}_{int} = e'J'_\mu A'^\mu + \left(-\frac{e'\epsilon}{\sqrt{1-\epsilon^2}}J'_\mu + \frac{e}{\sqrt{1-\epsilon^2}}J_\mu\right)A^\mu \,. \tag{2.4.7}$$

Consider now the massive case. A minimal approach, without introducing a dark scalar field to give mass to the dark photon, is to consider the Stueckelberg mechanism [158], which adds mass terms the Lagrangian in Eq. (2.4.2)

$$\mathcal{L} \supset -\frac{1}{2}m_a^2 A_a^\mu A_{a\mu} - \frac{1}{2}m_b^2 A_b^\mu A_{b\mu} - m_a m_b A_a^\mu A_{b\mu} \,. \tag{2.4.8}$$

Since the SM photon is massless, rotating to the physical basis and setting $m_A = 0$ constrains the angle θ to satisfy $\sin\theta = 0$, so that the interaction Lagrangian reduces to Eq. (2.4.6). The parameter space for this model is only spanned by $(\epsilon, m_{A'})$ and the interaction with the SM matter is given by the term

$$\mathcal{L}_{int} \supset -\frac{e\epsilon}{\sqrt{1-\epsilon^2}}J_\mu A'^\mu \simeq -e\epsilon J_\mu A'^\mu \,. \tag{2.4.9}$$

On the experimental side, a massive dark photon can be produced through several processes [45, 46, 155]. Examples include bremsstrahlung, $e^-Z \to e^-ZA'$, where an electron scatters off a nuclear target of atomic number Z; pair annihilation, $e^-e^+ \to \gamma A'$, involving an electron-positron pair; meson decays, $M \to \gamma A'$, where M may be π^0, η, K, or D; and Drell-Yan production, $q\bar{q} \to A' \to l^+l^-/h^+h^-$, where a quark-antiquark pair annihilates into a dark photon that subsequently decays into either a lepton pair l^+l^- or a hadron pair h^+h^-.

Detection strategies depend on the nature of the final states. In visible decay channels, the dark photon can appear as a resonance over the background in collider or beam-dump experiments. Alternatively, invisible decays into undetectable dark matter particles can be probed through missing momentum/energy signatures, providing indirect evidence of the A'_μ. Finally, the missing-mass technique allows the detection of invisible particles when the initial state is fully reconstructed.

Another way to generate the dark photon mass is through the Higgs mechanism, by introducing a dark scalar field S that acquires a VEV after SSB. Therefore, we extend the Lagrangian in Eq. (2.4.2) with the kinetic term and potential of the dark scalar S

$$\mathcal{L} \supset (D_\mu S)^\dagger (D^\mu S) - V(S) \,, \tag{2.4.10}$$

where $D_\mu = \partial_\mu + ig_3 T^\alpha G^\alpha_\mu + ig_2 T^a W^a_\mu + ig_1 Y B_\mu + i(g_m Y + g'_1 Q')B'_\mu$ is the covariant derivative. g_m accounts for the kinetic mixing. If the dark scalar S is charged only under the dark $U(1)_D$ gauge group, the covariant derivative reduces to $D_\mu = \partial_\mu + ig'_1 Q' B'_\mu$. Applying the rotation in Eq. (2.4.3) with $\sin\theta = 0$

$$\begin{bmatrix} A^\mu_a \\ A^\mu_b \end{bmatrix} = \begin{bmatrix} \frac{1}{\sqrt{1-\epsilon^2}} & 0 \\ -\frac{\epsilon}{\sqrt{1-\epsilon^2}} & 1 \end{bmatrix} \begin{bmatrix} A'^\mu \\ A^\mu \end{bmatrix} \,, \tag{2.4.11}$$

the kinetic term of the dark scalar S in Eq. (2.4.10) becomes

$$(D_\mu S)^\dagger D^\mu S = (\partial_\mu S)^\dagger (\partial^\mu S) + \frac{{g'_1}^2 |S|^2 A'_\mu A'^\mu}{2(1-\epsilon^2)} + \frac{g'_1 J'_\mu A'^\mu}{\sqrt{1-\epsilon^2}} \,. \tag{2.4.12}$$

After SSB, when the dark scalar acquires a VEV $S = \frac{v_s}{\sqrt{2}}$, the second term in Eq. (2.4.12) yields the squared mass of the dark photon

$$m^2_{A'} = \frac{{g'_1}^2 v_s^2}{1-\epsilon^2} \,. \tag{2.4.13}$$

The parameter space of this model is spanned by $(\epsilon, m_{A'}, v_s)$. In order to satisfy the experimental constraints [155], the mixing parameter ϵ must be small, i.e. $\epsilon \ll 1$, so that Eq. (2.4.13) reduces to

$$m^2_{A'} \simeq {g'_1}^2 v_s^2 \,. \tag{2.4.14}$$

2.4.2 Dark scalar

In the scalar extension of the SM, the dark scalar field S, introduced via the Higgs mechanism to give mass to the dark photon, can also interact with the Higgs boson

$$\mathcal{L}_{HS} = \frac{1}{2}\lambda_{HS} |H|^2 |S|^2 \,, \tag{2.4.15}$$

where λ_{HS} is the coupling between the Higgs and the dark scalar. The introduction of the term in Eq. (2.4.15) has the implication that the mass matrix is not diagonal and is given by

$$\mathcal{M} = \begin{bmatrix} m^2_h & m^2_{sh} \\ m^2_{sh} & m^2_s \end{bmatrix} \,, \tag{2.4.16}$$

where $m^2_{sh} = \lambda_{HS} v v_S$. Therefore, a rotation of the fields into the physical basis is needed to extract the physical mass eigenstates

$$h = H\cos\alpha + S\sin\alpha \,, \quad s = -H\sin\alpha + S\cos\alpha \,. \tag{2.4.17}$$

Assuming the hierarchy $v_S \ll v_H$ and $\lambda_{HS} \ll 1$, we can infer that the mixing angle is approximately $\sin\alpha \simeq \frac{\lambda_{HS} v_S}{\lambda_H v_H}$. The parameter space of this model is given by $(m_s, \sin\alpha)$. The mixed quartic coupling

in Eq. (2.4.15) translates into mass mixing in Eq. (2.4.16), which, after diagonalisation, results in the mixing between scalar fields. Dark scalars are under scrutiny in experimental searches [45, 46].

3 Cosmological phase transitions

The theory of cosmological PTs took root in the second half of the 20th century. The effective potential in QFT was first introduced by Euler, Heisenberg and Schwinger [159, 160]. It was then applied to spontaneous symmetry breaking in the 1960s by Goldstone, Salam, S. Weinberg and Jona-Lasinio [141, 161], generalised in the 1970s to one-loop by Coleman and E. Weinberg [162] and later to higher-loop order by Jackiw, Iliopoulos, Itzykson and Martin [163, 164]. The generalisation to finite temperature and the discovery of symmetry restoration was introduced in the 1970s by Kirzhnits, Linde, Bernard, Dolan, Jackiw and S. Weinberg [165–169]. The false vacuum decay was first introduced in QFT in 1974 by Kobzarev, Okun and Voloshin [170] and in 1977 by Coleman and Callan [29, 30], then generalised for finite-temperature in late 1970s by Linde [31–33]. The breakdown of perturbation theory at high temperatures was noted by Kirzhnits and Linde [171–173]. The concept of false vacuum fraction is attributed to Guth, Tye and Weinberg from the 1980s [47, 174]. Supercooled PT was studied by Witten [175] and by Hawking and Moss [50]. Finally, GWs from cosmological FOPTs were first studied by Witten and Hogan [34, 35].

The main physical quantities necessary to describe cosmological FOPTs are built from the effective potential and the false vacuum decay rate, which are reviewed in Secs. 3.1 and 3.2, respectively. Then, we characterise the cosmological FOPT by means of the thermal parameters in Section 3.3 and the expected SGWB spectrum in Section 3.4.

3.1 Effective potential

The most general form of the effective potential is written as a sum of different contributions. Beginning with the tree-level potential from the Lagrangian, we need to add the effects of the interactions with virtual loop particles as dictated by quantum mechanics and the interactions with the thermal bath in the early Universe. In this section, we compute each of these building blocks, following Refs. [149, 162, 176, 177].

3.1.1 Functional methods

The effective potential arises naturally from the path integral formalism of QFT, in which it is useful to consider the presence of a classical external field.

Consider a theory described by a scalar field ϕ with a Lagrangian density $\mathcal{L}(\phi, \partial_\mu \phi)$ and a classical action $S[\phi] = \int d^4x\, \mathcal{L}(\phi, \partial_\mu \phi)$. In the path integral representation, correlation functions, i.e. the vacuum-to-vacuum amplitude in the presence of an external source $J(x)$, contain the essential information needed to extract observables in QFT, such as cross sections and decay rates. The presence of the source $J(x)$ implies the appearance of vertices in Feynman diagrams with a single external line attached. There are different generating functionals that can be introduced to obtain correlation functions. We begin with the generating functional of correlation functions $Z[J]$, also known as the partition function, defined as

$$Z[J] = \langle 0_{\text{out}} | 0_{\text{in}} \rangle_J = \int \mathcal{D}\phi\, e^{iS[\phi] + i\int d^4x\; J(x)\phi(x)}\,, \tag{3.1.1}$$

where $\mathcal{D}\phi$ is the path integral measure and a linear coupling of ϕ to an external source $J(x)$ is added. We can obtain correlation functions from the functional derivatives of the partition function. In fact,

using Eq. (3.1.1), the n-point correlation function $\langle\phi(x_1)\dots\phi(x_n)\rangle$ reads

$$\langle\phi(x_1)\dots\phi(x_n)\rangle = \frac{1}{Z[0]}\left(\frac{1}{i}\right)^n \frac{\delta^n Z[J]}{\delta J(x_1)\dots\delta J(x_n)}\Big|_{J=0}\,, \tag{3.1.2}$$

where the overall normalisation of the path integral $Z[0]=\langle 1\rangle$ is the sum of all bubble graphs, both connected and disconnected.

To isolate only connected diagrams[18], we define the generating functional of connected correlation functions $W[J]$ as

$$Z[J] = e^{iW[J]}\,, \quad iW[J] = \ln Z[J]\,. \tag{3.1.3}$$

$W[J]$ removes disconnected diagrams and leaves only connected ones. Similarly to Eq. (3.1.2), the n-point connected correlation functions $\langle\phi(x_1)\dots\phi(x_n)\rangle_c$ read

$$\langle\phi(x_1)\dots\phi(x_n)\rangle_c = \frac{\delta^n iW[J]}{\delta J(x_1)\dots\delta J(x_n)}\Big|_{J=0}\,. \tag{3.1.4}$$

From Eqs. (3.1.2) and (3.1.3), we obtain the connected one-point function in the presence of a non-vanishing source $J(x)$

$$\langle\phi(x)\rangle_{c,\,J} = \frac{\delta W[J]}{\delta J(x)} = \frac{\langle 0_{\text{out}}|\phi(x)|0_{\text{in}}\rangle_J}{\langle 0_{\text{out}}|0_{\text{in}}\rangle_J} = \frac{\int\mathcal{D}\phi\;\phi(x)e^{iS[\phi]+i\int d^4x\;J(x)\phi(x)}}{\int\mathcal{D}\phi\;e^{iS[\phi]+i\int d^4x\;J(x)\phi(x)}}\,, \tag{3.1.5}$$

which is called the classical or mean field, since it is a weighted average over all possible fluctuations. If we set the source to zero $J=0$, we obtain the VEV of the field $\phi(x)$

$$\varphi(x) = \langle\phi(x)\rangle_{c,\,J=0}\,. \tag{3.1.6}$$

In order to respect the full Poincaré symmetry, it must be a constant

$$\varphi(x) = \varphi_{cl} = \text{const}\,. \tag{3.1.7}$$

In fact, translation invariance forces it to be the same at all spacetime points, and Lorentz invariance guarantees it cannot get any special direction, so it must be a single spacetime point-independent number.

We introduce the generating functional of one-particle-irreducible (1PI)[19] correlation functions, also known as the effective action, as the Legendre transform of $W[J]$ in Eq. (3.1.3)

$$\Gamma[\varphi] = \min_J\left(W[J] - \int d^4x\;J(x)\varphi(x)\right)\,. \tag{3.1.8}$$

The minimality condition in its definition means that there is a relation $\varphi=\varphi(J)$ between the source

[18] Connected diagrams are those with all connected internal lines. In other words, it cannot be split into two or more disconnected parts.

[19] 1PI diagrams are those that cannot be disconnected by cutting a single internal line and have external lines amputated, i.e. without propagators associated with them.

$J(x)$ and the field $\varphi(x)$, which is given by

$$\frac{\delta W[J]}{\delta J(x)} - \varphi(x) = 0 \,, \tag{3.1.9}$$

and, by inverting it to express J as a functional of φ, we obtain

$$\Gamma[\varphi] = W[J] - \int d^4x \; J(\varphi(x))\varphi(x) \,. \tag{3.1.10}$$

Another property of the effective action is

$$\frac{\delta \Gamma[\varphi]}{\delta \varphi(x)} = -J(x) \,, \tag{3.1.11}$$

which implies that, in the absence of external sources, the vacuum of the theory is determined by the condition

$$\frac{\delta \Gamma[\varphi]}{\delta \varphi}\Big|_{J=0} = 0 \,. \tag{3.1.12}$$

Eq. (3.1.12) can be interpreted as an equation of motion, since its solution is the stable quantum state of the theory, hence the name effective action. Similarly to Eq. (3.1.2), the n-point 1PI correlation functions $\Gamma^{(n)}(x_1, \ldots, x_n)$ read

$$\Gamma^{(n)}(x_1, \ldots, x_n) = \langle \phi(x_1) \ldots \phi(x_n) \rangle_{\text{1PI}} = \frac{\delta^n \Gamma[\varphi]}{\delta\varphi(x_1) \ldots \delta\varphi(x_n)}\Big|_{\varphi=0} \,. \tag{3.1.13}$$

We express the 1PI correlation functions as the coefficients of the Taylor expansion of $\Gamma[\varphi]$ in Eq. (3.1.10) in powers of the external source $J(x)$

$$\Gamma[\varphi] = \sum_{n=0}^{\infty} \frac{1}{n!} \int d^4x_1 \ldots d^4x_n \; \varphi(x_1) \ldots \varphi(x_n) \Gamma^{(n)}(x_1, \ldots, x_n) \,. \tag{3.1.14}$$

In momentum space, the Fourier transform of the 1PI correlation functions is

$$\Gamma^{(n)}(x_1, \ldots x_n) = \int \frac{d^4p_1}{(2\pi)^4} \ldots \frac{d^4p_n}{(2\pi)^4} \; e^{ip_1x_1 + \ldots + ip_nx_n} \tilde{\Gamma}^{(n)}(p_1, \ldots, p_n) \,. \tag{3.1.15}$$

Then, we introduce the 1PI correlation function in momentum space $\tilde{\Gamma}^{(n)}(p_1, \ldots, p_n) = (2\pi)^4 \delta^4(p_1 + \ldots + p_n)\Gamma^{(n)}(p_1, \ldots, p_n)$, in which the momentum conservation has been extracted out. Using the definition of the delta function in momentum space $\delta^4(p_1 + \ldots + p_n) = \int \frac{d^4x}{(2\pi)^4} e^{-ip_1x - \ldots - ip_nx}$ and position space $\delta^4(x_i - x) = \int \frac{d^4p_i}{(2\pi)^4} e^{ip_i(x_i - x)}$, we insert Eq. (3.1.15) into Eq. (3.1.14) to obtain

$$\Gamma[\varphi] = \sum_{n=0}^{\infty} \frac{1}{n!} \int d^4x \; \varphi^n(x) \Gamma^{(n)}(p_1, \ldots, p_n) \,. \tag{3.1.16}$$

For a constant field φ_{cl}, we define the effective potential $V_{\text{eff}}(\varphi_{cl})$ as

$$\Gamma[\varphi_{cl}] = -\int d^4x\, V_{\text{eff}}(\varphi_{cl}) = -VT\, V_{\text{eff}}(\varphi_{cl})\,, \tag{3.1.17}$$

which follows from the fact that Γ is an extensive quantity and it is proportional to the volume of the spacetime region over which the functional integral is taken, so that we can factor out the spacetime volume VT. Then, it is possible to extract the effective potential $V_{\text{eff}}(\varphi_{cl})$ from Eq. (3.1.16) as

$$V_{\text{eff}}(\varphi_{cl}) = -\sum_{n=0}^{\infty} \frac{1}{n!}\varphi_{cl}^n \Gamma^{(n)}(0,\dots,0)\,, \tag{3.1.18}$$

where $\Gamma^{(n)}(p_i = 0)$ is the sum of all 1PI n-point functions evaluated at zero external momenta.

3.1.2 One-loop effective potential

The effective action Γ encodes the complete set of physical predictions:

- its minimum corresponds to the vacuum state of the theory, whose location determines whether the symmetries of the Lagrangian are preserved or spontaneously broken;
- its second derivative is the inverse of the propagator, whose poles give the particle masses;
- its higher derivatives yield one-particle-irreducible amplitudes, from which higher-point connected amplitudes and the S-matrix are constructed.

Intuitively, the potential is the sum of non-derivative Lagrangian interactions involving only scalar fields, with a negative sign in front. Its minima correspond to the classical vacua of the theory. The most general renormalisable tree-level potential is given by [178]

$$V(\phi_i) = V_0 + t_i\phi_i + \frac{1}{2}m_{ij}^2\phi_i\phi_j + \frac{1}{3!}k_{ijk}\phi_i\phi_j\phi_k + \frac{1}{4!}\lambda_{ijkl}\phi_i\phi_j\phi_k\phi_l\,, \tag{3.1.19}$$

where ϕ_i is a set of N real scalar fields with $i = 1,\dots N$. The constant term V_0, usually written as Λ^4 and referred to as the cosmological constant, can be neglected in the absence of gravity, since only energy differences matter. Since a constant shift of the field corresponds only to a reparametrisation, it does not change the physics of the theory. This freedom is often used to redefine the field such that the linear term is removed from the potential. For a given model, the Lagrangian must respect further internal symmetries.

Stationary points of the tree-level potential in Eq. (3.1.19) are field locations where first derivatives with respect to each field vanish, i.e. $\left.\frac{\partial V_{\text{tree}}(\phi_i)}{\partial\phi_i}\right|_{\langle\phi_i\rangle} = 0$. Whether they are minima, maxima, or saddle points can be investigated by looking at the Hessian matrix evaluated at stationary points $\langle\phi_i\rangle$, defined as $H_{ij} = \left.\frac{\partial^2 V_{\text{tree}}(\phi_i)}{\partial\phi_i\partial\phi_j}\right|_{\langle\phi_i\rangle}$. The scalar mass matrix is given by the Hessian at the minimum, i.e. $m^2_{\phi_i\phi_j} = \left.\frac{\partial^2 V_{\text{tree}}(\phi_i)}{\partial\phi_i\partial\phi_j}\right|_{\langle\phi_i\rangle}$. If it is not diagonal, a rotation of fields is necessary in order to find physical mass eigenstates, as shown in Sec. 2.4.2. The analysis of the potential in classical field theory follows a geometrical approach: we need to minimise the potential in order to find the vacuum state of the theory, and then we study the stability of this vacuum by looking at the second derivative of

the potential. In QFT, this approach is not spoiled, even though one could think that quantum corrections would do so, but instead we only need to substitute the classical potential with the effective potential, so that the minimisation condition follows from Eq. (3.1.12) and reads

$$\left.\frac{\partial V_{\text{eff}}}{\partial \varphi_{cl}}\right|_{\langle\phi_i\rangle} = 0 \,. \tag{3.1.20}$$

There are different ways to compute the one-loop contribution to the effective potential, using Feynman diagrams à la Coleman in Ref. [162] or using functional methods à la Jackiw in Ref. [163]. In the following, we use the Coleman's approach.

Consider a massless real scalar field with quartic self-interaction

$$\mathcal{L} = \frac{1}{2}\partial_\mu\phi\partial^\mu\phi - \frac{\lambda}{4!}\phi^4 \,. \tag{3.1.21}$$

The zeroth-order, the effective potential is given by the tree-level potential

$$V_{\text{tree}}(\varphi_{cl}) = \frac{\lambda}{4!}\varphi_{cl}^4 \,. \tag{3.1.22}$$

From Eq. (3.1.18), the effective potential is the infinite sum of all connected 1PI diagrams with external classical fields, evaluated at zero external momentum. Since the only interactions have an even number of legs, we can only have an even number of external legs. As illustrated in Fig. 5, the n-th one-loop diagram has the following structure:

- a single loop, giving an integral $\int \frac{d^4p}{(2\pi)^4}$;
- n propagators, each contributing with $\frac{i}{p^2+i\epsilon}$;
- n vertices, each contributing with $-\frac{i\lambda}{2}$;
- $2n$ external legs, each contributing with a factor of φ_{cl};
- a symmetry factor $\frac{1}{2n}$, from rotational ($\frac{1}{n}$) and reflection ($\frac{1}{2}$) symmetries;
- and an extra factor of i from the definition of the generating functional.

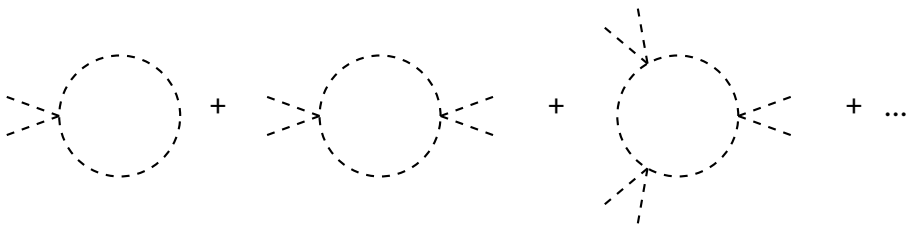

Figure 5: One-loop Feynman diagrams contributing to the effective potential for a scalar field theory.

Putting everything together, the one-loop contribution to the effective potential is

$$V_{\text{1-loop}}(\varphi_{cl}) = \sum_{n=1}^{\infty}\frac{i}{2n}\int\frac{d^4p}{(2\pi)^4}\left(\frac{\lambda\varphi_{cl}^2/2}{p^2+i\epsilon}\right)^n = -\frac{i}{2}\int\frac{d^4p}{(2\pi)^4}\ln\left(1-\frac{\lambda\varphi_{cl}^2/2}{p^2+i\epsilon}\right) \,, \tag{3.1.23}$$

where we have used the series expansion $\ln(1-x) = -\sum_{n=1}^{\infty} \frac{x^n}{n}$. Performing a Wick rotation $p_E = (-ip_0, \vec{p})$ such that $p^2 = p_0^2 - |\vec{p}|^2 = -p_E^2$, we obtain

$$V_{\text{1-loop}}(\varphi_{cl}) = \frac{1}{2}\int \frac{d^4p_E}{(2\pi)^4} \ln\left(1 + \frac{\lambda\varphi_{cl}^2/2}{p_E^2}\right) = \frac{1}{2}\int \frac{d^4p_E}{(2\pi)^4} \ln\left(p_E^2 + \frac{\lambda\varphi_{cl}^2}{2}\right) , \tag{3.1.24}$$

where we have dropped φ_{cl}-independent terms, since they do not contribute to the effective potential. Noting that the field-dependent mass can be written as $m^2(\varphi_{cl}) = \frac{d^2V_{\text{tree}}(\varphi_{cl})}{d\varphi_{cl}^2} = \frac{\lambda\varphi_{cl}^2}{2}$, we rewrite the one-loop effective potential in Eq. (3.1.24) as

$$V_{\text{1-loop}}(\varphi_{cl}) = \frac{1}{2}\int \frac{d^4p}{(2\pi)^4} \ln\left(p^2 + m^2(\varphi_{cl})\right) . \tag{3.1.25}$$

We generalise to the case of a fermion spin-$1/2$ field ψ

$$\mathcal{L} = i\bar{\psi}\partial\!\!\!/\psi - (\frac{y}{\sqrt{2}}\phi\bar{\psi}\psi + h.c.) . \tag{3.1.26}$$

Since the trace of an odd number of gamma matrices vanishes, only an even number of external legs appear. As illustrated in Fig. 6, the $2n$-th one-loop diagram has the following structure:

- a single loop, which gives an integral $\int \frac{d^4p}{(2\pi)^4}$;
- $2n$ propagators, each contributing with a factor $\frac{ip\!\!\!/}{p^2+i\epsilon}$;
- $2n$ vertices, each contributing with a factor $-iy$;
- $2n$ external legs, each contributing with a factor φ_{cl};
- a symmetry factor of $\frac{1}{2n}$, due to symmetry under rotation $\frac{1}{n}$ and reflection $\frac{1}{2}$;
- a trace over fermionic loop with a minus sign;
- an extra factor i coming from the generating functional definition.

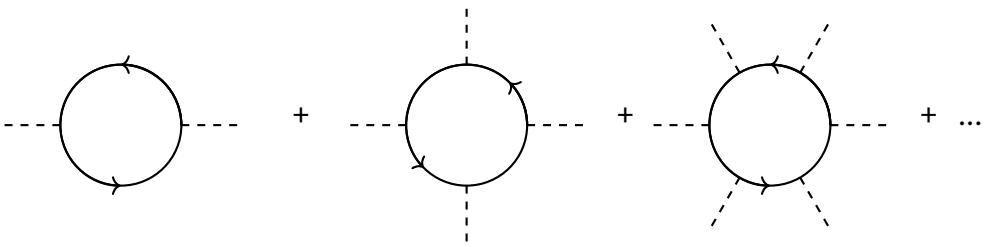

Figure 6: One-loop diagrams contributing to the effective potential for a fermion theory.

Putting everything together, the one-loop contribution to the effective potential is

$$V_{\text{1-loop}}(\varphi_{cl}) = -i\sum_n \frac{1}{2n}\text{tr}\int \frac{d^4p}{(2\pi)^4}\left(\frac{ip\!\!\!/\,(-iy)\,\varphi_{cl}/\sqrt{2}}{p^2+i\epsilon}\right)^{2n} = -\sum_n \frac{i}{2n}\text{tr}\int \frac{d^4p}{(2\pi)^4}\left(\frac{p^2y^2\varphi_{cl}^2/2}{(p^2+i\epsilon)^2}\right)^n , \tag{3.1.27}$$

where we have added a trace over fermionic degrees of freedom and used the property $\not{p}^2 = p^2$. Hence, using the same procedure as in the scalar case and recognising the field-dependent mass $m^2(\varphi_{cl}) = \frac{y^2\varphi_{cl}^2}{2}$, the one-loop contribution to the effective potential is given by

$$V_{\text{1-loop}}(\varphi_{cl}) = -\frac{g}{2}\int \frac{d^4p}{(2\pi)^4}\ln\left(p^2 + m^2(\varphi_{cl})\right) \ , \tag{3.1.28}$$

where we have computed the trace over the fermionic degrees of freedom, which gives $g = 4(2)$ for Dirac (Weyl) fermions.

Finally, we generalise to a gauge boson field A_μ

$$\mathcal{L} = -\frac{1}{4}F_{\mu\nu}F^{\mu\nu} + (D_\mu\phi)^\dagger D^\mu\phi \, . \tag{3.1.29}$$

In Landau gauge, we do not require ghost-compensating terms. Derivative coupling diagrams vanish, such as cubic ones, following from $p_\mu\Delta^{\mu\nu}(p) = 0$. As illustrated in Fig. 7, the n-th one-loop diagram has the following structure:

- a single loop, giving an integral $\int \frac{d^4p}{(2\pi)^4}$;
- n propagators, each contributing with $-i\frac{\eta_{\mu\nu} - \frac{p_\mu p_\nu}{p^2}}{p^2+i\epsilon} = -\frac{i\Delta^{\mu\nu}}{p^2+i\epsilon}$;
- n vertices, each contributing with $2ig^2$;
- $2n$ external legs, each contributing with φ_{cl};
- a symmetry factor $\frac{1}{2n}$, from rotational ($\frac{1}{n}$) and reflection ($\frac{1}{2}$) symmetries;
- and an extra factor of i from the definition of the generating functional.

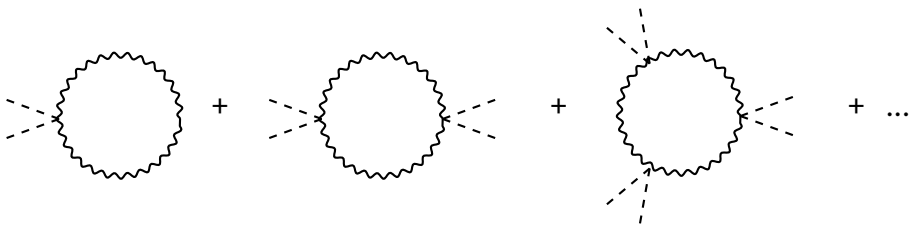

Figure 7: One-loop diagrams contributing to the effective potential for a gauge boson theory.

Combining, the one-loop contribution to the effective potential is

$$V_{\text{1-loop}}(\varphi_{cl}) = -i\sum_n \frac{1}{2n}\text{tr}\int\frac{d^4p}{(2\pi)^4}\left(-\frac{i\Delta^{\mu\nu}\,(2ig^2)\,\varphi_{cl}^2/2}{p^2+i\epsilon}\right)^n = -\sum_n \frac{i\text{tr}\Delta^{\mu\nu}}{2n}\int\frac{d^4p}{(2\pi)^4}\left(\frac{g^2\varphi_{cl}^2}{p^2+i\epsilon}\right)^n , \tag{3.1.30}$$

where we have used the convolution property of the propagator $\Delta^{\mu\alpha}\Delta_\alpha{}^\nu = \Delta^{\mu\nu}$. Hence, using the same procedure as in the scalar case and recognising the field-dependent mass $m^2(\varphi_{cl}) = g^2\varphi_{cl}^2$, the one-loop contribution to the effective potential is given by

$$V_{\text{1-loop}}(\varphi_{cl}) = \frac{3}{2}\int \frac{d^4p}{(2\pi)^4}\ln\left(p^2 + m^2(\varphi_{cl})\right) \ , \tag{3.1.31}$$

where we have computed the trace over the Lorentz indices, i.e. $\mathrm{tr}\Delta^{\mu\nu} = 3$.

The scalar in Eq. (3.1.25), fermion in Eq. (3.1.28) and a gauge boson in Eq. (3.1.31) cases can be condensed into a single expression

$$V_{\text{1-loop}}(\varphi_{cl}) = \sum_i \frac{(-1)^{2s_i+1} n_i}{2} \int \frac{d^4p}{(2\pi)^4} \ln\left(p^2 + m^2(\varphi_{cl})\right) \ , \tag{3.1.32}$$

where s_i is the spin and n_i are the degrees of freedom of the i-th particle: $n_i = 1$ for real scalars, $n_i = 2$ for complex scalars or Majorana fermions, $n_i = 3$ for gauge bosons[20] and $n_i = 4$ for Dirac fermions.

The general expression for the one-loop effective potential in Eq. (3.1.32) is ultraviolet divergent, so to make sense out of it, we apply the renormalisation procedure of QFT. First, we need to make it finite with regularisation, and then infinities are absorbed by appropriate counterterms with a choice of the renormalisation conditions. Common regularisation methods include dimensional and cut-off regularisations, while the most widely used renormalisation schemes are modified minimal subtraction ($\overline{\text{MS}}$) and on-shell renormalisation schemes.

In cut-off regularisation, we introduce a cut-off Λ in the momentum integrals, i.e. $|p^2| \leq \Lambda^2$, and the one-loop effective potential in Eq. (3.1.32) becomes

$$V_{\text{1-loop}}(\varphi_{cl}) = \sum_i (-1)^{2s_i+1} n_i \left(\frac{1}{32\pi^2} m_i^2(\varphi_{cl}) \Lambda^2 + \frac{1}{64\pi^2} m_i^4(\varphi_{cl}) \left(\ln \frac{m_i^2(\varphi_{cl})}{\Lambda^2} - \frac{1}{2} \right) \right) \ . \tag{3.1.33}$$

In dimensional regularisation [144, 179, 180], we treat the dimensionality of the space-time as a continuous number $D = 4 - 2\epsilon$, where ϵ is a small parameter, we introduce a mass scale μ to maintain the right dimensionality and the effective potential in Eq. (3.1.32) yields

$$V_{\text{1-loop}}(\varphi_{cl}) = \sum_i (-1)^{2s_i+1} n_i \left(\frac{m_i^4(\varphi_{cl})}{64\pi^2} \left(-\left(\frac{1}{\epsilon} - \gamma_E + \ln 4\pi \right) + \ln \frac{m_i^2(\varphi_{cl})}{\mu^2} - \frac{3}{2} \right) \right) \ . \tag{3.1.34}$$

In the on-shell renormalisation scheme [181], we apply renormalisation conditions such that the minimum of the effective potential is not modified by the quantum corrections

$$\frac{dV_{\text{1-loop}}(\varphi_{cl})}{d\varphi_{cl}}\Big|_{\varphi_{cl}=v} = 0 \ , \quad \frac{d^2V_{\text{1-loop}}(\varphi_{cl})}{d\varphi_{cl}^2}\Big|_{\varphi_{cl}=v} = 0 \ , \tag{3.1.35}$$

and the one-loop effective potential reads

$$V_{\text{1-loop}}(\varphi_{cl}) = \sum_i (-1)^{2s_i+1} n_i \left(\frac{1}{64\pi^2} \left(m_i^4(\varphi_{cl}) \left(\ln \frac{m_i^2(\varphi_{cl})}{m_i^2(v)} - \frac{3}{2} \right) + 2m_i^2(v) m_i^2(\varphi_{cl}) \right) \right) \ . \tag{3.1.36}$$

In the $\overline{\text{MS}}$ scheme [182, 183] the renormalisation conditions are such that we subtract the diver-

[20] Even for massless gauge bosons, like the photon, you need to count 3 degrees of freedom, because they acquire a thermal mass.

gent terms[21], and the one-loop effective potential is given by

$$V_{\text{1-loop}}(\varphi_{cl}) = \sum_i (-1)^{2s_i+1} n_i \left(\frac{1}{64\pi^2} m_i^4(\varphi_{cl}) \left(\ln \frac{m_i^2(\varphi_{cl})}{\mu^2} - \frac{3}{2} \right) \right) . \tag{3.1.37}$$

3.1.3 Renormalisation group equation

In dimensional regularisation, the one-loop effective potential in Eq. (3.1.34) depends on a renormalisation scale μ. An appropriate choice is to keep the logarithms appearing from higher order corrections small, thus avoiding large logarithms which can appear as multiplicative factors with each power of the expansion parameter and maintaining perturbative control. Since the one-loop effective potential depends on the field-dependent masses, evaluating the potential at field values that vary several orders of magnitude, while the renormalisation scale is kept fixed, can lead to large uncertainties. The renormalisation scale μ is unphysical, since physical observables are independent of its choice. This implies that a change in μ should be compensated by a change in the parameters of the theory. In mathematical terms this translates into

$$\frac{d\Gamma[\varphi_{cl}]}{d\mu} = \left(\mu \frac{\partial}{\partial \mu} + \beta_i \frac{\partial}{\partial \lambda_i} - \gamma \varphi_{cl} \frac{\partial}{\partial \varphi_{cl}} \right) \Gamma[\varphi_{cl}] = 0 , \tag{3.1.38}$$

where Γ is the effective action, β_i are the beta functions of the couplings λ_i and γ is the anomalous dimension of the field φ_{cl}. In terms of the effective potential, it reads

$$\frac{dV_{\text{eff}}(\varphi_{cl})}{d\mu} = \left(\mu \frac{\partial}{\partial \mu} + \beta_i \frac{\partial}{\partial \lambda_i} - \gamma \varphi_{cl} \frac{\partial}{\partial \varphi_{cl}} \right) V_{\text{eff}}(\varphi_{cl}) = 0 , \tag{3.1.39}$$

which is the Renormalisation Group Equation (RGE) or Callan-Symanzik equation. Its formal solution is given by

$$V_{\text{eff}} = V_{\text{eff}}(\mu,\ \lambda_i,\ \varphi_{cl}) = V_{\text{eff}}(\mu(t),\ \lambda_i(t),\ \varphi_{cl}(t)) , \tag{3.1.40}$$

where

$$\mu(t) = \mu(0) e^t , \quad \varphi_{cl}(t) = \varphi_{cl}(0) e^{-\int_0^t dt' \gamma(\lambda_i(t))} , \quad \beta_i(t) = \frac{d\lambda_i(t)}{dt} . \tag{3.1.41}$$

The RGE in Eq. (3.1.39) can be solved numerically by integrating the beta functions and the anomalous dimension, and then substituting them back into the one-loop effective potential.

3.1.4 Thermal field theory

The formalism of QFT is suitable to describe physics at zero-temperature, like in particle colliders. However, in the early Universe, the temperature is not negligible and the thermal bath of particles needs to be taken into account. Therefore, thermal field theory or finite temperature field theory, which is the combination of QFT and thermodynamics, is the appropriate framework to use.

Consider the canonical ensemble, in which the system is in contact with a heat reservoir with fixed temperature T, particle number N and volume V. Given a Hamiltonian H, the canonical density

[21] To be precise, it is MS scheme in which we subtract only the divergent part, in $\overline{\text{MS}}$ scheme, we subtract also constant terms such as γ_E and 4π.

operator is given by

$$\rho = \frac{e^{-\beta H}}{\text{tr}\, e^{-\beta H}} = \frac{1}{Z} e^{-\beta H} \,, \tag{3.1.42}$$

where $\beta = \frac{1}{T}$ is the inverse temperature of the thermal bath and $Z = \text{tr}\, e^{-\beta H}$ is the partition function. The density matrix in Eq. (3.1.42) is used to describe the equilibrium state of the system, by means of the canonical average of an arbitrary operator O

$$\langle O \rangle = \frac{1}{Z} \text{tr}(O\rho) \,, \tag{3.1.43}$$

satisfying the property $\langle 1 \rangle = 1$. An important relation is the Kubo-Martin-Schwinger (KMS) condition [184, 185], which states that bosonic (fermionic) field is symmetric (anti-symmetric) and cyclic in time, with $-i\beta$ periodicity

$$\begin{aligned} \langle \phi(\mathbf{y}, t)\phi(\mathbf{x}, 0)\rangle_T &= \text{tr}\left(\phi(\mathbf{y}, t)\phi(\mathbf{x}, 0)\rho\right) = \frac{1}{Z}\text{tr}\left(\phi(\mathbf{y}, t)\phi(\mathbf{x}, 0)e^{-\beta H}\right) \\ &= \frac{1}{Z}\text{tr}\left(\phi(\mathbf{y}, t)e^{i(-i\beta H)}\phi(\mathbf{x}, 0)e^{-i(-i\beta H)}e^{-\beta H}\right) = \frac{1}{Z}\text{tr}\left(\phi(\mathbf{y}, t)\phi(\mathbf{x}, -i\beta)e^{-\beta H}\right) \\ &= \frac{1}{Z}\text{tr}\left(\phi(\mathbf{x}, -i\beta)e^{-\beta H}\phi(\mathbf{y}, t)\right) = \pm\langle \phi(\mathbf{y}, 0)\phi(\mathbf{x}, t - i\beta)\rangle \,, \end{aligned} \tag{3.1.44}$$

where we have used the canonical average in Eq. (3.1.43), the cyclicity property of the trace, the time evolution $\phi(\mathbf{x}, t) = e^{itH}\phi(0, \mathbf{x})e^{-itH}$ and the fact that fermionic fields anti-commute, while bosonic fields commute. Performing a Wick rotation $t \to \tau = -it$, we identify the imaginary time τ with the inverse temperature β[22]. At finite temperature, Fourier transforms are modified by replacing the integral over time components with a discrete sum

$$\int \frac{d^4p}{(2\pi)^4} f(p) \to T \sum_{n=-\infty}^{\infty} \int \frac{d^3p}{(2\pi)^3} f(\omega_n, \mathbf{p}) \,, \tag{3.1.45}$$

where the Matsubara frequencies are given by

$$\omega_n = \begin{cases} 2n\pi T & \text{for bosons} \\ (2n+1)\pi T & \text{for fermions} \end{cases} . \tag{3.1.46}$$

The role of the Matsubara sum is to add all contributions allowed by KMS relations in Eq. (3.1.44). In perturbative theory, this implies that the Feynman rules must be modified in the following way:

- For each propagator, we have for bosons $\frac{i}{p^2 - m^2}$ with $p_\mu = (2ni\pi\beta^{-1}, \mathbf{p})$ or for fermions $\frac{i}{\not{p} - m}$ with $p_\mu = ((2n+1)i\pi\beta^{-1}, \mathbf{p})$.
- For each loop integral, as in Eq. (3.1.45), we substitute the integral over d^4p with the integral over d^3p and the sum over the Matsubara frequencies $\frac{i}{\beta}\sum_{n=-\infty}^{\infty}\int \frac{d^3p}{(2\pi)^3}$.
- For each vertex, $-i\beta(2\pi)^3\delta\left(\sum_i \omega_i\right)\delta^3\left(\sum_i \mathbf{p}_i\right)$ is given by Matsubara frequencies and momentum conservation.

[22] This is called imaginary-time or Matsubara formalism, which has the advantage to describe the system in thermal equilibrium but loses access to the dynamics. The alternative is the real-time formalism, which succeeds in describing the out-of-equilibrium dynamics.

3.1.5 Finite-temperature effective potential

For the scalar field theory in Eq. (3.1.21), using the diagrams in Fig. 5 with the finite-temperature Feynman rules, the finite-temperature effective potential is given by

$$V_{1T}(\varphi_{cl}, T) = \frac{1}{2\beta} \sum_{n=-\infty}^{\infty} \int \frac{d^3p}{(2\pi)^3} \, \ln(\omega_n^2 + \omega^2) \, , \tag{3.1.47}$$

where $\omega^2 = |\mathbf{p}|^2 + m^2(\varphi_{cl})$ and $\omega_n = 2\pi n T$ are the Matsubara frequencies in Eq. (3.1.46). By differentiating with respect to ω the integrand in Eq. (3.1.47)

$$f(\omega) = \sum_{n=-\infty}^{\infty} \ln(\omega_n^2 + \omega^2) \quad \Rightarrow \quad \frac{\partial f(\omega)}{\partial \omega} = \sum_{n=-\infty}^{\infty} \frac{2\omega}{\omega_n^2 + \omega^2} = 2\beta \left(\frac{\omega}{2} + \frac{e^{-\beta\omega}}{1 - e^{-\beta\omega}} \right) \, , \tag{3.1.48}$$

and integrate back with respect to ω, Eq. (3.1.47) becomes

$$V_{1T}(\varphi_{cl}, \, T) = \int \frac{d^3p}{(2\pi)^3} \, \left(\frac{\omega}{2} + \frac{1}{\beta} \ln(1 - e^{-\beta\omega}) \right) \, . \tag{3.1.49}$$

Using the following identity

$$-\frac{i}{2} \int_{-\infty}^{\infty} \frac{dx}{2\pi} \ln(-x^2 + \omega^2 - i\epsilon) = \frac{\omega}{2} + \text{const} \, , \tag{3.1.50}$$

which can be proved with the residue theorem or taking the derivative with respect to ω and integrating back, the first term in the integrand of the effective potential in Eq. (3.1.49) can be written as

$$V_{1T}(\varphi_{cl}, T = 0) = \frac{1}{2} \int \frac{d^3p}{(2\pi)^3} \omega = \frac{1}{2} \int \frac{d^4p}{(2\pi)^4} \ln(p^2 + m^2(\varphi_{cl})) \, , \tag{3.1.51}$$

which is exactly the zero-temperature effective potential in Eq. (3.1.25). On the other hand, the temperature-dependent part of the integral of the effective potential in Eq. (3.1.49) cannot be written in a closed form, but, after switching to spherical coordinates

$$V_{1T}(\varphi_{cl}, T \neq 0) = \frac{1}{\beta} \int \frac{d^3p}{(2\pi)^3} \, \ln(1 - e^{-\beta\omega}) = \frac{1}{2\pi^2\beta} \int_0^{\infty} dp \, p^2 \ln(1 - e^{-\beta\omega}) \, , \tag{3.1.52}$$

and making a change of variable $x = \beta p$, we find

$$V_{1T}(\varphi_{cl}, T \neq 0) = \frac{1}{2\pi^2\beta^4} \int_0^{\infty} dx \, x^2 \ln(1 - e^{-\sqrt{x^2 + \beta^2 m^2(\varphi_{cl})}}) = \frac{1}{2\pi^2\beta^4} J_b(m^2(\varphi_{cl})\beta^2) \, , \tag{3.1.53}$$

where the bosonic thermal function is defined as

$$J_b(m^2\beta^2) = \int_0^{\infty} dx \, x^2 \ln(1 - e^{-\sqrt{x^2 + \beta^2 m^2}}) \, . \tag{3.1.54}$$

The case with a gauge boson is treated in the same way, while for the fermionic case in Eq. (3.1.26), using the finite-temperature Feynman rules for the diagrams in Fig. 6, the finite-temperature effec-

tive potential is given by

$$V_{1T}(\varphi_{cl},T)=-\frac{1}{2\beta}\sum_{n=-\infty}^{\infty}\int\frac{d^3p}{(2\pi)^3}\,\ln(\omega_n^2+\omega^2)\,, \tag{3.1.55}$$

where $\omega=|\mathbf{p}|^2+m^2(\varphi_{cl})$ and $\omega_n=(2n+1)\pi T$ are the Matsubara frequencies in Eq. (3.1.46). Using the same procedure for the bosonic case, we obtain

$$V_{1T}(\varphi_{cl},T)=-\int\frac{d^3p}{(2\pi)^3}\,\left(\frac{\omega}{2}+\frac{1}{\beta}\ln(1+e^{-\beta\omega})\right)\,, \tag{3.1.56}$$

where the first term in the integrand is the zero-temperature effective potential in Eq. (3.1.28) and the second term is the temperature-dependent part, which can be written as

$$V_{1T}(\varphi_{cl},T\neq 0)=-\frac{g}{\beta}\int\frac{d^3p}{(2\pi)^3}\,\ln(1-e^{-\beta\omega})=-\frac{g}{2\pi^2\beta^4}J_f(m^2(\varphi_{cl})\beta^2)\,, \tag{3.1.57}$$

where we introduced the number of degrees of freedom g and the fermionic thermal function is defined as

$$J_f(m^2\beta^2)=\int_0^\infty dx\,x^2\ln(1+e^{-\sqrt{x^2+\beta^2m^2}})\,. \tag{3.1.58}$$

To summarise, the finite-temperature contributions to the effective potential are given by

$$V_{1T}(\varphi_{cl},T)=\frac{T^4}{2\pi^2}\Big(\sum_b n_bJ_b\Big(\frac{m_b^2(\chi)}{T^2}\Big)-\sum_f n_fJ_f\Big(\frac{m_f^2(\chi)}{T^2}\Big)\Big)\,. \tag{3.1.59}$$

A useful expression is the high-temperature expansion for $y\ll 1$ of the thermal functions in Eqs. (3.1.54) and (3.1.58)

$$J_b(y)=\int_0^\infty dx\,x^2\ln(1-e^{-\sqrt{x^2+y}})\,,\simeq-\frac{\pi^4}{45}+\frac{\pi^2}{12}y-\frac{\pi}{6}y^{\frac{3}{2}}-\frac{1}{32}y^2\ln\frac{y}{a_b}\,, \tag{3.1.60}$$

$$J_f(y)=\int_0^\infty dx\,x^2\ln(1+e^{-\sqrt{x^2+y}})\,,\simeq\frac{7\pi^4}{360}-\frac{\pi^2}{24}y-\frac{1}{32}y^2\ln\frac{y}{a_f}\,, \tag{3.1.61}$$

where $a_b=16\pi^2e^{3/2-2\gamma_E}$ and $a_f=\pi^2e^{3/2-2\gamma_E}$. Note that in the bosonic expansion in Eq. (3.1.60), a non-analytic term appears $-\frac{\pi}{6}x^{3/2}$, which is not present in the fermionic expansion in Eq. (3.1.61).

An important feature of the finite temperature effective potential at high temperature is that its leading contribution in Eqs. (3.1.60) and (3.1.61) is given by $\varphi_{cl}^2T^2$, meaning that the symmetry is restored [165, 166, 168, 169, 172, 186]: at sufficiently high temperatures, this temperature-dependent mass term dominates over any other mass contribution, forcing the minimum of the potential to be at $\varphi_{cl}=0$. While at low temperatures, the effective potential has an absolute minimum at $\langle\phi\rangle\neq 0$, at high temperatures, the absolute minimum due to the $\varphi_{cl}^2T^2$ term is $\langle\phi\rangle=0$. Therefore, the symmetry breaking is not present anymore in the latter regime, because the vacuum of the theory is at $\langle\phi\rangle=0$ and the field has no VEV. We can understand the cosmological history of the Universe: after the Big Bang, the Universe is in a symmetric phase $\langle\phi\rangle=0$, however, as it expands and the temperature decreases, the absolute minimum of the potential is no longer at $\langle\phi\rangle=0$, but instead

at $\langle\phi\rangle \neq 0$. This means that the minimum at $\phi = 0$ becomes metastable, and a PT can take place.

Depending on the shape of the effective potential as the temperature decreases, the transition can proceed in different ways. If the PT is of second-order, the minimum of the effective potential changes smoothly as the temperature decreases, and the transition proceeds continuously. In this case, thermal fluctuations drive the scalar field to evolve homogeneously toward the new vacuum state. Since the two phases are analytically connected, there is no discontinuity in the order parameter, and therefore no release of latent heat. On the other hand, if the PT is of first-order, the effective potential develops two distinct minima, separated by a barrier. The system initially is in the metastable false vacuum, and the transition to the true vacuum occurs discontinuously, with the order parameter exhibiting a finite jump at the critical temperature. The process takes place through the nucleation of bubbles of true vacuum within the false one, induced either by quantum tunneling or thermal fluctuations.

3.1.6 Daisy resummation

Symmetry restoration at high temperature leads to a breakdown of perturbation theory, otherwise temperature-dependent radiative corrections should not be able to restore the symmetry broken by the temperature-independent tree-level potential. It is expected, given the presence of another energy scale in the theory, namely the temperature T. The failure of perturbation theory is linked to the appearance of infrared divergences for the zero Matsubara modes of bosonic degrees of freedom, which is restored by the resummation of higher-order finite-temperature diagrams.

The T-dependence of a loop amplitude can be obtained from its superficial degree of divergence D[23]: for $D > 0$, it goes as T^D. This implies that, for a scalar theory with a quartic self-interacting coupling λ, such as in Eq. (3.1.21), the diagram contributing to the self-energy on the left in Fig. 8 is quadratically divergent and behaves as λT^2.

Furthermore, consider the daisy diagram, consisting of a main central loop and $N-1$ self-energy diagrams attached to it, called petals, illustrated on the right in Fig. 8. Since each petal gives a contribution of λT^2 and introducing the mass scale of the theory m, for a daisy diagrams with $N-1$ petals, gives $\lambda^N \frac{T^{2N-1}}{m^{2N-3}} = \alpha^N \frac{m^3}{T}$, where we have introduced the effective coupling $\alpha = \frac{\lambda T^2}{m^2}$. The competition between the tree-level mass m and the thermal corrections T triggers the PT when they are comparable $m^2 \sim \lambda T^2$ or $\alpha \sim 1$, leading to a daisy diagrams of the order $\lambda^{\frac{3}{2}} T^2$. This implies that daisy diagrams have the same values at each order in perturbation theory, as they do not depend on the number N of loops, and do not recede with increasing loop order, which contradicts the usual expectation of perturbation theory [177].

Effectively, following the Arnold-Espinosa procedure [187] to resum daisy diagram in the effective potential, a new term needs to be included [188]

$$V_{\text{daisy}}(\varphi_{cl}, T) = -\sum_b \frac{T}{12\pi} \left((m_b^2(\varphi_{cl}) + \Pi(T))^{3/2} - (m_b^2(\varphi_{cl}))^{3/2} \right) . \tag{3.1.62}$$

Since the infrared divergence occurs only for zero Matsubara mode, this term must be added only for scalar and longitudinal gauge vector bosons, since fermions do not have zero Matsubara modes and transverse gauge bosons are protected by gauge symmetry.

[23] The superficial degree of divergence is given by $D = 4L - 2B - F$, where L is the number of loops, B is the number of boson propagators and F is the number of fermion propagators.

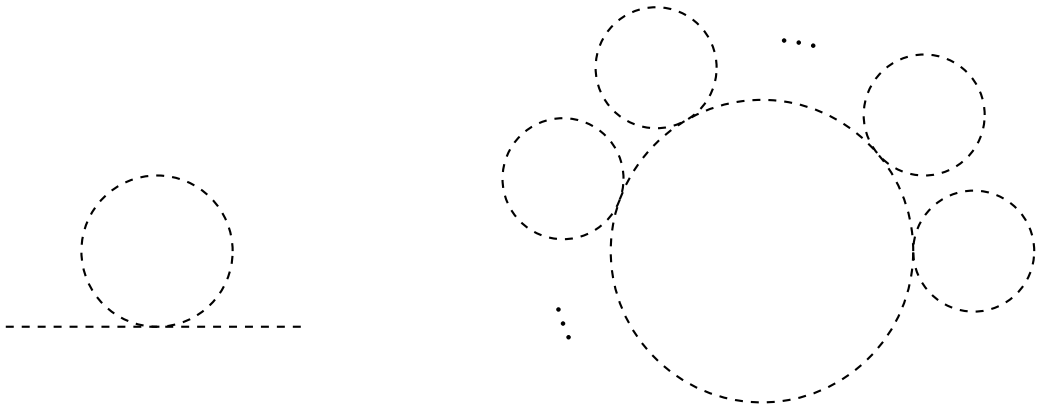

Figure 8: Self-energy one-loop diagram (left) and daisy diagram (right) for a scalar field theory.

To summarise, the effective potential at finite temperature can be expressed as a sum of different contributions: the tree-level in Eq. (3.1.19), the one-loop in on-shell in Eq. (3.1.36) or $\overline{\text{MS}}$ scheme in Eq. (3.1.37), the finite-temperature in Eq. (3.1.59) and the daisy in Eq. (3.1.62)

$$V_{\text{eff}}(\varphi_{cl}, T) = V_{\text{tree}}(\varphi_{cl}) + V_{\text{1-loop}}(\varphi_{cl}) + V_{1T}(\varphi_{cl}, T) + V_{\text{daisy}}(\varphi_{cl}, T)\,. \tag{3.1.63}$$

3.2 False vacuum decay

As seen in Sec. 3.1.5, the shape of the effective potential changes with the temperature, shifting the position of the vacuum. Therefore, in the potential two vacua can appear: an absolute minimum, the true vacuum, and a local minimum, the false vacuum. If the PT is first-order, there is a barrier between the two states, making the false vacuum metastable. In this section, we derive the most general expression for the false vacuum decay rate, i.e. the probability per unit time and volume for the field to escape the barrier via quantum tunneling or thermal fluctuations, following Refs. [29–33, 178].

3.2.1 Tunneling in quantum mechanics

We begin with quantum tunneling in quantum mechanics. Consider a unit-mass particle in a one-dimensional potential $V(x)$, with Hamiltonian $H(x,p) = \frac{p^2}{2} + V(x)$. In classical mechanics, the only allowed region for the particle motion is where the energy E is greater than the potential $V(x)$, i.e. $E \geq V(x)$. However, in quantum mechanics, there is a non-zero probability that the particle tunnels through the potential in the classically-forbidden region with $E < V(x)$. There are equivalent ways to compute this probability, for example solving the time-independent Schrödinger equation, but we will make use of the path integral representation, because it can be easily generalised to QFT .

In the path integral representation, the transition amplitude for the particle to start at $(t_i,\ q_i)$ and end at $(t_f,\ q_f)$ is given by[24]

$$\langle q_i | e^{-\frac{i\hat{H}T}{\hbar}} | q_f \rangle = \mathcal{N} \int_{q_i}^{q_f} \mathcal{D}q\, e^{\frac{iS[q]}{\hbar}}\,, \tag{3.2.1}$$

where $T = t_f - t_i > 0$ is the time of the process, $\mathcal{N}$ is a normalisation factor, $|q_i\rangle,\ |q_f\rangle$ are position eigenstates, $\mathcal{D}q$ denotes the path integral measure, i.e. integration over all functions $q(t)$ satisfying

[24] In this section, we restore $\hbar$.

the boundary conditions $q(t_i) = q_i$ and $q(t_f) = q_f$, and the action is

$$S[q] = \int_{t_i}^{t_f} dt \, \left(\frac{1}{2} \left(\frac{dq}{dt} \right)^2 - V(q) \right) \, . \tag{3.2.2}$$

It is convenient to perform a Wick rotation $\tau = it$, where τ is the Euclidean imaginary time, to obtain the Euclidean action S_E from Eq. (3.2.2)

$$iS[q] = i \int_{t_i}^{t_f} dt \, \left(\frac{1}{2} \left(\frac{dq}{dt} \right)^2 - V(q) \right) = - \int_{\tau_i}^{\tau_f} d\tau \, \left(\frac{1}{2} \left(\frac{dq}{d\tau} \right)^2 + V(q) \right) = -S_E[q] \, , \tag{3.2.3}$$

and write Eq. (3.2.1) as

$$\langle q_i | e^{-\frac{\hat{H}\mathcal{T}}{\hbar}} | q_f \rangle = \mathcal{N} \int_{q_i}^{q_f} \mathcal{D}q \, e^{-\frac{S_E[q]}{\hbar}} \, , \tag{3.2.4}$$

where now $\mathcal{T} = \tau_f - \tau_i$ is the Euclidean time of the process, which turns oscillatory integrals into convergent Gaussian ones. If we consider a complete set of eigenstates of the Hamiltonian $\hat{H}|n\rangle = E_n|n\rangle$ such that $\langle n|m\rangle = \delta_{mn}$, we can insert the completeness relation $\sum_n |n\rangle\langle n| = 1$ into the left-hand side of Eq. (3.2.4) to write

$$\begin{aligned} \langle q_i | e^{-\frac{\hat{H}\mathcal{T}}{\hbar}} | q_f \rangle &= \sum_{n,m} \langle q_i | n \rangle \langle n | e^{-\frac{\hat{H}\mathcal{T}}{\hbar}} | m \rangle \langle m | q_f \rangle = \sum_{n,m} e^{-\frac{E_m \mathcal{T}}{\hbar}} \langle q_i | n \rangle \langle n | m \rangle \langle m | q_f \rangle \\ &= \sum_n e^{-\frac{E_n \mathcal{T}}{\hbar}} \langle q_i | n \rangle \langle n | q_f \rangle \, , \end{aligned} \tag{3.2.5}$$

and, supposing ordered energy eigenvalues $E_0 < E_1 \leq E_2 \leq \ldots$, for large $\mathcal{T}$, only the lowest-energy eigenstate of the Hamiltonian E_0 contributes, i.e. the ground state, since all the others are exponentially suppressed

$$\langle q_i | e^{-\frac{\hat{H}\mathcal{T}}{\hbar}} | q_f \rangle \xrightarrow{\mathcal{T} \to \infty} e^{-\frac{E_0 \mathcal{T}}{\hbar}} \langle q_i | 0 \rangle \langle 0 | q_f \rangle \, . \tag{3.2.6}$$

Looking at the right-handed side of Eq. (3.2.4), we expect that, in the semi-classical approximation for small $\hbar$, the dominant contribution to the path integral comes from the path $\bar{q}$ that minimises the action $\bar{S}_E = \bar{S}_E[\bar{q}]$, since all other paths are exponentially suppressed, i.e. the solution of the classical Euler-Lagrange equations of motion

$$\frac{\delta S_E}{\delta \bar{q}} = -\frac{d^2 \bar{q}}{d\tau^2} + \frac{dV(\bar{q})}{dq} = 0 \, , \tag{3.2.7}$$

which is Newton's second law with an upturned potential $V(q) \to -V(q)$, and the Euclidean energy is a constant of motion

$$E = \frac{1}{2} \left(\frac{d\bar{q}}{d\tau} \right)^2 - V(\bar{q}) \, . \tag{3.2.8}$$

Therefore, the Euclidean trajectory is the motion of a classical particle in the inverted potential $-V(q)$. In particular, we are interested in the case in which the particle starts and ends at the same position, i.e. $q_i = q_f = 0$, called the bounce solution, with boundary conditions $\bar{q}(\tau_i) = \bar{q}(\tau_f) = 0$.

Using the saddle-point approximation or method of the steepest descent[25], we expand the Euclidean action around the bounce solution $S_E \simeq \bar{S}_E + \delta S_E$, so that the path integral in Eq. (3.2.4) becomes

$$\int \mathcal{D}q\, e^{-\frac{S_E[q]}{\hbar}} \simeq \int \mathcal{D}q\, e^{-\frac{\bar{S}_E - \delta S_E}{\hbar}} = e^{-\frac{\bar{S}_E}{\hbar}} \int \mathcal{D}q\, e^{-\frac{\delta S_E}{\hbar}} = C e^{-\frac{\bar{S}}{\hbar}} , \tag{3.2.9}$$

where C is defined to be

$$C = \int \mathcal{D}q\, e^{-\frac{\delta S_E}{\hbar}} . \tag{3.2.10}$$

Since the bounce solution $\bar{q}$ is a minimum of the Euclidean action S_E in Eq. (3.2.7), the first-order variation vanishes and the prefactor C gets contributions only from the second-order variation, which after integrating by parts, is given by

$$\delta S_E = \frac{1}{2} \int d\tau\, \delta q \left(-\frac{d^2}{d\tau^2} + \frac{d^2 V(\bar{q})}{dq^2} \right) \delta q = \frac{1}{2} \int d\tau\, \delta q \hat{M} \delta q \, , \tag{3.2.11}$$

where we have introduced the operator $\hat{M}$ defined by

$$\hat{M} = -\frac{d^2}{d\tau^2} + \frac{d^2 V(\bar{q})}{dq^2} . \tag{3.2.12}$$

Hence, we treat the prefactor in Eq. (3.2.10) as a Gaussian integral in the path integral representation to obtain

$$C = (\det \hat{M})^{-1/2} = \left[\det(-\partial_\tau^2 + V''(\bar{q})) \right]^{-1/2} = \prod_n \lambda_n^{-1/2} , \tag{3.2.13}$$

where λ_n are the eigenvalues of $\hat{M}$ subject to the boundary conditions. Using the saddle-point approximation of the path integral in Eq. (3.2.9) and the prefactor in Eq. (3.2.13), we can write the transition amplitude in Eq. (3.2.4) as

$$\langle q_i | e^{-\frac{\hat{H}\mathcal{T}}{\hbar}} | q_f \rangle = \mathcal{N} \prod_n \lambda_n^{-\frac{1}{2}} e^{-\frac{\bar{S}}{\hbar}} (1 + \mathcal{O}(\hbar)) = \mathcal{N} \left[\det(-\partial_\tau^2 + V''(\bar{q})) \right]^{-\frac{1}{2}} e^{-\frac{\bar{S}}{\hbar}} (1 + \mathcal{O}(\hbar)) . \tag{3.2.14}$$

Note that, by time translation invariance, the center of the bounce, defined as the point where $\frac{dq}{d\tau} = 0$, can be placed anywhere in time. This implies that the matrix $\hat{M}$ is singular and has a zero eigenvalue. To see this, consider the function $\dot{\bar{q}}$ and apply the operator $\hat{M}$ to it

$$\hat{M}\dot{\bar{q}} = \left(-\frac{d^2}{d\tau^2} + \frac{d^2 V}{dq^2} \right) \dot{\bar{q}} = -\frac{d^2}{d\tau^2}\frac{d\bar{q}}{d\tau} + \frac{d^2 V}{dq^2}\frac{d\bar{q}}{d\tau} = \frac{d}{d\tau} \left(-\frac{d^2 \bar{q}}{d\tau^2} + \frac{dV}{dq} \right) = 0 , \tag{3.2.15}$$

where we have used the fact that derivatives commute and the equations of motion in Eq. (3.2.7).

From the imaginary part of the ground-state energy, the decay rate of an unstable state read [189]

$$\Gamma = -2\frac{\mathrm{Im} E_0}{\hbar} = \sqrt{\frac{\bar{S}}{2\pi\hbar}} \left| \frac{\det'(-\partial_t^2 + V''(\bar{q}))}{\det(-\partial_t^2 + \omega^2)} \right|^{-\frac{1}{2}} e^{-\frac{\bar{S}}{\hbar}} (1 + \mathcal{O}(\hbar)) , \tag{3.2.16}$$

[25] The saddle-point approximation is used to approximate integrals of the form $I = \int dx\, e^{-f(x)}$, if we Taylor expand around a minimum x_0 such that $f'(x_0) = 0$, i.e. $f(x) \simeq f(x_0) + \frac{1}{2} f''(x_0)(x - x_0)^2 + \ldots$, we approximate the integral as $I \simeq e^{-f(x_0)} \int dx\, e^{-\frac{1}{2} f''(x_0)(x - x_0)^2} = e^{-f(x_0)} \sqrt{\frac{2\pi}{f''(x_0)}}$.

where $\det'$ denotes the determinant with the zero mode removed and the bounce solution is indeed characterised by the fact that at $\tau \to -\infty$ the particle is at rest in $q = 0$, at $\tau = 0$, it reaches the turning point, then it bounces back to $q = 0$ at $\tau \to +\infty$, i.e.

$$\lim_{\tau\to\pm\infty} q(\tau) = 0 \,, \quad \left.\frac{dq}{d\tau}\right|_{\tau=0} = 0 \,. \tag{3.2.17}$$

3.2.2 Tunneling in quantum field theory

We now generalise the results in Eq. (3.2.16) to QFT. Consider a scalar field $\phi(x)$ in D-dimensional spacetime with action

$$S[\phi] = \int d^D x \, \left(\frac{1}{2}\partial_\mu\phi\partial^\mu\phi - V(\phi)\right) \,, \tag{3.2.18}$$

where the potential $V(\phi)$ has two minima: a local minimum ϕ_f (false vacuum) and a global minimum ϕ_t (true vacuum). By shifting the potential by a constant, we may set $V(\phi_f) = 0$. To ensure metastability, the true vacuum must satisfy $V(\phi_t) < 0$. he role of the quantum-mechanical coordinate q is now played by the scalar field $\phi(x)$. After a Wick rotation in Eq. (3.2.3), the action in Eq. (3.2.18) becomes

$$S_E[\phi] = \int d^D x \, \left(\frac{1}{2}\left(\frac{d\phi}{d\tau}\right)^2 + \frac{1}{2}(\nabla\phi)^2 + V(\phi)\right) \,, \tag{3.2.19}$$

and the Euclidean equations of motion in Eq. (3.2.7) are given by

$$\frac{d^2\phi}{d\tau^2} + \nabla^2\phi = \frac{dV(\phi)}{d\phi} \,, \tag{3.2.20}$$

where $\nabla^2 = \sum_i \partial_i^2$ is the spatial Laplace operator. The boundary conditions are the QFT analogue of Eq. (3.2.17):, i.e. the field begins and ends at rest at the false vacuum at $\tau \to \pm\infty$

$$\lim_{\tau\to\pm\infty} \phi(\tau, \mathbf{x}) = \phi_f \,, \tag{3.2.21}$$

and it is at rest at the center of the bounce $\tau = 0$

$$\left.\frac{\partial\phi(\tau, \mathbf{x})}{\partial\tau}\right|_{\tau=0} = 0 \,. \tag{3.2.22}$$

Furthermore, because the action involves spatial derivatives, the field must approach the false vacuum at spatial infinity to ensure finiteness of the action

$$\lim_{|\mathbf{x}|\to\infty} \phi(\tau, \mathbf{x}) = \phi_f \,. \tag{3.2.23}$$

Since ϕ is invariant under D-dimensional Euclidean rotations, any non-trivial bounce solution that minimises the action obeys an $O(D)$ symmetry around a center of the bounce. By translation symmetry, taking the center at $\tau = 0$ and $\mathbf{x} = 0$, the solution must be a function of

$$\rho = \sqrt{\tau^2 + |\mathbf{x}|^2} \,, \tag{3.2.24}$$

i.e. $\phi = \phi(\rho)$. We then write the equations of motion in Eq. (3.2.20) in terms of the radial coordinate

ρ

$$\frac{d^2\phi}{d\rho^2} + \frac{D-1}{\rho}\frac{d\phi}{d\rho} = \frac{dV}{d\phi} \,. \tag{3.2.25}$$

Furthermore, the boundary conditions in Eqs. (3.2.21), (3.2.22) and (3.2.23) become

$$\frac{d\phi(\rho)}{d\rho}\Big|_{\rho=0} = 0 \,, \quad \lim_{\rho\to\infty}\phi(\rho) = \phi_f \,. \tag{3.2.26}$$

In terms of the radial coordinate ρ, the Euclidean action in Eq. (3.2.19) becomes

$$S_E[\phi] = \mathcal{S}_{D-1}\int_0^\infty d\rho\, \rho^{D-1}\left(\frac{1}{2}\left(\frac{d\phi}{d\rho}\right)^2 + V(\phi)\right) \,, \tag{3.2.27}$$

where $\mathcal{S}_{D-1}$ is the surface area of a $D-1$-sphere with unit radius

$$\mathcal{S}_{D-1} = \frac{2\pi^{D/2}}{\Gamma(D/2)} \,. \tag{3.2.28}$$

In analogy with the previous section, if we interpret ϕ as a particle position and ρ as time, Eq. (3.2.25) is the mechanical equation for a particle moving in an inverted potential $-V$ and subject to a damping force with friction coefficient $\eta \propto \frac{1}{\rho}$. In the bounce solution, the particle starts at rest at $\rho = 0$ with $\frac{d\phi}{d\rho} = 0$ and an initial condition

$$\phi(\rho = 0) = \phi_0 \,, \tag{3.2.29}$$

such that it ends up at the false vacuum ϕ_f at $\rho \to \infty$[26].

For computational convenience, it is useful to write the action S_E in Eq. (3.2.27) in terms of only an integral of the potential

$$S_E = \frac{2}{2-D}S_V = \frac{2}{2-D}\mathcal{S}_{D-1}\int_0^\infty d\rho\, \rho^{D-1}V(\phi) \,. \tag{3.2.30}$$

Let us set the dimension of the spacetime to $D = 4$. To obtain the explicit expression for the decay rate, we need to understand the differences with the quantum mechanical case. First, in quantum mechanics there is only time translation invariance, so only one zero eigenvalue with eigenfunction proportional to $\dot{q}$. However, in QFT there is also spatial translation invariance to be taken into account, so we expect to have four eigenfunctions proportional to $\partial_\mu\phi$ with zero eigenvalues. Each of them contributes with the same normalisation factor as in the quantum mechanical case, in which we removed each zero-eigenvalue from the determinant and replaced it with a factor $\left(\frac{\bar{S}}{2\pi\hbar}\right)^{\frac{1}{2}}$, in this case 4 of them. In addition, integrating over the center of the bounce gives a factor of the volume V of 3-space together with the time $\mathcal{T}$, which factors out. Therefore, looking at Eq. (3.2.16), we can write the decay rate per unit volume as

$$\frac{\Gamma}{V} = \left(\frac{\bar{S}}{2\pi\hbar}\right)^2 e^{-\frac{\bar{S}}{\hbar}}\left|\frac{\det'(-\partial_\tau^2 + V''(\phi))}{\det(-\partial_\tau^2 + V''(\phi_f))}\right|^{-\frac{1}{2}}(1 + \mathcal{O}(\hbar)) \,. \tag{3.2.31}$$

[26] Ref. [30] showed that a solution always exists via the undershoot-overshoot method.

To summarise, you solve the Euclidean $O(4)$-symmetric equations of motion in Eq. (3.2.25) with the boundary conditions in Eq. (3.2.26), and you find the bounce solution $\phi(\rho)$. The initial condition ϕ_0 in Eq. (3.2.29) is the value of the field at which the center of the bounce tunnels, from which it will evolve classically and roll down to the true vacuum ϕ_t.

3.2.3 Tunneling at finite-temperature

As already argued in Subsec. 3.1.5, in the early Universe, the temperature is not negligible, so we need to generalise the zero-temperature results in the case of finite temperature, in which the decay rate at $T \neq 0$ is formally equivalent to the one in QFT with periodicity $\beta = \frac{1}{T}$ in the time direction

$$\sum \langle q_i | e^{-\beta \hat{H}} | q_f \rangle = \int_{q(\tau)=q(\tau+\beta)} \mathcal{D}q \, e^{-S_E[q]} \, . \tag{3.2.32}$$

Thus, at finite temperature we apply the same formalism as at zero temperature to extract the imaginary part from the path integral, but restrict the Euclidean time direction to period β. Denoting R_0 with the bubble size at $T = 0$, in the high-temperature regime at $T \gg R_0^{-1}$, the solution is a cylinder $\mathcal{S}^1 \times \mathbb{R}^3$, whose time slices correspond to $O(3)$-symmetric bubble of size $R(T) \sim \frac{1}{T}$, so that the action S_4 at high temperatures is replaced by $\frac{S_3}{T}$, where $S_3(\phi)$ is the action corresponding to the $O(3)$-symmetric bubble. Hence, the decay rate per unit volume of the false vacuum is given by

$$\frac{\Gamma}{V} = T \left(\frac{S_3}{2\pi T} \right)^{\frac{3}{2}} e^{-\frac{S_3}{T}} \left| \frac{\det'(-\partial_\tau^2 + V''(\phi))}{\det(-\partial_\tau^2 + V''(\phi_f))} \right|^{-\frac{1}{2}} \, , \tag{3.2.33}$$

with only three zero modes, so the prefactor $\left(\frac{S_3}{2\pi T}\right)^{\frac{1}{2}}$ appears three times and the prefactor T comes from the fact that we are integrating over the time direction with periodicity $\beta = \frac{1}{T}$.

By means of dimensional analysis, we can approximate the functional determinants. At zero-temperature, we have

$$\left| \frac{\det'(-\Box + V''(\phi))}{\det(-\Box + V''(\phi_+))} \right|^{-1/2} \sim R_0^{-4} \, , \tag{3.2.34}$$

where the relevant dimensional quantity is taken to be the radius of a critical bubble R_0, whereas at finite-temperature, we find

$$\left| \frac{\det'(-\Box + V''(\phi))}{\det(-\Box + V''(\phi_+))} \right|^{-1/2} \sim T^3 \, , \tag{3.2.35}$$

where the relevant dimensional quantity is taken to be the temperature T.

Therefore, in the zero-temperature case, the decay rate per unit volume of the false vacuum is given by

$$\frac{\Gamma}{V} \simeq R_0^{-4} \left(\frac{S_4}{2\pi} \right)^2 e^{-S_4} \, , \tag{3.2.36}$$

where S_4 is the 4-dimensional action

$$S_4 = 4\pi^2 \int_0^\infty d\rho \, \rho^3 \left(\frac{1}{2} \left(\frac{d\phi}{d\rho} \right)^2 + V(\phi) \right) \, , \tag{3.2.37}$$

evaluated at the $O(4)$-symmetric bounce solution of the ordinary differential equation

$$\frac{d^2\phi}{d\rho^2} + \frac{3}{\rho}\frac{d\phi}{d\rho} = \frac{dV(\phi)}{d\phi} \,. \tag{3.2.38}$$

In the finite-temperature case, the decay rate per unit volume of the false vacuum is given by

$$\frac{\Gamma}{V} = T^4 \left(\frac{S_3}{2\pi T}\right)^{\frac{3}{2}} e^{-\frac{S_3}{T}} \,, \tag{3.2.39}$$

where S_3 is the 3-dimensional action

$$S_3 = 2\pi^2 \int_0^\infty d\rho\, \rho^2 \left(\frac{1}{2}\left(\frac{d\phi}{d\rho}\right)^2 + V(\phi)\right) \,, \tag{3.2.40}$$

evaluated at the $O(3)$-symmetric bounce solution of the ordinary differential equation

$$\frac{d^2\phi}{d\rho^2} + \frac{2}{\rho}\frac{d\phi}{d\rho} = \frac{dV(\phi)}{d\phi} \,. \tag{3.2.41}$$

Combining the two cases, we can write the decay rate per unit volume of the false vacuum as

$$\frac{\Gamma}{V} \simeq R_0^{-4} \left(\frac{S_4}{2\pi}\right)^2 e^{-S_4} + T^4 \left(\frac{S_3}{2\pi T}\right)^{\frac{3}{2}} e^{-\frac{S_3}{T}} \,. \tag{3.2.42}$$

When it is not possible to find an analytical bounce solution, we rely on numerical methods. There are several publicly available software packages. In `Python`, there is `CosmoTransitions` [190]. In `Mathematica`, there are `AnyBubble` [191] and `FindBounce` [192]. In `C++`, there are `BubbleProfiler` [193] and `SimpleBounce` [194, 195].

3.3 Thermal parameters

The effective potential studied in Sec. 3.1 and the false vacuum decay rate studied in Sec. 3.2 depend on the microphysics. The bridge between the particle physics model and the predicted SGWB spectrum is given by thermal parameters, which enter into lattice simulations or analytic approximations of GWs computations.

In this section, after describing the phenomenon of true vacuum bubble nucleation and how to trace the evolution of the FOPT by means of the false vacuum fraction, we introduce these thermal parameters, following Refs. [178]:

- a transition temperature T_* that marks the stage of the FOPT when the production of GWs takes place;
- the strength of the FOPT, which parametrises the vacuum energy density that is converted into GWs,
- the characteristic timescale β, which measures the duration of the FOPT;
- the velocity of the bubble wall v_w.

3.3.1 Phase transition

In a FOPT, the bounce solution derived in Sec. 3.2 is directly related to the nucleation of bubbles. In the boiling of a liquid, thermodynamic fluctuations continuously cause vapor bubbles to nucleate. Bubbles that are large enough expand, whereas smaller ones shrink due to their surface tension. Similarly, in a cosmological FOPT, bubbles of true vacuum nucleate within the false vacuum sea, and if they are sufficiently large to be energetically favorable, they expand and convert portions of the false vacuum into the true one. Bubbles form around the center of the bounce, where the field is at rest, and they will propagate classically, with radius given by $r = |\mathbf{x}| = \sqrt{R_0^2 + t^2}$, where R_0 is the initial radius and t is the time elapsed since nucleation, if interactions with the surrounding plasma are negligible.

To measure the progress of the FOPT, we can quantify and track the evolution of the fraction of the Universe that remains in the false vacuum phase, $P_f(t)$, or equivalently the fraction converted into the true vacuum, $P_t(t) = 1 - P_f(t)$, given by

$$P_f(t) = e^{-I(t)} \,, \tag{3.3.1}$$

where $I(t)$ is the fractional extended volume of true vacuum bubbles at time t. Eq. (3.3.1) is known as the Kolmogorov-Johnson-Mehl-Avrami-Korbel equation or JMAK equation [196–200].

The fractional extended volume $I(t)$ in Eq. (3.3.1) can be computed following Ref. [178]. Starting from the equivalence between the false vacuum fraction P_f and the probability of a random point being in the false vacuum, consider bubbles of true vacuum in a fraction volume between $\mathcal{V}_1$ and $\mathcal{V}_2$, and define $P_f(\mathcal{V}_1, \mathcal{V}_2)$ as the probability of a random point not being inside at least one bubble. For an infinitesimally increased volume range $[\mathcal{V}_1, \mathcal{V}_2 + d\mathcal{V}]$, since the two probabilities are independent, we have

$$P_f(\mathcal{V}_1, \mathcal{V}_2 + d\mathcal{V}) = P_f(\mathcal{V}_1, \mathcal{V}_2) P_f(\mathcal{V}_2, \mathcal{V}_2 + d\mathcal{V}) \,. \tag{3.3.2}$$

Given that the probability of a random point being inside true vacuum bubbles is the total volume of bubbles multiplied by the infinitesimal volume, we obtain $P_t(\mathcal{V}_2, \mathcal{V}_2 + d\mathcal{V}) = n(\mathcal{V}_2)\mathcal{V}_2 d\mathcal{V}$, where $n(\mathcal{V})$ is the distribution for the number density of bubbles. $P_f = 1 - P_t$ yields

$$P_f(\mathcal{V}_2, \mathcal{V}_2 + d\mathcal{V}) = 1 - n(\mathcal{V}_2)\mathcal{V}_2 d\mathcal{V} \,. \tag{3.3.3}$$

Hence, inserting Eq. (3.3.3) into Eq. (3.3.2), we obtain the differential equation

$$\frac{1}{P_f(\mathcal{V}_1, \mathcal{V}_2)} \frac{P_f(\mathcal{V}_1, \mathcal{V}_2 + d\mathcal{V}) - P_f(\mathcal{V}_1, \mathcal{V}_2)}{d\mathcal{V}_2} = \frac{1}{P_f(\mathcal{V}_1, \mathcal{V}_2)} \frac{dP_f(\mathcal{V}_1, \mathcal{V}_2)}{d\mathcal{V}_2} = -n(\mathcal{V}_2)\mathcal{V}_2 \,. \tag{3.3.4}$$

We introduce the time t' at which bubbles form, a sample time t and the volume $\mathcal{V}(t', t)$. The latter is a monotonically decreasing function of the nucleation time t' given that bubble have grown since nucleation. We take into account the beginning of the FOPT with the critical time t_c, which is defined by the fact that the moment after which the absolute minimum of the potential becomes the true vacuum and the false vacuum becomes metastable. We can then integrate Eq. (3.3.4)

$$\int_{\mathcal{V}(t,t)}^{\mathcal{V}(t_c,t)} d\mathcal{V}' \frac{d \ln P_f(\mathcal{V}', \mathcal{V}(t_c, t))}{d\mathcal{V}'} = - \int_{\mathcal{V}(t,t)}^{\mathcal{V}(t_c,t)} d\mathcal{V}' n(\mathcal{V}') \mathcal{V}' \,, \tag{3.3.5}$$

which, using $P_f(\mathcal{V},\mathcal{V})=1$, gives the false vacuum fraction

$$P_f(t)=P_f(\mathcal{V}(t,t),\mathcal{V}(t_c,t))=\exp\left(-\int_{\mathcal{V}(t,t)}^{\mathcal{V}(t_c,t)}d\mathcal{V}'n(\mathcal{V}')\mathcal{V}'\right)\,. \tag{3.3.6}$$

The integral in the argument of the exponent in Eq. (3.3.6) can be performed over time by introducing the Jacobian

$$P_f(t)=\exp\left(-\int_{t_c}^{t}dt'\frac{\partial V}{\partial t'}n(\mathcal{V}(t',t))\mathcal{V}(t',t)\right)\,. \tag{3.3.7}$$

We define the total number of bubbles with volume $\mathcal{V}'\leq\mathcal{V}$ as $N(\mathcal{V})=\int_0^{\mathcal{V}}d\mathcal{V}'n(\mathcal{V}')$ with corresponding density $n(\mathcal{V}')=\frac{dN}{d\mathcal{V}}\Big|_{\mathcal{V}'}$, and the false vacuum decay rate $\Gamma(t)=\frac{dN}{dt}=\frac{dN}{d\mathcal{V}}\frac{\partial V}{\partial t}$. Finally, taking into account the expansion of the Universe through the cosmic scale factor $a(t)$, we obtain the false vacuum fraction as in the JMAK equation in Eq. (3.3.1), with the explicit expression for the fractional extended volume

$$P_f(t)=\exp\Big(-\int_{t_c}^{t}dt'\,\Gamma(t')\frac{a^3(t')}{a^3(t)}V(t',t)\Big)\,. \tag{3.3.8}$$

The volume $V(t',t)$ in Eq. (3.3.8) can be estimated as a 3-dimensional spherical bubble with an initial radius $R_0(t')$ that grows with a bubble wall velocity $v_w(t',t'')$

$$V(t',t)=\frac{4\pi}{3}R^3(t',t)\,,\quad R(t',t)=\frac{a(t)}{a(t')}R_0(t')+\int_{t'}^{t}dt''\,v_w(t',t'')\frac{a(t)}{a(t'')}\,. \tag{3.3.9}$$

Neglecting the initial bubble radius R_0, which is justified for transitions below the Planck scale [201, 202], and assuming that bubbles quickly reach a constant terminal velocity, Eq. (3.3.9) becomes

$$V(t',t)=\frac{4\pi}{3}\Big(v_w\int_{t'}^{t}dt''\,\frac{a(t)}{a(t'')}\Big)^3\,. \tag{3.3.10}$$

The factor that accounts for the expansion of the Universe is given by integrating the Hubble parameter

$$\frac{a(t_1)}{a(t_2)}=\exp\Big(\int_{t_1}^{t_2}dt'\,H(t')\Big)\,. \tag{3.3.11}$$

The last step is to find a relation between time t and temperature T, so that the integration variable in the false vacuum fraction in Eq. (3.3.8), in the bubble volume in Eq. (3.3.10) and in the expansion factor in Eq. (3.3.11) can be expressed in terms of the temperature T. Entropy conservation leads to the general expression [178]

$$\frac{dT}{dt}=-3H(T)\frac{V'(\phi_f(T),T)}{V''(\phi_f(T),T)}\,. \tag{3.3.12}$$

This can be approximated by parameterising the effective potential near the false vacuum with the bag equation of state [203]

$$V(\phi_f(T),T)=aT^4+b\,, \tag{3.3.13}$$

where a is the radiation contribution and b is the vacuum one. Using Eq. (3.3.13), Eq. (3.3.12) becomes

$$\frac{dT}{dt} = -TH(T)\,. \tag{3.3.14}$$

Using Eq. (3.3.14), the volume V in Eq. (3.3.10) can be written as

$$V(T',T) = \frac{4\pi}{3}\Big(\frac{v_w}{T}\int_T^{T'}\frac{dT''}{H(T'')}\Big)^3\,, \tag{3.3.15}$$

and the expansion factor in Eq. (3.3.11) as

$$\frac{a(t_1)}{a(t_2)} = \frac{T_2}{T_1}\,. \tag{3.3.16}$$

Finally, the false vacuum fraction in Eq. (3.3.8) is given by [178]

$$P_f(T) = \exp\Big(-\frac{4\pi}{3}v_w^3\int_T^{T_c}dT'\,\frac{\Gamma(T')}{T'^4H(T')}\Big(\int_T^{T'}\frac{dT''}{H(T'')}\Big)^3\Big)\,. \tag{3.3.17}$$

3.3.2 Transition temperatures

The evolution of a FOPT can be characterised by identifying specific temperature milestones, each marking a physically relevant stage of the transition [178].

The critical temperature T_c is defined as the temperature at which the two minima are degenerate, i.e. the effective potential evaluated at the true vacuum is equal to the one at the false vacuum. For $T > T_c$, the false vacuum remains the absolute minimum of the effective potential, the bounce action diverges, and the false vacuum decay rate in Eq. (3.2.42) vanishes. On the other hand, for $T < T_c$, the true vacuum becomes the absolute minimum of the effective potential, transforming the false vacuum into a metastable state and allowing for its decay.

The nucleation temperature T_n is defined as the temperature at which, on average, there is a nucleated bubble per Hubble volume per Hubble time, given by the condition

$$1 = N(t_n) = \int_{t_c}^{t_n}dt\,\frac{\Gamma(T(t))}{H^3(t)} = \int_{T_n}^{T_c}\frac{dT}{T}\,\frac{\Gamma(T)}{H^4(T)}\,, \tag{3.3.18}$$

where we have used the bag relation from Eq. (3.3.14). An approximate value of T_n can be obtained by neglecting the integral and requiring that the number of bubbles per Hubble spacetime volume be of order one

$$\frac{\Gamma(T_n)}{H^4(T_n)} = 1\,. \tag{3.3.19}$$

This is justified by observing that the decay rate in Eq. (3.2.42) is dominated by the exponential behaviour of the bounce action. Thus, the nucleation temperature T_n is interpreted as the onset of the FOPT.

The percolation temperature T_p is defined as the temperature at which bubbles form a connected cluster throughout the Universe. For uniformly spherical bubbles, percolation theory suggests that,

in cosmological FOPTs, this occurs when $P_t \simeq 0.29$ [204–209], or, equivalently,

$$P_f(T_p) \simeq 0.71 \,, \quad I(T_p) \simeq 0.34 \,, \tag{3.3.20}$$

where $P_f(T_p)$ is given by Eq. (3.3.17). Simulations show that GWs from FOPT are generated at the percolation temperature T_p, since it is when bubbles are really colliding and permeating abundantly the Universe.

In supercooled FOPTs, cosmic expansion is significant and may prevent the transition from completing. It is necessaary to ensure that the volume of the false vacuum monotonically decreases at the percolation temperature T_p, otherwise, although bubbles continue to grow, so does the space in the false vacuum between them, preventing them from meeting. The volume of false vacuum is given by [210]

$$\mathcal{V}_f(t) = a^3(t) P_f(t) \quad \Rightarrow \quad \frac{d\mathcal{V}_f}{dt} = \mathcal{V}_f(t)\Big(\frac{d}{dt}\ln P_f(t) + 3H(t)\Big) \,. \tag{3.3.21}$$

leading to the condition

$$\frac{1}{\mathcal{V}_f}\frac{d\mathcal{V}_f}{dt} < 0 \quad \Rightarrow \quad \frac{d}{dt}\ln P_f(t) < -3H(t) \,, \tag{3.3.22}$$

or in terms of temperature via Eq. (3.3.14)

$$H(T)\left(3 + T\frac{dI(T)}{dT}\right)\Big|_{T_p} < 0 \,. \tag{3.3.23}$$

For completeness, there is also another temperature, the reheating temperature T_{reh}, which is defined as the temperature at which the energy released during the FOPT reheats the plasma. It is determined by the decay rate of the scalar field into radiation and it can be approximated by [211]

$$T_{\text{reh}} = T_p(1+\alpha)^{\frac{1}{4}} \,. \tag{3.3.24}$$

3.3.3 Hydrodynamics and the transition strength

In order to determine the strength of the transition and how much energy is available to generate GWs, a hydrodynamic analysis of the system composed of the scalar field and the thermal plasma is required, studying the energy budget of the cosmological FOPT.

The effective potential is equal to the free energy density $\mathcal{F}$ and the negative of the pressure p

$$\mathcal{F} = V_{\text{eff}} \,, \quad p = -\mathcal{F} \,. \tag{3.3.25}$$

so that, using thermodynamic relations, we can write the energy density ρ, enthalpy $w = \rho + p$, and entropy s as [212]

$$\rho = T\frac{\partial p}{\partial T} - p = V - T\frac{\partial V}{\partial T} \,, \quad w = T\frac{\partial p}{\partial T} = -T\frac{\partial V}{\partial T} \,, \quad s = \frac{\partial p}{\partial T} = -\frac{\partial V}{\partial T} \,. \tag{3.3.26}$$

The energy-momentum tensor is given by the sum of contributions from the scalar field

$$T^{\phi}_{\mu\nu} = \partial_\mu\phi\partial_\nu\phi - g_{\mu\nu}\left(\frac{1}{2}\partial_\rho\phi\partial^\rho\phi - V_{\text{eff}}(\phi)\right) , \tag{3.3.27}$$

and the thermal plasma, which can be described as a perfect relativistic fluid[27],

$$T^{\text{plasma}}_{\mu\nu} = w u_\mu u_\nu - g_{\mu\nu} p , \tag{3.3.28}$$

where $u^\mu = \gamma(1, v)$ is the fluid four-velocity in the reference frame of the bubble center and $\gamma = \frac{1}{\sqrt{1-v^2}}$ is the Lorentz factor. Combining Eqs. (3.3.27) and (3.3.28), we obtain the total energy-momentum tensor of the system

$$T^{\mu\nu} = \partial^\mu\phi\partial^\nu\phi - \frac{1}{2}g^{\mu\nu}\partial^\rho\phi\partial_\rho\phi + (\rho + p)u^\mu u^\nu - g^{\mu\nu}p , \tag{3.3.29}$$

where we have absorbed the effective potential into the definition of the pressure, using Eq. (3.3.25). Then, we can extract the total energy density by looking at the 00-component of the energy-momentum tensor

$$T^{00} = w\gamma^2 + \frac{1}{2}\sum_i\left(\dot\phi^2 + (\nabla\phi)^2\right) - p = w\gamma^2 v^2 + \frac{1}{2}\sum_i\left(\dot\phi^2 + (\nabla\phi)^2\right) + \rho , \tag{3.3.30}$$

where we have used $p = w - \rho$ and $\gamma^2 - 1 = v^2\gamma^2$. Using the trace anomaly θ, which defined as

$$\theta = \frac{1}{4}g^{\mu\nu}T^{\text{plasma}}_{\mu\nu} = \frac{1}{4}(\rho - 3p) = \frac{w}{4} - p = V_{\text{eff}} - \frac{T}{4}\frac{\partial V_{\text{eff}}}{\partial T} , \tag{3.3.31}$$

Eq. (3.3.30) can be decomposed into

$$T^{00} = w\gamma^2 v^2 + \frac{1}{2}\sum_i\left(\dot\phi^2 + (\nabla\phi)^2\right) + \frac{3}{4}w + \theta , \tag{3.3.32}$$

where $\rho_{kin} = w\gamma^2 v^2$ is the fluid kinetic energy density, $\rho_Q = \frac{3}{4}w$ is the thermal energy density, $\rho^\phi_{kin} = \frac{1}{2}\dot\phi^2$ is the scalar field kinetic energy, $\rho^\phi_{grad} = \frac{1}{2}(\nabla\phi)^2$ is the scalar field gradient energy and $\rho_\theta = \theta$ is the potential energy density available in the transition. Kinetic and gradient energies can contribute to GW production, whereas the thermal energy only reheats the plasma and does not generate GWs. The source tensor for GWs is given by the stress tensor

$$\tau_{ij} = \tau^\phi_{ij} + \tau^{\text{plasma}}_{ij} , \tag{3.3.33}$$

where $\tau^\phi_{ij} = \partial_i\phi\partial_j\phi$ and $\tau^{\text{plasma}}_{ij} = w\gamma^2 v_i v_j$.

To quantify the energy density released in GWs, we introduce the transition strength α, defined as the trace anomaly between the false and true vacuum, i.e. $\rho_{vac} = \theta_f - \theta_t$, normalised over the

[27] The general expression of the energy-momentum of the plasma is given by $T_{\mu\nu} = \sum_i \int \frac{d^3p}{(2\pi)^3 E_i} p_\mu p_\nu f_i(p, x)$, where the sum is over the species i and $f_i(p, x)$ is the distribution function.

radiation energy density ρ_{rad}[28]

$$\alpha = \frac{\Delta\theta}{\rho_{rad}}\Big|_{T_*} = \frac{1}{\rho_{rad}}\Delta\left(V_{\text{eff}} - \frac{T}{4}\frac{\partial V_{\text{eff}}}{\partial T}\right)\Big|_{T_*}, \tag{3.3.34}$$

where Δ indicates the difference of quantities evaluated at the false and true vacuum. This definition is justified by the fact that the first contribution ΔV_{eff} is the difference in free energy density in Eq. (3.3.25) and the second contribution $\frac{\partial V_{\text{eff}}}{\partial T}$ is related to the entropy change in Eq. (3.3.26). The transition strength in Eq. (3.3.34) is evaluated at the transition temperature T_*.

The vacuum energy density converted into kinetic plasma energy can be parameterised by the kinetic energy fraction

$$K = \frac{\rho_{\text{kin}}}{\rho_{\text{tot}}}, \tag{3.3.35}$$

with $\rho_{tot} = \rho_{rad} + \rho_{vac}$. In fact, using the bag equation of state in Eq. (3.3.13), written as $V = \epsilon - aT^4 = \rho_{vac} - \frac{1}{3}\rho_{rad}$, we introduce the efficiency factor, which measures the efficiency of converting vacuum energy into plasma kinetic energy,

$$\kappa = \frac{\rho_{\text{kin}}}{\rho_{\text{vac}}}, \tag{3.3.36}$$

so that the kinetic energy fraction in Eq. (3.3.35) becomes

$$K = \kappa\frac{\rho_{\text{vac}}}{\rho_{\text{rad}} + \rho_{\text{vac}}} = \frac{\kappa\alpha}{1+\alpha}, \tag{3.3.37}$$

where we have used $\alpha \simeq \frac{\rho_{\text{vac}}}{\rho_{\text{rad}}}$.

According to the value of the transition strength, FOPTs are commonly classified as weak $\alpha \sim O(0.01)$, intermediate $\alpha \sim O(0.1)$, or strong $\alpha \gtrsim O(1)$.

3.3.4 Inverse transition duration

The duration of the FOPT can be estimated by the bounce action S. Assuming that the transition is fast enough to Taylor expand the bounce action around the transition time t_* at first linear order

$$S(t) \simeq S(t_*) - \beta(t - t_*), \tag{3.3.38}$$

we can express the decay rate as

$$\Gamma(t) \propto \Gamma(t_*)e^{\beta(t-t_*)}, \tag{3.3.39}$$

where we have defined the inverse transition duration β defined as

$$\beta = -\frac{dS}{dt}\Big|_{t_*} \simeq \frac{1}{\Gamma}\frac{d\Gamma}{dt}\Big|_{t_*}. \tag{3.3.40}$$

Using the bag relation in Eq. (3.3.14), we can express the inverse transition duration β in Eq. (3.3.40) over the Hubble parameter H as

$$\frac{\beta}{H_*} = -\frac{T}{\Gamma}\frac{d\Gamma}{dT}\Big|_{T_*} \simeq -T\frac{d}{dT}\left(\frac{S(T)}{T}\right)\Big|_{T_*}, \tag{3.3.41}$$

[28] There are other definitions of the transition strength, substituting the trace anomaly with the energy density ρ, the negative pressure -p or the latent heat q.

where the approximation is justified by the fact that the decay rate is dominated by the exponential.

The characteristic length scale can be alternatively estimated without using the bounce action, but introducing the mean bubble separation

$$R(t) = n(t)^{-1/3} \,, \tag{3.3.42}$$

where $n(t)$ is the bubble number density, defined as

$$n(t) = \int_{t_c}^{t} dt' \Gamma(t') P_f(t') \frac{a^3(t')}{a^3(t)} = T^3 \int_{T}^{T_c} \frac{dT'}{T'^4} \frac{\Gamma(T')}{H(T')} e^{-I(T')} \,. \tag{3.3.43}$$

There is a relation between the inverse transition duration in Eq. (3.3.41) and the mean bubble separation in Eq. (3.3.42) which is given by

$$\frac{\beta}{H_*} = (8\pi)^{1/3} \frac{\max(v_w, c_s)}{H_* R_*} \,, \tag{3.3.44}$$

where $c_s = \frac{1}{\sqrt{3}}$ is the sound speed in the plasma and v_w is the bubble wall velocity. Here, the subscript $*$ means evaluated at the transition temperature T_*.

3.3.5 Bubble wall velocity

The final parameter to determine is the bubble wall velocity v_w, which depends on the transition strength in Eq. (3.3.34) and is model-dependent, since it is determined by the interaction between the bubble wall and the surrounding plasma. There are two competing contributions: the pressure difference between the false and true vacuum ΔV_{eff}, which drives the bubble to expand, and the friction due to particle collisions in the thermal plasma against the bubble wall that slows it down. In fact, particles changing their mass when crossing the wall result is an inward pressure [213–216].

The dominant contribution can be identified from the total pressure difference across the wall [215–217]

$$\Delta p_{\text{tot}} = \Delta V - p_{\text{LO}} - \gamma p_{\text{NLO}} \,. \tag{3.3.45}$$

Here, p_{LO} is the leading-order (LO) friction force associated with $1 \to 1$ scattering and p_{NLO} is the next-to-leading order (NLO) friction force associated with $1 \to N$ splitting, for relativistic bubble walls, are given by

$$p_{\text{LO}} = \frac{T^2}{24} \left(\sum_b n_b \Delta m_b^2 + \frac{1}{2} \sum_f n_f \Delta m_f^2 \right) \,, \quad p_{\text{NLO}} = T^3 \sum_b n_b g_b^2 \Delta m_b \,, \tag{3.3.46}$$

where Δm is the mass change across the wall. Note that Eq. (3.3.45) shows that p_{LO} does not depend on the Lorentz factor γ, but p_{NLO} does, so the NLO becomes important only for relativistic bubbles.

A good estimate for the bubble wall velocity approaching $v_w \to 1$ is provided by the runaway condition, for which bubble collisions happen during the accelerating stage, before the walls reach terminal velocity, which occurs when

$$\alpha > \alpha_\infty \,, \tag{3.3.47}$$

where α is the transition strength and α_∞ represents the weakest transition strength such that p_{LO}

is overcome, defined by

$$\alpha_\infty = \frac{\Delta p_{\text{LO}}}{\rho_{\text{rad}}} = \frac{T^2}{24\rho_{\text{rad}}}\left(\sum_b n_b \Delta m_b^2 + \frac{1}{2}\sum_f n_f \Delta m_f^2\right) . \tag{3.3.48}$$

On the other hand, taking into account the NLO friction term, the bubble wall reaches a terminal Lorentz factor γ_{eq}, defined by the condition $\Delta p_{\text{tot}} = 0$ in Eq. (3.3.45)

$$\gamma_{\text{eq}} = \frac{\Delta V - \Delta p_{LO}}{\Delta p_{NLO}} = \frac{\alpha - \alpha_\infty}{\alpha_{\text{eq}}} , \tag{3.3.49}$$

where α_∞ is given in Eq. (3.3.48) and we have defined

$$\alpha_{\text{eq}} = \frac{\Delta p_{NLO}}{\rho_{\text{rad}}} = \frac{T^3}{\rho_{\text{rad}}}\sum_b n_b g_b^2 \Delta m_b . \tag{3.3.50}$$

The Lorentz factor γ_* that the bubble wall would reach if the NLO friction term were neglected is

$$\gamma_* = \frac{2}{3}\frac{R_*}{R_0} , \tag{3.3.51}$$

where R_* is given by (3.3.42) and R_0 can be estimated using the thin-wall approximation [33]

$$R_0 = \left(\frac{3S_3}{2\pi\Delta V}\right)^{\frac{1}{3}} . \tag{3.3.52}$$

As we will explain in Sec. 3.4, the main sources of GWs are bubble collisions, sound waves, and turbulence. The efficiency factor for bubble collisions κ_{col}, defined as the fraction of total energy stored in the bubble wall [217]

$$\kappa_{\text{col}} = \begin{cases} \frac{\gamma_{\text{eq}}}{\gamma_*}\left(1 - \frac{\alpha_\infty}{\alpha}\left(\frac{\gamma_{\text{eq}}}{\gamma_*}\right)^2\right) & \gamma_* > \gamma_{\text{eq}} \\ 1 - \frac{\alpha_\infty}{\alpha} & \gamma_* \leq \gamma_{\text{eq}} \end{cases} . \tag{3.3.53}$$

If $\gamma_* \leq \gamma_{\text{eq}}$, the terminal velocity due to friction terms is not reached and all the vacuum energy is transferred to the bubble wall acceleration. Conversely, if $\gamma_* > \gamma_{\text{eq}}$, after the bubble wall stops accelerating, the remaining energy is transferred to the surrounding thermal plasma, generating sound waves (and turbulence). The efficiency factor for sound waves is given by [216]

$$\kappa_{\text{sw}} = \frac{\alpha_{\text{eff}}^2/\alpha}{0.73 + 0.083\sqrt{\alpha_{\text{eff}}} + \alpha_{\text{eff}}} , \quad \alpha_{\text{eff}} = \alpha(1 - \kappa_{\text{col}}) . \tag{3.3.54}$$

3.4 Gravitational waves from first-order phase transitions

As shown in Sec. 2.2.2, GWs are sourced by a non-vanishing time-varying quadrupole moment, since monopole and dipole radiation are forbidden by energy-momentum conservation. Thus, spherically symmetric configurations do not radiate: anisotropy and inhomogeneity are necessary. Further-

more, the weakness of the gravitational interaction implies that only highly energetic processes can produce observable GWs. In the context of cosmological FOPT, these conditions are naturally fulfilled by three different sources: bubble collisions, sound waves and magnetohydrodynamic (MHD) turbulence.

The nucleation and expansion of single isolated spherical bubbles preserves isotropy and has a vanishing quadrupole moment, so they cannot emit GWs. However, towards the completion of the PT, the random process of nucleation occurs in different locations and at different times, allowing a large number of bubbles to eventually collide, break spherical symmetry and convert the kinetic energy stored in the bubble walls into GWs. Additionally, expanding bubbles interact with the surrounding thermal plasma: bubble walls are slowed down due to friction effects discussed in Sec. 3.3.5, while simultaneously stirring the plasma and transferring energy to the it. This induces bulk motions, which manifest as long-lived sound waves and turbulent flows, once non-linearities take over.

In this section, after estimating the dependence of the SGWB spectrum on the thermal parameters through dimensional analysis and computing the redshift factors that relate the SGWB spectrum observed today with the one produced in the early Universe, we present the most up-to-date SGWB spectrum templates.

3.4.1 Dimensional estimate and redshift

We begin by performing a dimensional analysis to determine how the SGWB depends on the transition strength α, the inverse duration of the transition β, and the efficiency factor κ, following Ref. [178].

As suggested by inserting Eq. (2.2.46) inside Eq. (2.2.41), the GW energy E_{GW} is proportional to the Newton's constant G. In addition, it depends on the efficiency factor multiplied by the vacuum energy density $\kappa\rho_{\mathsf{vac}}$ and the characteristic scale β^{-1}, setting $v_w \simeq 1$. Dimensional analysis gives

$$E_{\mathsf{GW}} \sim G\kappa^2\rho_{\mathsf{vac}}^2\beta^{-5} \,. \tag{3.4.1}$$

On the other hand, the vacuum energy can be estimated by the vacuum energy density ρ_{vac} multiplied by the volume

$$E_{\mathsf{vac}} \sim \rho_{\mathsf{vac}}\beta^{-3} \,. \tag{3.4.2}$$

Therefore, the fraction of vacuum energy converted into GWs is given by the ratio of the energy of GWs in Eq. (3.4.1) over the vacuum energy in Eq. (3.4.2)

$$\frac{E_{\mathsf{GW}}}{E_{\mathsf{vac}}} \sim G\kappa^2\rho_{\mathsf{vac}}\beta^{-2} = \kappa^2\frac{\rho_{\mathsf{vac}}}{\rho_{\mathsf{vac}}+\rho_{\mathsf{rad}}}G\rho_{\mathsf{tot}}\beta^{-2} = \kappa^2\frac{\alpha}{\alpha+1}\left(\frac{\beta}{H}\right)^{-2} \,, \tag{3.4.3}$$

where we have used $H \sim \sqrt{G\rho_{tot}}$, $\rho_{\mathsf{tot}} = \rho_{\mathsf{vac}} + \rho_{\mathsf{rad}}$ and $\alpha \simeq \frac{\rho_{\mathsf{vac}}}{\rho_{\mathsf{rad}}}$. The expression in Eq. (3.4.3) can be used to estimate the SGWB spectrum. Using the definition in Eq. (2.2.51), we obtain

$$\Omega_{\mathsf{GW}} = \frac{1}{\rho_{\mathsf{tot}}}\frac{d\rho_{\mathsf{GW}}}{d\ln f} \sim \frac{\rho_{\mathsf{vac}}}{\rho_{\mathsf{tot}}}\frac{E_{\mathsf{GW}}}{E_{\mathsf{vac}}}g(f\beta^{-1}) \sim \kappa^2\left(\frac{\alpha}{1+\alpha}\right)^2\left(\frac{\beta}{H}\right)^{-2}g(f\beta^{-1}) \,, \tag{3.4.4}$$

where the dimensionless function g encodes the spectral shape and depends only on the combination $f\beta^{-1}$, since β^{-1} is the only relevant timescale. From Eq. (3.4.4), we observe that $\Omega_{\mathsf{GW}} \propto \left(\frac{\beta}{H}\right)^{-2}$,

which implies that stronger supercooling, which decreases $\frac{\beta}{H}$, enhances the amplitude of the SGWB. This is a feature of the bubble collision SGWB spectrum, while, for long-lasting sources such as sound waves and turbulence, the dependence is weaker as $\Omega_{\text{GW}} \propto \left(\frac{\beta}{H}\right)^{-1}$ [218]. Furthermore, we note that $\Omega_{\text{GW}} \propto \left(\frac{\alpha}{1+\alpha}\right)^2$, which indicates that, for strong PT in which $\alpha \gg 1$, the SGWB spectrum is weakly sensitive to α.

The SGWB spectrum estimated in Eq. (3.4.4) does not directly correspond to the signal observable today. Since GWs decouple from the thermal plasma around the Planck scale, as shown in Eq. (2.1.57), after production, they freely propagate throughout the cosmic history until today, but their spectrum is continuously redshifted by the expansion of the Universe. To account for this, we compute the redshift factors of the frequency f and the SGWB spectrum.

Using entropy conservation in Eq. (2.1.40), the ratio of the cosmic scale factor at two different epochs with temperatures T_1 and T_2 is

$$\frac{a(T_1)}{a(T_2)} = \left(\frac{g_*(T_2)}{g_*(T_1)}\right)^{\frac{1}{3}} \frac{T_2}{T_1}\,, \tag{3.4.5}$$

where we have used g_* instead of g_{*s}, valid in the early Universe where all relativistic species are in equilibrium with the plasma. Since frequencies redshift as $f \propto a^{-1}$, the frequency today at $T_0 \simeq 2.725$ K is related to the one at production at T_* by [62]

$$f_0 = H_{*,0}\frac{f_*}{H_*} = \frac{a(T_*)}{a(T_0)} f_* \simeq 1.65 \times 10^{-5} \left(\frac{g_*(T_*)}{100}\right)^{\frac{1}{6}} \left(\frac{T_*}{100\ \text{GeV}}\right) \frac{f_*}{H_*}\text{Hz}\,, \tag{3.4.6}$$

where we have used Eq. (3.4.5). Here, the normalization to $g_*(T) = 100$ corresponds to the SM value around the EW scale and the factor H_* was introduced using Eq. (2.1.35). Eq. (3.4.6) shows that the frequency of the SGWB spectrum can be directly linked to the temperature at which it was generated: EW scale ($T \sim 100$ GeV) transition yields a mHz signal, which will be tested by the LISA collaboration [62, 218, 219], while nHz frequencies correspond to MeV temperatures, which are the focus of this thesis.

Assuming a radiation-dominated epoch, the ratio of the Hubble parameter in Eq. (2.1.35) at two different epochs with temperatures T_1 and T_2 is

$$\frac{H(T_1)}{H(T_2)} = \left(\frac{g_*(T_1)}{g_*(T_2)}\right)^{\frac{1}{2}} \frac{T_1^2}{T_2^2}\,. \tag{3.4.7}$$

Since an energy density redshifts as $\rho_{\text{gw}} \propto a^{-4}$ and the critical density as $\rho_c \propto H^2$, looking at the definition of the SGWB spectrum in Eq. (2.2.51), we can extract the overall redshift factor

$$\left(\frac{a(T_1)}{a(T_2)}\right)^4 \left(\frac{H(T_1)}{H(T_2)}\right)^2\,, \tag{3.4.8}$$

and the SGWB spectrum at $T_0 \simeq 2.725$ K is related to the SGWB spectrum at production at T_* by [62]

$$h^2\Omega_0 = h^2 F_{\text{GW},0}\Omega_* = \left(\frac{a(T_0)}{a(T_*)}\right)^4 \left(\frac{H(T_0)}{H(T_*)}\right)^2 h^2\Omega_* \simeq 1.64 \times 10^{-5} \left(\frac{100}{g_*(T_*)}\right)^{\frac{1}{3}} \Omega_*\,, \tag{3.4.9}$$

where we have used Eqs. (3.4.5) and (3.4.7).

3.4.2 Templates

At the time of writing, the state-of-the-art templates for the SGWB spectrum from cosmological PT are those of the LISA collaboration [62], collecting both analytic approximations and numerical simulations. The SGWB spectrum from bubble collisions is modelled by a Broken Power Law (BPL), while the contributions from sound waves and turbulence are described by Double Broken Power Laws (DBPLs). All three sources are parametrised in terms of the thermal parameters: the transition temperature T_*, which is identified with the percolation one T_p, the transition strength α, the transition inverse duration β and the bubble wall velocity, which is set to $v_w = 1$. The redshift factors F_{GW} and $H_{*,0}$ are given in Eqs. (3.4.9) and (3.4.6), respectively.

In terms of the geometrical parameters $\vec{\theta}_{\mathsf{cosmo}} = (f_p, \Omega_p)$ and the source-dependent exponents (n_1, n_2, a_1), the BPL is given by

$$\Omega_{\mathsf{GW}}^{\mathsf{BPL}}(f, \vec{\theta}_{\mathsf{cosmo}}) = \Omega_p \frac{(n_1 - n_2)^{\frac{n_1 - n_2}{a_1}}}{\left(-n_2 \left(\frac{f}{f_p}\right)^{-\frac{n_1 a_1}{n_1 - n_2}} + n_1 \left(\frac{f}{f_p}\right)^{-\frac{n_2 a_1}{n_1 - n_2}}\right)^{\frac{n_1 - n_2}{a_1}}} \,. \tag{3.4.10}$$

Here, f_p is the peak frequency, while Ω_p is the amplitude at f_p. At low frequencies $f \ll f_p$, the SGWB spectrum in Eq. (3.4.10) increases as $\Omega_{\mathsf{GW}} \propto f^{n_1}$, while at high frequencies $f \gg f_p$ it decreases as $\Omega_{\mathsf{GW}} \propto f^{n_2}$. The parameter a_1 describes the behaviour around f_p.

The BPL in Eq. (3.4.10) describes the SGWB spectrum of bubble collisions, with source-dependent exponents fixed as $n_1 = 2.4$, $n_2 = -2.4$, $a_1 = 1.2$. The peak amplitude Ω_p and the frequency f_p in terms of the thermal parameters are given by

$$h^2 \Omega_p = h^2 F_{\mathsf{GW},0} A_{\mathsf{str}} K^2 \left(\frac{H_*}{\beta}\right)^2 \,, \quad f_p \simeq 0.11 H_{*,0} \frac{\beta}{H_*} \,, \tag{3.4.11}$$

where $A_{\mathsf{str}} \simeq 0.05$ and the fractional energy density is $K = \kappa_{\mathsf{coll}} \frac{\alpha}{\alpha+1}$, with κ_{coll} the collision efficiency fraction defined in Eq. (3.3.53).

In terms of the geometrical parameters $\vec{\theta}_{\mathsf{cosmo}} = (f_1, f_2, \Omega_2)$ and the source-dependent exponents $(n_1, n_2, n_3, a_1, a_2)$, the DBPL is given by

$$\Omega_{\mathsf{GW}}^{\mathsf{DBPL}}(f, \vec{\theta}_{\mathsf{cosmo}}) = \Omega_{\mathsf{int}} S(f) = \Omega_2 S_2(f) \,, \tag{3.4.12}$$

where the shape function $S(f)$ is

$$S(f) = N \left(\frac{f}{f_1}\right)^{n_1} \left(1 + \left(\frac{f}{f_1}\right)^{a_1}\right)^{\frac{-n_1+n_2}{a_1}} \left(1 + \left(\frac{f}{f_2}\right)^{a_2}\right)^{\frac{-n_2+n_3}{a_2}} \,. \tag{3.4.13}$$

The SGWB spectrum in Eq. (3.4.12) grows as $\Omega_{\mathsf{GW}} \propto f^{n_1}$ for $f < f_1$, as $\Omega_{\mathsf{GW}} \propto f^{n_2}$ for $f_1 < f < f_2$ and as $\Omega_{\mathsf{GW}} \propto f^{n_3}$ for $f > f_2$. The parameters a_1 and a_2 describe the spectrum near the frequency breaks f_1 and f_2, respectively. The normalization factor N is chosen such that $S_2(f_2) = 1$, i.e. $S_2(f) =$

$S(f)/S(f_2)$, although in principle it should be fixed by $\int_{-\infty}^{\infty} d\ln f, S(f) = 1$.

The DBPL in Eq. (3.4.12) describes the SGWB spectrum of both sound waves and turbulence contributions. For sound waves, the source-dependent exponents are fixed as $n_1 = 3$, $n_2 = 1$, $n_3 = -3$, $a_1 = 2$, $a_2 = 4$. The frequency breaks f_1 and f_2 are given by

$$f_1 \simeq 0.2 H_{*,0}(H_* R_*)^{-1} , \quad f_2 \simeq 0.5 H_{*,0} \Delta_w^{-1} (H_* R_*)^{-1} , \tag{3.4.14}$$

where $\Delta_w = \frac{\xi_{shell}}{\max(v_w, c_s)}$, with sound speed $c_s = \frac{1}{\sqrt{3}}$, bubble wall speed $v_w = 1$ and dimensionless sound shell thickness $\xi_{shell} = |v_w - c_s|$. The amplitude at the second frequency break Ω_2 is given by

$$h^2 \Omega_{\text{int}} = h^2 F_{\text{GW},0} A_{sw} K^2 (H_* \tau_{sw})(H_* R_*) , \tag{3.4.15}$$

where $A_{sw} \simeq 0.11$, τ_{sw} is the sound wave source duration and R_* is the average bubble size related to the inverse transition duration β by Eq. (3.3.44). The kinetic energy fraction is $K \simeq 0.6 \kappa_{sw} \frac{\alpha}{1+\alpha}$, where κ_{sw} is the sound wave efficiency fraction defined in Eq. (3.3.54). Ω_2 and Ω_{int} in Eq. (3.4.12) are related by $\Omega_2 \simeq 0.55 \Omega_{\text{int}}$. The prescription to compute the sound wave source duration τ_{sw} is [217]

$$\tau_{sw} = \min(H_*^{-1}, R_* U_f^{-1}) , \tag{3.4.16}$$

where the root-mean-square fluid velocity is

$$U_f^2 \simeq \frac{3}{4} \frac{\alpha_{\text{eff}}}{1 + \alpha_{\text{eff}}} \kappa_{sw} , \tag{3.4.17}$$

with α_{eff} defined in Eq. (3.3.54).

For MHD turbulence, the source-dependent exponents are fixed as $n_1 = 3$, $n_2 = 1$, $n_3 = -\frac{8}{3}$, $a_1 = 4$, $a_2 = 2.15$. The frequency breaks f_1 and f_2 are given by

$$f_1 \simeq \frac{\sqrt{3\Omega_s}}{2\mathcal{N}} H_{*,0} (H_* R_*)^{-1} , \quad f_2 \simeq 2.2 H_{*,0} (H_* R_*)^{-1} , \tag{3.4.18}$$

while the amplitude at the second frequency break Ω_2 is given by

$$h^2 \Omega_2 = h^2 F_{\text{GW},0} A_{\text{MHD}} \Omega_s^2 (H_* R_*)^2 . \tag{3.4.19}$$

Here, $\Omega_s \simeq \frac{4U_f^2}{3}$ with U_f given in Eq. (3.4.17), $\mathcal{N} \simeq 2$, $A_{\text{MHD}} \simeq 4.37 \times 10^{-3}$, R_* is the average bubble size related to the inverse transition duration β by Eq. (3.3.44). For further details, see Ref [62].

4 Model-independent framework

A FOPT in classically scale-invariant or nearly-conformal models[29] typically gives rise to a strong SGWB, making this class of models of particular interest to explain the observed PTA signal, see e.g.

[29] Conformal symmetry refers to invariance under transformations that preserve angles but not necessarily distances. This includes translations, Lorentz transformations, dilatations (scale transformations), and special conformal transformations [151, 220]. Scale invariance is a particular case of conformal invariance. Models exhibiting this feature are referred to as conformal models, while the term nearly reflects the fact that this symmetry is broken perturbatively at the quantum level.

Refs. [51–61] for recent works.

This chapter presents a new semi-analytic, model-independent framework to study supercooled FOPTs in classically scale-invariant models. Our approach builds upon and supersedes previous results developed in the literature, see Refs. [58–61], which we review in Sec. 4.1. The main idea is to approximate the effective potential by a polynomial containing only quadratic, cubic and quartic terms, and then exploiting analytic expressions to compute the bounce action S_3. In Sec. 4.2, we improve this framework by obtaining more accurate approximations for the polynomial coefficients of the effective potential. We introduce a root-finding equation to compute the percolation temperature T_p, which replaces the numerically expensive integrals required for its evaluation. Previous results focused only on the nucleation temperature T_n, even though the percolation temperature T_p determines when GWs are expected to be produced for supercooled FOPTs. Furthermore, Sec. 4.2 provides analytic expressions for the transition strength α and the inverse duration parameter β. Finally, in Sec. 4.3, we apply our framework to phenomenological dark Abelian $U(1)_D$ extensions of the SM: a minimal model, consisting of a dark scalar and a dark photon, and a non-minimal one, with the addition of a dark fermion. A cosmological FOPT in these models is able to explain the PTA signal, making interesting to study them from a semi-analytic point of view. We compare the approaches developed in Sec. 4.1 and Sec. 4.2 against full numerical computations using `CosmoTransitions` [190]. We validate our approach by overlapping posterior distributions over the NANOGrav 15-year dataset, while also extracting physical insights on the parameter space of the models.

4.1 Established model-independent framework

In this section, we will write the general form of the effective potential for classically scale-invariant models and go through the details of the approximations and methodologies introduced in Refs. [58–61]. The aim is to understand FOPT semi-analytically by approximating the effective potential as a polynomial in Subsec. 4.1.3 and then use the analytic expression for the bounce action S_3 given in Subsec. 4.1.4.

Consider the most general renormalisable Lagrangian, symmetric under the Lorentz group and a gauge group $\mathcal{G}$, containing an arbitrary number of gauge vector boson fields V_μ^A, real scalar fields ϕ_a and Weyl fermions ψ_i [59]

$$\mathcal{L} = -\frac{1}{4}F_{\mu\nu}^A F^{\mu\nu A} + i\bar{\psi}_i \not{D}\psi_i - \frac{1}{2}(Y_{ij}^a \psi_i \psi_j \phi_a + \text{h.c.}) + \frac{1}{2}D_\mu\phi_a D^\mu\phi_a - V_{\text{tree}}(\phi_a)\,, \tag{4.1.1}$$

where covariant derivatives are given by $D_\mu\phi_a = \partial_\mu\phi_a + i\theta_{ab}^A V_\mu^A \phi_b$ and $D_\mu\psi_i = \partial_\mu\psi_i + it_{ij}^A V_\mu^A \psi_j$, with θ^A and t^A generators of the gauge group $\mathcal{G}$ in the scalar and fermion representations, respectively. The gauge couplings are incorporated in the generators.

4.1.1 Classically scale-invariant effective potential

Scale invariance constrains the form of the tree-level potential $V_{\text{tree}}(\phi_a)$ in Eq. (4.1.1). In fact, under a scale transformation, spacetime coordinates are rescaled as

$$x'^\mu = \sigma x^\mu\,, \tag{4.1.2}$$

where σ is a constant scale factor. For the action to remain invariant under Eq. (4.1.2), the Lagrangian must transform as

$$S' = \int d^D x' \, \mathcal{L}' = \int d^D x \, \sigma^D \mathcal{L}' \stackrel{!}{=} S = \int d^D x \, \mathcal{L} \quad \Rightarrow \quad \mathcal{L} \to \mathcal{L}' = \sigma^{-D} \mathcal{L} \, . \tag{4.1.3}$$

By requiring that the kinetic term $\mathcal{L}_{kin} = \frac{1}{2} \partial_\mu \phi \partial^\mu \phi$ transforms as the Lagrangian in Eq. (4.1.3), we derive the scaling dimension Δ of the scalar field under a scale transformation $\phi \to \phi' = \sigma^\Delta \phi$

$$\mathcal{L}'_{kin} = \frac{1}{2} \partial'_\mu \phi' \partial'^\mu \phi' = \sigma^{2\Delta - 2} \frac{1}{2} \partial_\mu \phi \partial^\mu \phi \stackrel{!}{=} \sigma^{-D} \mathcal{L}_{kin} = \sigma^{-D} \frac{1}{2} \partial_\mu \phi \partial^\mu \phi \quad \Rightarrow \quad \phi \to \phi' = \sigma^{\frac{2-D}{2}} \phi \, . \tag{4.1.4}$$

Imposing that the tree-level potential $V_{\text{tree}}(\phi_a)$ transforms as the Lagrangian does in Eq. (4.1.3) and using the scale transformation of the scalar field in Eq. (4.1.4), the allowed scalar field powers of the tree-level potential are uniquely determined by the dimension D

$$V'_{\text{tree}} = a \phi'^N = a \sigma^{\frac{2-D}{2} N} \phi^N \stackrel{!}{=} \sigma^{-D} V_{\text{tree}} = a \sigma^{-D} \phi^N \quad \Rightarrow \quad V = a \phi^{\frac{2D}{D-2}} \, . \tag{4.1.5}$$

Therefore, in $D = 4$ dimensions, scale invariance rescricts the tree-level potential to be quartic: $\frac{2D}{D-2} = 4$.

It can be shown that gauge bosons and fermions have scaling dimensions $A_\mu \to A'_\mu = \sigma^{-1} A_\mu$ and $\psi \to \psi' = \sigma^{-3/2} \psi$, respectively. Since scale invariance forbids any dimensionful parameter in the Lagrangian, explicit mass terms are not allowed, such as $m_\psi \bar{\psi} \psi$ for fermions or $m_A A_\mu A^\mu$ for gauge bosons. However, masses can be generated through the mechanism of SSB, explained in Sec. 2.3.3.

Generalising the result in Eq. (4.1.5) to a theory with an arbitrary number of real scalar fields ϕ_a, the most general scale-invariant tree-level potential reads

$$V_{\text{tree}}(\phi) = \frac{\lambda_{abcd}}{4!} \phi_a \phi_b \phi_c \phi_d \, , \tag{4.1.6}$$

where λ_{abcd} is the totally symmetric quartic coupling. Therefore, scale invariance allows only dimensionless couplings in the tree-level potential, such as the quartic coupling in Eq. (4.1.6), and no mass terms are allowed, such as the $-\mu^2$ coupling in the Higgs potential in Eq. (2.3.15) and the quadratic coupling m_{ij}^2 in the most general expression of the tree-level potential in Eq. (3.1.19). Nevertheless, this symmetry is irremediably broken perturbatively at the quantum level, whereby loop corrections dynamically generate a mass scale, which is not present at the classical level. This mechanism is called Radiative Symmetry Breaking (RSB) or dimensional transmutation.

The basic idea was first introduced in Ref. [221]. When the theory is renormalised to tame ultraviolet divergences, a renormalisation scale μ is introduced to regularise loop integrals. Consequently, the bare quartic coupling becomes a μ-dependent quantity $\lambda_{abcd} = \lambda_{abcd}(\mu)$, and there may exist a specific value $\tilde{\mu}$ such that the tree-level potential in Eq. (4.1.6) develops a flat direction, i.e. a direction in field space along which the potential vanishes. Let us parametrise such flat direction by $\phi_a = \chi \nu_a$, where ν_a is a unit vector, i.e. $\nu_a \nu_a = 1$, and χ its magnitude, capturing the radial direction. In this parametrisation, the multi-field tree-level potential in Eq. (4.1.6) can be rewritten in terms of a single

scalar field χ as

$$V_{\text{tree}}(\chi) = \frac{\lambda_{abcd}(\mu)}{4!}\nu_a\nu_b\nu_c\nu_d\chi^4 = \frac{\lambda_\chi(\mu)}{4}\chi^4\,, \quad \lambda_\chi(\mu) = \frac{\lambda_{abcd}(\mu)}{3!}\nu_a\nu_b\nu_c\nu_d\,. \tag{4.1.7}$$

To understand how quantum corrections lift this flat direction, we need the expression of the one-loop effective potential. Requiring that the effective potential does not depend on the renormalisation scale μ, expressed by the RGE in Eq. (3.1.39) as

$$\frac{dV_{\text{eff}}}{d\ln\mu} = \mu\frac{dV_{\text{eff}}}{d\mu} = 0\,, \tag{4.1.8}$$

at one-loop approximation $V_{\text{eff}} = V_{\text{tree}} + V_{\text{1-loop}}$, the effective potential is given by [59]

$$V_{\text{eff}}(\chi) = \frac{\lambda_\chi}{4}\chi^4 + \frac{\beta_{\lambda_\chi}}{4}\Big(\ln\frac{\chi}{\mu} + a_s\Big)\chi^4\,, \tag{4.1.9}$$

where $\beta_{\lambda_\chi} = \mu\frac{d\lambda_\chi}{d\mu}$ is the beta function of the quartic coupling λ_χ and a_s is a renormalisation scheme-dependent constant.

At the renormalisation scale $\tilde{\mu}$, where the quartic coupling vanishes along the flat direction $\lambda_\chi(\tilde{\mu}) = 0$, the effective potential in Eq. (4.1.9) becomes [59]

$$V_{\text{eff}}(\chi) = \frac{\tilde{\beta}_{\lambda_\chi}}{4}\Big(\ln\frac{\chi}{\tilde{\mu}} + a_s\Big)\chi^4\,, \tag{4.1.10}$$

where $\tilde{\beta}_{\lambda_\chi} = \beta_{\lambda_\chi}|_{\mu=\tilde{\mu}}$ is the beta function of the quartic coupling λ_χ at the scale $\tilde{\mu}$ such that $\lambda_\chi(\tilde{\mu}) = 0$.

It is not necessary to compute the renormalisation scale $\tilde{\mu}$, because it can be traded with the minimum of the effective potential χ_0, which plays the role of the VEV. Imposing that the first derivative of the one-loop effective potential in Eq. (4.1.10) vanishes, we obtain the stationary points

$$0 = \frac{dV_{\text{eff}}}{d\chi}\Big|_{\chi_0} = \tilde{\beta}_{\lambda_\chi}\chi_0^3\Big(\ln\frac{\chi_0}{\tilde{\mu}} + a_s\Big) + \frac{\tilde{\beta}}{4}\chi_0^3 \quad \Rightarrow \quad \chi_0 = 0 \quad \text{or} \quad \chi_0 = \tilde{\mu}e^{-a_s-1/4}\,. \tag{4.1.11}$$

The potential evaluated at $\chi_0 = 0$ is $V_{\text{eff}}(\chi_0 = 0) \to 0$, where we have used the limit $\lim_{x\to 0} x^4\ln x = 0$, whereas the potential evaluated at $\chi_0 \neq 0$ is $V_{\text{eff}}(\chi \neq 0) = -\frac{\tilde{\beta}_{\lambda_\chi}}{16}\chi_0^4$. This means that the absolute minimum of the effective potential is at non-vanishing field value $\chi_0 \neq 0$ and the SSB mechanism occurs. The second derivative of the one-loop effective potential in Eq. (4.1.10)

$$\frac{d^2V_{\text{eff}}}{d\chi^2} = \tilde{\beta}_{\lambda_\chi}\chi^2\left(3\ln\frac{\chi}{\chi_0} + 1\right)\,, \quad \frac{d^2V_{\text{eff}}}{d\chi^2}\Big|_{\chi_0} = \tilde{\beta}_{\lambda_\chi}\chi_0^2\,, \tag{4.1.12}$$

implies that, as long as $\tilde{\beta}_{\lambda_\chi} > 0$, χ_0 is an absolute minimum. Note that the effective potential is flat at $\chi_0 = 0$, since also the second derivative vanishes there. From the second derivative of the one-loop potential in Eq. (4.1.12), we can read the mass of the scalar field χ

$$m_\chi^2 = \tilde{\beta}_{\lambda_\chi}\chi_0^2\,. \tag{4.1.13}$$

Finally, the effective potential in Eq. (4.1.10) in terms of χ_0 given by Eq. (4.1.11) becomes [59]

$$V_{\text{eff}}(\chi) = \frac{\tilde{\beta}_{\lambda_\chi}}{4}\Big(\ln\frac{\chi}{\chi_0} - \frac{1}{4}\Big)\chi^4 \,. \tag{4.1.14}$$

In the scalar sector, the masses are given by elements of the Hessian matrix of the tree-level potential in Eq. (4.1.6)

$$m_{ab}^2(\chi) = \frac{\partial^2 V_{\text{tree}}}{\partial\phi_a\partial\phi_b} = \frac{1}{2}\lambda_{abcd}\phi_c\phi_d = \frac{1}{2}\lambda_{abcd}\nu_c\nu_d\chi^2 \,. \tag{4.1.15}$$

Since m_{ab}^2 is real and symmetric, it can be diagonalised and its eigenvalues $m_s(\chi)$ are the field-dependent masses of scalar particles. The potential is bounded from below only if all eigenvalues of the scalar mass matrix are non-negative: a negative eigenvalue would define a field direction along which the potential decreases boundlessly, contradicting the assumption that $\phi = 0$ is a minimum where the tree-level potential vanishes. In the fermion sector, we choose a fermion basis such that $\mu = Y^a\phi_a$ is diagonal

$$m_f^2(\chi) = \mu\mu^\dagger = Y^a Y^{b\dagger}\phi_a\phi_b = Y_\nu Y_\nu^\dagger\chi^2 \,, \tag{4.1.16}$$

where we have defined $Y_\nu = Y^a\nu_a$. Then $m_f^2(\chi)$ is diagonal and the diagonal entries $m_f^2(\chi)$ are the field-dependent masses of fermionic particles, which are real and non-negative. In the gauge vector boson sector, the mass matrix is given by

$$m_{AB}^2(\chi) = \phi^T\theta^A\theta^B\phi = \nu^T\theta^A\theta^B\nu\chi^2 \,. \tag{4.1.17}$$

The generators θ^A are Hermitian, purely imaginary and antisymmetric, which implies that $m_{AB}^2(\chi)$ is real, symmetric and positive definite, so that it can be diagonalised and its eigenvalues $m_v(\chi)$ are the field-dependent masses of gauge vector boson particles. The fact that all squared masses of scalars in Eq. (4.1.15), fermions in Eq. (4.1.16) and gauge bosons in Eq. (4.1.17) are positive ensures that the effective potential is always real in RSB, which does not spoil perturbation theory. This is in contrast to what happens in the Higgs mechanism, where the effective potential acquires an imaginary part due to the fact that some squared masses become negative around the origin and thus the effective potential is not guaranteed to be convex in perturbation theory.

Including thermal corrections in Eq. (3.1.59), the effective potential takes the form

$$V_{\text{eff}}(\chi,T) = \frac{\tilde{\beta}_{\lambda_\chi}}{4}\Big(\ln\frac{\chi}{\chi_0} - \frac{1}{4}\Big)\chi^4 + \frac{T^4}{2\pi^2}\Big(\sum_b n_b J_b\Big(\frac{m_b^2(\chi)}{T^2}\Big) - \sum_f n_f J_f\Big(\frac{m_f^2(\chi)}{T^2}\Big)\Big) \,, \tag{4.1.18}$$

where n_b and n_f are the degrees of freedom of bosons and fermions, respectively. The thermal functions $J_b(x)$ and $J_f(x)$ are given by Eqs. (3.1.60) and (3.1.61)

$$J_b(x) = \int_0^\infty dp\, p^2 \log\left(1 - e^{-\sqrt{p^2+x}}\right) \simeq -\frac{\pi^4}{45} + \frac{\pi^2}{12}x - \frac{\pi}{6}x^{3/2} - \frac{x^2}{32}\ln\left(\frac{x}{a_b}\right) \,, \tag{4.1.19}$$

$$J_f(x) = \int_0^\infty dp\, p^2 \log\left(1 + e^{-\sqrt{p^2+x}}\right) \simeq \frac{7\pi^4}{360} - \frac{\pi^2}{24}x - \frac{x^2}{32}\ln\left(\frac{x}{a_f}\right) \,, \tag{4.1.20}$$

where we have also written the high-temperature expansions, with $a_b = 16\pi^2 e^{3/2-2\gamma_E}$, $a_f = \pi^2 e^{3/2-2\gamma_E}$

and γ_E is the Euler-Mascheroni constant.

For further convenience, we define the effective potential $\bar{V}_{\text{eff}}$, such that it vanishes at the false vacuum $\bar{V}_{\text{eff}}(\chi = 0, T) = 0$

$$\bar{V}_{\text{eff}}(\chi, T) = V_{\text{eff}}(\chi, T) - V_{\text{eff}}(0, T) \, . \tag{4.1.21}$$

4.1.2 First-order phase transition

An important feature is that PTs associated to RSB are always first-order [59]. This can be seen by showing that the false vacuum is a local minimum. As illustrated by Eqs. (4.1.11) and (4.1.12), the first three derivatives of the one-loop effective potential vanish at $\chi = 0$, which means that it is very flat around the origin $\chi = 0$. The thermal functions in the high-temperature expansion of Eqs. (4.1.19) and (4.1.20) have a positive term[30] that goes as the square of the masses m^2, which are proportional to the square of the scalar field χ^2. Since near the origin $\chi = 0$, the quadratic part of the thermal potential dominates over the almost flat one-loop effective potential, the origin becomes at least metastable at non-vanishing temperatures: the false vacuum is a local minimum and a barrier is present between the false and the true vacuum. Note that this would not happen for a non-RSB, because the contribution of the negative quadratic term, e.g. the $-\mu^2$ term in the Higgs potential in Eq. (2.3.15), may be dominant with respect to the positive quadratic thermal one, resulting in no barrier around the false vacuum $\chi = 0$.

Therefore, the absolute minimum of the effective potential is $\chi = 0$ for $T > T_c$ and $\chi \neq 0$ for $T < T_c$, where T_c is the critical temperature introduced in Sec. 3.3.2. Assuming that the bounce solution is dominated by time-independent thermal tunnelling, which can be justified by checking that the Euclidean action for the time-dependent bounce is larger than the one of the time-independent bounce, the false vacuum decay rate in Eq. (3.2.39) reads

$$\Gamma \simeq T^4 \Big(\frac{S_3}{2\pi T} \Big)^{3/2} e^{-\frac{S_3}{T}} \, , \tag{4.1.22}$$

where the 3-dimensional action S_3 in Eq. (3.2.40) is

$$S_3 = 4\pi \int_0^\infty d\rho \, \rho^2 \Big(\frac{1}{2} \left(\frac{d\chi}{d\rho} \right)^2 + \bar{V}_{\text{eff}}(\chi, T) \Big) = -8\pi \int_0^\infty d\rho \, \rho^2 \bar{V}_{\text{eff}}(\chi, T) \, , \tag{4.1.23}$$

where in the second passage we have used Eq. (3.2.30). The bounce solution corresponds to the solution of the ordinary differential equation with suitable boundary conditions in Eq. (3.2.41)

$$\frac{d^2\chi}{d\rho^2} + \frac{2}{\rho} \frac{d\chi}{d\rho} = \frac{d\bar{V}_{\text{eff}}}{d\chi} \, , \quad \frac{d\chi}{d\rho}(0) = \lim_{\rho \to \infty} \chi(\rho) = 0 \, . \tag{4.1.24}$$

4.1.3 Supercooling expansion

The field values that give the dominant contributions to the bounce action S_3 are those near the potential barrier, where the tunneling probability is largest. Moreover, the tunneling path is controlled by the barrier separating the false and true vacuum. Therefore, in order to compute the bounce action S_3, we need to track down the behaviour of these field values, neglecting those that

[30] The fermionic thermal function in Eq. (4.1.20) has a negative linear term, but the sign becomes positive once inserted in the thermal potential in Eq. (4.1.18).

are away from the metastable vacuum, e.g. near χ_0. It is useful to define the barrier width $\chi_b = \chi_b(T)$, which is the T-dependent field value at which the effective potential V_{eff} is equal to its value at the false vacuum $\chi = 0$, i.e.

$$\bar{V}_{\text{eff}}(\chi_b, T) = 0 \,. \tag{4.1.25}$$

Under the assumption of large supercooling $T \ll \chi_0$, for field values near χ_b, the effective potential in Eq. (4.1.18) can be approximated to a polynomial

$$\bar{V}_{\text{eff}}(\chi, T) \simeq \frac{m^2(T)}{2}\chi^2 - \frac{\lambda(T)}{4}\chi^4 \,, \tag{4.1.26}$$

where the quadratic $m(T)$ and the quartic $\lambda(T)$ coefficients are given by

$$m^2(T) = \frac{g^2 T^2}{12} \,, \quad \lambda(T) = \tilde{\beta}_{\lambda_\chi} \ln \frac{\chi_0}{T} \,, \tag{4.1.27}$$

and we have introduced the collective real non-negative coupling[31]

$$g^2\chi^2 = \sum_b n_b m_b^2(\chi) + \sum_f \frac{n_f}{2} m_f^2(\chi) \,. \tag{4.1.28}$$

The crucial approximation necessary to obtain Eq. (4.1.26) comes from the logarithmic part of the one-loop effective potential in Eq. (4.1.14): the χ-dependent logarithmic term is substituted by a T-dependent one

$$\ln \frac{\chi_b}{\chi_0} - \frac{1}{4} = \ln \frac{\chi_b}{T} - \frac{1}{4} + \ln \frac{T}{\chi_0} \simeq \ln \frac{T}{\chi_0} \,, \tag{4.1.29}$$

where we have used the fact that in presence of large supercooling $T \ll \chi_0$, the first two terms in Eq. (4.1.29) are subleading compared to the third one. Note that there is a logarithmic dependence on the ratio $\frac{T}{\chi_0}$, so we need indeed very large supercooling to make this approximation work. We introduce the collective thermal function J_T to simplify the finite temperature effective potential in Eq. (4.1.18)

$$J_T\left(\frac{\chi^2}{T^2}\right) = \sum_b n_b J_b\left(\frac{m_b^2(\chi)}{T^2}\right) - \sum_f n_f J_f\left(\frac{m_f^2(\chi)}{T^2}\right) , \tag{4.1.30}$$

approximate at leading order (LO) the thermal functions in Eq. (4.1.19) and (4.1.20)

$$J_b(x) \simeq J_b(0) + \frac{\pi^2}{12}x \,, \quad J_f(x) \simeq J_f(0) - \frac{\pi^2}{24}x \,, \tag{4.1.31}$$

and write the collective thermal function J_T in Eq. (4.1.30) in terms of the collective coupling g in Eq. (4.1.28)

$$J_T\left(\frac{\chi^2}{T^2}\right) - J_T(0) \simeq \sum_b n_b \frac{\pi^2}{12}\frac{m_b^2(\chi)}{T^2} + \sum_f n_f \frac{\pi^2}{24}\frac{m_f^2(\chi)}{T^2} = \frac{\pi^2 g^2}{12}\frac{\chi^2}{T^2} \,. \tag{4.1.32}$$

Then, we make use of the approximation of the one-loop contribution in Eq. (4.1.29) and the thermal

[31] Note that in Ref. [59], there is a difference in the prefactor of fermion masses $\frac{n_f}{2}$, due to a different convention to define the thermal contributions in Eq. (4.1.18).

one in Eq. (4.1.32), to obtain the polynomial potential in Eq. (4.1.26)

$$\begin{aligned}\bar{V}_{\text{eff}}(\chi,T) &= \frac{\tilde{\beta}_{\lambda_\chi}}{4}\Big(\ln\frac{\chi}{\chi_0}-\frac{1}{4}\Big)\chi^4+\frac{T^4}{2\pi^2}\left(J_T\left(\frac{\chi^2}{T^2}\right)-J_T(0)\right)\\ &\simeq -\frac{\tilde{\beta}_{\lambda_\chi}}{4}\ln\frac{\chi_0}{T}\chi^4+\frac{g^2T^2}{24}\chi^2=\frac{m^2(T)}{2}\chi^2-\frac{\lambda(T)}{4}\chi^4\,,\end{aligned} \tag{4.1.33}$$

where we have used the definitions of the coefficients in Eq. (4.1.27). To check that the approximation for the one-loop contribution in Eq. (4.1.29) is valid, we make an estimate of the barrier width χ_b over temperature T. In fact, using the definition of χ_b in Eq. (4.1.25) with the approximated polynomial potential in Eq. (4.1.26)

$$\bar{V}_{\text{eff}}(\chi_b,T)\simeq\frac{m^2(T)}{2}\chi_b^2-\frac{\lambda(T)}{4}\chi_b^4=0\,, \tag{4.1.34}$$

leads to

$$\chi_b^2\simeq\frac{2m^2(T)}{\lambda(T)}\,,\quad \frac{\chi_b^2}{T^2}\simeq\frac{g^2}{6\tilde{\beta}_{\lambda_\chi}\ln\frac{\chi_0}{T}}\,, \tag{4.1.35}$$

where we have again used the definitions of the coefficients in Eq. (4.1.27). The expression of the barrier width over temperature in Eq. (4.1.35) shows that the ratio is only logarithmically suppressed in the presence of large supercooling $T\ll\chi_0$, validating the approximation since in Eq. (4.1.29) the ratio $\frac{T}{\chi_0}$ directly appears. The main advantage of this approximation is that, for relevant values of the scalar field χ, the effective action can be parametrised by only three quantities: χ_0, $\tilde{\beta}_{\lambda_\chi}$ and g. Since the arguments of the collective thermal function in Eq. (4.1.30) are the square masses of the fields over the square temperature, we can introduce a quantity to check if the LO approximation of the thermal functions in Eqs. (4.1.19) and (4.1.20) is valid

$$\epsilon=g^2\frac{\chi_b^2}{T^2}\simeq\frac{g^4}{6\tilde{\beta}_{\lambda_\chi}\ln\frac{\chi_0}{T}}\,, \tag{4.1.36}$$

where we have used the expression in Eq. (4.1.35). Thus, $\epsilon\ll1$ is an internal consistency check.

We can improve this approximation by considering the next-to-leading (NLO) order in the thermal functions J_T, which leads to an addition of a cubic term in the polynomial effective potential in Eq. (4.1.26)

$$\bar{V}_{\text{eff}}(\chi,T)\simeq\frac{m^2(T)}{2}\chi^2-\frac{\lambda(T)}{4}\chi^4-\frac{k(T)}{3}\chi^3\,, \tag{4.1.37}$$

where $m^2(T)$ and $\lambda(T)$ are given by Eq. (4.1.27),

$$k(T)=\frac{\tilde{g}^3T}{4\pi}\,, \tag{4.1.38}$$

and we introduced another collective real non-negative coupling

$$\tilde{g}^3\chi^3=\sum_b n_b m_b^3(\chi)\,. \tag{4.1.39}$$

The procedure to obtain this approximated potential in Eq. (4.1.37) is the same as in Eq. (4.1.26). We

approximate the thermal functions in Eqs. (4.1.19) and (4.1.20) at NLO

$$J_b(x) \simeq J_b(0) + \frac{\pi^2}{12}x - \frac{\pi}{6}x^{3/2}\,, \quad J_f(x) \simeq J_f(0) - \frac{\pi^2}{24}x\,, \tag{4.1.40}$$

and write the collective thermal function J_T in Eq. (4.1.30) in terms of the collective couplings g and $\tilde{g}$ in Eqs. (4.1.28) and (4.1.39)

$$\begin{aligned} J_T\left(\frac{\chi^2}{T^2}\right) - J_T(0) &\simeq \sum_b n_b \frac{\pi^2}{12}\frac{m_b^2(\chi)}{T^2} + \sum_f n_f \frac{\pi^2}{24}\frac{m_f^2(\chi)}{T^2} - \sum_b n_b \frac{\pi}{6}\frac{m_b^3(\chi)}{T^3} \\ &= \frac{\pi^2 g^2}{12}\frac{\chi^2}{T^2} - \frac{\pi}{6}\tilde{g}^3\frac{\chi^3}{T^3}\,. \end{aligned} \tag{4.1.41}$$

Then, we make use of the approximation of the one-loop contribution in Eq. (4.1.29) and the thermal one in Eq. (4.1.41), to obtain the polynomial potential in Eq. (4.1.37)

$$\begin{aligned} \bar{V}_{\text{eff}}(\chi, T) &= \frac{\tilde{\beta}_{\lambda_\chi}}{4}\Big(\ln\frac{\chi}{\chi_0} - \frac{1}{4}\Big)\chi^4 + \frac{T^4}{2\pi^2}\left(J_T\left(\frac{\chi^2}{T^2}\right) - J_T(0)\right) \\ &= -\frac{\tilde{\beta}_{\lambda_\chi}}{4}\ln\frac{\chi_0}{T}\chi^4 + \frac{g^2T^2}{24}\chi^2 - \frac{\tilde{g}^3T}{12\pi}\chi^3 = \frac{m^2(T)}{2}\chi^2 - \frac{k(T)}{3}\chi^3 - \frac{\lambda(T)}{4}\chi^4\,, \end{aligned} \tag{4.1.42}$$

where we have used the definitions of the coefficients in Eqs. (4.1.27) and (4.1.38). We can improve the estimate of the barrier width over temperature, using the definition of χ_b in Eq. (4.1.25) with the approximated polynomial potential in Eq. (4.1.37)

$$\bar{V}_{\text{eff}}(\chi_b, T) \simeq \frac{m^2(T)}{2}\chi_b^2 - \frac{k(T)}{3}\chi_b^3 - \frac{\lambda(T)}{4}\chi_b^4 = 0\,, \tag{4.1.43}$$

leading to

$$\chi_b \simeq \frac{2k(T)}{3\lambda(T)}\left(\sqrt{1 + \frac{9\lambda(T)m^2(T)}{2k^2(T)}} - 1\right)\,, \quad \frac{\chi_b}{T} \simeq \frac{\tilde{g}^3}{6\pi\tilde{\beta}_{\lambda_\chi}\ln\frac{\chi_0}{T}}\left(\sqrt{1 + \frac{6\pi^2 g^2\tilde{\beta}_{\lambda_\chi}\ln\frac{\chi_0}{T}}{\tilde{g}^6}} - 1\right) \tag{4.1.44}$$

where we have again used the definitions of the coefficients in Eqs. (4.1.27) and (4.1.38), and considered only the positive solution. The parameter ϵ can be defined in the same way as in Eq. (4.1.36) but using the cubic term in the effective potential in Eq. (4.1.37)

$$\epsilon = g^2\frac{\chi_b^2}{T^2} = g^2\left(\frac{\tilde{g}^3}{6\pi\tilde{\beta}_{\lambda_\chi}\ln\frac{\chi_0}{T}}\right)^2\left(\sqrt{1 + \frac{6\pi^2 g^2\tilde{\beta}_{\lambda_\chi}\ln\frac{\chi_0}{T}}{\tilde{g}^6}} - 1\right)^2\,. \tag{4.1.45}$$

where we have used the expression in Eq. (4.1.44).

4.1.4 Analytic bounce action

For polynomial potentials such as those in Eq. (4.1.37), we can use expressions present in the literature, see e.g. Refs [222–226]. In particular, we need a bounce action S_3 for a polynomial potential with a negative quartic coefficient, which is provided by Ref. [58]. In fact, it is possible to

write the bounce action in terms of only one free parameter, after appropriate field and coordinate transformations, and obtain an analytic expression by fitting it with a suitable expression.

We begin with the D-dimensional bounce action in Eq. (3.2.27)

$$S_D = \frac{2\pi^{\frac{D}{2}}}{\Gamma(\frac{D}{2})} \int dr\, r^{D-1} \left(\frac{Z_\chi}{2} \left(\frac{d\chi}{dr} \right)^2 + V_{\text{eff}}(\chi) \right) , \tag{4.1.46}$$

where $Z_\chi = 1$ is canonically normalised. We rescale the integration variable $r = L\rho$ and the field $\chi = \xi\varphi$, so that

$$S_D = \xi^2 L^{D-2} \tilde{S}_D , \quad V_{\text{eff}}(\chi) = \xi^2 L^{-2} \tilde{V}_{\text{eff}}(\chi) , \tag{4.1.47}$$

where $\tilde{S}_D$ is the dimensionless action and $\tilde{V}_{\text{eff}}$ is the dimensionless effective potential. In particular, for a polynomial potential such as in Eq. (4.1.37), we identify

$$\xi = \frac{m^2(T)}{k(T)} , \quad L = \frac{1}{m(T)} , \tag{4.1.48}$$

to obtain a dimensionless potential

$$\tilde{V}_{\text{eff}}(\chi, T) = \frac{1}{2}\varphi^2 - \frac{1}{3}\varphi^3 - \frac{\tilde{\lambda}(T)}{4}\varphi^4 , \tag{4.1.49}$$

where we have defined[32]

$$\tilde{\lambda}(T) = \frac{\lambda(T) m^2(T)}{k^2(T)} . \tag{4.1.50}$$

Note that $\tilde{\lambda} \in [-\tilde{\lambda}_c, \infty]$ where $\tilde{\lambda}_c = \tilde{\lambda}(T_c)$ is evaluated at the critical temperature T_c. For weakly coupled theories, the 3-dimensional thermal bounce action dominates and we can perform a one-parameter fit over $\tilde{\lambda}$. We identify three limiting cases and fit the intermediate region: the thin-wall approximation $\tilde{\lambda} \to \tilde{\lambda}_c = -2/9$, where the two potential vacua are degenerate; the limit $\tilde{\lambda} \to \infty$, where the potential has a negative quartic with a vanishing cubic term [227], referred to as the BP case, and the limit $\tilde{\lambda} \to 0$, where the quartic interaction term vanishes and the cubic dominates

$$S_3^{\text{thin}}(T) \simeq \frac{32\pi m^3(T)}{729 k^2(T)} \frac{1}{(\tilde{\lambda}(T) + \frac{2}{9})^2} , \quad S_3^{\text{BP}}(T) \simeq \frac{6\pi m(T)}{\lambda(T)} , \quad S_3^{\text{cubic}}(T) \simeq \frac{27\pi m^3(T)}{2k^2(T)} . \tag{4.1.51}$$

Requiring smoothness at the transition point $\tilde{\lambda} = 0$ and normalising over the thin wall approximation for $\tilde{\lambda} < 0$ and over the cubic approximation for $\tilde{\lambda} > 0$

$$B_3^+ = \frac{\tilde{S}_3}{\tilde{S}_3^{\text{thin}}} , \quad B_3^- = \frac{\tilde{S}_3}{\tilde{S}_3^{\text{BP}}} , \tag{4.1.52}$$

[32] We use the nomenclature of Ref. [59] in which the quartic coefficient $\tilde{\lambda}$ is negative, opposite to the one in Ref. [58] in which κ is positive. The two are just related by a sign $\tilde{\lambda} = -\kappa$.

we obtain

$$\begin{aligned}\frac{243}{16}B_3^+(\tilde{\lambda}) = 1 + 38.23\left(\tilde{\lambda}+\frac{2}{9}\right) + 115.26\left(\tilde{\lambda}+\frac{2}{9}\right)^2 \\ + 58.07\sqrt{-\tilde{\lambda}}\left(\tilde{\lambda}+\frac{2}{9}\right)^2 - 229.07\tilde{\lambda}\left(\tilde{\lambda}+\frac{2}{9}\right)^2 ,\end{aligned} \tag{4.1.53}$$

$$B_3^-(\tilde{\lambda}) = \frac{9\tilde{\lambda}}{4}\frac{1+e^{-\frac{1}{\sqrt{\tilde{\lambda}}}}}{1+\frac{9}{2}\tilde{\lambda}} . \tag{4.1.54}$$

Therefore, the ratio of the bounce action S_3 over the temperature T is given by

$$F(T) = \frac{S_3(T)}{T} = \begin{cases} \dfrac{27\pi m^3(T)}{2k^2T}F_+(\tilde{\lambda}(T)) & \text{if } \tilde{\lambda}(T) > 0, \\ \dfrac{32\pi m^3(T)}{729k^2T}F_-(\tilde{\lambda}(T)) & \text{if } \tilde{\lambda}(T) < 0, \end{cases} , \tag{4.1.55}$$

where we have defined the dimensionless functions $F_\pm(\tilde{\lambda})$ as

$$F_+(\tilde{\lambda}) = \frac{1+e^{-\frac{1}{\sqrt{\tilde{\lambda}}}}}{1+\frac{9}{2}\tilde{\lambda}} , \tag{4.1.56}$$

$$F_-(\tilde{\lambda}) = \frac{1 + 38.23\left(\tilde{\lambda}+\frac{2}{9}\right) + 115.26\left(\tilde{\lambda}+\frac{2}{9}\right)^2 + 58.07\sqrt{-\tilde{\lambda}}\left(\tilde{\lambda}+\frac{2}{9}\right)^2 - 229.07\tilde{\lambda}\left(\tilde{\lambda}+\frac{2}{9}\right)^2}{(\tilde{\lambda}+\frac{2}{9})^2} . \tag{4.1.57}$$

Note that the prefactor ratio $\frac{m^3(T)}{k^2(T)T}$ does not depend on T, so only $F_\pm(\tilde{\lambda}(T))$ are T-dependent. The functions $F_\pm$, presented in Eqs. (4.1.56) and (4.1.57), are empirical fits to numerical bounce solutions, that smoothly interpolate between regimes where analytic results are known.

4.2 Revisited model-independent framework

The approach developed in Sec. 4.1 is based on the assumption that, with large enough supercooling $T \ll \chi_0$, the field-dependent logarithmic term in the one-loop effective potential can be rewritten in terms of a T-dependent logarithm in Eq. (4.1.29) and the finite-temperature contribution can be expanded in the high-temperature limit up to cubic order in Eqs. (4.1.19) and (4.1.20), so that the effective potential can be approximated as a polynomial in Eq. (4.1.37) for small field values $\chi \ll \chi_0$. In this section, we propose a novel method that does not rely on the approximation made in Eq. (4.1.29) and extend the high-temperature expansion in Eqs. (4.1.19) and (4.1.20) to the logarithmic order. In this way, the effective potential can still be approximated by the polynomial in Eq. (4.1.37) with a different quartic coefficient and better precision. Furthermore, we focus on the thermal parameters. In particular, together with analytical expressions for the transition strength α and inverse transition duration β, we compute the integral in the expression for the percolation temperature T_p in Eq. (3.3.17) to find an analytic solution in terms of the bounce action S_3 and its derivatives. In this way, the percolation temperature T_p can be simply computed with a root-finding equation.

4.2.1 Classically scale-invariant effective potential

We begin by explicitly justifying the effective potential provided in Eq. (4.1.18), starting from the most general effective potential depending on a single scalar field χ in a classically scale-invariant theory, including both the one-loop in Eq. (3.1.37), with the $\overline{\text{MS}}$ scheme at a generic energy scale μ, and thermal contributions in Eq. (3.1.59)

$$V_{\text{eff}}(\chi,T) = \frac{\lambda}{4}\chi^4 + \frac{T^4}{2\pi^2}\left(\sum_b n_b J_b\left(\frac{m_b^2(\chi)}{T^2}\right) - \sum_f n_f J_f\left(\frac{m_f^2(\chi)}{T^2}\right)\right) + \frac{1}{64\pi^2}\left(\sum_b n_b m_b^4(\chi)\left(\ln\frac{m_b^2(\chi)}{\mu^2} - c_b\right) - \sum_f n_f m_f^4(\chi)\left(\ln\frac{m_f^2(\chi)}{\mu^2} - c_f\right)\right), \tag{4.2.1}$$

where $c_b = \frac{3}{2}\left(\frac{5}{6}\right)$ for scalar (gauge boson) fields and $c_f = \frac{3}{2}$ for fermionic fields. The scalar field χ may be the only scalar field in the theory or the flat direction in a multi-field scenario, as explained in Sec. 4.1.

Since we are interested in the effective potential for small field values near the barrier, we expand the thermal functions J_b and J_f in the high-temperature limit in Eqs. (4.1.19) and (4.1.20) to logarithmic terms, and express the high-temperature expanded effective potential in Eq. (4.2.1) as

$$V_{\text{eff}}(\chi,T) = \frac{\lambda}{4}\chi^4 + \frac{T^2}{24}\left(\sum_b n_b m_b^2(\chi) + \frac{1}{2}\sum_f n_f m_f^2(\chi)\right) - \frac{T}{12\pi}\sum_b n_b m_b^3(\chi) + \frac{1}{64\pi^2}\left(\sum_b n_b m_b^4(\chi)\left(\ln\frac{a_b T^2}{\mu^2} - c_b\right) - \sum_f n_f m_f^4(\chi)\left(\ln\frac{a_f T^2}{\mu^2} - c_f\right)\right). \tag{4.2.2}$$

Note that all χ-dependent logarithms cancel between the one-loop and the finite-temperature contributions, yet the potential remains μ-dependent. In a classically scale-invariant theory, field-dependent masses m_b and m_f are proportional to the scalar field χ, so that we introduce the couplings g_b and g_f defined as

$$m_b(\chi) = g_b\chi\,, \quad m_f(\chi) = g_f\chi\,, \tag{4.2.3}$$

to obtain an explicit polynomial form of the effective potential in Eq. (4.2.2)

$$V_{\text{eff}}(\chi,T) = \left[\frac{\lambda}{4} + \frac{1}{64\pi^2}\left(\sum_b n_b g_b^4\left(\ln\frac{a_b T^2}{\mu^2} - c_b\right) - \sum_f n_f g_f^4\left(\ln\frac{a_f T^2}{\mu^2} - c_f\right)\right)\right]\chi^4 + \frac{T^2}{24}\left(\sum_b n_b g_b^2 + \frac{1}{2}\sum_f n_f g_f^2\right)\chi^2 - \frac{T}{12\pi}\left(\sum_b n_b g_b^3\right)\chi^3\,. \tag{4.2.4}$$

In contrast with the method introduced in Sec. 4.1, Eq. (4.2.4) shows explicitly that, in order to find a polynomial potential without field-independent terms, we do not approximate the one-loop effective potential as in Eq. (4.1.29) but we rely only on the high-temperature expansion, retaining terms up to logarithmic order rather than truncating at cubic order.

It is convenient to define collective couplings that depend only on the parameters of the model[33]

$$g_2^2 = \sum_b n_b g_b^2 + \frac{1}{2}\sum_f n_f g_f^2 \,, \quad g_3 = \sum_b n_b g_b^3 \,, \tag{4.2.5}$$

together with another collective coupling that depends on the renormalisation scale μ and on the temperature T

$$g_4(T,\mu) = -\left(\sum_b n_b g_b^4 \left(\ln\frac{a_b T^2}{\mu^2} - c_b\right) - \sum_f n_f g_f^4 \left(\ln\frac{a_f T^2}{\mu^2} - c_f\right)\right) \,, \tag{4.2.6}$$

which allows us to simplify the polynomial effective potential in Eq. (4.2.4) as

$$V_{\text{eff}}(\chi,T) = -\left(-\frac{\lambda}{4} + \frac{g_4(T,\mu)}{64\pi^2}\right)\chi^4 + \frac{g_2^2 T^2}{24}\chi^2 - \frac{g_3 T}{12\pi}\chi^3 \,. \tag{4.2.7}$$

Then, we extract the coefficients $m(T)$, $k(T)$ and $\lambda(T)$ to write Eq. (4.2.7) as Eq. (4.1.37)

$$m^2(T) = \frac{g_2^2 T^2}{12} \,, \quad k(T) = \frac{g_3 T}{4\pi} \,, \quad \lambda(T) = -\lambda + \frac{g_4(T,\mu)}{16\pi^2} \,. \tag{4.2.8}$$

We deal with the renormalisation scale μ as proposed in Sec. 4.1, by choosing the renormalisation scale $\mu = \tilde{\mu}$ such that the quartic coupling vanishes, i.e $\lambda(\tilde{\mu}) = 0$, so that $\lambda(T)$ in Eq. (4.2.8) and $g_4(T,\mu)$ in Eq. (4.2.6) becomes

$$\lambda(T) = \frac{g_4(T,\tilde{\mu})}{16\pi^2} \,, \quad g_4(T,\tilde{\mu}) = -\left(\sum_b n_b g_b^4 \left(\ln\frac{a_b T^2}{\tilde{\mu}^2} - c_b\right) - \sum_f n_f g_f^4 \left(\ln\frac{a_f T^2}{\tilde{\mu}^2} - c_f\right)\right) \,. \tag{4.2.9}$$

For later convenience, consider the μ-dependent terms of the effective potential in Eq. (4.2.1)

$$V_{\text{eff}}(\chi,T) \supset \frac{\lambda(\mu)}{4}\chi^4 - \frac{1}{64\pi^2}\left(2\sum_b n_b g_b^4 \chi^4 \ln\mu - 2\sum_f n_f g_f^4 \chi^4 \ln\mu\right) \,, \tag{4.2.10}$$

and apply the RGE in Eq. (4.1.8) for the effective potential

$$\mu\frac{dV_{\text{eff}}(\chi,T)}{d\mu} = \frac{\chi^4}{4}\left(\beta_{\lambda_\chi} - \frac{1}{16\pi^2}\left(2\sum_b n_b g_b^4 - 2\sum_f n_f g_f^4\right)\right) = 0 \,, \tag{4.2.11}$$

where we have used the definition of the beta function of the quartic coupling $\beta_{\lambda_\chi} = \mu\frac{d\lambda}{d\mu}$. Eq. (4.2.11) implies a relation between the beta function of the quartic coupling $\tilde{\beta}_{\lambda_\chi}$, at the renormalisation scale $\tilde{\mu}$ such that the quartic coupling vanishes, and the couplings g_b and g_f in Eq. (4.2.3)

$$\tilde{\beta}_{\lambda_\chi} = \frac{1}{16\pi^2}\left(2\sum_b n_b g_b^4 - 2\sum_f n_f g_f^4\right) \,. \tag{4.2.12}$$

[33] Note that these collective couplings are similar to the ones introduced in Sec. 4.1 in Eqs.(4.1.28) and (4.1.39), with a different notation: g has become g_2 and $\tilde{g}^3$ has become g_3.

Consider the zero temperature effective potential in Eq. (4.2.1) at the renormalisation scale $\tilde{\mu}$ where the quartic coupling vanishes

$$V_{\text{eff}}(\chi, T=0) = \frac{\chi^4}{64\pi^2}\left[\sum_b n_b g_b^4\left(\ln\frac{g_b^2\chi^2}{\tilde{\mu}^2} - c_b\right) - \sum_f n_f g_f^4\left(\ln\frac{g_f^2\chi^2}{\tilde{\mu}^2} - c_f\right)\right] , \tag{4.2.13}$$

and trade the renormalisation scale $\tilde{\mu}$ for the VEV of the scalar field χ_0, by imposing that χ_0 is a stationary point of the zero-temperature effective potential

$$\begin{aligned} 0 &= \frac{dV_{\text{eff}}(\chi, T=0)}{d\chi}\Big|_{\chi=\chi_0} \\ &= \frac{1}{16\pi^2}\left[\sum_b n_b g_b^4\left(\ln\frac{g_b^2\chi_0^2}{\tilde{\mu}^2} - c_b\right) - \sum_f n_f g_f^4\left(\ln\frac{g_f^2\chi_0^2}{\tilde{\mu}^2} - c_f\right)\right] \\ &\quad + \frac{1}{64\pi^2}\left(2\sum_b n_b g_b^4 - 2\sum_f n_f g_f^4\right) , \end{aligned} \tag{4.2.14}$$

Using the expression for the beta function in Eq. (4.2.12), we can rewrite the condition in Eq. (4.2.14) as

$$\frac{\tilde{\beta}_{\lambda_\chi}}{4} = -\frac{1}{16\pi^2}\left[\sum_b n_b g_b^4\left(\ln\frac{g_b^2\chi_0^2}{\tilde{\mu}^2} - c_b\right) - \sum_f n_f g_f^4\left(\ln\frac{g_f^2\chi_0^2}{\tilde{\mu}^2} - c_f\right)\right] . \tag{4.2.15}$$

Finally, substituting back the two expression of the beta function in Eqs. (4.2.12) and (4.2.15) into the effective potential at zero temperature in Eq. (4.2.13), we obtain

$$\begin{aligned} V_{\text{eff}}(\chi, T=0) &= \frac{\chi^4}{64\pi^2}\left[\sum_b n_b g_b^4\left(\ln\frac{g_b^2\chi^2}{\tilde{\mu}^2} - c_b\right) - \sum_f n_f g_f^4\left(\ln\frac{g_f^2\chi^2}{\tilde{\mu}^2} - c_f\right)\right] \\ &= \frac{\chi^4}{4}\Big(\frac{1}{16\pi^2}\left[\sum_b n_b g_b^4\left(\ln\frac{g_b^2\chi_0^2}{\tilde{\mu}^2} - c_b\right) - \sum_f n_f g_f^4\left(\ln\frac{g_f^2\chi_0^2}{\tilde{\mu}^2} - c_f\right)\right] \\ &\qquad + \frac{1}{16\pi^2}\left(2\sum_b n_b g_b^4 \ln\frac{\chi}{\chi_0} - 2\sum_f n_f g_f^4 \ln\frac{\chi}{\chi_0}\right)\Big) \\ &= \frac{\tilde{\beta}_{\lambda_\chi}}{4}\chi^4\left(\ln\frac{\chi}{\chi_0} - \frac{1}{4}\right) . \end{aligned} \tag{4.2.16}$$

Thus, the full effective potential reads

$$V_{\text{eff}}(\chi, T) = \frac{\tilde{\beta}}{4}\chi^4\left(\ln\frac{\chi}{\chi_0} - \frac{1}{4}\right) + \frac{T^4}{2\pi^2}\left(\sum_b n_b J_b\left(\frac{m_b^2(\chi)}{T^2}\right) - \sum_f n_f J_f\left(\frac{m_f^2(\chi)}{T^2}\right)\right) . \tag{4.2.17}$$

which is in agreement with the result in Sec. 4.1 in Eq. (4.1.18).

The quartic coefficient $\lambda(T)$ in Eq. (4.2.9) becomes

$$\lambda(T) = \frac{1}{32\pi^2}\left(\sum_b n_b g_b^4 \ln\frac{g_b^4\chi_0^4 e}{a_b^2 T^4} - \sum_f n_f g_f^4 \ln\frac{g_f^4\chi_0^4 e}{a_f^2 T^4}\right) = \frac{g_4(T)}{32\pi^2}\,. \tag{4.2.18}$$

where we have used the two expressions of the beta function in Eq. (4.2.12) and in Eq. (4.2.15) and we have obtained the expression for the collective coupling $g_4(T)$ in Eq. (4.2.6)

$$g_4(T) = \left(\sum_b n_b g_b^4 \ln\frac{g_b^4\chi_0^4 e}{a_b^2 T^4} - \sum_f n_f g_f^4 \ln\frac{g_f^4\chi_0^4 e}{a_f^2 T^4}\right)\,. \tag{4.2.19}$$

Furthermore, we extract the T-independent parts of this coefficient in Eq. (4.2.19) and define new collective couplings

$$g_4' = \sum_b n_b g_b^4 \ln\frac{g_b^4 e}{a_b^2} - \sum_f n_f g_f^4 \ln\frac{g_f^4 e}{a_f^2}\,, \quad g_4'' = 4\left(\sum_b n_b g_b^4 - \sum_f n_f g_f^4\right)\,, \tag{4.2.20}$$

so that the quartic coefficient $\lambda(T)$ in Eq. (4.2.18) can be written as

$$\lambda(T) = \frac{g_4(T)}{32\pi^2} = \frac{g_4' - g_4''\ln\frac{T}{\chi_0}}{32\pi^2}\,. \tag{4.2.21}$$

To summarise, for field values near the barrier, we can approximate the effective potential as a polynomial of the form of Eq. (4.1.37)

$$V(\chi,T) = \frac{m^2(T)}{2}\chi^2 - \frac{k(T)}{3}\chi^3 - \frac{\lambda(T)}{4}\chi^4\,, \tag{4.2.22}$$

with the coefficients given by Eqs. (4.2.8) and (4.2.21)

$$m^2(T) = \frac{T^2}{12}g_2^2\,, \quad k(T) = \frac{T}{4\pi}g_3\,, \quad \lambda(T) = \frac{g_4(T)}{32\pi^2} = \frac{g_4' - g_4''\ln\frac{T}{\chi_0}}{32\pi^2}\,, \tag{4.2.23}$$

in terms of the collective couplings in Eqs. (4.2.5), (4.2.19) and (4.2.20)

$$\begin{gathered} g_2^2 = \sum_b n_b g_b^2 + \frac{1}{2}\sum_f n_f g_f^2\,, \quad g_3 = \sum_b n_b g_b^3\,, \quad g_4(T) = \sum_b n_b g_b^4 \ln\frac{g_b^4\chi_0^4 e}{a_b^2 T^4} - \sum_f n_f g_f^4 \ln\frac{g_f^4\chi_0^4 e}{a_f^2 T^4}\,, \\ g_4' = \sum_b n_b g_b^4 \ln\frac{g_b^4 e}{a_b^2} - \sum_f n_f g_f^4 \ln\frac{g_f^4 e}{a_f^2}\,, \quad g_4'' = 4\left(\sum_b n_b g_b^4 - \sum_f n_f g_f^4\right)\,. \end{gathered} \tag{4.2.24}$$

It is convenient to compute the fit parameter $\tilde{\lambda}(T)$ for the analytic bounce action S_3 in terms of the collective couplings in Eq. (4.2.24), which from the definition in Eq. (4.1.50) reads

$$\tilde{\lambda}(T) = \frac{\lambda(T)m^2(T)}{k^2(T)} = \frac{g_2^2 g_4'}{24 g_3^2} - \frac{g_2^2 g_4''}{24 g_3^2}\ln\frac{T}{\chi_0} = l_1 - l_2\ln\frac{T}{\chi_0}\,, \tag{4.2.25}$$

which is a function of the temperature T and the collective couplings g_2, g_3, g_4' and g_4'', and we have defined the two coefficients

$$l_1 = \frac{g_2^2 g_4'}{24 g_3^2} \,, \quad l_2 = \frac{g_2^2 g_4''}{24 g_3^2} \,. \tag{4.2.26}$$

Note that the quadratic $m^2(T)$ and the cubic $k(T)$ coefficients are always positive, so the only one that can change sign is $\lambda(T)$. In terms of the collective couplings, this means that the quartic coupling $g_4(T)$ also changes sign, which happens when

$$g_4' - g_4'' \ln \frac{T}{\chi_0} > 0 \quad \Rightarrow \quad \begin{cases} T < \chi_0 e^{g_4'/g_4''} & \text{if } g_4' g_4'' > 0 \\ T > \chi_0 e^{g_4'/g_4''} & \text{otherwise} \end{cases} \,. \tag{4.2.27}$$

This condition sets which of the two expressions for the piecewise bounce action in Eq. (4.1.55) should be used.

4.2.2 Semi-analytic nucleation temperature

In the remainder of the section, equipped with the expressions for the effective potential in Eq. (4.2.22) and the bounce action in Eq. (4.1.55), we compute the thermal parameters necessary to describe the FOPT, using the false vacuum decay rate provided in Eq. (4.1.22)

$$\Gamma(T) \simeq T^4 \left(\frac{F(T)}{2\pi} \right)^{\frac{3}{2}} e^{-F(T)} \,, \tag{4.2.28}$$

where as in Eq. (4.1.55) we have defined

$$F(T) = \frac{S_3(T)}{T} \,. \tag{4.2.29}$$

We begin with the nucleation temperature T_n, given by the condition Eq. (3.3.19)

$$\Gamma(T_n) = H^4(T_n) \,, \tag{4.2.30}$$

which, after taking the logarithm on both sides and using the expression for the false vacuum decay rate in Eq. (4.2.28), becomes

$$F(T_n) + \frac{3}{2} \ln \frac{F(T_n)}{2\pi} = 4 \ln T_n - 4 \ln H(T_n) \,. \tag{4.2.31}$$

The Hubble parameter $H(T)$ can be expressed in terms of the energy density $\rho(T)$, by means of the Friedmann equation in Eq. (2.1.9) in a flat universe $k = 0$ as

$$H^2(T) = \frac{\rho(T)}{3 \bar{m}_{\text{pl}}^2} \,, \tag{4.2.32}$$

where $\bar{m}_{\text{pl}} = \sqrt{\frac{1}{8\pi G}}$ is the reduced Planck mass. The energy density $\rho(T)$ of the Universe at temperature T is the sum of the contributions from the thermal plasma, dominated by radiation, and from

the vacuum, which is given by the effective potential difference between the false and true vacuum

$$H^2(T) = \frac{\Delta V_{\text{eff}}}{3\bar{m}_{\text{pl}}^2} + \frac{\pi^2 g_*(T) T^4}{90\bar{m}_{\text{pl}}^2} \,. \tag{4.2.33}$$

Given that the vacuum contribution is independent of the temperature, while the radiation contribution is proportional to T^4, as the Universe cools and temperature decreases, there exists an equality temperature T_{v}, at which the Universe passes from a radiation-dominated to a vacuum-dominated phase. T_{v} can be computed by equating the two contributions

$$\Delta V_{\text{eff}} = \frac{\pi^2 g_*(T_{\text{v}}) T_{\text{v}}^4}{30} \quad \Rightarrow \quad T_{\text{v}} = \left(\frac{30 \Delta V_{\text{eff}}}{\pi^2 g_*(T_{\text{v}})} \right)^{\frac{1}{4}} \,. \tag{4.2.34}$$

In a supercooled FOPT, the relevant temperatures for the nucleation of bubbles are smaller than the equality temperature T_{v} [33], so we can neglect the radiation contribution and approximate the Hubble parameter in Eq. (4.2.33) as

$$H^2(T) \simeq \frac{\Delta V_{\text{eff}}}{3\bar{m}_{\text{pl}}^2} \,. \tag{4.2.35}$$

At these temperatures, the effective potential difference ΔV_{eff} is given by the zero-temperature contribution in Eq. (4.2.17)

$$\Delta V_{\text{eff}} = V_{\text{eff}}(0, T=0) - V_{\text{eff}}(\chi_0, T=0) = -V_{\text{eff}}(\chi_0, T=0) = \frac{\tilde{\beta}_{\lambda_\chi} \chi_0^4}{16} \,, \tag{4.2.36}$$

and the Hubble parameter in Eq. (4.2.35) becomes

$$H^2(T) \simeq \frac{\tilde{\beta}_{\lambda_\chi} \chi_0^4}{48\bar{m}_{\text{pl}}^2} \,. \tag{4.2.37}$$

Thus, the nucleation condition in Eq. (4.2.31) reads

$$F(T_n) + \frac{3}{2} \ln \frac{F(T_n)}{2\pi} = 4 \ln T_n - 4 \ln \frac{\sqrt{\tilde{\beta}_{\lambda_\chi}} \chi_0^2}{4\sqrt{3}\bar{m}_{\text{pl}}} \,. \tag{4.2.38}$$

4.2.3 Semi-analytic percolation temperature

The transition temperature that enters the SGWB spectrum is the temperature at which GW production occurs. For fast transitions, the nucleation temperature is a good approximation, which is not the case for supercooled FOPT, in which the nucleation temperature T_n and the percolation temperature T_p can be very different. Motivated by this, we study the percolation temperature T_p, which is defined by the condition in Eq. (3.3.20)

$$\mathcal{P}_f(T_p) = e^{-I(T_p)} \simeq 0.71 \,, \quad I(T_p) \simeq 0.34 \,, \tag{4.2.39}$$

where $\mathcal{P}_f(T)$ is the probability that a point in the Universe remains in the false vacuum and $I(T)$ is the fractional extended volume, introduced in Sec. 3.3.1 and given by Eq. (3.3.17)

$$I(T) = \frac{4\pi}{3}\int_T^{T_c} dT' \, \frac{\Gamma(T')}{T'^4 H(T')} \left(\int_T^{T'} \frac{dT''}{H(T'')} \right)^3 . \tag{4.2.40}$$

In writing the integral in Eq. (4.2.40), we assumed that the bubble wall velocity is $v_w \simeq 1$ and the bag relation $\frac{dT}{dt} = -TH(T)$ holds. To justify the latter, we consider the only non-vanishing contribution of the effective potential at the false vacuum $\chi = 0$

$$V_{\text{eff}}(\chi, T) \supset \frac{\pi^2 T^4}{90} \left(\sum_f \frac{7n_f}{8} - \sum_b n_b \right) , \tag{4.2.41}$$

compute its first and second derivatives

$$\frac{\partial V_{\text{eff}}(\chi,T)}{\partial T} = \frac{4\pi^2 T^3}{90} \left(\sum_f \frac{7n_f}{8} - \sum_b n_b \right) , \quad \frac{\partial^2 V_{\text{eff}}(\chi,T)}{\partial T^2} = \frac{12\pi^2 T^2}{90} \left(\sum_f \frac{7n_f}{8} - \sum_b n_b \right) , \tag{4.2.42}$$

and plug them into the most general expression for the Jacobian in Eq. (3.3.12)

$$\frac{dT}{dt} = -3H(T) \frac{V''(\chi,T)}{V'(\chi,T)}\Big|_{\chi=0} = -TH(T) , \tag{4.2.43}$$

which is the same as the bag model in Eq. (3.3.14).

We simplify the integral in Eq. (4.2.40) by splitting it into two parts: one for the radiation-dominated era and one for the vacuum-dominated era, separated by the equality temperature T_v in Eq. (4.2.34). For the he vacuum-dominated epoch, we approximate the Hubble parameter H to be constant as in Eq. (4.2.37), to obtain

$$\begin{aligned} I(T) &\simeq \frac{4\pi}{3}\int_{T_v}^{T_c} dT' \, \frac{\Gamma(T')}{T'^4 H(T')} \left(\int_T^{T'} \frac{dT''}{H(T'')} \right)^3 + \frac{4\pi}{3}\int_T^{T_v} dT' \, \frac{\Gamma(T')}{T'^4 H} \left(\int_T^{T'} \frac{dT''}{H} \right)^3 \\ &= \frac{4\pi}{3}\int_{T_v}^{T_c} dT' \, \frac{\Gamma(T')}{T'^4 H(T')} \left(\int_T^{T'} \frac{dT''}{H(T'')} \right)^3 + \frac{4\pi}{3}\frac{1}{H^4}\int_T^{T_v} dT' \, \frac{\Gamma(T')}{T'^4} (T'-T)^3 , \end{aligned} \tag{4.2.44}$$

where the inner integral in the second term has been evaluated. For supercooled FOPT, in radiation dominated era for $T' \in [T_v, T_c]$, the false-vacuum decay rate is sufficiently suppressed that the first integral in Eq. (4.2.44) can be neglected, so that

$$I(T) \simeq \frac{4\pi}{3}\frac{1}{H^4}\int_T^{T_v} dT' \, e^{-F(T')} \left(\frac{F(T')}{2\pi} \right)^{\frac{3}{2}} (T'-T)^3 , \tag{4.2.45}$$

where we have used the expression for the nucleation rate in Eq. (4.2.28) and $F(T)$ given in Eq. (4.2.29).

Note that the integral in Eq. (4.2.45) is dominated by the exponential factor $e^{-F(T')}$, except for the regions near $T' = T$, where the effects of the factor $(T'-T)^3$ start to become relevant. This

means that the prefactor $\left(\frac{F(T)}{2\pi}\right)^{\frac{3}{2}}$ is a subleading contribution, which only rescales the integral by a finite factor since it never vanishes, and can be taken outside the integral in Eq. (4.2.45), evaluated at $T' = T$

$$I(T) \simeq \frac{4\pi}{3}\frac{1}{H^4}\left(\frac{F(T)}{2\pi}\right)^{\frac{3}{2}} \int_T^{T_v} dT'\, e^{-F(T')}\,(T'-T)^3 \ . \tag{4.2.46}$$

Furthermore, at temperatures near T, the integrand is dominated by the factor $(T'-T)^3$, making it go to zero as $T' \to T$, while at temperatures near T_v, the integrand is dominated by the exponential factor $e^{-F(T')}$. This implies that in the intermediate region, there exists a temperature such that the integrand is peaked around it, which we denote as $T' = T_{\text{peak}}$. In other words, there is an intermediate temperature T_{peak} such that

- for $T < T_{\text{peak}}$, $(T'-T)^3$ dominates;
- for $T > T_{\text{peak}}$, $e^{-F(T')}$ dominates.

This is the typical situation where the saddle-point approximation applies , see footnote [25]. We rewrite the integrand of Eq. (4.2.46) as an exponential

$$e^{-F(T')}\,(T'-T)^3 = e^{-F(T')+3\ln(T'-T)} = e^{-G(T',T)} \ , \tag{4.2.47}$$

where we have defined the auxiliary function

$$G(T',T) = F(T') - 3\ln(T'-T) \ . \tag{4.2.48}$$

We then determine the temperature where the auxiliary function in Eq. (4.2.48) has a minimum by solving the stationary condition

$$\left.\frac{dG(T',T)}{dT'}\right|_{T'=T_{\text{peak}}} = F'(T_{\text{peak}}) - \frac{3}{T_{\text{peak}}-T} = 0 \quad \Rightarrow \quad F'(T_{\text{peak}}) = \frac{3}{T_{\text{peak}}-T} \ , \tag{4.2.49}$$

and we expand the auxiliary function G in Eq. (4.2.48) around its minimum $T' = T_{\text{peak}}$

$$G(T',T) \simeq G(T_{\text{peak}},T) + \frac{1}{2}G''(T_{\text{peak}},T)(T'-T_{\text{peak}})^2 \ , \tag{4.2.50}$$

so that the integral in Eq. (4.2.46) becomes a Gaussian integral

$$I(T) \simeq \frac{4\pi}{3}\frac{e^{-G(T_{\text{peak}},T)}}{H^4}\left(\frac{F(T)}{2\pi}\right)^{\frac{3}{2}} \int_T^{T_v} dT'\, e^{-\frac{1}{2}G''(T_{\text{peak}},T)(T'-T_{\text{peak}})^2} \ . \tag{4.2.51}$$

We make a change of variable $x = T' - T_{\text{peak}}$ in the integral in Eq. (4.2.51) to obtain

$$I(T) \simeq \frac{4\pi}{3}\frac{e^{-G(T_{\text{peak}},T)}}{H^4}\left(\frac{F(T)}{2\pi}\right)^{\frac{3}{2}} \int_{T-T_{\text{peak}}}^{T_v-T_{\text{peak}}} dx\, e^{-\frac{1}{2}G''(T_{\text{peak}},T)x^2} \ . \tag{4.2.52}$$

Since the integrand is sharply peaked around the temperature $T' = T_{\text{peak}}$, we extend the domain of

integration from $[T - T_{\text{peak}}, T_v - T_{\text{peak}}]$ to $[-\infty, \infty]$ and we integrate

$$I(T) \simeq \frac{4\pi}{3} \frac{e^{-G(T_{\text{peak}},T)}}{H^4} \left(\frac{F(T)}{2\pi}\right)^{\frac{3}{2}} \sqrt{\frac{2\pi}{G''(T_{\text{peak}},T)}} \,, \tag{4.2.53}$$

where we have used the Gaussian integral $\int_{-\infty}^{\infty} dx\, e^{-\frac{1}{2}ax^2} = \sqrt{\frac{2\pi}{a}}$. Finally, plugging the expression for the integral in Eq. (4.2.53) into the percolation condition in Eq. (4.2.39) yields

$$\frac{4\pi}{3H^4} e^{-G(T_{\text{peak}},T)} \left(\frac{F(T)}{2\pi}\right)^{\frac{3}{2}} \sqrt{\frac{2\pi}{G''(T_{\text{peak}},T)}} \simeq 0.34 \,, \tag{4.2.54}$$

which after taking the logarithm on both sides gives

$$\ln \frac{2}{3H^4} - G(T_{\text{peak}},T) + \frac{3}{2} \ln F(T) - \frac{1}{2} \ln G''(T_{\text{peak}},T) \simeq \ln 0.34 \,. \tag{4.2.55}$$

Substituting back the definition of the auxiliary function G in Eq. (4.2.48)

$$\ln \frac{2}{3H^4} - F(T_{\text{peak}}) + 3\ln(T_{\text{peak}} - T) + \frac{3}{2} \ln F(T) - \frac{1}{2} \ln \left(F''(T_{\text{peak}}) + \frac{3}{(T_{\text{peak}} - T)^2}\right) \simeq \ln 0.34 \,. \tag{4.2.56}$$

Using the Gaussian approximation, we have traded the computation of the original double integral in Eq. (4.2.40) for the search of the root of an equation and T_{peak}. Therefore, the computation of the percolation temperature is much simplified: you compute the peak temperature T_{peak} using the condition in Eq. (4.2.49) and then you solve Eq. (4.2.56), which depends only on the derivatives of $F(T)$ with no integral involved.

For fast transitions and less supercooling, we can simplify further the expression for the integral in Eq. (4.2.56). In this case, the relevant temperatures will be close to the lower bound T of the integral in Eq. (4.2.46) and we can approximate it by expanding the function $F(T')$ as a linear function of T' around T

$$F(T') \simeq F(T) + F'(T)(T' - T) \,, \tag{4.2.57}$$

so that the integral in Eq. (4.2.46) becomes

$$I(T) \simeq \frac{4\pi}{3} \frac{e^{-F(T)}}{H^4} \left(\frac{F(T)}{2\pi}\right)^{\frac{3}{2}} \int_T^{T_v} dT'\, e^{-F'(T)(T'-T)} \left(T' - T\right)^3 \,. \tag{4.2.58}$$

We make a change of variable $x = T' - T$ in the integral in Eq. (4.2.58) to find

$$I(T) \simeq \frac{4\pi}{3} \frac{e^{-F(T)}}{H^4} \left(\frac{F(T)}{2\pi}\right)^{\frac{3}{2}} \int_0^{T_v - T} dx\, e^{-F'(T)x} x^3 \,, \tag{4.2.59}$$

and we extend the domain of integration to $[0, \infty]$ since the integrand is exponentially suppressed for large x. We compute the integral using the Feynman technique

$$\int_0^{\infty} dx\, e^{-bx} x^3 = -\frac{\partial^3}{\partial b^3} \int_0^{\infty} dx\, e^{-bx} = \frac{\partial^3}{\partial b^3} \frac{e^{-bx}}{b}\Big|_0^{\infty} = -\frac{\partial^3}{\partial b^3} \frac{1}{b} = \frac{6}{b^4} \,, \tag{4.2.60}$$

to obtain the final expression for the integral in Eq. (4.2.59) after recognising $b = F'(T)$ in Eq. (4.2.60)

$$I(T) \simeq \frac{4\pi}{3} \frac{6e^{-F(T)}}{H^4 F'(T)^4} \left(\frac{F(T)}{2\pi} \right)^{\frac{3}{2}} . \tag{4.2.61}$$

Finally, plugging the expression for the integral in Eq. (4.2.61) into the percolation condition in Eq. (4.2.39) yields

$$\frac{8\pi}{H^4} \frac{e^{-F(T)}}{F'(T)^4} \left(\frac{F(T)}{2\pi} \right)^{\frac{3}{2}} \simeq 0.34 , \tag{4.2.62}$$

which after taking the logarithm on both sides gives

$$\ln \frac{8\pi}{H^4} - F(T) + \frac{3}{2} \ln \frac{F(T)}{2\pi} - 4 \ln F'(T) \simeq \ln 0.34 . \tag{4.2.63}$$

The linear approximation in Eq. (4.2.63) is simpler than the Gaussian one in Eq. (4.2.56), since there is no need to compute any intermediate peak temperature T_{peak} in Eq. (4.2.49). However, its use is more restricted, because the assumption of linear expansion in Eq. (4.2.57) is satisfied only for less supercooled PTs

In any case, the only quantities that enter in both approximations of the percolation condition are the bounce action $F(T)$ and its second derivative $F''(T)$ or first derivative $F'(T)$ with respect to temperature. Their expression can be computed analytically from the fit bounce action in Eq. (4.1.55).

As shown in Sec. 3.3.2, for the PT to complete without being prevented by the expansion of the Universe, Eq. (3.3.23) needs to be satisfied at the percolation temperature T_p

$$T \frac{dI(T)}{dT} < -3 , \tag{4.2.64}$$

where we have assumed a constant Hubble parameter H. For the Gaussian approximation of the integral $I(T)$ given by Eq. (4.2.53), Eq. (4.2.64) reads

$$I(T) T \left(-G'(T_{\text{peak}}, T) + \frac{3}{2} \frac{F'(T)}{F(T)} - \frac{1}{2} \frac{G'''(T_{\text{peak}}, T)}{G''(T_{\text{peak}}, T)} \right) < -3 , \tag{4.2.65}$$

whereas for the linear approximation of the integral $I(T)$ given by Eq. (4.2.61), the condition becomes

$$I(T) T \left(-F'(T) + \frac{3}{2} \frac{F'(T)}{F(T)} - \frac{4}{F'(T)} \right) < -3 . \tag{4.2.66}$$

4.2.4 Analytic thermal parameters

The final step in order to obtain the SGWB spectrum is to compute the transition strength α and the inverse duration β, since the bubble wall velocity is set to $v_w \simeq 1$, as the runaway condition $\alpha > \alpha_\infty$ in Eq. (3.3.47) is expected to be satisfied.

The general expression for the transition strength α is given by Eq. (3.3.34)

$$\alpha = \frac{1}{\rho_{\text{rad}}} \Delta \left(\bar{V}_{\text{eff}} - \frac{T}{4} \frac{d\bar{V}_{\text{eff}}}{dT} \right) \Big|_{T_p} , \tag{4.2.67}$$

where Δ means the difference between the effective potential at the false vacuum $\chi = 0$ and the true vacuum $\chi = \langle \chi \rangle$ at the percolation temperature T_p. However, for supercooled FOPT, the derivative with respect to the temperature T of the effective potential is small, so we approximate the transition strength by

$$\alpha = \frac{\Delta V_{\text{eff}}}{\rho_{\text{rad}}} \Big|_{T_p} . \tag{4.2.68}$$

Furthermore, using the expression for the effective potential difference in Eq. (4.2.36) given by the zero-temperature one-loop contributions, we rewrite the transition strength in Eq. (4.2.68) as

$$\alpha = \frac{30 \tilde{\beta}_{\lambda_\chi} \chi_0^4}{16 \pi^2 g_*(T_p) T_p^4} , \tag{4.2.69}$$

where we have substituted the expression for the radiation energy density in Eq. (2.1.33). The transition is expected to be strong, meaning $\alpha \gg 1$ and a negligible contribution to the SGWB spectrum, since it enters with the ratio $\frac{\alpha}{\alpha+1}$ as discussed in Sec. 3.4.2.

Therefore, the only relevant thermal parameter is the inverse transition duration β, which is defined in Eq. (3.3.41) as

$$\frac{\beta}{H_*} = -\frac{T}{\Gamma} \frac{d\Gamma}{dT} \Big|_{T_p} , \tag{4.2.70}$$

and can be rewritten using the false vacuum decay rate in Eq. (4.2.28) as

$$\frac{\beta}{H_*} = T \frac{dF(T)}{dT} - \frac{3}{2} T \frac{d}{dT} \ln F(T) - 4 \Big|_{T=T_p} . \tag{4.2.71}$$

Finally, the SGWB spectrum is given by the sum of the three contributions: bubble collisions, sound waves, and turbulence

$$h^2 \Omega_{\text{tot}}(f) \simeq h^2 \Omega_{\text{bubble}}(f) + h^2 \Omega_{\text{sound}}(f) + h^2 \Omega_{\text{turb}}(f) . \tag{4.2.72}$$

The explicit expressions for each term are discussed in Sec. 3.4.2.

4.3 Dark $U(1)_D$ models

The most relevant results of Sec. 4.2 are the revisited model-independent approach to write the effective potential as a polynomial in Eq. (4.2.22) with coefficients in Eq. (4.2.23), built upon the previous results of Sec. 4.1, and the semi-analytic method to compute the percolation temperature T_p, both in the linear approximation in Eq. (4.2.63) and in the Gaussian one in Eq. (4.2.56). The latter has not appeared previously in the literature.

In this section, we apply both the established framework of Sec. 4.1 and the revisited one of Sec.

4.2 to phenomenological dark $U(1)$ extensions of the SM that can explain the PTA signal. We first consider a minimal model containing a dark scalar and a dark photon: the dark scalar drives the PT, while the dark photon is required to make it first order. We compare the effective potential V_{eff}, the bounce action S_3, and the nucleation temperature T_n obtained with the established and revisited approaches to the results of a full numerical analysis, where the effective potential is computed from its exact non-approximated expression and the bounce action is evaluated using `CosmoTransitions` [190]. Next, focusing on the revisited approach, we study the percolation temperature T_p, the transition strength α, and the inverse duration β, and we validate our framework by showing the posterior distributions over the NANOGrav 15-year dataset. We draw physical insights about how the parameters of the model influence the PT. Finally, we extend the model by adding a dark fermion and analyze the effect of its Yukawa coupling.

4.3.1 Minimal $U(1)_D$ model

Consider an extension of the Standard Model gauge group by a dark abelian $U(1)_D$ and extend the particle content with the associated gauge vector boson, referred to as the dark photon A'_μ, and a dark scalar S, with a classically scale-invariant potential. The Lagrangian is given by

$$\mathcal{L} = \mathcal{L}_{SM} - \frac{1}{4}F'_{\mu\nu}F'^{\mu\nu} + (D_\mu S)^\dagger D^\mu S - \lambda_\chi |S|^4 \,, \tag{4.3.1}$$

where the covariant derivative is

$$D_\mu = D_\mu^{SM} + i g'_1 Q' A'_\mu \,. \tag{4.3.2}$$

The new fields are taken such that they are singlets of the SM gauge group. For simplicity, we assume that $Q' = 1$. This model was studied in Sec. 2.4.1, in which, after diagonalisation of the kinetic mixing between the dark photon and the SM one, we found that the field-dependent dark photon mass is given by Eq. (2.4.14)

$$m^2_{A'}(\chi) \simeq {g'_1}^2 \chi^2 \,. \tag{4.3.3}$$

We identify χ with the magnitude of the real component of the dark scalar, $\chi = \sqrt{2}|S|$, which is the flat direction for RSB. The one-loop β function for the quartic self-interaction coupling of χ is computed using `pyr@te` [228, 229]

$$(16\pi^2)\beta_{\lambda_\chi} = 20\lambda_\chi^2 + 6{g'_1}^4 - 12{g'_1}^2\lambda_\chi \,, \tag{4.3.4}$$

which, evaluated at the energy scale $\tilde{\mu}$ in which the quartic coupling vanishes $\lambda_\chi = 0$, becomes

$$(16\pi^2)\tilde{\beta}_{\lambda_\chi} = 6{g'_1}^4 \,. \tag{4.3.5}$$

Note that Eq. (4.3.5) is in agreement with the expression for the one-loop beta function for the quartic self-interaction coupling of the scalar field χ found in Eq. (4.2.12). Therefore, the field-dependent masses of the DS particles read

$$m^2_A(\chi) = {g'_1}^2\chi^2 \,, \quad m^2_S(\chi) = \tilde{\beta}_{\lambda_\chi}\chi^2 = \frac{6g'^4_1}{16\pi^2}\chi^2 \,. \tag{4.3.6}$$

This model has been studied using the established approach in Ref. [61]. It relies on the quadratic

collective coupling in Eq. (4.1.28) and the cubic collective coupling in Eq. (4.1.39)

$$g^2 = 3{g'_1}^2 \,, \quad \tilde{g}^3 = 3{g'_1}^3 \,, \tag{4.3.7}$$

which are used to write the coefficients of the polynomial effective potential in Eq. (4.1.37) by means of Eq. (4.1.38) and Eq. (4.1.27)

$$m^2(T) = \frac{g^2T^2}{12} = \frac{{g'_1}^2T^2}{4} \,, \quad k(T) = \frac{\tilde{g}^3T}{4\pi} = \frac{3{g'_1}^3T}{4\pi} \,, \quad \lambda(T) = \tilde{\beta}_{\lambda_\chi} \ln \frac{\chi_0}{T} \,. \tag{4.3.8}$$

On the other hand, the revisited approach we propose here relies on the square, cubic and quartic collective couplings in Eq. (4.2.24)

$$g_2^2 = 3{g'_1}^2 \,, \quad g_3 = 3{g'_1}^3 \,, \quad g_4(T) = 3{g'_1}^4 \ln \frac{{g'_1}^4\chi_0^4 e}{a_b^2T^4} \,, \tag{4.3.9}$$

which are used to write the coefficients of the polynomial effective potential in Eq. (4.2.22) by means of Eq. (4.2.23)

$$m^2(T) = \frac{g_2^2T^2}{12} = \frac{{g'_1}^2T^2}{4} \,, \quad k(T) = \frac{g_3T}{4\pi} = \frac{3{g'_1}^3T}{4\pi} \,, \quad \lambda(T) = \frac{g_4(T)}{32\pi^2} = \frac{3{g'_1}^4}{32\pi^2} \ln \frac{{g'_1}^4\chi_0^4 e}{a_b^2T^4} \,. \tag{4.3.10}$$

Note that the square and cubic coefficients in Eq. (4.3.9) are the same as in the established one in Eq. (4.3.7), while the quartic collective couplings in Eqs. (4.3.8) and (4.3.10) are different.

Effective potential. In Sec. 4.1, we argued that the relevant field values of the effective potential to compute the bounce action are those near the barrier. Therefore, a first qualitative analysis can be performed by tracking the behaviour of the approximations of the effective potential for field values near the barrier, which we parametrised by the barrier width χ_b defined in Eq. (4.1.25). We compare the full effective potential in Eq. (4.2.17)

$$V_{\text{full}}(\chi, T) = \frac{\tilde{\beta}}{4}\chi^4 \left(\ln \frac{\chi}{\chi_0} - \frac{1}{4} \right) + 3\frac{T^4}{2\pi^2} J_B \left(\frac{{g'_1}^2\chi^2}{T^2} \right) \,, \tag{4.3.11}$$

where the thermal function is given by Eq. (4.1.19), against its approximations: the established polynomial potential in Eq. (4.1.37) with coefficients in Eq. (4.3.8)

$$V_{\text{Established}}(\chi, T) = \frac{{g'_1}^2T^2}{8}\chi^2 - \frac{{g'_1}^3T}{4\pi}\chi^3 - \frac{\tilde{\beta}_{\lambda_\chi}}{4} \ln \frac{\chi_0}{T}\chi^4 \,, \tag{4.3.12}$$

and the revisited polynomial potential in Eq. (4.2.22) with coefficients in Eq. (4.3.9)

$$V_{\text{Revisited}}(\chi, T) = \frac{{g'_1}^2T^2}{8}\chi^2 - \frac{{g'_1}^3T}{4\pi}\chi^3 - \frac{3{g'_1}^4}{128\pi^2} \ln \frac{{g'_1}^4\chi_0^4 e}{a_b^2T^4}\chi^4 \,. \tag{4.3.13}$$

We take the nucleation temperature T_n as a reference, computed numerically with the full potential (4.3.11) using `CosmoTransitions`, and the same gauge couplings g'_1 present in Fig. 1 of [61], which are $g = 0.81, 0.9$ or equivalently $g'_1 = 0.47, 0.52$, fixing the VEV to $\chi_0 = 1$ GeV.

The plot of the three potentials in Eqs. (4.3.11), (4.3.12) and (4.3.9) at field values $\chi \in [0, \chi_b]$ in Fig.

9 shows a slight disagreement for the established approach (green), while the revisited one (orange) is in very good agreement, when compared to the full potential (blue). In fact, not only the barrier width χ_b is poorly reproduced, but also the height of the barrier has a similar misbehaviour for the established approach. Instead, these arguments do not hold for the revisited one, suggesting that the revisited model-independent framework is better suited to describe the effective potential.

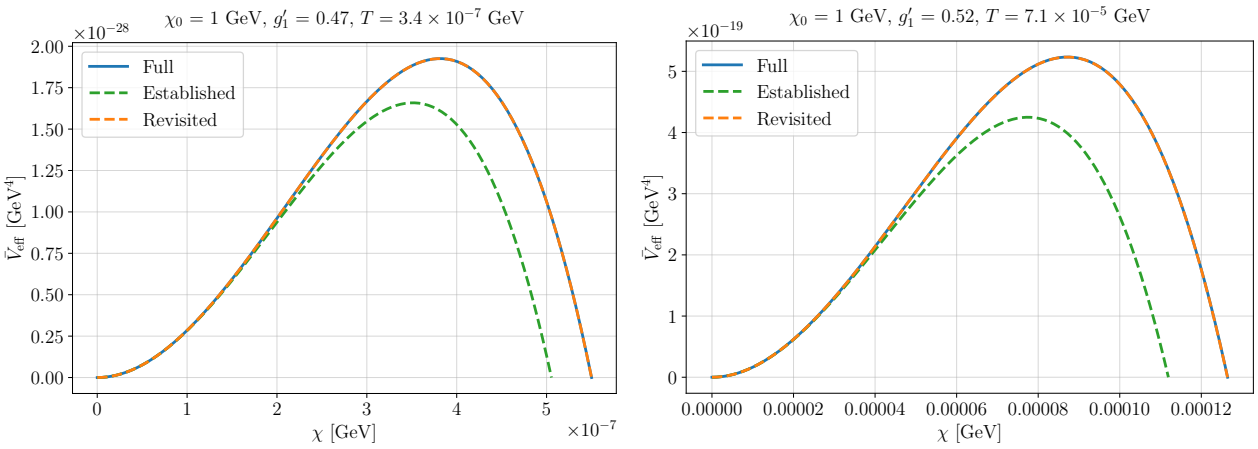

Figure 9: The effective potential for the established, revisited and full approaches, at small field values $\chi \in [0, \chi_b]$.

To understand from where this discrepancy comes from, we investigate the different contributions to the effective potential by separating the one-loop and the finite-temperature parts. Regarding the former, we compare the one-loop potential computed using the approximation in Eq. (4.1.29) against the full χ-dependent logarithmic one in Eq. (4.1.14)

$$V_{\text{one-loop}}(\chi, T) = \frac{\tilde{\beta}_{\lambda_\chi}}{4}\chi^4\left(\ln\frac{\chi}{\chi_0} - \frac{1}{4}\right), \quad V^{\text{approx}}_{\text{one-loop}}(\chi, T) = \frac{\tilde{\beta}_{\lambda_\chi}}{4}\chi^4 \ln\frac{T}{\chi_0}. \tag{4.3.14}$$

To scrutinize the finite-temperature part, we compare the full thermal potential in Eq. (4.3.11)

$$V_{1\text{T}}(\chi, T) = 3\frac{T^4}{2\pi^2} J_B\left(\frac{g_1'^2\chi^2}{T^2}\right), \tag{4.3.15}$$

against the LO, NLO and NNLO approximations of the high-temperature expansion in Eq. (4.1.19) valid for small field values, i.e. up to quadratic, cubic and logarithmic terms, respectively

$$V^{\text{quadratic}}_{1\text{T}}(\chi, T) = 3\frac{T^4}{2\pi^2}\left(\frac{\pi^2}{12}\frac{g_1'^2\chi^2}{T^2}\right), \quad V^{\text{cubic}}_{1\text{T}}(\chi, T) = 3\frac{T^4}{2\pi^2}\left(\frac{\pi^2}{12}\frac{g_1'^2\chi^2}{T^2} - \frac{\pi}{6}\left(\frac{g_1'^2\chi^2}{T^2}\right)^{3/2}\right),$$
$$V^{\text{log}}_{1\text{T}}(\chi, T) = 3\frac{T^4}{2\pi^2}\left(\frac{\pi^2}{12}\frac{g_1'^2\chi^2}{T^2} - \frac{\pi}{6}\left(\frac{g_1'^2\chi^2}{T^2}\right)^{3/2} - \frac{1}{32}\left(\frac{g_1'^2\chi^2}{T^2}\right)^2 \ln\left(\frac{g_1'^2\chi^2}{a_b T^2}\right)\right). \tag{4.3.16}$$

In order to compute the bounce action in Eq. (4.1.23), one needs to integrate the effective potential over the field values $\chi \in [0, \chi_e]$, where χ_e is the escape field value where the field tunnels, i.e. the initial condition of the bounce differential equation in Eq. (3.2.29), which is typically larger than the barrier width χ_b. Therefore, a better range to plot the effective potential is $\chi \in [0, \chi_e]$ rather

than $\chi \in [0, \chi_b]$. We take again the nucleation temperature T_n as a reference and the parameters fixed to $(\chi_0, g_1') = (1\ \text{GeV}, 0.47)$, where the largest supercooling is expected. The left plot of Fig. 10 shows that the approximated one-loop potential (red) starts to deviate from the full χ-dependent logarithmic one (blue). The right plot of Fig. 10 is of more interest. It shows that the LO quadratic (red) and NLO cubic (orange) do not capture the shape of the thermal integral (blue), while the NNLO logarithmic approximation (green) does so with great accuracy, even near the escape field value χ_e. Consequently, we argue that the mismatch between the established approach and the full numerical potential in Fig. 9 is due to the fact that the approximated one-loop contribution in Eq. (4.1.29) is slightly inaccurate, but mostly the thermal part up to cubic terms underestimates its numerical counterpart. Conversely, the revisited model-independent framework is able to accomplish this task, since the one-loop contribution is not approximated and the thermal part is well approximated up to logarithmic terms.

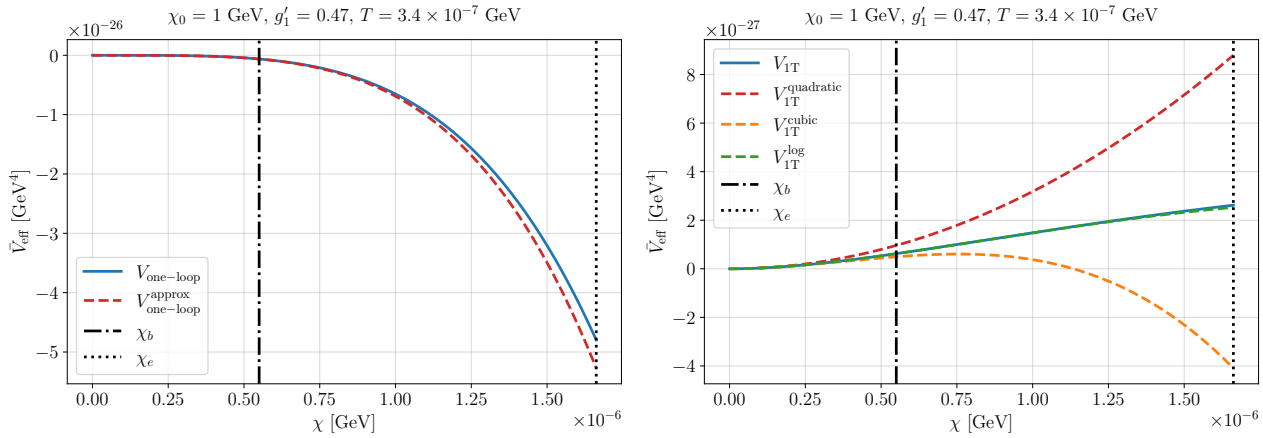

Figure 10: The different approximations for the one-loop (left) and the thermal (right) effective potentials, at small field values $\chi \in [0, \chi_e]$.

Nucleation temperature. To make our analysis quantitative, we compute the value of the barrier width χ_b and the bounce action S_3, keeping in mind that the former reflects the pure behaviour of the effective potential, while the latter introduces another source of error, because we compute the full effective potential with the shooting method in `CosmoTransitions`, whereas for the established and revisited approaches we use the fit action in Eq. (4.1.55). The results in Fig. 11 reveal that an error in the barrier width χ_b translates into a larger error in the bounce action S_3 for the established approach, while the revisited one shows only a small deviation. Both quantities are evaluated again at the nucleation temperature T_n computed with the full potential in Eq. (4.3.11) using `CosmoTransitions`, and plotted as a function of the gauge coupling g_1' in the range of values $g_1' \in [0.47, 0.52]$. The VEV is fixed at $\chi_0 = 1$.

A small error in the bounce action S_3 translates into a larger error in the nucleation temperature T_n, since it enters exponentially in the false vacuum decay rate in Eq. (4.2.28). Computing the nucleation temperature T_n using the nucleation condition in Eq. (4.2.38), we find that the established approach differs by orders of magnitude from the full numerical result, while the revisited one is in very good agreement with it. This is shown in the left plot of Fig. 12, where the nucleation temperature T_n is plotted as a function of the gauge coupling g_1' at fixed VEV $\chi_0 = 1$. In the right plot of Fig. 12, we reproduce the lower plot in Fig. 2 of Ref. [61], proving that the established approach fails

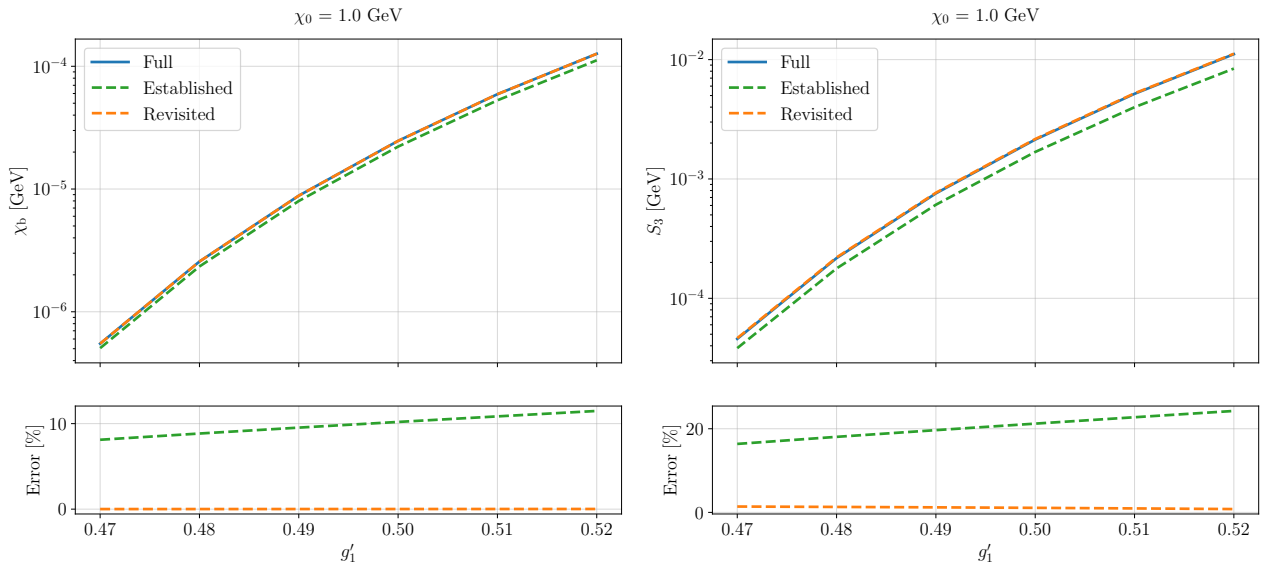

Figure 11: The barrier width χ_b (left) and the bounce action S_3 (right) as a function of the gauge coupling g_1' for the established, revisited and full approaches. In the bottom panel, the percent relative errors are shown with respect to the full one.

to reproduce the nucleation temperature T_n, while the revisited one manages to do so with great accuracy.

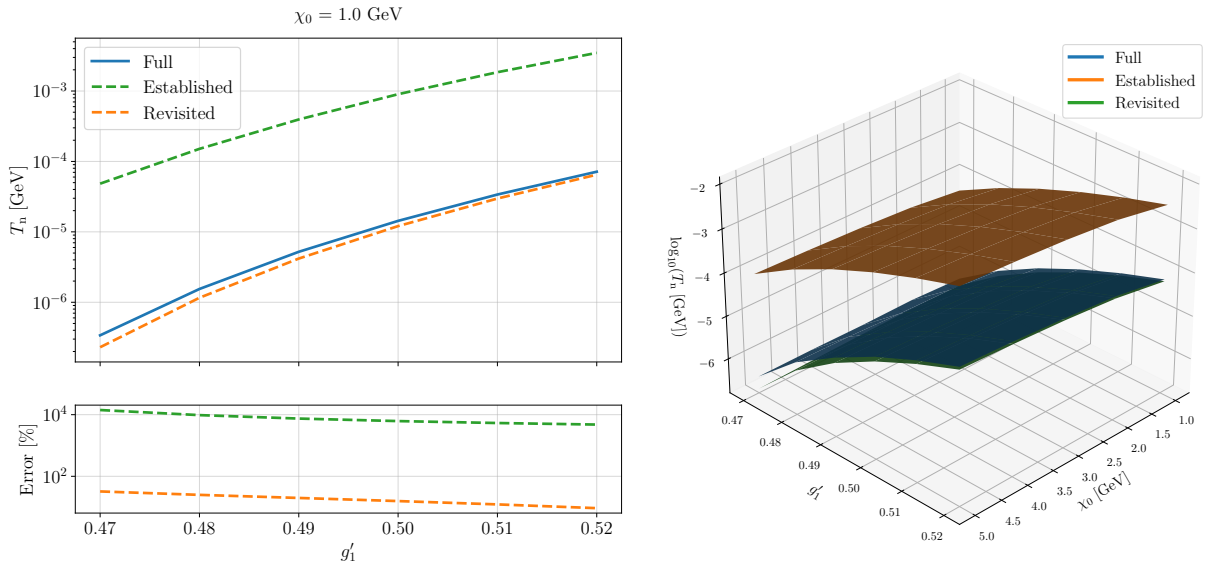

Figure 12: The nucleation temperature T_n as a function of the gauge coupling g_1' at fixed (left) and as a function (right) of the VEV χ_0, for the established, revisited and full approaches. In the bottom left panel, the percent relative errors are shown with respect to the full one.

Therefore, we conclude that, in order to obtain reliable results within a reasonable percent-level error, one needs to trace the effective potential at field values near the barrier χ_b and the escape field value χ_e. However, as mentioned before, another source of error can be inherent to the fit action, so we check that indeed there is an intrinsic few percent error in the bounce action in Eq. (4.1.55) compared to the one computed using `CosmoTransitions` for the same polynomial effective potential in

Eq. (4.2.22). The results in the left plot of Fig. 13 show that there is an oscillatory behaviour in the error, which remains at the few-percent level but must always be taken into account when using the fit action in Eq. (4.1.55) to compute the bounce action S_3. We also compute the quantity $\tilde{\lambda}$, defined in Eq. (4.1.50), which is the fit parameter used in Ref. [58] to compute the fit action in Eq. (4.1.55), in the right plot of Fig. 13 to illustrate the correlation between the error from using the fit action and the value of $\tilde{\lambda}$. Note that $\tilde{\lambda}$ changes sign at gauge coupling values $g_1' \simeq 0.8$, so for fast transitions with small supercooling, T_n always lies in the region $\tilde{\lambda}(T_n) < 0$ and does not cross zero.

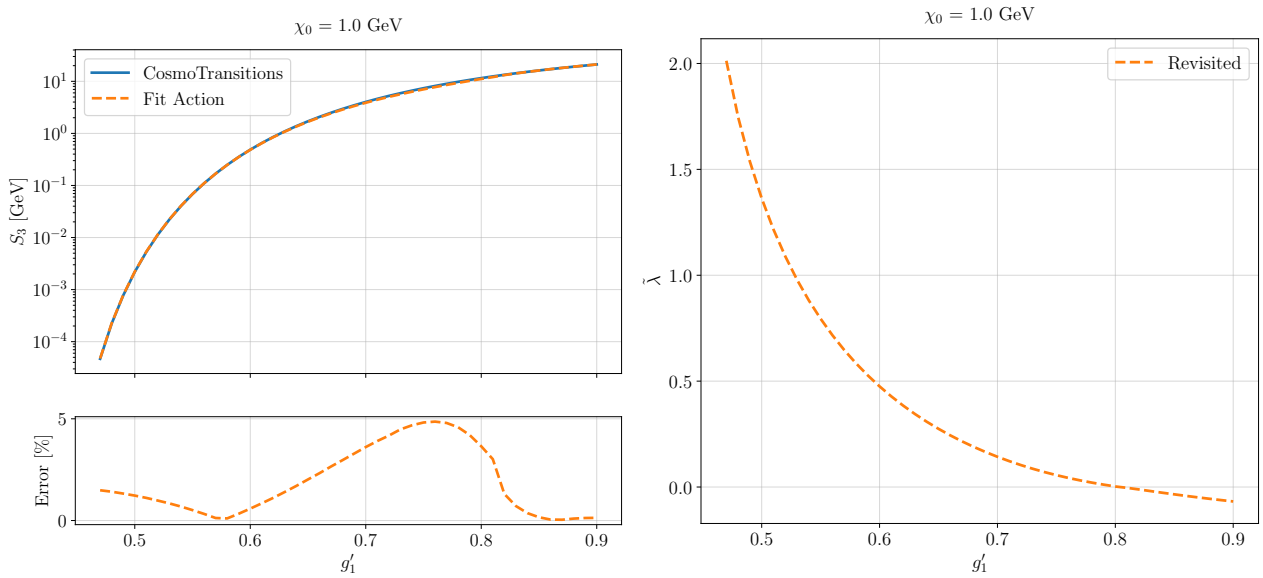

Figure 13: The bounce action S_3 (left) computed using `CosmoTransitions` and the fit action, and the fit parameter $\tilde{\lambda}$ (right), for the revisited approach, as a function of the gauge coupling g_1'. In the bottom left panel, the percent relative errors are shown with respect to the numerical one.

Percolation temperature. The established framework in Refs. [58–61] uses the nucleation temperature T_n and does not provide any semi-analytic method to compute the percolation temperature T_p, which is better suited for supercooled FOPT as it is the moment when GWs production is expected. On the other hand, the revisited framework provides a simple equation to evaluate the percolation temperature T_p. Therefore, we continue our analysis by considering only the revisited framework. Since it does not rely on large supercooling approximations, we extend the range of the gauge coupling to $g_1' \in [0.47, 0.9]$. First, to validate the accuracy of the implemented methods and neglect the error that comes from using the fit action rather than the numerical shooting method, we compare the percolation temperature T_p computed using the linear method in Eq. (4.2.56) and the Gaussian method in Eq. (4.2.63) against the one computed using the full integral in Eq. (4.2.45), always using the fit bounce action (4.1.55). The results in the left plot of Fig. 14 show that both methods are able to compute the percolation temperature T_p with percent-level accuracy, which means that both methods are accurate enough to substitute the full integral in Eq. (4.2.45). However, for large supercooling, the Gaussian method is more accurate than the linear one, as expected, since the latter is more appropriate for fast transitions. In the following, we will use the Gaussian method in Eq. (4.2.56) to compute the percolation temperature T_p, which is compared in the right plot of Fig. 14 against the one computed using the full integral in Eq. (4.2.45) with the numerical action computed

using `CosmoTransitions`. This tcaptures both sources of error coming from the use of the fit action in Eq. (4.1.55) and the Gaussian method in Eq. (4.2.63). Putting it all together, we conclude that the main source of error in computing the percolation temperature T_p is given by the fit action, with only few percent to be attributed to the Gaussian approximation.

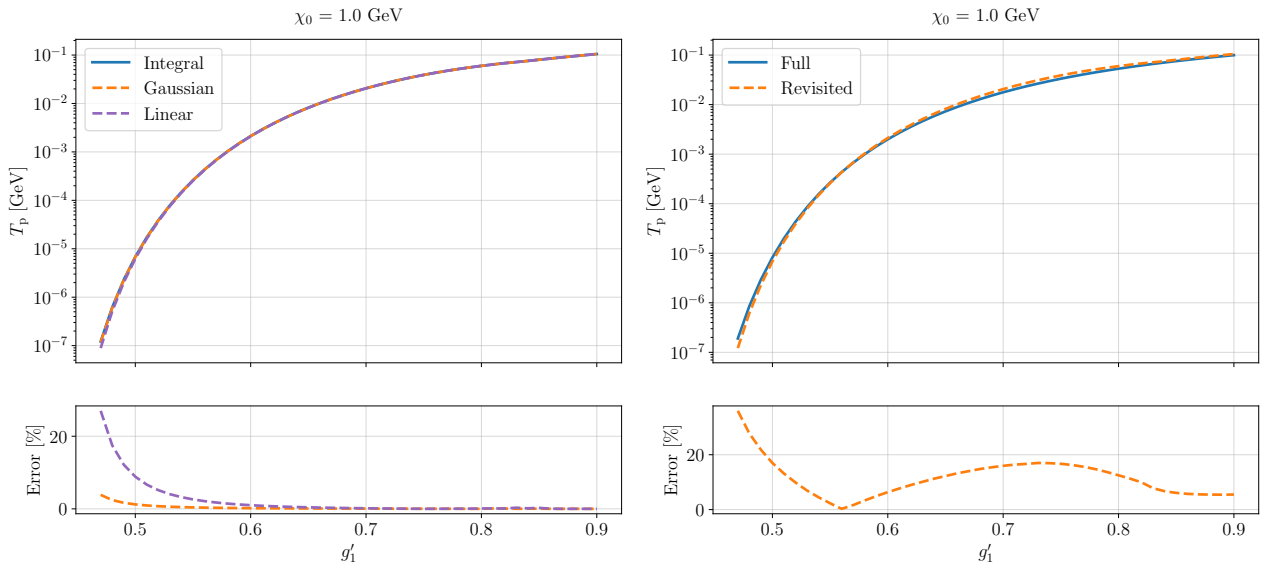

Figure 14: The percolation temperature T_p as a function of the gauge coupling g_1', for the integral, Gaussian or integral methods (left) or for the revisited and full approaches (right). In the bottom panel, the percent relative errors are shown with respect to the integral method (left) or the full one (right).

In the left plot of Fig. 15, we compare the percolation temperature T_p and the nucleation temperature T_n, computed with the full numerical method, to highlight their difference. Furthermore, the ratio $\frac{T_n}{T_p}$ shown in the right plot of Fig. 15 confirms that our efforts to develop a semi-analytic method to obtain the percolation temperature T_p are justified.

Thermal parameters. Equipped with the percolation temperature T_p, we compute the thermal parameters that describe the PT, i.e. the transition strength α and the inverse transition duration β/H, using the expressions in Eqs. (4.2.69) and (4.2.71), respectively. The results in the left plot of Fig. 16 show that the transition strength α is large, $\alpha \gg 1$, which means that the PT is strong, even when the error in the revisited approach is significant. This implies that we can safely neglect the contribution to α in the computation of the SGWB spectrum. The large errors at small gauge couplings arise from the fourth power of the percolation temperature, which enters the denominator in the definition of α. On the other hand, the inverse transition duration β/H in the right plot of Fig. 16 shows good agreement, except for the region in which the fit parameter $\tilde{\lambda}$ changes sign, as shown in the right plot of Fig. 13. The bump at gauge coupling near $g_1' \simeq 0.8$ can be explained by the fact that in the computation of the inverse transition duration β/H, the first derivative of the bounce action is present. Thus, the fit action in Eq. (4.1.55) is continuous at $\tilde{\lambda} = 0$, but its derivative is not sufficiently smooth.

SGWB spectrum. We validate the revisited approach by computing the Bayesian posterior distribution over the NANOGrav 15-years dataset using the package `PTArcade` [230]. The results in

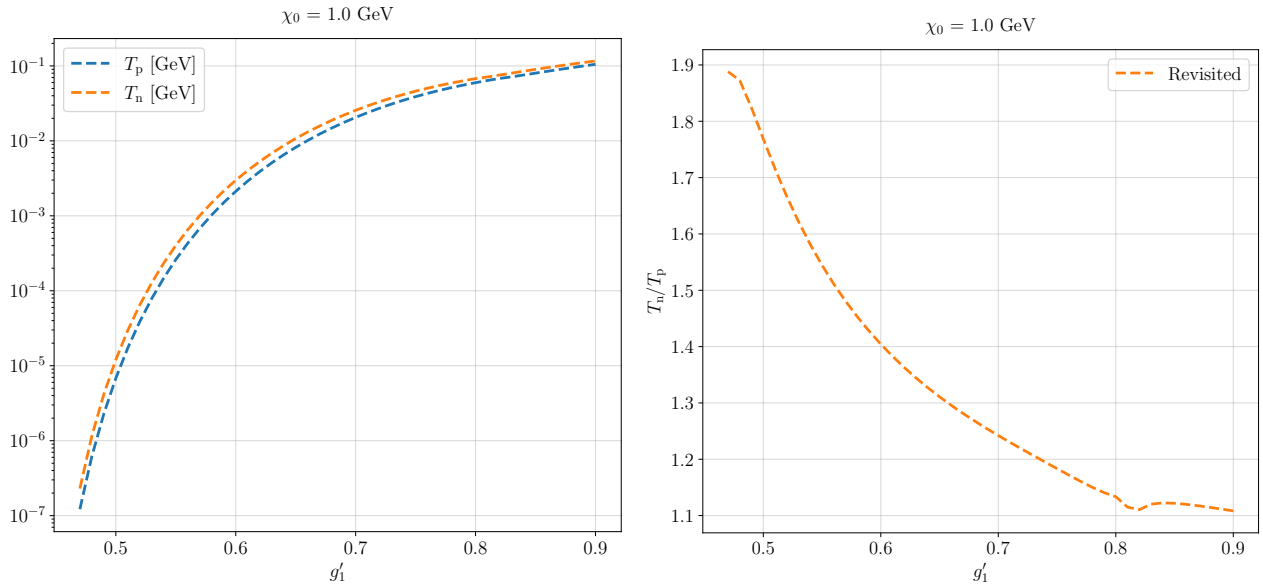

Figure 15: The percolation temperature T_p and the nucleation temperature T_n (left) and their ratio $\frac{T_n}{T_p}$ (right) as a function of the gauge coupling g_1', for the revisited and full approaches.

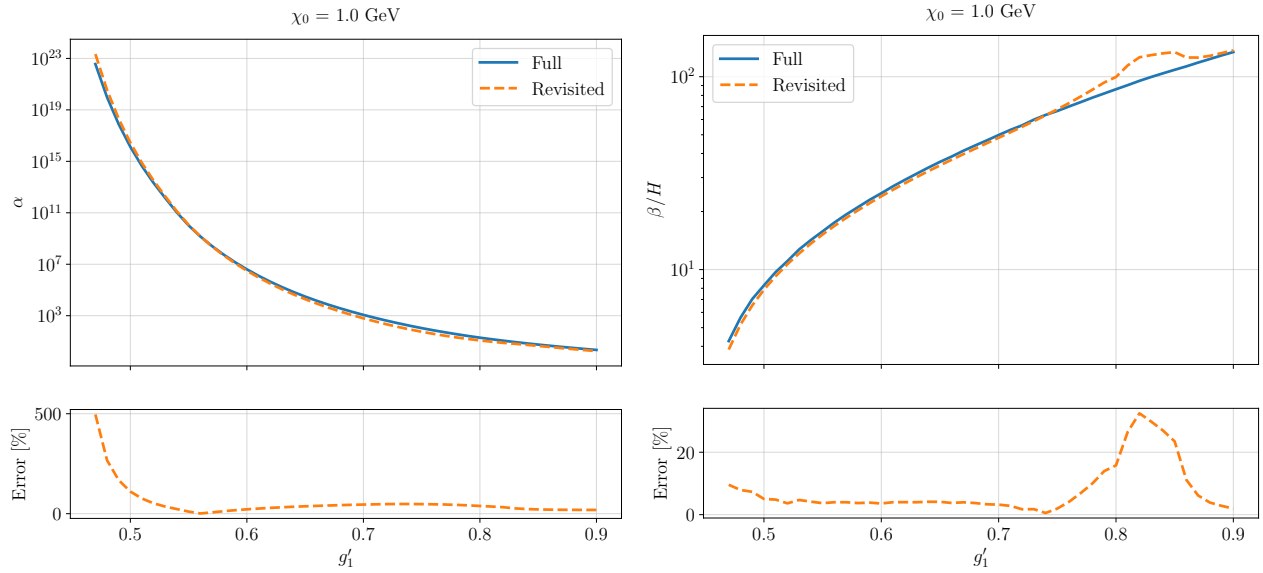

Figure 16: The transition strength α (left) and the inverse transition duration β/H (right) as a function of the gauge coupling g_1', for the revisited and full approaches. In the bottom left panel, the percent relative errors are shown with respect to the full one.

the left plot of Fig. 17 show that the 68% and 95% confidence regions overlap and are mutually consistent. In the right plot of Fig. 17, we compare the SGWB spectrum obtained with the revisited approach against the one obtained with the full numerical results, for the best-fit parameters $(\chi_0[\text{GeV}], g_1') = (0.79, 0.68)$. The masses of the DS particles in Eq. (4.3.6) are

$$m_A = g_1'\chi_0 = 0.537 \text{ GeV}\,, \quad m_S = \frac{\sqrt{6}g_1'^2}{4\pi}\chi_0 = 0.071 \text{ GeV}\,. \tag{4.3.17}$$

An important advantage of the revisited framework is that the time required to compute the pos-

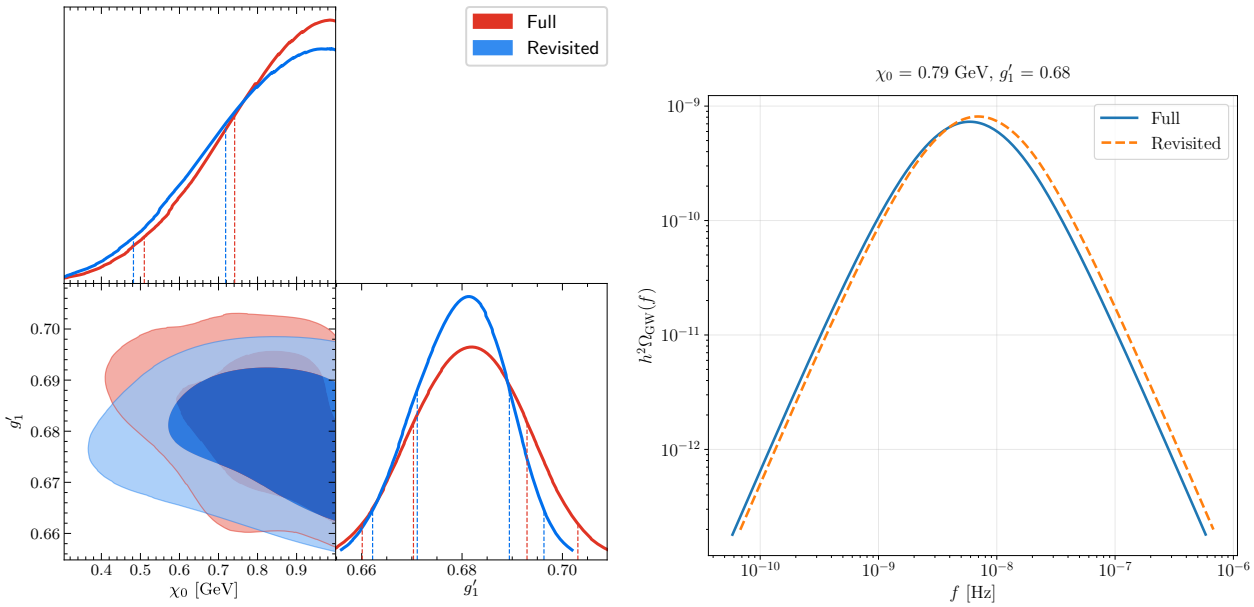

Figure 17: Bayesian posterior distribution over the NANOGrav dataset as a function of the gauge coupling g_1' and the VEV χ_0 (left) and the SGWB spectrum $h^2\Omega_{\rm GW}$ (right) of best-fit parameters as a function of the frequency f.

terior distributions using the Markov chain Monte Carlo algorithm in `PTArcade`: from days for the full numerical approach with the numerical integration of Eq. (3.3.17) to minutes with the revisited framework.

Physical insights. The framework developed in this chapter, not only simplifies the computation allowing for a faster estimate of the SGWB spectrum, but also provides some physical insights as well. Looking at the percolation temperature T_p and the peak frequency $f_{\rm peak}$ of bubble collision SGWB spectrum in Fig. 18 for the range of values $g_1' \in [0.47, 0.9]$ and $\chi_0 \in [0.1, 1]$, we observe that there is only a mild dependence on the VEV χ_0, but a strong dependence on the gauge coupling g_1', since the smaller g_1' corresponds to stronger supercooling, leading to lower T_p and, consequently, a lower $f_{\rm peak}$. We can justify this behaviour by looking at the revisited polynomial effective potential in Eq. (4.2.22) and the fit bounce action in Eq. (4.1.55) in terms of the revisited collective couplings in Eq. (4.2.24). In fact, the dependence on the VEV χ_0 of the coefficients in Eq. (4.3.10) is only logarithmic in the quartic one

$$\lambda(T) = \frac{3{g_1'}^4}{32\pi^2} \ln \frac{{g_1'}^4 \chi_0^4 e}{a_b^2 T^4} \,, \tag{4.3.18}$$

which means that the impact of the VEV χ_0 is visible only with orders of magnitude changes.

On the other hand, the dependence on the gauge coupling g_1' is more significant, as it appears in all the coefficients. To make this analysis quantitative, we first estimate how the parameter $\tilde{\lambda}$ in Eq. (4.1.50) changes as the parameters vary. With the collective couplings in Eq. (4.2.24)

$$g_2^2 = 3{g_1'}^2 \,, \quad g_3 = 3{g_1'}^3 \,, \quad g_4' = 3{g_1'}^4 \ln \frac{{g_1'}^4 e}{a_b^2} \,, \quad g_4'' = 12{g_1'}^4 \,, \tag{4.3.19}$$

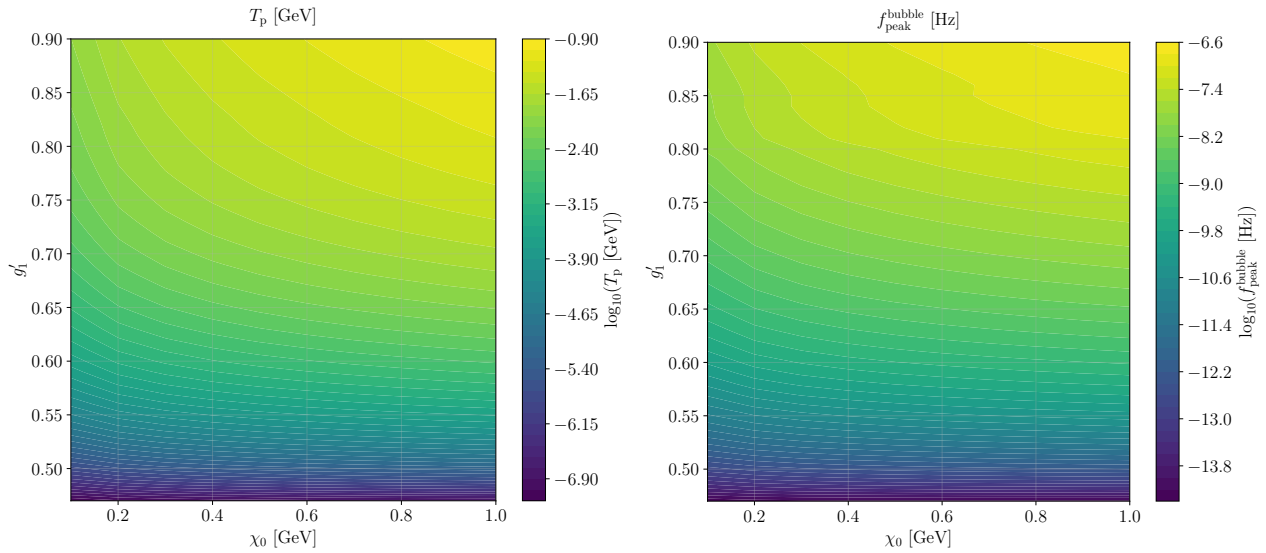

Figure 18: Values of the percolation temperature T_p (left) and the peak frequency f_{peak} (right) as a function of the gauge coupling g_1' and the VEV χ_0.

and (4.2.26)

$$l_1 = \frac{g_2^2 g_4'}{24 g_3^2} = \frac{1}{24} \ln \frac{{g_1'}^4 e}{a_b^2} \,, \quad l_2 = \frac{g_2^2 g_4''}{24 g_3^2} = \frac{1}{6} \,, \tag{4.3.20}$$

we obtain the dependence of $\tilde{\lambda}$ in Eq. (4.2.25) on the gauge coupling g_1' and the VEV χ_0

$$\tilde{\lambda} = \frac{1}{24} \ln \frac{{g_1'}^4 e}{a_b^2} - \frac{1}{6} \ln \frac{T}{\chi_0} \,. \tag{4.3.21}$$

This means that the dependence of $\tilde{\lambda}$ in the parameters is only logarithmic, which is nearly constant and can therefore be neglected. Then, we estimate the effective potential at two relevant points: the barrier width χ_b and the barrier height $V_{\text{eff}}(\chi_t)$. The former is computed using the definition in Eq. (4.1.25)

$$V_{\text{eff}}(\chi_b, T) = \frac{m(T)^2}{2}\chi_b^2 - \frac{k(T)}{3}\chi_b^3 - \frac{\lambda(T)}{4}\chi_b^4 = 0 \quad \Rightarrow \quad \chi_b = \frac{2k(T)}{3\lambda(T)} \left(\sqrt{1 + \frac{9}{2}\tilde{\lambda}(T)} - 1 \right) \,, \tag{4.3.22}$$

which implies that, at fixed T, the barrier width in Eq. (4.3.22) roughly goes as

$$\chi_b \propto \frac{k(T)}{\lambda(T)} \propto \frac{1}{g_1'} \,, \tag{4.3.23}$$

where we have substituted in Eq. (4.3.10) and again neglected the logarithmic contribution. The relation in Eq. (4.3.23) shows that the barrier width χ_b is inversely proportional to the gauge coupling g_1', which means that the smaller the gauge coupling, the larger the barrier width. Regarding the barrier height, we determine it by taking the first derivative of the polynomial effective potential in

Eq. (4.2.22) to find the location of the maximum χ_t

$$\frac{dV_{\text{eff}}}{d\chi}\Big|_{\chi_t} = m^2(T)\chi - k(T)\chi^2 - \lambda(T)\chi^3 = 0 \quad \Rightarrow \quad \chi_t = \frac{k(T)}{2\lambda(T)}\left(\sqrt{1+4\tilde{\lambda}(T)}-1\right) , \tag{4.3.24}$$

which implies that, under the same consideration as before, the location of the maximum χ_t behaves as

$$\chi_t \propto \frac{k(T)}{\lambda(T)} \propto \frac{1}{g_1'} . \tag{4.3.25}$$

Note that the ratio between the barrier width χ_b in Eq. (4.3.23) and the barrier height χ_t in Eq. (4.3.25) is almost constant. Furthermore, we substitute in Eq. (4.3.25) back into the polynomial effective potential in Eq. (4.2.22) to find that the height of the barrier mildly depends on the gauge coupling g_1'

$$V_{\text{eff}}(\chi_t) = \frac{m^2(T)}{2}\chi_t^2 - \frac{k(T)}{3}\chi_t^3 - \frac{\lambda(T)}{4}\chi_t^4 \simeq \text{constant} . \tag{4.3.26}$$

Physically, this implies that small gauge couplings g_1' tend to delay or suppress nucleation, since tunneling occurs through a broader barrier, while large couplings make the transition faster. This is explicitly seen by showing that the ratio between the bounce action S_3 and the temperature T given in Eq. (4.1.55) is proportional to

$$\frac{S_3}{T} \propto \frac{m^3(T)}{Tk^2(T)} \propto \frac{1}{{g_1'}^3} , \tag{4.3.27}$$

which implies that the false vacuum decay rate Γ, given by Eq. (4.2.28), increases as the gauge coupling g_1' increases, because it is dominated by the exponentially sensitive to $\frac{S_3}{T}$, meaning a less supercooled FOPT.

4.3.2 Non-minimal $U(1)_D$ model

One of the strengths of the revisited model-independent framework is that it can be applied to more complicated models than the minimal one, and it also provides physical insights.

We extend the minimal $U(1)_D$ model with the addition of a fermion, which is phenomenologically interesting for dark matter. With respect to the minimal one, the Lagrangian in Eq. (4.3.1) of the non-minimal $U(1)_D$ model takes the form

$$\mathcal{L} = \mathcal{L}_{SM} - \frac{1}{4}F'_{\mu\nu}F'^{\mu\nu} + (D_\mu S)^\dagger D^\mu S - \lambda_\chi |S|^4 + i\bar{N}_R \not{D} N_R + i\bar{N}_L \not{D} N_L - (yS\bar{N}_L N_R + \text{h.c.}) . \tag{4.3.28}$$

In order to respect gauge invariance of the Yukawa term and to keep the model anomaly-free, we set $Q_L = 1/2$ and $Q_R = -1/2$ for the left-handed and right-handed components of the fermion N, respectively. The charge of the scalar field S is set to $Q_S = 1$.

As in the minimal $U(1)$ model, we identify χ with the magnitude of the real part of the scalar field S, i.e. $\chi = \sqrt{2}|S|$. The one-loop β function for the quartic self-interaction coupling of χ is

$$(16\pi^2)\beta_{\lambda_\chi} = 20\lambda_\chi^2 + 6{g_1'}^4 - 12{g_1'}^2\lambda_\chi + 4\lambda_\chi y^2 - 2y^4 , \tag{4.3.29}$$

which, evaluated at the energy scale $\tilde{\mu}$ where the quartic coupling vanishes $\lambda_\chi = 0$, becomes

$$(16\pi^2)\tilde{\beta}_{\lambda_\chi} = 6{g_1'}^4 - 2y^4 , \tag{4.3.30}$$

which agrees with Eq. (4.2.12). An additional feature we need to ensure is that the one-loop beta function is positive. This condition imposes a relation between the gauge coupling g_1' and the Yukawa coupling y

$$\tilde{\beta}_{\lambda_\chi} > 0\,, \quad 6g_1'^4 - 2y^4 > 0\,, \quad y < 3^{1/4} g_1' \simeq 1.31 g_1'\,. \tag{4.3.31}$$

After SSB, the field-dependent masses of the DS particles read

$$m_{A'}^2(\chi) = g_1'^{\,2}\chi^2\,, \quad m_S^2(\chi) = \tilde{\beta}_{\lambda_\chi}\chi^2 = \frac{6g_1'^4 - 2y^4}{16\pi^2}\chi^2\,, \quad m_N^2(\chi) = \frac{y^2}{2}\chi^2\,. \tag{4.3.32}$$

Using the revisited model-independent framework, we write the quadratic, cubic and, quartic collective couplings in Eq. (4.2.24)

$$g_2^2 = 3g_1'^{\,2} + y^2\,, \quad g_3 = 3g_1'^{\,3}\,, \quad g_4(T) = 3g_1'^{\,4}\ln\frac{g_1'^{\,4}\chi_0^4 e}{a_b^2 T^4} - y^4 \ln\frac{y^4\chi_0^4 e}{4a_f^2 T^4}\,, \tag{4.3.33}$$

which are used to write the coefficients of the polynomial effective potential in Eq. (4.2.22) by means of Eq. (4.2.23)

$$\begin{aligned} m^2(T) &= \frac{g_2^2 T^2}{12} = \frac{T^2}{12}\left(3g_1'^{\,2} + y^2\right)\,, \quad k(T) = \frac{g_3 T}{4\pi} = \frac{3g_1'^{\,3}T}{4\pi}\,, \\ \lambda(T) &= \frac{g_4(T)}{32\pi^2} = \frac{3g_1'^{\,4}}{32\pi^2}\ln\frac{g_1'^{\,4}\chi_0^4 e}{a_b^2 T^4} - \frac{y^4}{32\pi^2}\ln\frac{y^4\chi_0^4 e}{4a_f^2 T^4}\,. \end{aligned} \tag{4.3.34}$$

SGWB spectrum. We compute the Bayesian posterior distribution over the NANOGrav dataset using the package `PTArcade` [230]. The results in the left plot of Fig. 19 show that the introduction of the Yukawa coupling changes the 68% and 95% confidence regions, compared to the previous analysis in the left plot of Fig. 17. In the right plot of Fig. 19, we compute the SGWB spectrum obtained with the revisited approach for the best-fit parameters $(\chi_0, g_1', y) = (0.70\,\text{GeV}, 0.75, 0.62)$. The masses of the DS particles in Eq. (4.3.35) are

$$m_{A'}(\chi) = g_1'\chi_0 = 0.525\,\text{GeV}\,, \quad m_S = \frac{\sqrt{6g_1'^4 - 2y^4}}{4\pi}\chi_0 = 0.071\,\text{GeV}\,, \quad m_N = \frac{y}{\sqrt{2}}\chi_0 = 0.307\,\text{GeV}\,. \tag{4.3.35}$$

Physical insights. Looking at the percolation temperature T_p and the peak frequency f_{peak} of the SGWB spectrum from bubble collisions in Fig. 20 for the range of values $g_1' \in [0.47, 0.9]$ and $y \in [0.1, 1]$, at fixed $\chi_0 = 1$ GeV since there is only a mild dependence on it, we appreciate the same behaviour as in the minimal model, the larger the gauge coupling g_1', the smaller the supercooling. The white region indicates that the beta function does not satisfy the positivity condition in Eq. (4.3.31) or excessive supercooling. Furthermore, we can see that for very small Yukawa coupling y, there is almost no difference compared to the minimal model, as it enters with the second or fourth power in the polynomial potential coefficients in Eq. (4.3.33). However, the larger the Yukawa coupling y, the more the supercooling. As we did for the minimal model, we can justify this behaviour by looking at the revisited polynomial effective potential in Eq. (4.2.22). The gauge coupling g_1' appears in all the coefficients, while the Yukawa coupling y only enters in the quartic and quadratic terms,

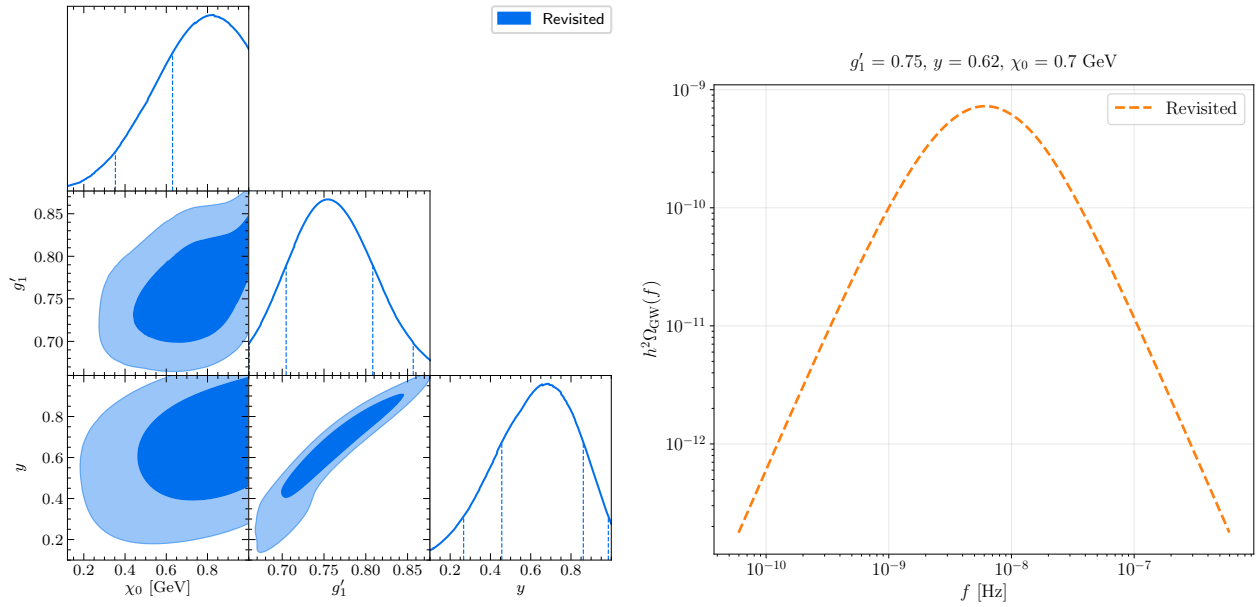

Figure 19: Bayesian posterior distribution over the NANOGrav dataset as a function of the gauge coupling g_1' and the Yukawa coupling y (left) and the SGWB spectrum $h^2\Omega_{\rm GW}$ (right) of the best-fit parameters as a function of the frequency f.

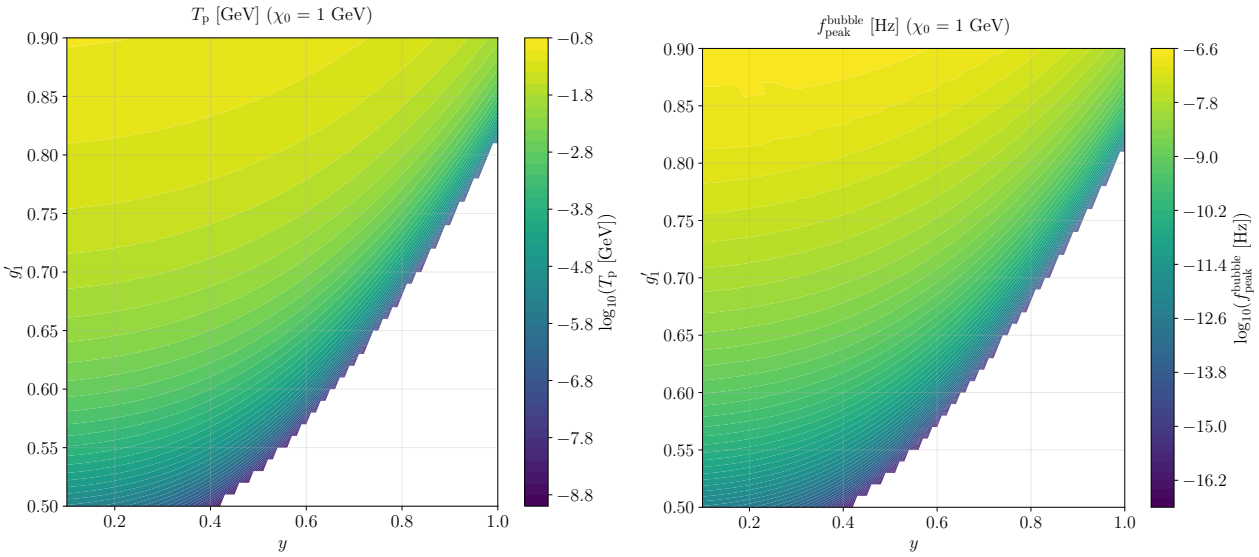

Figure 20: Values of the percolation temperature T_p (left) and the peak frequency f_{peak} (right) as a function of the gauge coupling g_1' and the Yukawa coupling y.

but not in the cubic one in Eq. (4.3.33).

We start by investigating $\tilde{\lambda}(T)$, by computing the collective couplings in Eq. (4.2.24)

$$g_2^2 = 3{g_1'}^2 + y^2\,, \quad g_3 = 3{g_1'}^3\,, \quad g_4' = 3{g_1'}^4 \ln\frac{{g_1'}^4 e}{a_b^2} - y^4 \ln\frac{y^4 e}{4a_f^2}\,, \quad g_4'' = 12{g_1'}^4 - 4y^4\,, \tag{4.3.36}$$

and (4.2.26)

$$l_1 = \frac{3{g_1'}^2 + y^2}{72{g_1'}^2} \ln\left(\frac{{g_1'}^4 e}{a_b^2}\right) - \frac{(3{g_1'}^2 + y^2)y^4}{216{g_1'}^6} \ln\left(\frac{y^4 e}{4a_f^2}\right) , \quad l_2 = \frac{3{g_1'}^2 + y^2}{18{g_1'}^2} - \frac{(3{g_1'}^2 + y^2)\, y^4}{54{g_1'}^6} . \tag{4.3.37}$$

Hence, $\tilde{\lambda}(T)$ in Eq. (4.2.25) is not almost constant but, at fixed g_1', the minus signs in front of the terms contributing to the fourth power of y makes it decrease as the Yukawa coupling y increases. With this result, we compute the barrier width χ_b in Eq. (4.3.22) at fixed gauge coupling g_1'

$$\chi_b = \frac{2k(T)}{3\lambda(T)} \left(\sqrt{1 + \frac{9}{2}\tilde{\lambda}(T)} - 1\right) . \tag{4.3.38}$$

The prefactor in Eq. (4.3.38) goes roughly as $\frac{k(T)}{\lambda(T)} \sim \frac{{g_1'}^3}{3{g_1'}^4 - y^4}$, neglecting the logarithmic contribution, and shows that, at fixed gauge coupling g_1', the barrier width χ_b increases as the Yukawa coupling y decreases, together with the fact that also $\tilde{\lambda}$ is small with large y. The stronger fourth-power dependence on the Yukawa coupling y has a more significant impact on the barrier width χ_b compared to the gauge coupling g_1' and both the percolation temperature and the peak frequency decrease more rapidly with increasing y. The same considerations apply for the barrier height χ_t using the definition in Eq. (4.3.24). Physically, this implies that large Yukawa coupling y tends to delay or suppress nucleation, since tunneling occurs through a broader barrier, explicitly seen in the prefactor of the ratio between the bounce action S_3 and the temperature T given in Eq. (4.1.55). In fact, the prefactor going as $\frac{m^3(T)}{Tk^2(T)} \sim \frac{(3{g_1'}^3 + y^2)^{3/2}}{{g_1'}^6}$, and the fact that also the $\tilde{\lambda}$-dependent part of the fit action in Eq. (4.1.55) increases, imply that the Yukawa coupling y plays the opposite role compared to the gauge coupling g_1'. While increasing g_1' leads to a decrease in the bounce action S_3, increasing y has the opposite effect, enhancing S_3. This means that the decay rate Γ given by (4.2.28) decreases as the Yukawa coupling y increases, meaning a more supercooled PT.

5 Conclusions

Motivated by the compelling evidence for a Stochastic Gravitational Wave Background (SGWB) in various Pulsar Timing Array (PTA) datasets, and the possibility that this signal has a cosmological First-Order Phase Transition (FOPT) origin, this thesis focused on the development of a novel semi-analytic, model-independent framework to study classically scale-invariant explanations, featuring Radiative Symmetry Breaking (RSB).

In chapter 2, we described the necessary ingredients from three different branches of physics that set the stage for understanding FOPT. First, we studied the thermal history of the Universe using the tools of cosmology, such as the Friedmann-Lemaitre-Robertson-Walker (FLRW) metric and the ΛCDM model, and thermodynamics, understanding the necessary conditions for a species to be in thermal equilibrium in the early Universe. We discussed the theory of Gravitational Wavess (GWs), in the linearised theory, shifting focus on the properties of a SGWB and its detection using PTAs, obtaining the famous Hellings-Downs correlation pattern. We reviewed the Standard Model (SM) with the mechanism of Spontaneous Symmetry Breaking (SSB) and introduced Dark Sector (DS) as Beyond the Standard Model (BSM) candidates. In chapter 3, we investigated the theory of cosmological Phase Transition (PT), starting with the computation of all the contributions to the effective potential, including the one-loop and finite-temperature ones, and the false vacuum decay, including quantum tunneling and thermal fluctuations. We discussed the nucleation of bubbles and how to track the progress of the phase transition, obtaining explicitly the false vacuum fraction. Finally, we defined the relevant thermal parameters that characterise a FOPT and how they enter the SGWB spectrum, as provided by the most recent results in the literature.

The main results of this thesis lie in chapter 4, where we constructed the new framework in detail. The motivation for a semi-analytic approach comes from the possibility of avoiding a full numerical analysis to compute the SGWB spectrum, but also to provide valuable insights into the parameter space of the particle physics model.

We began by reviewing the established approach, which was developed in Refs. [58–61], that relies on truncating the high-temperature expansion of the finite-temperature contribution at cubic order and approximating the one-loop contribution by substituting the field-dependent part with a temperature-dependent one, which is valid in the regime of large supercooling. In this way, the effective potential can be written as a polynomial, for small field values near the barrier, where tunneling of the scalar field is most probable. In this case, the coefficients of the polynomial are given directly by the Lagrangian parameters of the model, namely the Vacuum Expectation Value (VEV) of the scalar field χ_0 and collective couplings determined by the particle-mass couplings. For this kind of potentials, the bounce action S_3 can be obtained analytically. After the review of previous literature, we proposed a revisited method to write down the effective potential as a polynomial. Our proposal only relies on the high-temperature expansion of the thermal part of the effective potential. It naturally translates into a polynomial potential when extending one order beyond what previous literature did, i.e. including the logarithmic term in the expansion of the thermal functions. This result supersedes the previous approach, avoiding unnecessary approximations.

Furthermore, the established approach provided only the nucleation temperature T_n. Instead, motivated by the fact that the relevant temperature for the production of GWs during the PT is the percolation temperature T_p, we derived two straightforward root-finding equations to evaluate it:

under the assumption of a vacuum-dominated transition, we analytically computed the integral appearing in the false vacuum fraction, without specifying the expression for the decay rate, by applying a Gaussian approximation in the general case or by providing a simpler expression derived from a linear expansion of the bounce action S_3, valid only for less supercooling. In fact, the general procedure to compute the percolation temperature T_p is numerically expensive: it is the solution of an equation with a double integral coming from the false vacuum fraction, in which the percolation temperature we search for is in the lower integration limit. Thus, our proposal avoids the numerical integrals and reduces to a root-finding equation. Finally, we provided analytical expressions for the remaining thermal parameters, namely the transition strength α and the inverse transition duration β.

To validate but also illustrate our approach, we applied it to phenomenological models, consisting of dark $U(1)_D$ extensions of the SM, both in the minimal form, comprising a dark scalar, responsible for the FOPT, and a dark photon, necessary to have a first-order PT, and in the non-minimal form, including also a dark fermion. These models have been shown to explain the PTA signal, making them an interesting class to which test our semi-analytic approach. Focusing on the minimal model, whose parameter space is spanned by the VEV χ_0 of the scalar field and the gauge coupling g_1', we showed that the approach proposed in this thesis is able to reproduce the results of a full numerical analysis, conducted in parallel using the most general form of the effective potential, and `CosmoTransitions` to compute the bounce action S_3 using the shooting method, with greater precision than the established method. Furthermore, we found that the posterior distributions over the North American Nanohertz Observatory for Gravitational Waves (NANOGrav) 15-year dataset of our approach essentially overlaps the full numerical one. This demonstrates once again the validity of our framework, while also remarking that a FOPT in $U(1)_D$ model is able to explain the PTA signal. We highlight that the time required to obtain the results with our approach is much shorter than that required for a full numerical analysis. We reduced the evaluation time for each point in the parameter space from several minutes to a fraction of a second, cutting the time to obtain the best-fit parameters from days to minutes.

Additionally, in contrast to the numerical analysis, our approach allows for physical insights into the dependence of the SGWB spectrum on the Lagrangian parameters. We can justify the mild dependence on the VEV of the scalar field χ_0 by looking at the logarithmic dependence on the quartic coefficient of the polynomial potential. Moreover, we observe that decreasing the gauge coupling g_1' or increasing the Yukawa coupling y leads to large supercooling, which occurs when the onset of the PT is delayed such that a period of vacuum-dominated epoch is triggered, enhancing the SGWB spectrum and making it observable today. The dependence of the SGWB spectrum on the parameters can be understood by looking at their contribution to the barrier width χ_b or the ratio of the bounce action S_3 over the temperature T, which exponentially governs the false vacuum decay rate.

The success of this approach allows to extend its applicability to different models, modifying the particle content and the gauge group or testing different energy scales. On the other hand, further refinements of the methods introduced in this thesis are possible.

In Sec. 3.1.6, we argued that daisy resummation could improve the behavior of the effective potential in the high-temperature regime, but this term is included neither in the established approach nor in the revisited one, as it has been argued that it is unnecessary in Ref. [59]. A possible way to introduce daisy terms in the polynomial potential would be through its high-temperature expansion.

In Sec. (3.1.2), we showed that on-shell renormalisation conditions lead to a different one-loop effective potential. Furthermore, an alternative renormalisation scale μ can be applied to the $\overline{\text{MS}}$

effective potential, with a natural choice being μ proportional to the energy scale of the theory, such as the temperature T. A possible extension of this work is to study how the effective potential, and consequently the PT, behaves under on-shell renormalisation conditions, which leads to a similar polynomial potential with a different quadratic coefficient, or under variations of the renormalisation scale μ.

By developing a novel semi-analytic, model-independent framework for supercooled FOPTs, connecting microscopic couplings to macroscopic signals of GWs in DS models, such as the SGWB recently reported in PTAs, this thesis contributes to the quest for fundamental physics: a reminder that, though we know so little about the Universe, each step is necessary, even if it is small.

References

[1] N. Aghanim et al. “Planck 2018 results. VI. Cosmological parameters”. In: *Astron. Astrophys.* 641 (2020). [Erratum: Astron.Astrophys. 652, C4 (2021)], A6. DOI: 10.1051/0004-6361/201833910. arXiv: 1807.06209 [astro-ph.CO].

[2] S. Navas et al. “Review of particle physics”. In: *Phys. Rev. D* 110.3 (2024), p. 030001. DOI: 10.1103/PhysRevD.110.030001.

[3] B. P. Abbott et al. “Observation of Gravitational Waves from a Binary Black Hole Merger”. In: *Phys. Rev. Lett.* 116.6 (2016), p. 061102. DOI: 10.1103/PhysRevLett.116.061102. arXiv: 1602.03837 [gr-qc].

[4] Albert Einstein. “Approximative Integration of the Field Equations of Gravitation”. In: *Sitzungsber. Preuss. Akad. Wiss. Berlin (Math. Phys.)* 1916 (1916), pp. 688–696.

[5] Albert Einstein. “Über Gravitationswellen”. In: *Sitzungsber. Preuss. Akad. Wiss. Berlin (Math. Phys.)* 1918 (1918), pp. 154–167.

[6] Gabriella Agazie et al. “The NANOGrav 15 yr Data Set: Evidence for a Gravitational-wave Background”. In: *Astrophys. J. Lett.* 951.1 (2023), p. L8. DOI: 10.3847/2041-8213/acdac6. arXiv: 2306.16213 [astro-ph.HE].

[7] Heng Xu et al. “Searching for the Nano-Hertz Stochastic Gravitational Wave Background with the Chinese Pulsar Timing Array Data Release I”. In: *Res. Astron. Astrophys.* 23.7 (2023), p. 075024. DOI: 10.1088/1674-4527/acdfa5. arXiv: 2306.16216 [astro-ph.HE].

[8] J. Antoniadis et al. “The second data release from the European Pulsar Timing Array - III. Search for gravitational wave signals”. In: *Astron. Astrophys.* 678 (2023), A50. DOI: 10.1051/0004-6361/202346844. arXiv: 2306.16214 [astro-ph.HE].

[9] Daniel J. Reardon et al. “Search for an Isotropic Gravitational-wave Background with the Parkes Pulsar Timing Array”. In: *Astrophys. J. Lett.* 951.1 (2023), p. L6. DOI: 10.3847/2041-8213/acdd02. arXiv: 2306.16215 [astro-ph.HE].

[10] Mohan Rajagopal and Roger W. Romani. “Ultralow frequency gravitational radiation from massive black hole binaries”. In: *Astrophys. J.* 446 (1995), pp. 543–549. DOI: 10.1086/175813. arXiv: astro-ph/9412038.

[11] J. Stuart B. Wyithe and Abraham Loeb. “Low-Frequency Gravitational Waves from Massive Black Hole Binaries: Predictions for LISA and Pulsar Timing Arrays”. In: *The Astrophysical Journal* 590.2 (June 2003), p. 691. DOI: 10.1086/375187. URL: https://dx.doi.org/10.1086/375187.

[12] A. H. Jaffe and D. C. Backer. “Gravitational Waves Probe the Coalescence Rate of Massive Black Hole Binaries”. In: *The Astrophysical Journal* 583.2 (Feb. 2003), p. 616. DOI: 10.1086/345443. URL: https://dx.doi.org/10.1086/345443.

[13] Alberto Sesana et al. “Low - frequency gravitational radiation from coalescing massive black hole binaries in hierarchical cosmologies”. In: *Astrophys. J.* 611 (2004), pp. 623–632. DOI: 10.1086/422185. arXiv: astro-ph/0401543.

[14] Sarah Burke-Spolaor et al. “The Astrophysics of Nanohertz Gravitational Waves”. In: *Astron. Astrophys. Rev.* 27.1 (2019), p. 5. DOI: 10.1007/s00159-019-0115-7. arXiv: 1811.08826 [astro-ph.HE].

[15] Gabriella Agazie et al. “The NANOGrav 15 yr Data Set: Constraints on Supermassive Black Hole Binaries from the Gravitational-wave Background”. In: *Astrophys. J. Lett.* 952.2 (2023), p. L37. DOI: 10.3847/2041-8213/ace18b. arXiv: 2306.16220 [astro-ph.HE].

[16] Gabriella Agazie et al. “The NANOGrav 15 yr Data Set: Bayesian Limits on Gravitational Waves from Individual Supermassive Black Hole Binaries”. In: *Astrophys. J. Lett.* 951.2 (2023), p. L50. DOI: 10.3847/2041-8213/ace18a. arXiv: 2306.16222 [astro-ph.HE].

[17] Adeela Afzal et al. “The NANOGrav 15 yr Data Set: Search for Signals from New Physics”. In: *Astrophys. J. Lett.* 951.1 (2023). [Erratum: Astrophys.J.Lett. 971, L27 (2024), Erratum: Astrophys.J. 971, L27 (2024)], p. L11. DOI: 10.3847/2041-8213/acdc91. arXiv: 2306.16219 [astro-ph.HE].

[18] John Ellis et al. “What is the source of the PTA GW signal?” In: *Phys. Rev. D* 109.2 (2024), p. 023522. DOI: 10.1103/PhysRevD.109.023522. arXiv: 2308.08546 [astro-ph.CO].

[19] Daniel G. Figueroa et al. “Cosmological Background Interpretation of Pulsar Timing Array Data”. In: *Phys. Rev. Lett.* 132.17 (2024), p. 171002. DOI: 10.1103/PhysRevLett.132.171002. arXiv: 2307.02399 [astro-ph.CO].

[20] Eric Madge et al. “Primordial gravitational waves in the nano-Hertz regime and PTA data — towards solving the GW inverse problem”. In: *JHEP* 10 (2023), p. 171. DOI: 10.1007/JHEP10(2023)171. arXiv: 2306.14856 [hep-ph].

[21] Yu-Mei Wu, Zu-Cheng Chen, and Qing-Guo Huang. “Cosmological interpretation for the stochastic signal in pulsar timing arrays”. In: *Sci. China Phys. Mech. Astron.* 67.4 (2024), p. 240412. DOI: 10.1007/s11433-023-2298-7. arXiv: 2307.03141 [astro-ph.CO].

[22] John Ellis. “Gravitational Waves: Echoes of the Biggest Bangs Since the Big Bang and/or BSM Physics?” In: *Universe* 11.7 (2025), p. 213. DOI: 10.3390/universe11070213. arXiv: 2402.10755 [hep-ph].

[23] Torsten Bringmann et al. “Does NANOGrav observe a dark sector phase transition?” In: *JCAP* 11 (2023), p. 053. DOI: 10.1088/1475-7516/2023/11/053. arXiv: 2306.09411 [astro-ph.CO].

[24] Yann Gouttenoire. “First-Order Phase Transition Interpretation of Pulsar Timing Array Signal Is Consistent with Solar-Mass Black Holes”. In: *Phys. Rev. Lett.* 131.17 (2023), p. 171404. DOI: 10.1103/PhysRevLett.131.171404. arXiv: 2307.04239 [hep-ph].

[25] Deng Wang. “Constraining Cosmological Phase Transitions with Chinese Pulsar Timing Array Data Release 1”. In: (July 2023). arXiv: 2307.15970 [astro-ph.CO].

[26] Andrea Addazi et al. “Have pulsar timing array methods detected a cosmological phase transition?” In: *Phys. Rev. D* 109.1 (2024), p. 015028. DOI: 10.1103/PhysRevD.109.015028. arXiv: 2306.17205 [astro-ph.CO].

[27] Djuna Croon and David J. Weir. “Gravitational Waves from Phase Transitions”. In: *Contemp. Phys.* 65 (2024), p. 75. DOI: 10.1080/00107514.2024.2423496. arXiv: 2410.21509 [hep-ph].

[28] Martin Wolfgang Winkler and Katherine Freese. “Origin of the stochastic gravitational wave background: First-order phase transition versus black hole mergers”. In: *Phys. Rev. D* 111.8 (2025), p. 083509. DOI: 10.1103/PhysRevD.111.083509. arXiv: 2401.13729 [astro-ph.CO].

[29] Sidney R. Coleman. “The Fate of the False Vacuum. 1. Semiclassical Theory”. In: *Phys. Rev. D* 15 (1977). [Erratum: Phys.Rev.D 16, 1248 (1977)], pp. 2929–2936. DOI: 10.1103/PhysRevD.16.1248.

[30] Curtis G. Callan Jr. and Sidney R. Coleman. “The Fate of the False Vacuum. 2. First Quantum Corrections”. In: *Phys. Rev. D* 16 (1977), pp. 1762–1768. DOI: 10.1103/PhysRevD.16.1762.

[31] Andrei D. Linde. “On the Vacuum Instability and the Higgs Meson Mass”. In: *Phys. Lett. B* 70 (1977), pp. 306–308. DOI: 10.1016/0370-2693(77)90664-5.

[32] Andrei D. Linde. “Fate of the False Vacuum at Finite Temperature: Theory and Applications”. In: *Phys. Lett. B* 100 (1981), pp. 37–40. DOI: 10.1016/0370-2693(81)90281-1.

[33] Andrei D. Linde. “Decay of the False Vacuum at Finite Temperature”. In: *Nucl. Phys. B* 216 (1983). [Erratum: Nucl.Phys.B 223, 544 (1983)], p. 421. DOI: 10.1016/0550-3213(83)90072-X.

[34] Edward Witten. “Cosmic Separation of Phases”. In: *Phys. Rev. D* 30 (1984), pp. 272–285. DOI: 10.1103/PhysRevD.30.272.

[35] C. J. Hogan. “Gravitational radiation from cosmological phase transitions”. In: *Mon. Not. Roy. Astron. Soc.* 218 (1986), pp. 629–636.

[36] Arthur Kosowsky, Michael S. Turner, and Richard Watkins. “Gravitational waves from first order cosmological phase transitions”. In: *Phys. Rev. Lett.* 69 (1992), pp. 2026–2029. DOI: 10.1103/PhysRevLett.69.2026.

[37] Marc Kamionkowski, Arthur Kosowsky, and Michael S. Turner. “Gravitational radiation from first order phase transitions”. In: *Phys. Rev. D* 49 (1994), pp. 2837–2851. DOI: 10.1103/PhysRevD.49.2837. arXiv: astro-ph/9310044.

[38] K. Kajantie et al. “Is there a hot electroweak phase transition at $m_H \gtrsim m_W$?” In: *Phys. Rev. Lett.* 77 (1996), pp. 2887–2890. DOI: 10.1103/PhysRevLett.77.2887. arXiv: hep-ph/9605288.

[39] K. Kajantie et al. “A Nonperturbative analysis of the finite T phase transition in SU(2) x U(1) electroweak theory”. In: *Nucl. Phys. B* 493 (1997), pp. 413–438. DOI: 10.1016/S0550-3213(97)00164-8. arXiv: hep-lat/9612006.

[40] F. Csikor, Z. Fodor, and J. Heitger. “Endpoint of the hot electroweak phase transition”. In: *Phys. Rev. Lett.* 82 (1999), pp. 21–24. DOI: 10.1103/PhysRevLett.82.21. arXiv: hep-ph/9809291.

[41] M. Laine, G. Nardini, and K. Rummukainen. “Lattice study of an electroweak phase transition at $m_h \simeq 126$ GeV”. In: *Journal of Cosmology and Astroparticle Physics* 2013.01 (Jan. 2013), p. 011. DOI: 10.1088/1475-7516/2013/01/011. URL: https://dx.doi.org/10.1088/1475-7516/2013/01/011.

[42] Michela D’Onofrio and Kari Rummukainen. “Standard model cross-over on the lattice”. In: *Phys. Rev. D* 93.2 (2016), p. 025003. DOI: 10.1103/PhysRevD.93.025003. arXiv: 1508.07161 [hep-ph].

[43] Z. Fodor and S. D. Katz. "Critical point of QCD at finite T and mu, lattice results for physical quark masses". In: *JHEP* 04 (2004), p. 050. DOI: 10.1088/1126-6708/2004/04/050. arXiv: hep-lat/0402006.

[44] Y. Aoki et al. "The Order of the quantum chromodynamics transition predicted by the standard model of particle physics". In: *Nature* 443 (2006), pp. 675–678. DOI: 10.1038/nature05120. arXiv: hep-lat/0611014.

[45] Prateek Agrawal et al. "Feebly-interacting particles: FIPs 2020 workshop report". In: *Eur. Phys. J. C* 81.11 (2021), p. 1015. DOI: 10.1140/epjc/s10052-021-09703-7. arXiv: 2102.12143 [hep-ph].

[46] C. Antel et al. "Feebly-interacting particles: FIPs 2022 Workshop Report". In: *Eur. Phys. J. C* 83.12 (2023), p. 1122. DOI: 10.1140/epjc/s10052-023-12168-5. arXiv: 2305.01715 [hep-ph].

[47] Alan H. Guth and S. H. H. Tye. "Phase Transitions and Magnetic Monopole Production in the Very Early Universe". In: *Phys. Rev. Lett.* 44 (1980). [Erratum: Phys.Rev.Lett. 44, 963 (1980)], p. 631. DOI: 10.1103/PhysRevLett.44.631.

[48] Alan H. Guth. "Inflationary universe: A possible solution to the horizon and flatness problems". In: *Phys. Rev. D* 23 (2 Jan. 1981), pp. 347–356. DOI: 10.1103/PhysRevD.23.347. URL: https://link.aps.org/doi/10.1103/PhysRevD.23.347.

[49] Alan H. Guth and Erick J. Weinberg. "Cosmological consequences of a first-order phase transition in the SU_5 grand unified model". In: *Phys. Rev. D* 23 (4 Feb. 1981), pp. 876–885. DOI: 10.1103/PhysRevD.23.876. URL: https://link.aps.org/doi/10.1103/PhysRevD.23.876.

[50] S. W. Hawking and I. G. Moss. "Supercooled Phase Transitions in the Very Early Universe". In: *Phys. Lett. B* 110 (1982), pp. 35–38. DOI: 10.1016/0370-2693(82)90946-7.

[51] Tomislav Prokopec, Jonas Rezacek, and Bogumi la Świeżewska. "Gravitational waves from conformal symmetry breaking". In: *JCAP* 02 (2019), p. 009. DOI: 10.1088/1475-7516/2019/02/009. arXiv: 1809.11129 [hep-ph].

[52] Maciej Kierkla, Alexandros Karam, and Bogumila Swiezewska. "Conformal model for gravitational waves and dark matter: a status update". In: *JHEP* 03 (2023), p. 007. DOI: 10.1007/JHEP03(2023)007. arXiv: 2210.07075 [astro-ph.CO].

[53] Maciej Kierkla et al. "Gravitational waves from supercooled phase transitions: dimensional transmutation meets dimensional reduction". In: *JHEP* 02 (2024), p. 234. DOI: 10.1007/JHEP02(2024)234. arXiv: 2312.12413 [hep-ph].

[54] João Gonçalves et al. "Gravitational waves from supercooled phase transitions in conformal Majoron models of neutrino mass". In: *JHEP* 02 (2025), p. 110. DOI: 10.1007/JHEP02(2025)110. arXiv: 2412.02645 [hep-ph].

[55] João Gonçalves et al. "Supercooled phase transitions in conformal dark sectors explain NANOGrav data". In: (Jan. 2025). arXiv: 2501.11619 [hep-ph].

[56] Yann Gouttenoire. "Primordial black holes from conformal Higgs". In: *Phys. Lett. B* 855 (2024), p. 138800. DOI: 10.1016/j.physletb.2024.138800. arXiv: 2311.13640 [hep-ph].

[57] Sowmiya Balan et al. “Sub-GeV dark matter and nano-Hertz gravitational waves from a classically conformal dark sector”. In: (Feb. 2025). arXiv: 2502.19478 [hep-ph].

[58] Noam Levi, Toby Opferkuch, and Diego Redigolo. “The supercooling window at weak and strong coupling”. In: *JHEP* 02 (2023), p. 125. DOI: 10.1007/JHEP02(2023)125. arXiv: 2212.08085 [hep-ph].

[59] Alberto Salvio. “Model-independent radiative symmetry breaking and gravitational waves”. In: *JCAP* 04 (2023), p. 051. DOI: 10.1088/1475-7516/2023/04/051. arXiv: 2302.10212 [hep-ph].

[60] Alberto Salvio. “Supercooling in radiative symmetry breaking: theory extensions, gravitational wave detection and primordial black holes”. In: *JCAP* 12 (2023), p. 046. DOI: 10.1088/1475-7516/2023/12/046. arXiv: 2307.04694 [hep-ph].

[61] Alberto Salvio. “Pulsar timing arrays and primordial black holes from a supercooled phase transition”. In: *Phys. Lett. B* 852 (2024), p. 138639. DOI: 10.1016/j.physletb.2024.138639. arXiv: 2312.04628 [hep-ph].

[62] Chiara Caprini et al. “Gravitational waves from first-order phase transitions in LISA: reconstruction pipeline and physics interpretation”. In: *JCAP* 10 (2024), p. 020. DOI: 10.1088/1475-7516/2024/10/020. arXiv: 2403.03723 [astro-ph.CO].

[63] Albert Einstein. “The Field Equations of Gravitation”. In: *Sitzungsber. Preuss. Akad. Wiss. Berlin (Math. Phys.)* 1915 (1915), pp. 844–847.

[64] Albert Einstein. “The foundation of the general theory of relativity.” In: *Annalen Phys.* 49.7 (1916). Ed. by Jong-Ping Hsu and D. Fine, pp. 769–822. DOI: 10.1002/andp.19163540702.

[65] A. Friedman. “On the Curvature of space”. In: *Z. Phys.* 10 (1922), pp. 377–386. DOI: 10.1007/BF01332580.

[66] A. Friedmann. “On the Possibility of a world with constant negative curvature of space”. In: *Z. Phys.* 21 (1924), pp. 326–332. DOI: 10.1007/BF01328280.

[67] Georges Lemaitre. “A Homogeneous Universe of Constant Mass and Growing Radius Accounting for the Radial Velocity of Extragalactic Nebulae”. In: *Annales Soc. Sci. Bruxelles A* 47 (1927), pp. 49–59. DOI: 10.1007/s10714-013-1548-3.

[68] Georges Lemaitre. “The Expanding Universe”. In: *Mon. Not. Roy. Astron. Soc.* 91 (1931), pp. 490–501.

[69] Georges Lemaitre. “A Homogeneous Universe of Constant Mass and Increasing Radius accounting for the Radial Velocity of Extra-galactic Nebulæ”. In: *Mon. Not. Roy. Astron. Soc.* 91.5 (1931), pp. 483–490. DOI: 10.1093/mnras/91.5.483.

[70] H. P. Robertson. “Kinematics and World-Structure. 2”. In: *Astrophys. J.* 83 (1935), pp. 187–201. DOI: 10.1086/143716.

[71] H. P. Robertson. “Kinematics and World-Structure”. In: *Astrophys. J.* 82 (1935), pp. 284–301. DOI: 10.1086/143681.

[72] H. P. Robertson. “Kinematics and World-Structure. 3”. In: *Astrophys. J.* 83 (1936), pp. 257–271. DOI: 10.1086/143726.

[73] A. G. Walker. “On Milne’s Theory of World-Structure”. In: *Proc. Lond. Math. Soc. s* 2-42.1 (1937), pp. 90–127. DOI: 10.1112/plms/s2-42.1.90.

[74] Edwin Hubble. “A relation between distance and radial velocity among extra-galactic nebulae”. In: *Proc. Nat. Acad. Sci.* 15 (1929), pp. 168–173. DOI: 10.1073/pnas.15.3.168.

[75] F. Hoyle. “A New Model for the Expanding Universe”. In: *Mon. Not. Roy. Astron. Soc.* 108 (1948), pp. 372–382.

[76] H. Bondi and T. Gold. “The Steady-State Theory of the Expanding Universe”. In: *Mon. Not. Roy. Astron. Soc.* 108 (1948), p. 252.

[77] R. A. Alpher, H. Bethe, and G. Gamow. “The origin of chemical elements”. In: *Phys. Rev.* 73 (1948), pp. 803–804. DOI: 10.1103/PhysRev.73.803.

[78] R. A. Alpher. “A Neutron-Capture Theory of the Formation and Relative Abundance of the Elements”. In: *Phys. Rev.* 74.11 (1948), pp. 1577–1589. DOI: 10.1103/PhysRev.74.1577.

[79] Ralph A. Alpher and Robert C. Herman. “On the Relative Abundance of the Elements”. In: *Phys. Rev.* 74.12 (1948), pp. 1737–1742. DOI: 10.1103/physrev.74.1737.

[80] R. H. Dicke et al. “Cosmic Black-Body Radiation”. In: *Astrophys. J.* 142 (1965), pp. 414–419. DOI: 10.1086/148306.

[81] Arno A. Penzias and Robert Woodrow Wilson. “A Measurement of excess antenna temperature at 4080-Mc/s”. In: *Astrophys. J.* 142 (1965), pp. 419–421. DOI: 10.1086/148307.

[82] F. Zwicky. “Die Rotverschiebung von extragalaktischen Nebeln”. In: *Helv. Phys. Acta* 6 (1933), pp. 110–127. DOI: 10.1007/s10714-008-0707-4.

[83] F. Zwicky. “On the Masses of Nebulae and of Clusters of Nebulae”. In: *Astrophys. J.* 86 (1937), pp. 217–246. DOI: 10.1086/143864.

[84] Vera C. Rubin, W. Kent Ford Jr., and Norbert Thonnard. “Extended rotation curves of high-luminosity spiral galaxies. IV. Systematic dynamical properties, Sa through Sc”. In: *Astrophys. J. Lett.* 225 (1978), pp. L107–L111. DOI: 10.1086/182804.

[85] V. C. Rubin, N. Thonnard, and W. K. Ford Jr. “Rotational properties of 21 SC galaxies with a large range of luminosities and radii, from NGC 4605 /R = 4kpc/ to UGC 2885 /R = 122 kpc/”. In: *Astrophys. J.* 238 (1980), p. 471. DOI: 10.1086/158003.

[86] Ludovic van Waerbeke et al. “Detection of correlated galaxy ellipticities on CFHT data: First evidence for gravitational lensing by large scale structures”. In: *Astron. Astrophys.* 358 (2000), pp. 30–44. arXiv: astro-ph/0002500.

[87] David J. Bacon, Alexandre R. Refregier, and Richard S. Ellis. “Detection of weak gravitational lensing by large-scale structure”. In: *Mon. Not. Roy. Astron. Soc.* 318 (2000), p. 625. DOI: 10.1046/j.1365-8711.2000.03851.x. arXiv: astro-ph/0003008.

[88] David M. Wittman et al. “Detection of weak gravitational lensing distortions of distant galaxies by cosmic dark matter at large scales”. In: *Nature* 405 (2000), pp. 143–149. DOI: 10.1038/35012001. arXiv: astro-ph/0003014.

[89] Richard Massey, Thomas Kitching, and Johan Richard. “The dark matter of gravitational lensing”. In: *Rept. Prog. Phys.* 73 (2010), p. 086901. DOI: 10.1088/0034-4885/73/8/086901. arXiv: 1001.1739 [astro-ph.CO].

[90] Douglas Clowe et al. “A direct empirical proof of the existence of dark matter”. In: *Astrophys. J. Lett.* 648 (2006), pp. L109–L113. DOI: 10.1086/508162. arXiv: astro-ph/0608407.

[91] David Harvey et al. “The non-gravitational interactions of dark matter in colliding galaxy clusters”. In: *Science* 347 (2015), pp. 1462–1465. DOI: 10.1126/science.1261381. arXiv: 1503.07675 [astro-ph.CO].

[92] Andrew Robertson, Richard Massey, and Vincent Eke. “Cosmic particle colliders: simulations of self-interacting dark matter with anisotropic scattering”. In: *Mon. Not. Roy. Astron. Soc.* 467.4 (2017), pp. 4719–4730. DOI: 10.1093/mnras/stx463. arXiv: 1612.03906 [astro-ph.CO].

[93] Adam G. Riess et al. “Observational evidence from supernovae for an accelerating universe and a cosmological constant”. In: *Astron. J.* 116 (1998), pp. 1009–1038. DOI: 10.1086/300499. arXiv: astro-ph/9805201.

[94] S. Perlmutter et al. “Measurements of Ω and Λ from 42 High Redshift Supernovae”. In: *Astrophys. J.* 517 (1999), pp. 565–586. DOI: 10.1086/307221. arXiv: astro-ph/9812133.

[95] Sean M. Carroll. *Spacetime and Geometry: An Introduction to General Relativity*. Cambridge University Press, July 2019. ISBN: 978-0-8053-8732-2, 978-1-108-48839-6, 978-1-108-77555-7. DOI: 10.1017/9781108770385.

[96] Edward W. Kolb and Michael S. Turner. *The Early Universe*. Vol. 69. Taylor and Francis, May 2019. ISBN: 978-0-429-49286-0, 978-0-201-62674-2. DOI: 10.1201/9780429492860.

[97] Daniel Baumann. *Cosmology*. Cambridge University Press, July 2022. ISBN: 978-1-108-93709-2, 978-1-108-83807-8. DOI: 10.1017/9781108937092.

[98] M. Tanabashi et al. “Review of Particle Physics”. In: *Phys. Rev. D* 98.3 (2018), p. 030001. DOI: 10.1103/PhysRevD.98.030001.

[99] Adam G. Riess et al. “Cosmic Distances Calibrated to 1% Precision with Gaia EDR3 Parallaxes and Hubble Space Telescope Photometry of 75 Milky Way Cepheids Confirm Tension with ΛCDM”. In: *Astrophys. J. Lett.* 908.1 (2021), p. L6. DOI: 10.3847/2041-8213/abdbaf. arXiv: 2012.08534 [astro-ph.CO].

[100] A. D. Sakharov. “Violation of CP Invariance, C asymmetry, and baryon asymmetry of the universe”. In: *Pisma Zh. Eksp. Teor. Fiz.* 5 (1967), pp. 32–35. DOI: 10.1070/PU1991v034n05ABEH002497.

[101] Jack J. Bennett et al. “Towards a precision calculation of $N_{\rm eff}$ in the Standard Model II: Neutrino decoupling in the presence of flavour oscillations and finite-temperature QED”. In: *JCAP* 04 (2021), p. 073. DOI: 10.1088/1475-7516/2021/04/073. arXiv: 2012.02726 [hep-ph].

[102] Tsung-Han Yeh et al. “Probing physics beyond the standard model: limits from BBN and the CMB independently and combined”. In: *JCAP* 10 (2022), p. 046. DOI: 10.1088/1475-7516/2022/10/046. arXiv: 2207.13133 [astro-ph.CO].

[103] Albert Einstein and N. Rosen. “On Gravitational waves”. In: *J. Franklin Inst.* 223 (1937), pp. 43–54. DOI: 10.1016/S0016-0032(37)90583-0.

[104] F. A. E. Pirani. “Invariant formulation of gravitational radiation theory”. In: *Phys. Rev.* 105 (1957), pp. 1089–1099. DOI: 10.1103/PhysRev.105.1089.

[105] R. A. Hulse and J. H. Taylor. “Discovery of a pulsar in a binary system”. In: *Astrophys. J. Lett.* 195 (1975), pp. L51–L53. DOI: 10.1086/181708.

[106] J. H. Taylor, L. A. Fowler, and P. M. McCulloch. “Measurements of general relativistic effects in the binary pulsar PSR 1913+16”. In: *Nature* 277 (1979), pp. 437–440. DOI: 10.1038/277437a0.

[107] G. E. Moss, L. R. Miller, and R. L. Forward. “Photon-noise-limited laser transducer for gravitational antenna”. In: *Appl. Opt.* 10 (1971), pp. 2495–2498. DOI: 10.1364/AO.10.002495.

[108] Rainer Weiss. “Republication of: Electromagnetically coupled broadband gravitational antenna”. In: *Gen. Rel. Grav.* 54.11 (2022), p. 153. DOI: 10.1007/s10714-022-03021-3.

[109] Albert Abraham Michelson and Edward Williams Morley. “On the Relative Motion of the Earth and the Luminiferous Ether”. In: *Am. J. Sci.* 34 (1887), pp. 333–345. DOI: 10.2475/ajs.s3-34.203.333.

[110] Mikhail V. Sazhin. “Opportunities for detecting ultralong gravitational waves”. In: *Sov. Astron.* 22 (1978), pp. 36–38.

[111] Steven L. Detweiler. “Pulsar timing measurements and the search for gravitational waves”. In: *Astrophys. J.* 234 (1979), pp. 1100–1104. DOI: 10.1086/157593.

[112] Michele Maggiore. *Gravitational Waves. Vol. 1: Theory and Experiments*. Oxford University Press, 2007. ISBN: 978-0-19-171766-6, 978-0-19-852074-0. DOI: 10.1093/acprof:oso/9780198570745.001.0001.

[113] Michele Maggiore. *Gravitational Waves. Vol. 2: Astrophysics and Cosmology*. Oxford University Press, Mar. 2018. ISBN: 978-0-19-857089-9.

[114] Chiara Caprini and Daniel G. Figueroa. “Cosmological Backgrounds of Gravitational Waves”. In: *Class. Quant. Grav.* 35.16 (2018), p. 163001. DOI: 10.1088/1361-6382/aac608. arXiv: 1801.04268 [astro-ph.CO].

[115] Lev Davidovich Landau. “On the theory of stars”. In: *Phys. Z. Sowjetunion* 1 (1932). Ed. by D. ter Haar, p. 285. DOI: 10.1016/B978-0-08-010586-4.50013-4.

[116] W. Baade and F. Zwicky. “On Super-Novae”. In: *Proc. Nat. Acad. Sci.* 20.5 (1934), pp. 254–259. DOI: 10.1073/pnas.20.5.254.

[117] F. Pacini. “Rotating Neutron Stars, Pulsars and Supernova Remnants”. In: *Nature* 219.5150 (1968), pp. 145–146. DOI: 10.1038/219145a0.

[118] T. Gold. “Rotating neutron stars as the origin of the pulsating radio sources”. In: *Nature* 218 (1968), pp. 731–732. DOI: 10.1038/218731a0.

[119] R. w. Hellings and G. s. Downs. “UPPER LIMITS ON THE ISOTROPIC GRAVITATIONAL RADIATION BACKGROUND FROM PULSAR TIMING ANALYSIS”. In: *Astrophys. J. Lett.* 265 (1983), pp. L39–L42. DOI: 10.1086/183954.

[120] R. S. Foster and D. C. Backer. “Constructing a Pulsar Timing Array”. In: *APJ* 361 (Sept. 1990), p. 300. DOI: 10.1086/169195.

[121] P. A. M. Dirac. “The Quantum theory of electron. 2.” In: *Proc. Roy. Soc. Lond. A* 118 (1928), p. 351. DOI: 10.1098/rspa.1928.0056.

[122] Paul A. M. Dirac. “The quantum theory of the electron”. In: *Proc. Roy. Soc. Lond. A* 117 (1928), pp. 610–624. DOI: 10.1098/rspa.1928.0023.

[123] Albert Einstein. “Concerning an heuristic point of view toward the emission and transformation of light”. In: *Annalen Phys.* 17 (1905), pp. 132–148.

[124] Oskar Klein. “Quantentheorie und fünfdimensionale Relativitätstheorie”. In: *Z. Phys.* 37 (1926). Ed. by J. C. Taylor, pp. 895–906. DOI: 10.1007/BF01397481.

[125] W. Gordon. “Der Comptoneffekt nach der Schrödingerschen Theorie”. In: *Z. Phys.* 40.1 (1926), pp. 117–133. DOI: 10.1007/BF01390840.

[126] H. Weyl. “Quantum mechanics and group theory”. In: *Z. Phys.* 46 (1927), p. 1. DOI: 10.1007/BF02055756.

[127] E. Fermi. “An attempt of a theory of beta radiation. 1.” In: *Z. Phys.* 88 (1934), pp. 161–177. DOI: 10.1007/BF01351864.

[128] R. P. Feynman. “Space - time approach to quantum electrodynamics”. In: *Phys. Rev.* 76 (1949). Ed. by L. M. Brown, pp. 769–789. DOI: 10.1103/PhysRev.76.769.

[129] Julian S. Schwinger. “On Quantum electrodynamics and the magnetic moment of the electron”. In: *Phys. Rev.* 73 (1948), pp. 416–417. DOI: 10.1103/PhysRev.73.416.

[130] S. Tomonaga. “On a relativistically invariant formulation of the quantum theory of wave fields”. In: *Prog. Theor. Phys.* 1 (1946), pp. 27–42. DOI: 10.1143/PTP.1.27.

[131] Chen-Ning Yang and Robert L. Mills. “Conservation of Isotopic Spin and Isotopic Gauge Invariance”. In: *Phys. Rev.* 96 (1954). Ed. by Jong-Ping Hsu and D. Fine, pp. 191–195. DOI: 10.1103/PhysRev.96.191.

[132] S. L. Glashow. “Partial Symmetries of Weak Interactions”. In: *Nucl. Phys.* 22 (1961), pp. 579–588. DOI: 10.1016/0029-5582(61)90469-2.

[133] Steven Weinberg. “A Model of Leptons”. In: *Phys. Rev. Lett.* 19 (1967), pp. 1264–1266. DOI: 10.1103/PhysRevLett.19.1264.

[134] Abdus Salam and John Clive Ward. “Weak and electromagnetic interactions”. In: *Nuovo Cim.* 11 (1959), pp. 568–577. DOI: 10.1007/BF02726525.

[135] Peter W. Higgs. “Broken symmetries, massless particles and gauge fields”. In: *Phys. Lett.* 12 (1964), pp. 132–133. DOI: 10.1016/0031-9163(64)91136-9.

[136] Peter W. Higgs. “Spontaneous Symmetry Breakdown without Massless Bosons”. In: *Phys. Rev.* 145 (1966), pp. 1156–1163. DOI: 10.1103/PhysRev.145.1156.

[137] F. Englert and R. Brout. “Broken Symmetry and the Mass of Gauge Vector Mesons”. In: *Phys. Rev. Lett.* 13 (1964). Ed. by J. C. Taylor, pp. 321–323. DOI: 10.1103/PhysRevLett.13.321.

[138] G. S. Guralnik, C. R. Hagen, and T. W. B. Kibble. “Global Conservation Laws and Massless Particles”. In: *Phys. Rev. Lett.* 13 (1964). Ed. by J. C. Taylor, pp. 585–587. DOI: 10.1103/PhysRevLett.13.585.

[139] Yoichiro Nambu. “Quasiparticles and Gauge Invariance in the Theory of Superconductivity”. In: *Phys. Rev.* 117 (1960). Ed. by J. C. Taylor, pp. 648–663. DOI: 10.1103/PhysRev.117.648.

[140] J. Goldstone. “Field Theories with Superconductor Solutions”. In: *Nuovo Cim.* 19 (1961), pp. 154–164. DOI: 10.1007/BF02812722.

[141] Jeffrey Goldstone, Abdus Salam, and Steven Weinberg. “Broken Symmetries”. In: *Phys. Rev.* 127 (1962), pp. 965–970. DOI: 10.1103/PhysRev.127.965.

[142] Gerard ’t Hooft. “Renormalization of Massless Yang-Mills Fields”. In: *Nucl. Phys. B* 33 (1971), pp. 173–199. DOI: 10.1016/0550-3213(71)90395-6.

[143] Gerard 't Hooft. "Renormalizable Lagrangians for Massive Yang-Mills Fields". In: *Nucl. Phys. B* 35 (1971). Ed. by J. C. Taylor, pp. 167–188. DOI: 10.1016/0550-3213(71)90139-8.

[144] Gerard 't Hooft and M. J. G. Veltman. "Regularization and Renormalization of Gauge Fields". In: *Nucl. Phys. B* 44 (1972), pp. 189–213. DOI: 10.1016/0550-3213(72)90279-9.

[145] Harald Fritzsch and Murray Gell-Mann. "Current algebra: Quarks and what else?" In: *eConf* C720906V2 (1972). Ed. by J. D. Jackson and A. Roberts, pp. 135–165. arXiv: hep-ph/0208010.

[146] H. Fritzsch, Murray Gell-Mann, and H. Leutwyler. "Advantages of the Color Octet Gluon Picture". In: *Phys. Lett. B* 47 (1973), pp. 365–368. DOI: 10.1016/0370-2693(73)90625-4.

[147] David J. Gross and Frank Wilczek. "Ultraviolet Behavior of Nonabelian Gauge Theories". In: *Phys. Rev. Lett.* 30 (1973). Ed. by J. C. Taylor, pp. 1343–1346. DOI: 10.1103/PhysRevLett.30.1343.

[148] H. David Politzer. "Reliable Perturbative Results for Strong Interactions?" In: *Phys. Rev. Lett.* 30 (1973). Ed. by J. C. Taylor, pp. 1346–1349. DOI: 10.1103/PhysRevLett.30.1346.

[149] Michael E. Peskin and Daniel V. Schroeder. *An Introduction to quantum field theory*. Reading, USA: Addison-Wesley, 1995. ISBN: 978-0-201-50397-5, 978-0-429-50355-9, 978-0-429-49417-8. DOI: 10.1201/9780429503559.

[150] Matthew D. Schwartz. *Quantum Field Theory and the Standard Model*. Cambridge University Press, Mar. 2014. ISBN: 978-1-107-03473-0, 978-1-107-03473-0.

[151] Matteo Zandi. "I teoremi di Noether: simmetrie, leggi di conservazione e teorie di gauge". Bachelor's Thesis. URL: https://amslaurea.unibo.it/id/eprint/29415/.

[152] Georges Aad et al. "Observation of a new particle in the search for the Standard Model Higgs boson with the ATLAS detector at the LHC". In: *Phys. Lett. B* 716 (2012), pp. 1–29. DOI: 10.1016/j.physletb.2012.08.020. arXiv: 1207.7214 [hep-ex].

[153] Serguei Chatrchyan et al. "Observation of a New Boson at a Mass of 125 GeV with the CMS Experiment at the LHC". In: *Phys. Lett. B* 716 (2012), pp. 30–61. DOI: 10.1016/j.physletb.2012.08.021. arXiv: 1207.7235 [hep-ex].

[154] Marco Cirelli, Alessandro Strumia, and Jure Zupan. "Dark Matter". In: (June 2024). arXiv: 2406.01705 [hep-ph].

[155] Marco Fabbrichesi, Emidio Gabrielli, and Gaia Lanfranchi. "The Dark Photon". In: (May 2020). DOI: 10.1007/978-3-030-62519-1. arXiv: 2005.01515 [hep-ph].

[156] Daniel Feldman, Zuowei Liu, and Pran Nath. "The Stueckelberg Z-prime Extension with Kinetic Mixing and Milli-Charged Dark Matter From the Hidden Sector". In: *Phys. Rev. D* 75 (2007), p. 115001. DOI: 10.1103/PhysRevD.75.115001. arXiv: hep-ph/0702123.

[157] Bob Holdom. "Two U(1)'s and Epsilon Charge Shifts". In: *Phys. Lett. B* 166 (1986), pp. 196–198. DOI: 10.1016/0370-2693(86)91377-8.

[158] E. C. G. Stueckelberg. "Interaction forces in electrodynamics and in the field theory of nuclear forces". In: *Helv. Phys. Acta* 11 (1938), pp. 299–328.

[159] W. Heisenberg and H. Euler. "Consequences of Dirac's theory of positrons". In: *Z. Phys.* 98.11-12 (1936), pp. 714–732. DOI: 10.1007/BF01343663. arXiv: physics/0605038.

[160] Julian S. Schwinger. “On gauge invariance and vacuum polarization”. In: *Phys. Rev.* 82 (1951). Ed. by K. A. Milton, pp. 664–679. DOI: 10.1103/PhysRev.82.664.

[161] G. Jona-Lasinio. “Relativistic field theories with symmetry breaking solutions”. In: *Nuovo Cim.* 34 (1964), pp. 1790–1795. DOI: 10.1007/BF02750573.

[162] Sidney R. Coleman and Erick J. Weinberg. “Radiative Corrections as the Origin of Spontaneous Symmetry Breaking”. In: *Phys. Rev. D* 7 (1973), pp. 1888–1910. DOI: 10.1103/PhysRevD.7.1888.

[163] R. Jackiw. “Functional evaluation of the effective potential”. In: *Phys. Rev. D* 9 (1974), p. 1686. DOI: 10.1103/PhysRevD.9.1686.

[164] J. Iliopoulos, C. Itzykson, and Andre Martin. “Functional Methods and Perturbation Theory”. In: *Rev. Mod. Phys.* 47 (1975), p. 165. DOI: 10.1103/RevModPhys.47.165.

[165] D. A. Kirzhnits. “Weinberg model in the hot universe”. In: *JETP Lett.* 15 (1972), pp. 529–531.

[166] D. A. Kirzhnits and Andrei D. Linde. “Macroscopic Consequences of the Weinberg Model”. In: *Phys. Lett. B* 42 (1972), pp. 471–474. DOI: 10.1016/0370-2693(72)90109-8.

[167] Claude W. Bernard. “Feynman Rules for Gauge Theories at Finite Temperature”. In: *Phys. Rev. D* 9 (1974), p. 3312. DOI: 10.1103/PhysRevD.9.3312.

[168] L. Dolan and R. Jackiw. “Symmetry Behavior at Finite Temperature”. In: *Phys. Rev. D* 9 (1974), pp. 3320–3341. DOI: 10.1103/PhysRevD.9.3320.

[169] Steven Weinberg. “Gauge and Global Symmetries at High Temperature”. In: *Phys. Rev. D* 9 (1974), pp. 3357–3378. DOI: 10.1103/PhysRevD.9.3357.

[170] I. Yu. Kobzarev, L. B. Okun, and M. B. Voloshin. “Bubbles in Metastable Vacuum”. In: *Yadernaya Fizika* 20 (1974). Sov. J. Nucl. Phys. 20 (1975) 644–646 [English translation], pp. 1229–1234. URL: https://inis.iaea.org/search/search.aspx?orig_q=RN:7276129.

[171] D. A. Kirzhnits and Andrei D. Linde. “A Relativistic phase transition”. In: *Zh. Eksp. Teor. Fiz.* 67 (1974), pp. 1263–1275.

[172] Andrei D. Linde. “Phase Transitions in Gauge Theories and Cosmology”. In: *Rept. Prog. Phys.* 42 (1979), p. 389. DOI: 10.1088/0034-4885/42/3/001.

[173] Andrei D. Linde. “Infrared Problem in Thermodynamics of the Yang-Mills Gas”. In: *Phys. Lett. B* 96 (1980), pp. 289–292. DOI: 10.1016/0370-2693(80)90769-8.

[174] Alan H. Guth and Erick J. Weinberg. “Cosmological Consequences of a First Order Phase Transition in the SU(5) Grand Unified Model”. In: *Phys. Rev. D* 23 (1981), p. 876. DOI: 10.1103/PhysRevD.23.876.

[175] Edward Witten. “Cosmological Consequences of a Light Higgs Boson”. In: *Nucl. Phys. B* 177 (1981), pp. 477–488. DOI: 10.1016/0550-3213(81)90182-6.

[176] Steven Weinberg. *The quantum theory of fields. Vol. 2: Modern applications*. Cambridge University Press, Aug. 2013. ISBN: 978-1-139-63247-8, 978-0-521-67054-8, 978-0-521-55002-4. DOI: 10.1017/CBO9781139644174.

[177] Mariano Quiros. “Finite temperature field theory and phase transitions”. In: *ICTP Summer School in High-Energy Physics and Cosmology*. Jan. 1999, pp. 187–259. arXiv: hep-ph/9901312.

[178] Peter Athron et al. “Cosmological phase transitions: From perturbative particle physics to gravitational waves”. In: *Prog. Part. Nucl. Phys.* 135 (2024), p. 104094. DOI: 10.1016/j.ppnp.2023.104094. arXiv: 2305.02357 [hep-ph].

[179] C. G. Bollini and J. J. Giambiagi. “Dimensional Renormalization: The Number of Dimensions as a Regularizing Parameter”. In: *Nuovo Cim. B* 12 (1972), pp. 20–26. DOI: 10.1007/BF02895558.

[180] J. F. Ashmore. “A Method of Gauge Invariant Regularization”. In: *Lett. Nuovo Cim.* 4 (1972), pp. 289–290. DOI: 10.1007/BF02824407.

[181] Greg W. Anderson and Lawrence J. Hall. “The Electroweak phase transition and baryogenesis”. In: *Phys. Rev. D* 45 (1992), pp. 2685–2698. DOI: 10.1103/PhysRevD.45.2685.

[182] Gerard ’t Hooft. “Dimensional regularization and the renormalization group”. In: *Nucl. Phys. B* 61 (1973), pp. 455–468. DOI: 10.1016/0550-3213(73)90376-3.

[183] William A. Bardeen et al. “Deep Inelastic Scattering Beyond the Leading Order in Asymptotically Free Gauge Theories”. In: *Phys. Rev. D* 18 (1978), p. 3998. DOI: 10.1103/PhysRevD.18.3998.

[184] R. Kubo. “Statistical mechanical theory of irreversible processes. 1. General theory and simple applications in magnetic and conduction problems”. In: *Journal of the Physical Society of Japan* 12 (1957), pp. 570–586. DOI: 10.1143/JPSJ.12.570.

[185] P. C. Martin and J. S. Schwinger. “Theory of many particle systems. 1.” In: *Physical Review* 115 (1959), pp. 1342–1373. DOI: 10.1103/PhysRev.115.1342.

[186] D. A. Kirzhnits and Andrei D. Linde. “Symmetry Behavior in Gauge Theories”. In: *Annals Phys.* 101 (1976), pp. 195–238. DOI: 10.1016/0003-4916(76)90279-7.

[187] Peter Arnold and Olivier Espinosa. “Effective potential and first-order phase transitions: Beyond leading order”. In: *Phys. Rev. D* 47 (8 Apr. 1993), pp. 3546–3579. DOI: 10.1103/PhysRevD.47.3546. URL: https://link.aps.org/doi/10.1103/PhysRevD.47.3546.

[188] M. E. Carrington. “Effective potential at finite temperature in the standard model”. In: *Phys. Rev. D* 45 (8 Apr. 1992), pp. 2933–2944. DOI: 10.1103/PhysRevD.45.2933. URL: https://link.aps.org/doi/10.1103/PhysRevD.45.2933.

[189] Lev Davidovich Landau and E. M. Lifshits. *Quantum Mechanics: Non-Relativistic Theory*. Vol. v.3. Course of Theoretical Physics. Oxford: Butterworth-Heinemann, 1991. ISBN: 978-0-7506-3539-4. DOI: 10.1016/C2013-0-02793-4.

[190] Carroll L. Wainwright. “CosmoTransitions: Computing Cosmological Phase Transition Temperatures and Bubble Profiles with Multiple Fields”. In: *Comput. Phys. Commun.* 183 (2012), pp. 2006–2013. DOI: 10.1016/j.cpc.2012.04.004. arXiv: 1109.4189 [hep-ph].

[191] Ali Masoumi, Ken D. Olum, and Jeremy M. Wachter. “Approximating tunneling rates in multi-dimensional field spaces”. In: *JCAP* 10 (2017). [Erratum: JCAP 05, E01 (2023)], p. 022. DOI: 10.1088/1475-7516/2017/10/022. arXiv: 1702.00356 [gr-qc].

[192] Victor Guada, Miha Nemevšek, and Matevž Pintar. “FindBounce: Package for multi-field bounce actions”. In: *Comput. Phys. Commun.* 256 (2020), p. 107480. DOI: 10.1016/j.cpc.2020.107480. arXiv: 2002.00881 [hep-ph].

[193] Peter Athron et al. “BubbleProfiler: finding the field profile and action for cosmological phase transitions”. In: *Comput. Phys. Commun.* 244 (2019), pp. 448–468. DOI: 10.1016/j.cpc.2019.05.017. arXiv: 1901.03714 [hep-ph].

[194] Ryosuke Sato. “Simple Gradient Flow Equation for the Bounce Solution”. In: *Phys. Rev. D* 101.1 (2020), p. 016012. DOI: 10.1103/PhysRevD.101.016012. arXiv: 1907.02417 [hep-ph].

[195] Ryosuke Sato. “SimpleBounce : a simple package for the false vacuum decay”. In: *Comput. Phys. Commun.* 258 (2021), p. 107566. DOI: 10.1016/j.cpc.2020.107566. arXiv: 1908.10868 [hep-ph].

[196] A. N. Kolmogorov. “On the statistical theory of metal crystallization”. In: *Izvestiya Akademii Nauk SSSR, Seriya Matematicheskaya* 1 (1937), pp. 355–359.

[197] W. A. Johnson and R. F. Mehl. “Reaction kinetics in processes of nucleation and growth”. In: *Transactions of the American Institute of Mining, Metallurgical, and Petroleum Engineers* 135 (1939), pp. 416–458.

[198] Melvin Avrami. “Kinetics of Phase Change. I General Theory”. In: *The Journal of Chemical Physics* 7.12 (Dec. 1939), pp. 1103–1112. ISSN: 0021-9606. DOI: 10.1063/1.1750380. eprint: https://pubs.aip.org/aip/jcp/article-pdf/7/12/1103/18791257/1103_1_online.pdf. URL: https://doi.org/10.1063/1.1750380.

[199] Melvin Avrami. “Kinetics of Phase Change. II Transformation-Time Relations for Random Distribution of Nuclei”. In: *The Journal of Chemical Physics* 8.2 (Feb. 1940), pp. 212–224. ISSN: 0021-9606. DOI: 10.1063/1.1750631. eprint: https://pubs.aip.org/aip/jcp/article-pdf/8/2/212/18791481/212_1_online.pdf. URL: https://doi.org/10.1063/1.1750631.

[200] Melvin Avrami. “Granulation, Phase Change, and Microstructure Kinetics of Phase Change. III”. In: *The Journal of Chemical Physics* 9.2 (Feb. 1941), pp. 177–184. ISSN: 0021-9606. DOI: 10.1063/1.1750872. eprint: https://pubs.aip.org/aip/jcp/article-pdf/9/2/177/18792034/177_1_online.pdf. URL: https://doi.org/10.1063/1.1750872.

[201] Ariel Megevand. “Development of the electroweak phase transition and baryogenesis”. In: *Int. J. Mod. Phys. D* 9 (2000), pp. 733–756. DOI: 10.1142/S0218271800000724. arXiv: hep-ph/0006177.

[202] Ariel Megevand and Alejandro D. Sanchez. “Supercooling and phase coexistence in cosmological phase transitions”. In: *Phys. Rev. D* 77 (2008), p. 063519. DOI: 10.1103/PhysRevD.77.063519. arXiv: 0712.1031 [hep-ph].

[203] A. Chodos et al. “A New Extended Model of Hadrons”. In: *Phys. Rev. D* 9 (1974), pp. 3471–3495. DOI: 10.1103/PhysRevD.9.3471.

[204] S.R. Broadbent and J.M. Hammersley. *Percolation processes: I. Crystals and mazes*. Vol. 53. 3. Cambridge University Press, 1957, pp. 629–641. DOI: 10.1017/S0305004100032680.

[205] V.K.S. Shante and S. Kirkpatrick. “An introduction to percolation theory”. In: *Advances in Physics* 20.85 (1971), pp. 325–357. DOI: 10.1080/00018737100101261.

[206] Allen Hunt, Robert Ewing, and Behzad Ghanbarian. *Percolation Theory for Flow in Porous Media*. Vol. 880. Lecture Notes in Physics. Springer, 2014. DOI: 10.1007/978-3-319-04044-8.

[207] Christian D. Lorenz and Robert M. Ziff. “Precise determination of the critical percolation threshold for the three-dimensional ”Swiss cheese” model using a growth algorithm”. In: *The Journal of Chemical Physics* 114.8 (2001), pp. 3659–3661. DOI: 10.1063/1.1338506.

[208] J. Lin and H. Chen. “Continuum percolation of porous media via random packing of overlapping cube-like particles”. In: *Theoretical and Applied Mechanics Letters* 8.5 (2018), pp. 299–303. DOI: 10.1016/j.taml.2018.06.004.

[209] M. Li, H. Chen, and J. Lin. “Numerical study for the percolation threshold and transport properties of porous composites comprising non-centrosymmetrical superovoidal pores”. In: *Computer Methods in Applied Mechanics and Engineering* 361 (2020), p. 112815. DOI: 10.1016/j.cma.2019.112815.

[210] Michael S. Turner, Erick J. Weinberg, and Lawrence M. Widrow. “Bubble nucleation in first order inflation and other cosmological phase transitions”. In: *Phys. Rev. D* 46 (1992), pp. 2384–2403. DOI: 10.1103/PhysRevD.46.2384.

[211] John Ellis, Marek Lewicki, and José Miguel No. “On the Maximal Strength of a First-Order Electroweak Phase Transition and its Gravitational Wave Signal”. In: *JCAP* 04 (2019), p. 003. DOI: 10.1088/1475-7516/2019/04/003. arXiv: 1809.08242 [hep-ph].

[212] Mark B. Hindmarsh et al. “Phase transitions in the early universe”. In: *SciPost Phys. Lect. Notes* 24 (2021), p. 1. DOI: 10.21468/SciPostPhysLectNotes.24. arXiv: 2008.09136 [astro-ph.CO].

[213] Aleksandr Azatov, Daniele Barducci, and Francesco Sgarlata. “Gravitational traces of broken gauge symmetries”. In: *JCAP* 07 (2020), p. 027. DOI: 10.1088/1475-7516/2020/07/027. arXiv: 1910.01124 [hep-ph].

[214] Dietrich Bodeker and Guy D. Moore. “Can electroweak bubble walls run away?” In: *JCAP* 05 (2009), p. 009. DOI: 10.1088/1475-7516/2009/05/009. arXiv: 0903.4099 [hep-ph].

[215] Dietrich Bodeker and Guy D. Moore. “Electroweak Bubble Wall Speed Limit”. In: *JCAP* 05 (2017), p. 025. DOI: 10.1088/1475-7516/2017/05/025. arXiv: 1703.08215 [hep-ph].

[216] Jose R. Espinosa et al. “Energy Budget of Cosmological First-order Phase Transitions”. In: *JCAP* 06 (2010), p. 028. DOI: 10.1088/1475-7516/2010/06/028. arXiv: 1004.4187 [hep-ph].

[217] John Ellis et al. “Gravitational wave energy budget in strongly supercooled phase transitions”. In: *JCAP* 06 (2019), p. 024. DOI: 10.1088/1475-7516/2019/06/024. arXiv: 1903.09642 [hep-ph].

[218] Chiara Caprini et al. “Science with the space-based interferometer eLISA. II: Gravitational waves from cosmological phase transitions”. In: *JCAP* 04 (2016), p. 001. DOI: 10.1088/1475-7516/2016/04/001. arXiv: 1512.06239 [astro-ph.CO].

[219] Chiara Caprini et al. “Detecting gravitational waves from cosmological phase transitions with LISA: an update”. In: *JCAP* 03 (2020), p. 024. DOI: 10.1088/1475-7516/2020/03/024. arXiv: 1910.13125 [astro-ph.CO].

[220] Máximo Bañados and Ignacio A. Reyes. “A short review on Noether’s theorems, gauge symmetries and boundary terms”. In: *Int. J. Mod. Phys. D* 25.10 (2016), p. 1630021. DOI: 10.1142/S0218271816300214. arXiv: 1601.03616 [hep-th].

[221] Eldad Gildener and Steven Weinberg. “Symmetry Breaking and Scalar Bosons”. In: *Phys. Rev. D* 13 (1976), p. 3333. DOI: 10.1103/PhysRevD.13.3333.

[222] Fred C. Adams. “General solutions for tunneling of scalar fields with quartic potentials”. In: *Phys. Rev. D* 48 (1993), pp. 2800–2805. DOI: 10.1103/PhysRevD.48.2800. arXiv: hep-ph/9302321.

[223] Uri Sarid. “Tools for tunneling”. In: *Phys. Rev. D* 58 (1998), p. 085017. DOI: 10.1103/PhysRevD.58.085017. arXiv: hep-ph/9804308.

[224] Michael Dine et al. “Towards the theory of the electroweak phase transition”. In: *Phys. Rev. D* 46 (1992), pp. 550–571. DOI: 10.1103/PhysRevD.46.550. arXiv: hep-ph/9203203.

[225] Sujeet Akula, Csaba Balázs, and Graham A. White. “Semi-analytic techniques for calculating bubble wall profiles”. In: *Eur. Phys. J. C* 76.12 (2016), p. 681. DOI: 10.1140/epjc/s10052-016-4519-5. arXiv: 1608.00008 [hep-ph].

[226] Marco Matteini et al. “False vacuum decay rate from thin to thick walls”. In: *JHEP* 04 (2025), p. 120. DOI: 10.1007/JHEP04(2025)120. arXiv: 2404.17632 [hep-th].

[227] E. Brezin and G. Parisi. “Critical exponents and large order behavior of perturbation theory”. In: (1992), pp. 269–292.

[228] Lohan Sartore and Ingo Schienbein. “PyR@TE 3”. In: *Comput. Phys. Commun.* 261 (2021), p. 107819. DOI: 10.1016/j.cpc.2020.107819. arXiv: 2007.12700 [hep-ph].

[229] Colin Poole and Anders Eller Thomsen. “Constraints on 3- and 4-loop β-functions in a general four-dimensional Quantum Field Theory”. In: *JHEP* 09 (2019), p. 055. DOI: 10.1007/JHEP09(2019)055. arXiv: 1906.04625 [hep-th].

[230] Andrea Mitridate et al. “PTArcade”. In: (June 2023). arXiv: 2306.16377 [hep-ph].